UNIVERSITY OF SOUTHAMPTON

Faculty of Engineering and the Environment

MULTI-FIDELITY STRATEGIES FOR LEAN BURN COMBUSTOR DESIGN

by

Moresh J. Wankhede

Thesis for the degree of Doctor of Philosophy

January 2012

University of Southampton

Faculty of Engineering and the Environment

ABSTRACT

Doctor of Philosophy

MULTI-FIDELITY STRATEGIES FOR LEAN BURN COMBUSTOR DESIGN

by Moresh J. Wankhede

In combustor design and development, the use of unsteady computational fluid dynamics (CFD) simulations of transient combustor aero-thermo-dynamics to provide an insight into the complex reacting flow-field is expensive in terms of computational time. A large number of such high-fidelity reactive CFD analyses of the objective and constraint functions are normally required in combustor design and optimisation process. Hence, traditional design strategies utilizing only high-fidelity CFD analyses are often ruled out, given the complexity in obtaining accurate flow predictions and limits on available computational resources and time. This necessitates a careful design of fast, reliable and efficient design strategies. Surrogate modeling design strategies, including Kriging models, are currently being used to balance the challenges of accuracy and computational resource to accelerate the combustor design process. However, its feasibility still largely relies on the total number of design variables, objective and constraint functions, as only high-fidelity CFD analyses are used to construct the surrogate model.

This thesis explores these issues in combustor design by aiming to minimize the total number of high fidelity CFD runs and to accelerate the process of finding a good design earlier in the design process. Initially, various multi-fidelity design strategies employing a co-Kriging surrogate modeling approach were developed and assessed for performance and confidence against a traditional Kriging based design strategy, within a fixed computational budget. Later, a time-parallel combustor CFD simulation methodology is proposed, based on temporal domain decomposition, and further developed into a novel time-parallel co-Kriging based multi-fidelity design strategy requiring only a single CFD simulation to be setup for various fidelities. The performance and confidence assessment of the newly developed multi-fidelity strategies shows that they are, in general, competitive against the traditional Kriging based design strategy, and evidence exists of finding a good design early in the design optimisation process.

"The Jet Engine is a heat engine and the combustor is where the heat is created by converting the chemical energy of the fuel into thermal energy. Historically, the combustor has always been one of the most difficult areas of the engine to get right"

- "The Jet Engine", Rolls-Royce PLC

Contents

Appendices

Declaration of authorship

I, Moresh Jagdish Wankhede, declare that the thesis entitled "**Multi-fidelity Strategies for Lean Burn Combustor Design**" and the work presented in this thesis are both my own, and have been generated by me as the result of my own original research. I confirm that:

- this work was done wholly or mainly while in candidature for a research degree at this University;
- where any part of this thesis has previously been submitted for a degree or any other qualification at this University or any other institution, this has been clearly stated;
- where I have consulted the published work of others, this is always clearly attributed
- where I have quoted from the work of others, the source is always given. With the exception of such quotations, this thesis is entirely my own work;
- I have acknowledged all main sources of help;
- where the thesis is based on work done by myself jointly with others, I have made clear exactly what was done by others and what I have contributed myself;
- parts of this work have been published or are under review/preparation (see list of publications)

Signed: _____ Date: _____

Acknowledgements

Firstly, I would like to thank my research supervisors Dr. Neil W. Bressloff, Prof. Andy J. Keane and Dr. Marco Zedda (Rolls-Royce PLC) for giving me this opportunity to work with them and guiding me through this research study. I have learned many things from them, both technically and philosophically, while undergoing this research work.

Secondly, I also wish to thank Dr. David Toal and Dr. Ivan Voutchkov for their constant support and advice in the times of 'it just doesn't work'. Without their support, this journey would have been much harder. I also wish extend my thanks to Rolls-Royce Combustion Systems Engineering department, particularly Mr. Luca Caracciolo, Dr. Nick Pilatis, Dr. Chris Goddard, Dr. Chong Cha, Dr. Ravikanti Murthy and Mr. Emmanuel Aurifeille for their contributions in my understanding of the complex Rolls-Royce lean burn combustion system.

Over the last three years, Ph.D research in the lab was 'never' dull. This is especially due to my past and current colleagues - Sanjay, Karnik, Joshua, Adam, Giles, Stephen, Chandra and Aditya who provided the necessary time-away from work and also times of interesting debates and discussions on whatever topic we may find.

I wish to thank my father Jagdish, my mother Vijaya and my two younger brothers Chetan and Lalit, for their constant support, praise and motivation and understanding my 'research' student life. This research work is dedicated to them. Also, I would like to thank my family friends Mr. Pravin Gandhi and Mr. Harshad Parekh for their kind support.

Finally, I would like to thank Miss Rucha Gajbhiye for her support, motivation and understanding, which helped to maintain focus on this research work.

List of publications

Parts of this thesis are published or under review/preparation as follows:

Peer-reviewed publications

1. M. J. Wankhede, N. W. Bressloff, A. J. Keane, L. Caracciolo, and M. Zedda, 2010, "An analysis of unstable flow dynamics and flashback mechanism inside a swirl-stabilized lean burn combustor", GT2010-22253, Proceedings of ASME Turbo Expo 2010: Power for Land, Sea and Air, Glasgow, UK (ISBN: 978-0-7918-4397-0, DOI: 10.1115/GT2010-22253)
2. M. J. Wankhede, N. W. Bressloff, A. J. Keane, 2011, "Combustor design optimisation using co- Kriging of time-dependent turbulent combustion", GT2011-46420, Proceedings of ASME Turbo Expo 2011, Vancouver, Canada
3. M. J. Wankhede, N. W. Bressloff, A. J. Keane, 2011, "Combustor design optimisation using co- Kriging of time-dependent turbulent combustion", GTP-11-1113, Journal of Engineering for Gas Turbines and Power, 133 (12),(DOI:10.1115/1.4004155)
4. M. J. Wankhede, N. W. Bressloff, A. J. Keane, 2012, "A time-parallel CFD approach for unsteady combustor flow analysis and design optimisation", GT2012-68164, Proceedings of ASME Turbo Expo 2012, Copenhagen, Denmark
5. M. J. Wankhede, N. W. Bressloff, A. J. Keane, 2012, "Time-parallel co-Kriging based multi-fidelity strategy for combustor design optimisation", for Computational Optimization and Applications (Submitted)
6. M. J. Wankhede, N. W. Bressloff, A. J. Keane, 2012, "Multi-fidelity design optimisation of a combustor using co-Kriging of varying spatio-temporal combustion dynamics", for Computational Optimization and Applications (Submitted)

Other publications/posters/seminars

1. M. J. Wankhede, N. W. Bressloff, A. J. Keane, M. Zedda, 2009, "An analysis of precessing vortex core inside a lean burn combustor", in Annual CFD Review, Rolls-Royce PLC., UK
2. M. J. Wankhede, N. W. Bressloff, A. J. Keane, M. Zedda, 2010, "Development of co-Kriging based design optimisation methodology for a lean burn combustor", in 8th Aerodynamic Design Optimisation Seminar (ADOS 2010), Rolls-Royce PLC., UK
3. M. J. Wankhede, N. W. Bressloff, A. J. Keane, M. Zedda, 2011, "Multi-fidelity strategies for combustor design using co-Kriging of spatio-temporal combustion dynamics", in 9th Aerodynamic Design Optimisation Seminar (ADOS 2011), Rolls-Royce PLC., UK
4. M. J. Wankhede, N. W. Bressloff, A. J. Keane, M. Zedda, 2011, "A time-parallel CFD simulation of unsteady combustor flow – method and challenges", Annual CFD Review, Rolls-Royce PLC., UK

Nomenclature

Greek characters

α	Significance level
α	Blending factor
ϕ	Equivalence ratio
$\boldsymbol{\theta}$	Hyperparameter governing rate of correlation decrease
θ	Angle
μ	Kriging mean
μ	Dynamic viscosity
ν	Kinematic viscosity
μ_T	Turbulent dynamic viscosity
ν_T	Turbulent kinematic viscosity
σ^2	Kriging variance
$\boldsymbol{\Phi}(.)$	Normal cumulative distribution function
$\emptyset(.)$	Normal probability distribution function
ρ	Density
$\dot{\omega}$	Reaction rate
τ_{ij}	Viscous stress tensor
δ_{ij}	Kronecker delta
ε	Dissipation rate
τ_t	Turbulence time scale
τ_c	Chemical time scale
p_u	Density of unburnt mixture
Δt	Time-step size
Δt_f	Fine time-step size operator
λ	Regression constant

Roman characters

A_{ref}	Cross sectional area
B	Number of bootstrap samples
C	Number of low-fidelity points
c	Progress variable
D_{ref}	Reference casing diameter
D_k	Diffusion co-efficient of species k
E	Number of high-fidelity points
E(I)	Expected improvement
$\overline{f}_i$	Reynolds average (ensemble average)
$\tilde{f}_i$	Favre average (density weighted ensemble average)
f_i'	Fluctuating component in Reynolds averaging process
f_i''	Fluctuating component in Favre averaging process
h_s	Sensible heat
I	Turbulence intensity
k	Factor
k	Number of species
k	Turbulent kinetic energy
M	Mean
M'	Bootstrap mean
$M_{w,NO}$	Molecular weight of NO
m	Mass
N	Number of samples
N_t	Number of time-steps
$\mathbf{N_C}$	Number of cheap DOE points
$\mathbf{N_E}$	Number of expensive DOE points
$\overline{NO}_a$	Time-averaged area-weighted thermal NO
$\boldsymbol{p}$	Hyperparameter governing the degree of smoothness
p	Static pressure
$\dot{Q}$	External heat source term
q	Heat flux term

$\mathbf{R}$	Kriging correlation matrix
$\mathbf{r}$	Vector of correlations
r	Correlation co-efficient
r^2	Co-efficient of determination
s	Stoichiometric ratio
$s^2(\mathbf{X}^*)$	Error of Kriging prediction at new point $\mathbf{X}^*$
t	Time
T	Temperature
$\mathbf{T}$	Total flow-time
$\overline{T}_a$	Time-averaged area-weighted temperature
U_T	Turbulent flame speed
$\mathbf{U}$	Update points
$\mathbf{U_C}$	Number of cheap update points
$\mathbf{U_E}$	Number of expensive update points
U	Unsteady RANS solution at any time-state in time-parallel simulation
u_i	Velocity in Einstein notation
u'	RMS velocity
$\widetilde{u''_i u''_j}$	Favre averaged Reynolds stresses
V	Diffusion velocity
V_i^c	Correction velocity to convective velocity field u_i
v	Volume
$\mathbf{v}$	Local mass-average velocity
$\mathbf{X}$	Initial sampling points
x_i	Coordinate direction in Einstein notation
$\mathbf{Y}$	Objective function values at initial sample points
Y	Mass fraction
Y_F	Fuel mass fraction
Y_O	Oxidizer mass fraction
Y_{NO}	NO Mass fraction
Y+	Dimensionless wall distance
z	Mixture fraction
z''	Mixture fraction variance

Abbreviations

ACARE	Advisory council for aeronautics research in Europe
BP	Best predicted
CAD	Computer aided design
CAE	Computer aided engineering
CI	Confidence interval
CAM	Computed aided manufacturing
CATIA	Computer aided three dimensional interactive application
CFD	Computational fluid dynamics
CIVB	Combustion induced vortex breakdown
CO	Carbon monoxide
CoSTUS	Co-Kriging using varying spatio-temporal unsteady RANS simulation
CoSUS	Co-Kriging using steady and unsteady RANS simulation
CoTGL	Co-Kriging using two different grid levels steady RANS simulations
CoTPUS	Co-Kriging using time-parallel unsteady RANS simulation
CoTUS	Co-Kriging using varying time-step sizes unsteady RANS simulation
DHC	Dynamic hill climbing
DNS	Direct numerical simulation
DOE	Design of experiments
EI	Expected improvement
ER	Maximum Error
FAR	Fuel-air ratio
GA	Genetic algorithm
Hi-fi	High fidelity
LES	Large eddy simulation
LHS	Latin hypercube sampling
Lo-fi	Low fidelity
NOx	Oxides of nitrogen
PIT	Parallel in time
ppm	Parts per million
PVC	Precessing vortex core

RANS	Reynolds-averaged Navier Stokes
RFZ	Recirculation flow zone
RMSD	Root mean squared deviation
RSM	Response surface model
RSM	Reynolds stress model
SIMPLE	Semi-implicit pressure linked equation
UHC	Unburnt hydrocarbons
URANS	Unsteady Reynolds-averaged Navier Stokes

List of Figures

List of Tables

Chapter 1

Introduction

1.1 Background and problem overview

Air traffic is rapidly increasing today [ACARE, European Aeronautics Report, 2001] and against this background, it is essential to consider the environmental impacts of aviation to ensure in advance that such a rate of development is sustainable. Since the initial demonstration of gas turbines in jet powered aircraft, substantial gains have been made in their performance. The operational performance, noise characteristics, and pollutant emissions of gas turbines for propulsive applications continue to improve. Contemporary gas turbines produce higher operating efficiencies and emit fewer pollutants than other major chemical-energy conversion devices. In addition, the ease of quick installation has made them attractive to investors and operators. As a result, gas turbines are currently, a dominant technology for propulsion and power generation applications.

Despite the continued expansion of gas turbine use for aircraft propulsion over the past 40 years, through the introduction of new technologies that have reduced CO_2, noise and other emissions, further substantial improvements are likely to be realized through breakthrough technologies and concepts. As per the Advisory Council for Aeronautical Research in Europe (ACARE) "Vision 2020" [ACARE Strategic Agenda Report, 2002], the aeronautical industry environmental challenges have been divided into four goals:

- To reduce fuel consumption and CO_2 emissions by 50%
- To reduce NOx emission by 80%
- To reduce perceived external noise by 50%
- To make substantial progress in reducing the environmental impact of the manufacture, maintenance and disposal of aircraft and related products

Over the last 40 years, despite major advances in gas turbine combustion technology, several design challenges remain to achieve further improvement in performance and to meet the desired requirements. Although the combustor must primarily be designed to ensure stable combustion, a high combustion efficiency and uniform exit temperature, the need to control emissions has been the major influence in recent years. While the legislation for emissions of oxides of nitrogen (NOx), carbon monoxide (CO), unburnt hydrocarbons (UHC) and smoke is becoming increasingly stringent, engine design trends, which have led to richer air/fuel ratios and high temperatures and pressures inside the combustor, make the control of NOx and smoke more difficult (Rolls-Royce, 2004). For this reason, a lean burn combustion system is a more attractive option to develop, which operates under fuel lean conditions that can have lower emissions of UHC, CO and NOx and simultaneously offer higher combustion efficiency. Unfortunately, achieving these improvements and designing a practical combustion system is complicated by low reaction rates, flame extinction, instabilities, mild heat release and sensitivity to fuel/air mixing. However, as a whole, the current and future ACARE targets can only be met by lean combustion systems (Derek Dunn-Rankin, 2008).

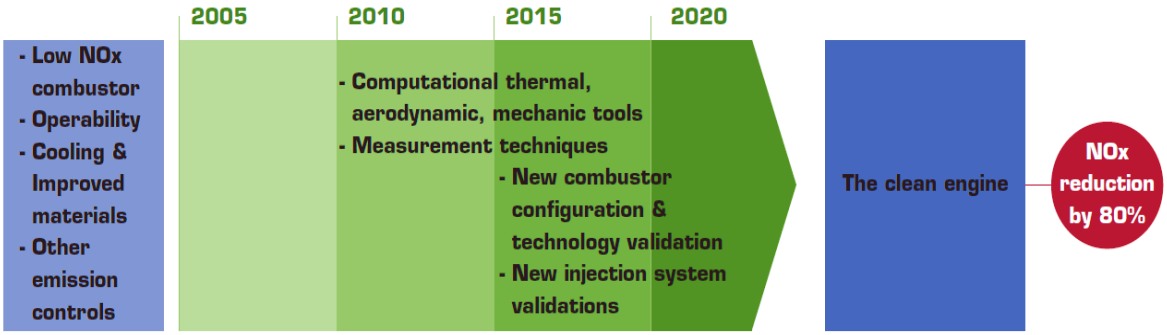

Fig. 1.1 ACARE Vision 2020 combustion systems target enabling path (ACARE strategic agenda report, volume 2(3), 2002)

Figure 1.1 shows an illustration of a target enabling path for combustion system development, mentioned in the ACARE "Vision 2020" strategic plan. Long term integrated work, including detailed understanding of the combustion process, development of new mathematical models of physical phenomena and efficient design optimisation strategies, is needed to develop new designs of combustion and fuel injection system.

1.2 Combustor design challenges

The current challenges faced by the gas turbine industry during the design process of combustors can be classified into two categories: (a) operational challenges faced in meeting the ACARE 2020 targets and (b) design strategy challenges faced in developing the combustor design.

1.2.1 Combustor operational challenges

A gas turbine combustor using liquid fuel is a complex combustion device within which there exist a wide range of interacting coupled physical and chemical phenomena including fuel spray atomization and vaporization, two-phase turbulent transport, thermal radiation and chemical kinetics. A combustor is primarily designed in such a way that it can contain and control the burning fuel-air mixture. The combustion chamber is required to burn large quantities of fuel with extensive volumes of air from the compressor. Heat must be released in such a way that the combustion gases are expanded in a smooth stream of uniformly heated gas – while also meeting the following tightly coupled operational targets (Lefebvre, 1983)

- high combustion efficiency
- wide range of combustion stability
- reliable ignition on cold days
- ability to restart the engine and pull away at high altitude
- low pressure loss in order to maximize the overall engine performance, but sufficient pressure loss to drive cooling air through the turbine.
- a temperature profile at the combustor exit that matches the life requirements of the turbine
- ability to burn a wide range of fuels
- low emissions of smoke, unburned fuel, and gaseous pollutant species
- design for minimum cost and ease of maintenance
- size and shape compatibility with engine development
- durability and manufacturability

Combustor performance often depends on subtle changes to the admission of air, the cooling features and the geometry of the fuel injector. If changes are made to improve one aspect of the combustor, it invariably has an impact, often adverse, elsewhere. In addition to the above mentioned challenges, the occurrence of instabilities during combustion is an important issue for combustor designers, particularly in low-emission gas turbines (Lieuwen and Yang, 2005).

Combustion instabilities encountered in conventional diffusion-flame-gas-turbine combustors can be eliminated, in general, with simple modifications to the design and operating parameters. However, the combustion processes in low-emission combustors are pushed close to the limits of lean flame stability and/or heat release rates that lead to strongly coupled non-linear interaction between the flame exothermicity, acoustic

behaviour of the system and components. Hence, it is necessary to consider combustion instabilities and the effects on the combustor design process.

1.2.2 Combustor design strategy challenges

In the early days of gas turbine combustor design, the combustor design process was considered more of an art than a science. It was mostly based on the "cut-and try" method where the approach was to repetitively test different variants of the combustor until a suitable arrangement could be found. A study concerning gas turbine design costs in the 1970s highlighted that some 75% of the total costs were spent on those "cut-and-try" design feedback cycles. The design methodology or strategy typically involved using a number of empirical relations in combination with semi-empirical techniques supported by experiments (Mongia, 1998 and 2001). In order to reach a good design this approach was costly and time-consuming (Nightingale, 2000).

Due to the recent advances in computing power and development of CFD codes, combustor design and development processes have changed significantly, and CFD has now become a valuable part of an overall integrated combustor design system (Anand et al., 2001). However, for combustor design and optimisation, the use of CFD has yet to overcome some obstacles in terms of combustion modelling accuracy and validation. It is well-known that an aero-engine gas turbine combustor consists of a turbulent reactive flow-field together with multiple time-dependent physical-chemical processes, occurring at varying time and length scales. Furthermore, the comprehensive physics implied by turbulent reacting flows involves strongly coupled behaviour between flow-field dynamics and combustion mixing processes. With respect to lean burn combustors, the key technical issues are associated instabilities, flame flashback, flame blow-off and auto-ignition. Hence, CFD simulation of a gas turbine combustor, embracing many complex thermal/fluid dynamic phenomena, presents an extremely challenging task requiring very fine spatial and temporal resolution of the computational domain and therefore very high computational expense (Wankhede et al., 2010). Given the complexity in obtaining accurate flow predictions and due to the expensive nature of simulations, conventional techniques (such as direct search strategy using evolutionary search algorithms) for CFD-based combustor design optimisation are often ruled out, primarily due to the limits on available computing resources and time (Mongia et al., 2005). Additionally, the combustor design optimisation process typically requires a large number of analyses of the objective and constraint functions (Dulikravich et al., 2001). This necessitates the careful selection of a fast, reliable and efficient computational design methodology for the combustor design and optimisation process.

Hence, currently, what has been proving more difficult during the combustor design development process is the application of the design and optimisation tools and the ability to obtain better results on performance targets within reasonable time and costs.

1.3 Motivation and research objectives

The motivation for this research work stems from the appreciation of the challenges faced in the process of gas turbine combustor design development, both in terms of combustor operational challenges and combustor design strategy challenges, as explained in the previous section.

Recent experimental and theoretical research on gas turbine combustors has resulted in better understanding of the physical processes taking place inside the combustor (Correa, 1998). This better understanding, in conjunction with increasingly powerful computational hardware, has facilitated the development of numerical techniques capable of simulating, with a relatively high accuracy, most of the phenomena encountered inside a combustor. Based on these simulation tools, design and optimisation strategies needs further development to make it more systematic and cost efficient, in order to accelerate the process of finding a good design configuration early on in the design process, given a performance target.

Surrogate modeling design strategies, including Kriging models, are currently being used to balance the challenges of accuracy and computational resource to accelerate the combustor design process. However, its feasibility still largely relies on the total number of design variables, objective and constraint functions, as only high-fidelity CFD analyses are used to construct the surrogate model. This could be further enhanced by using a co-Kriging (which is an extension to Kriging) based multi-fidelity strategy (Forrester et al., 2008), where information from two different analysis levels, a low fidelity (approximate) analysis and a high fidelity (accurate) analysis, are combined to accelerate the process of finding a good design.

Also, in order to facilitate faster combustor flow analysis, the CFD simulation is usually parallelized on multiple processors. The traditional approach for setting up a parallel combustor CFD simulation is to divide the spatial resolution between processors using spatial domain decomposition. However, it is well known that spatial domain decomposition techniques are not very efficient especially when the spatial dimension (or mesh count) of the problem is small and a large number of processors are used, as the communication costs between processors becomes significant per iteration (Trindade and Pereira, 2004). Hence, temporal domain decomposition has some attraction for unsteady CFD simulations, particularly on relatively coarse spatial meshes.

A time-parallel CFD simulation of a lean burn combustion system has never been approached before. Neither has the development of a multi-fidelity strategy for combustor design, particularly in the temporal domain using unsteady CFD, has been attempted previously. Hence the main objectives of this thesis are as follows:

- To develop a time-parallel CFD simulation methodology for simulating reactive combustor flow
- To develop a multi-fidelity strategy for combustor design comprising time-parallel CFD simulation and co-Kriging surrogate modelling
- To conduct performance assessment of time-parallel CFD and co-Kriging based multi-fidelity strategy relative to a Kriging based high-fidelity strategy for combustor design
- To develop and test different multi-fidelity strategies for combustor design using varying spatio-temporal combustion dynamics employing a co-Kriging surrogate model
- To perform combustor design optimisation using these multi-fidelity strategies and assess their performance relative to a traditional Kriging based strategy
- To perform confidence assessment of all proposed multi-fidelity strategies relative to Kriging based high-fidelity strategy through a Bootstrapping confidence interval method

1.4 Planning and progress

This PhD research project was sponsored by a Dorothy Hodgkin Postgraduate Award co-funded by Rolls-Royce PLC. The company's interest in this work is to develop advanced and efficient combustor design strategies which reduce the overall computational cost leading to optimal design configurations early on the design process.

For this purpose, initially, research was conducted in understanding the modern lean burn combustion system configuration and design challenges (c. f. section 1.1.1) faced within Rolls-Royce PLC. Key reactive flow-field phenomena were identified which are of interest from design optimisation perspective. Since the computational analysis cost of Rolls-Royce 3D combustor simulations is very high and unpractical for developing new design strategies, a 2D lean burn combustor test problem was identified from the literature, with similar reactive flow and unsteady flow features as the 3D combustor.

Throughout the PhD project, regular meetings have been held to review progress and plan ongoing tasks with inputs to and updates from Rolls-Royce PLC. An overview of the work plan undertaken over the three years is shown in Figure 1.2.

Task	Year 1				Year 2				Year 3			
	Q1	*Q2*	*Q3*	*Q4*	*Q1*	*Q2*	*Q3*	*Q4*	*Q1*	*Q2*	*Q3*	*Q4*
Understanding lean burn combustion system												
Identifying and formulating 2D lean burn combustor test problem												
Formulating 2D combustor design optimisation problem												
Applying Kriging based design strategy												
Developing multi-fidelity design strategies												
Applying multi-fidelity design strategies, performance and confidence assessment												
Developing time-parallel combustor CFD simulation methodology												
Developing and applying time-parallel simulation based multi-fidelity design strategy												
Presenting work at conferences, writing papers and thesis												

Fig. 1.2 Overview of PhD project plan and progress over 3 years

1.5 Thesis layout

With a focus on the development of a multi-fidelity design strategy for the design of lean burn gas turbine combustor, an overview of the combustor flow features and existing strategies for combustor design and optimisation is provided in Chapter 2. A brief overview of combustion instabilities and flame vortex dynamics inside the gas turbine combustor is also provided.

Chapter 3 presents a brief description of governing equations of reactive fluid dynamics and combustor flow modeling methods. Chapter 4 presents an analysis of Rolls-Royce three-dimensional lean burn combustor flow-field with an aim to develop an understanding of the modern lean burn combustion system, its key flow features and design challenges.

Since the computational analysis cost of Rolls-Royce three-dimensional combustor simulations is very high and unpractical for developing new design strategies, a two-dimensional test combustor problem is described and analyzed in Chapter 5. It models similar physical phenomena to the Rolls-Royce combustor discussed in Chapter 4 with respect to the reacting unsteady flow dynamics. The associated effects are captured to

different degrees of fidelity using various time-step sizes. Simulated phenomena such as recirculation zone, flame-front propagation and time-dependent flame/vortex dynamics are discussed in detail. The key focus in this chapter is the interaction between the flame front and vortex shedding behind the 2D flame stabilizer step, which results in an unsteady humming cycle. For this combusting flow, NOx formation is also discussed both in steady and unsteady states. The objective functions for design optimisation are also determined.

With the objective functions identified, a Kriging based design strategy is applied to the problem with different objective functions, both in spatial and temporal domains, in Chapter 6. The Kriging based design strategy is applied with multiple numbers of starting samples to understand how the results are affected by variations in available information.

Chapter 7 introduces various newly developed multi-fidelity strategies for combustor design employing a co-Kriging surrogate modeling technique. These strategies consist of two levels of fidelities, a fast but approximate low-fidelity and an expensive but accurate high-fidelity combustor solution, which are then used to construct a co-Kriging model on which design search is performed. Various low-fidelity solution models are developed and tested in different combinations leading to formation of strategies **CoSUS, CoTUS, CoSTUS** (c. f. Section 1.3). All strategies are run within fixed computational budgets and on multiple initial samples, to collect statistical data with mean convergence behaviour used as a performance indicator. A performance assessment of the newly developed strategies is also carried out and compared against the traditional Kriging based design strategy to identify potential benefits.

Chapter 8 introduces a time-parallel combustor CFD simulation methodology for solving the transient reactive flow-field in the 2D test combustor problem. The time-parallel method is then exploited in the **CoTPUS** co-Kriging strategy. It is also compared against the traditional Kriging based design strategy using performance assessment.

Conclusions are drawn in Chapter 9 based on the relative performances of the various co-Kriging strategies. Based on this possible future work is recommended.

Chapter 2

A review of gas turbine combustor design

Since the 1950's, gas turbine combustor technology has developed gradually and continuously rather than any dramatic changes, which is why most aero-engine combustor designs resemble each other (Mongia, 1998). Combustor design is a complex procedure due to simultaneous involvement of many conflicting performance requirements that are strongly coupled to each other. The literature on gas turbine combustor design requirements is well discussed in Lefebvre (1983), Mongia (1998, 2001) and Saravanamuttoo et al. (2008). In this chapter, a gas turbine combustor is discussed from a design development perspective. A consideration of its main flow features will help in determining a representative 2D combustor test problem for design strategy development and assessment in this thesis.

2.1 Combustor design evolution

Figure 2.1 shows the logical development of a conventional gas turbine combustor in its most widely used form. Figure 2.1a shows the simplest possible form of a combustion chamber, which has a straight-walled duct that connects the compressor to the turbine. However, such a simple arrangement is not practical because the incurred pressure loss would be excessive. In a combustor, the fundamental pressure loss due to combustion is proportional to the square of the air velocity. The outlet air velocity of a gas turbine compressor is approximately of 150 m/s. In such a case, the pressure loss in the combustor shown in Figure 2.1a could amount to about 25% of the pressure rise that is achieved in the compressor (Lefebvre, 1983). In order to reduce this pressure loss to an acceptable level, a diffuser is used at the exit of the compressor such that the air velocity is lowered by a factor of usually about five. Such an arrangement is shown in Figure 2.1b.

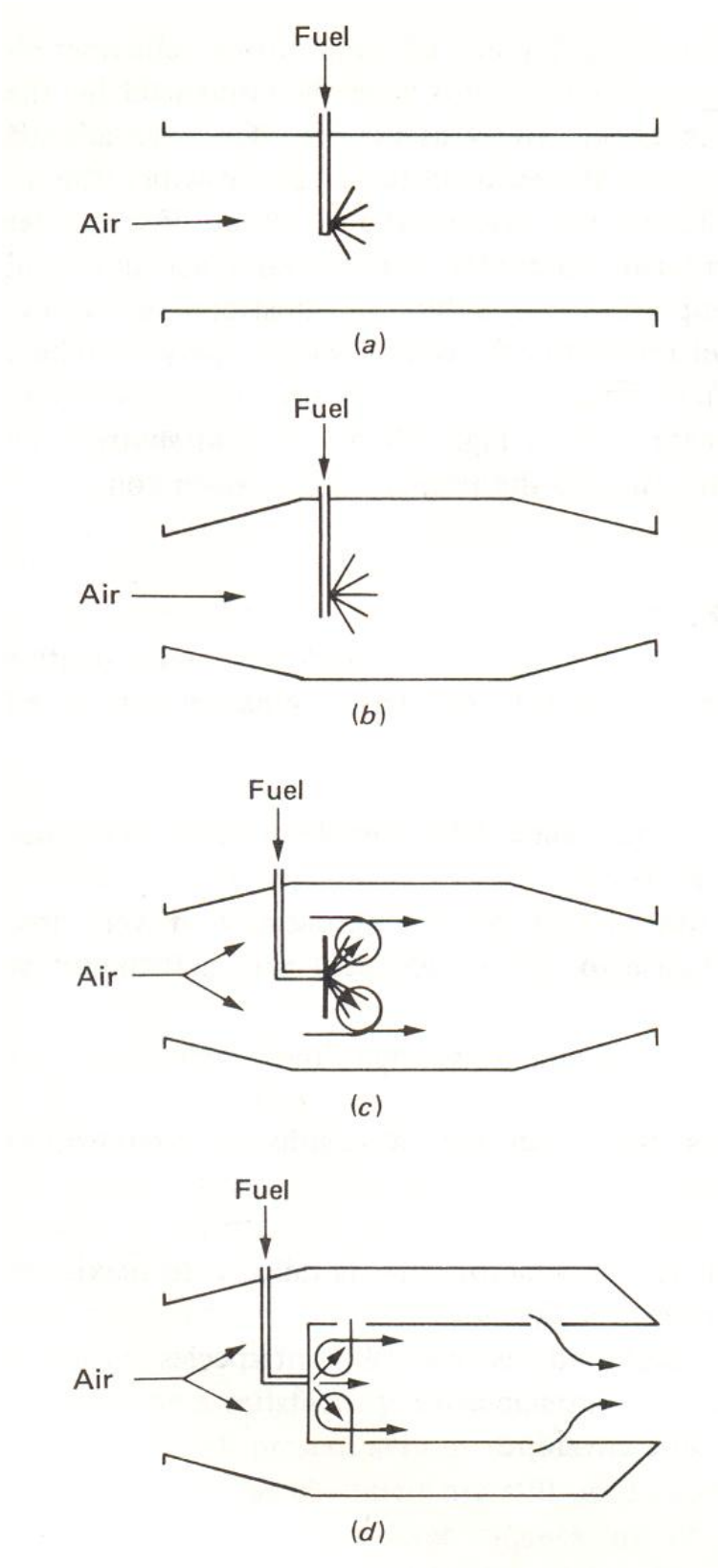

Fig. 2.1 Gas turbine combustor design evolution stages
(Lefebvre, 1983)

Even if a diffuser is used to lower the air velocity before it enters the combustion chamber, it is still high enough to blow out the flame. Hence, flow reversal must be created to provide a low-velocity region in which the flame can be continuously sustained. Figure 2.1c shows how this is achieved with the use of a plain baffle. However, to produce the desired temperature rise, the overall chamber air/fuel ratio must normally be around 50, which is well outside the limits of flammability for air-hydrocarbon mixtures. The equivalence ratio, ϕ, defined as fuel-air ratio to the stoichiometric fuel-air ratio, in the primary combustion zone should ideally be around 0.8; however lower values (~ 0.6) are sometimes preferred if the prime consideration is lower emission of nitric oxides (Lefebvre, 1983). To solve this problem, especially in the near injector end region, the simple baffle (c.f. Figure 2.1c) is replaced with a perforated liner, as illustrated in Figure 2.1d. The liner provides a region of low velocity in a recirculation zone, where combustion is sustained by a recirculatory flow of burned products providing a continuous source of ignition for the incoming fuel-air mixture. The air which is not required for combustion is admitted downstream of the combustion zone (primary zone) to mix with the hot burned products exiting the chamber. This arrangement reduces the outlet gas temperature to a value that is acceptable to the turbine blades.

There is also an intermediate zone between the primary and dilution zones, in which small discrete amounts of air are added to the flow to recover losses due to chemical dissociation of the primary combustion products. Many variations of the combustor design shown in Figure 2.1d exists but, in general, all designs comprise the key components of an air-casing, diffuser, liner, and fuel injector (Lefebvre, 1983).

2.1.1 Typical combustor flow features

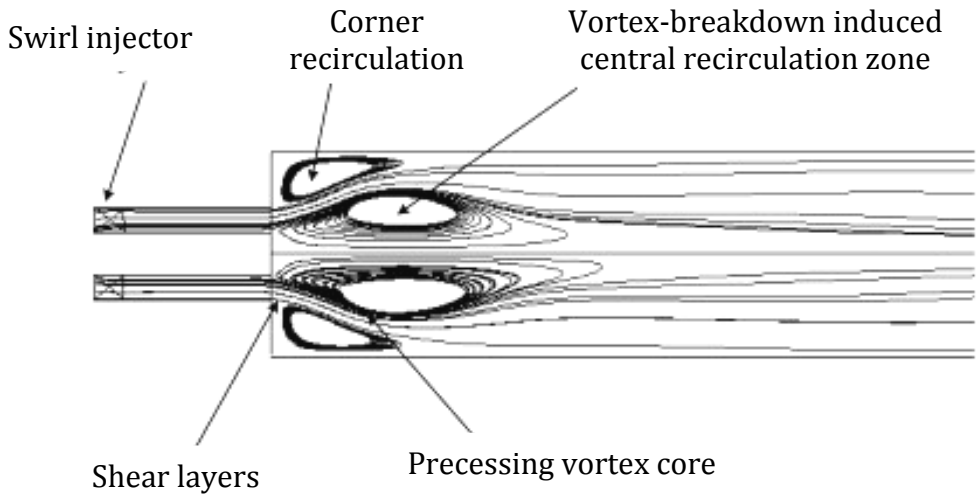

Fig. 2.2 Gas turbine combustor typical flow features (Huang Y. and Yang V., 2009)

In designing a gas turbine combustor, it is important to consider that combustion sustains a wide range of engine operating conditions and also ensures high combustion efficiency in turbulent airstreams flowing at velocities greater than the burning velocity of the fuel/air mixture (Lefebvre, 1983).Most gas-turbine combustors utilize swirling flows to stabilize the flame for efficient and clean combustion. A flame in a combustor is considered to be stable over a range of input parameters; (e.g., fuel flow rate, air/fuel ratio, degree of preheat) if the flame does not extinguish (blow-off) or flashback in to the combustor with variation in the above input parameters.

The swirl-injector induced flow structures in a typical gas turbine combustor are shown in Figure 2.2. According to Huang and Yang (2009), three important features exists in the flow field: a vortex breakdown-induced central recirculation zone (CRZ) downstream of the injector, a precessing vortex layer surrounding the center recirculation zone, and shear layers originating from the outer edge of the inlet annulus.

Vortex breakdown is a phenomenon that manifests itself as an abrupt change in the core of a slender vortex, and usually develops downstream into a recirculating bubble or a spiral pattern. This flow region provides the dominant flame stabilization mechanism, and is characterized by stagnation points and reversed flows. Reviews on this subject have been given by Hall M. G. (1972), Leibovich S. (1978, 1984) and Lucca-Negro and O'Doherty (2001).

Another distinct flow feature called the precessing vortex core (PVC), a three-dimensional unsteady asymmetric flow structure, has been reported in turbulent swirl combustion devices by Syred and Beer (1972, 1974), Gupta (1977) Dellenback et al. (1988), Froud et al. (1995), Fick et al. (1996) and Syred et al. (1997). The PVC develops when a central vortex core starts to precess around the axis of symmetry at a well-defined frequency. This phenomenon is usually linked to vortex breakdown and the associated recirculation zone in a high Reynolds number flow. The presence of shear layers modulates the fuel/air mixing process exerting significant influence on combustion processes.

The interaction between the turbulent flame and these vortex mechanisms plays a key role in the combustor driving a large class of combustion instability problems, and controlling the corresponding rates of reaction. Vortices of various types are also often used to enhance mixing, organize the flame region, and improve the flame stabilization process. It is clear that this complexity demands a clear understanding of the basic mechanisms in turbulent combustion and combustion instability, especially in relation to combustor design and development.

2.2 Iterative combustor design using 'trial and error' and semi-empirical, analytical and experimental evaluation

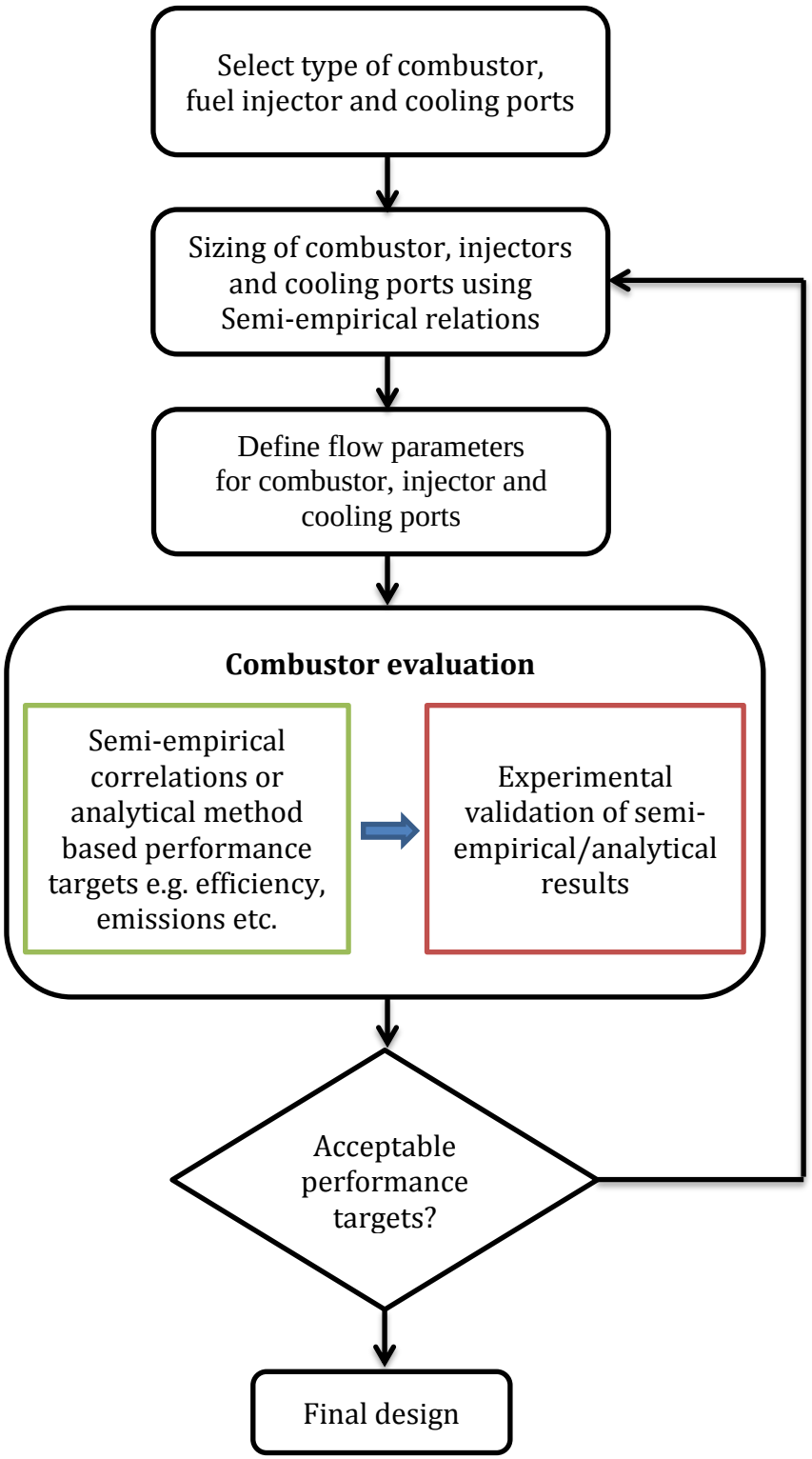

Fig. 2.3 Combustor design strategy based on 'trial and error' iterative approach

Design modification to improve one aspect of the combustor often has an adverse impact, elsewhere. This can be due to a lack of complete understanding of the combustion processes and how the modification should progress (Matthews, 2002). Several studies using successive design modification procedures for the development of gas turbine combustors are discussed in more detail in Lefebvre (1977, 1983), Rizk and Mongia (1986), Holdeman (1989) and Mellor (1990).

In the early days of gas turbine combustor development, the design process was largely trial and error based, where a new design concept or existing design would be iteratively evaluated for performance using semi-empirical correlations, analytical methods and experimental validation, until a suitable configuration of design parameters was found (Anand and Priddin, 2001). Figure 2.3 shows such a strategy employing a 'trial and error' iterative approach. Initially, after determining the type of combustor application, fuel injector type and required cooling method, the first step would involve the sizing† of the combustor and its system devices i.e. fuel injector, cooling ports etc. Figure 2.4 shows the reference dimensions of a typical gas turbine combustor for sizing.

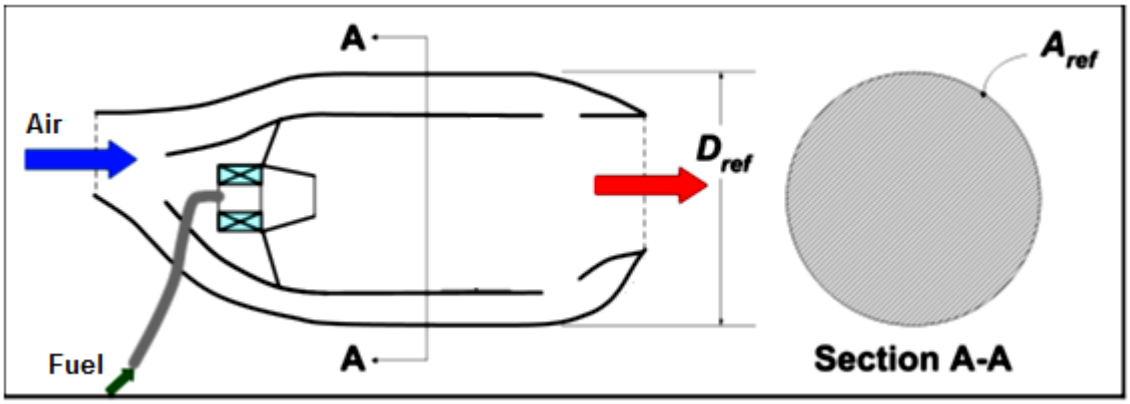

Fig. 2.4 Reference dimensions of a typical gas turbine combustor (Charest, 2005)

The geometric parameters such as reference casing diameter (D_{ref}) and the cross-sectional area (A_{ref}), which specifies the total ideal flow area inside the combustor, is defined during combustor sizing. Combustor performance such as flow residence time and combustion stability characteristics depends on combustor sizing. Next, for satisfactory performance in both combustion and dilution zones, air admission in to the combustor through injector and cooling holes are defined. For this, the momentum-flux ratio is the most significant parameter involved according to Holdeman et al. (1989), and Hammond et al. (1970). Later, the developed combustor is evaluated using semi-empirical or analytical methods, the results of which are then validated using experimental methods. If the performance results are acceptable, the design process is stopped or else it is repeated iteratively, by re-sizing the combustor, until an acceptable performance level is achieved. The advantage of such a strategy is that it is quick to

† For further reading on combustor sizing, refer Lefebvre (1983)

evaluate combustor performance using semi-empirical correlations. However, the cost of repeating combustion experiments is very high and time-consuming too, which is estimated to be almost 75 % of the entire design cycle cost (Anand and Priddin, 2001). Also, the semi-empirical correlations are limited to simple geometries and applicable to cases only for which past measured rig data is available. Thus, this requires intensive experimental rig testing at various operating parameters. The semi-empirical analysis could be replaced by analytical models, which are applicable to any generic operating conditions, at which rig testing is not performed (Lefebvre, 1983). However, analytical models face accuracy issues due to many simplifying assumptions made to reduce complexity and computational time (Anand and Priddin, 2001).

In light of the above observations, the strategy represented in Figure 2.3 is not particularly suitable for future combustor design development targets (c.f. Section 1.1.1), mainly due to not employing any systematic design search criteria for finding the optimum configuration.

2.3 Combustor design using integrated search algorithm

The concept of using a search algorithm to design a combustor was reported as long ago as 1997 by Despierre et al., who used network flow solver for combustor evaluation and a genetic algorithm search method for finding optimal combustor configuration. Figure 2.5 depicts a design strategy employing a network flow solver or CFD simulation for combustor analysis and a search algorithm [genetic algorithm (GA) in this case] for finding an optimal design given an initial dataset of design configurations.

The design and optimization of gas turbine combustors relies heavily on engineering know-how and experience. Initially, the variables which are to be optimized are chosen based on their importance to the particular problem of interest. These variables are determined on the basis of past experiences or preliminary experiments/simulations.

Later it involves using a random sampling method to define evaluation points **X** in a design search space. The performance target for each design in the initial population **X** is evaluated using a network solver code or a CFD simulation. Once the initial data points (or initial generation) performance targets **Y** are evaluated, the GA search algorithm is used to determine the next set of data points **M** (or next generation). Genetic algorithm, a search procedure originally conceptualise by Holland et al. (1975) on the theory of natural genetics and survival of the fittest model, was developed by Goldberg (1989). The GA search when applied on the first generation population set, results in new population of design configurations. The performance target, of each design in this newly produced population set, **N** is evaluated.

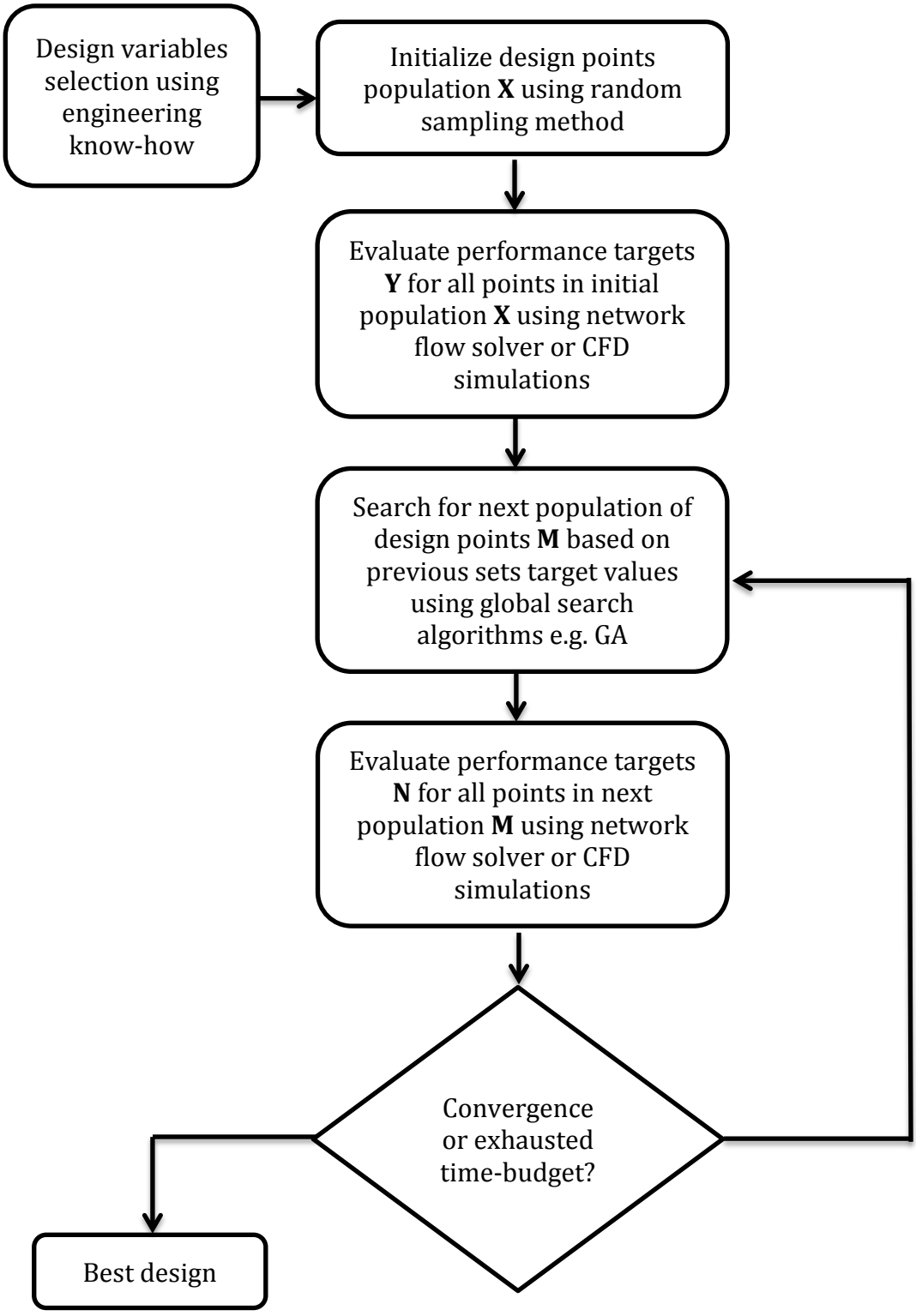

Fig. 2.5 Combustor design strategy based on integrated search algorithm

This process is repeated until convergence or for a fixed number of pre-specified generations. However, despite its advantage in rapidly finding a sufficiently good solution, the GA integrated design strategy has some drawbacks.

First, to perform its operations of reproduction, cross-over and mutation GA needs a relatively large set of individual design evaluations per population, thus requiring considerable computational effort. This increases the cost of overall design cycle significantly. Second, though it can find good region globally, it might have problem in converging to the local optimal point to find the exact optimal design. This drawback can be addressed by employing dynamic hill climbing (DHC) search method proposed by Yuret and Maza (1993) in combination with a GA.

As shown in Figure 2.5, the combustor performance evaluation could be carried out using either network flow solver or CFD simulation. Both methods are preferred over semi-empirical correlations (due to geometry restrictive issues) or analytical methods (due to accuracy issues).

2.3.1 Employing combustor network models

This approach was first conceptualised and developed by Stuttaford and Rubini (1996, 1997), who demonstrated and further extended the successful application of network flow solvers to the design of a combustor. In this approach, the combustor is divided in to a series of elements, which are described by one-dimensional sub-flows, containing appropriately modelled independent semi-empirical conservative governing equations, according to the geometric feature. Typical elements (or geometric features) of the combustor are dilution port and cooling rings. These are linked together by nodes to form an overall network of the combustor.

To obtain a complete solution of the combustor flow-field, the sub-flows are linked together by the overall governing equations (Despierre et al. 1997). Other parameters such as gas temperatures, combustion efficiency, gas emissivity, film cooling and heat transfer efficiencies are provided by separate empirical formulations (Gouws et al. 2007). For further details on combustor network model theory, see Stuttaford and Rubini (1996, 1997).

The network approach provides the ability to model the combustor flow in complex geometries and in reasonable time, making it computationally efficient and well suited to a GA search algorithm (c.f. Figure 2.5). However, this approach lacks the resolution and accuracy of three-dimensional flow features of the combustor making it applicable only at the preliminary design stage of the combustor, see Stuttaford and Rubini, (1996, 1997), Despierre et al. (1997), Rogero and Rubini (2001), Rogero (2003) and Gouws et

al. (2007). For more detailed design, higher fidelity combustor analysis is required, such as that provided by CFD.

2.3.2 Employing combustor CFD simulation

In the recent years, increases in the computational resources has made it possible to develop techniques such as numerical combustion CFD, to simulate three dimensional unsteady combustor flows with relatively higher accuracy compared to pure analytical predictions or empirical network flow solvers. This has also reduced the amount of experimentation needed for combustor flow assessment. Thus, combustor CFD had become an alternative tool with which different designs are currently assessed even before the designs are rig tested (McGuirk and Spencer, 2000, Lai et al., 2002, Motsamai, 2008, Sivaramakrishna, G., 2010).

The use of combustion CFD with integrated gradient based search optimisation algorithms has been successfully employed for combustor design previously. Anand et al. (2001) reported reduction in combustor design cycle lead times compared to traditional 'trial and error' based design cycles (c .f. Figure 2.3). Holdeman et al. (1997) and Gulati et al. (1994) also reported successful use of combustion CFD for design optimisation of the exit temperature profile. Recently, Motsamai (2008) successfully demonstrated the application of combustion CFD in combination with a gradient-based search algorithm to find an optimum combustor design configuration. Fuligno et al. (2009) presented a successful integrated approach of CFD analyses with game theory multi-objective optimisation to design a combustor.

However, even if combustion CFD is now a becoming a preferred choice over network and empirical methods, the use of combustion CFD has its own disadvantages. First, it is important to ensure that the modeling is sufficiently accurate and validated using experimental results. Additionally, if the design strategy uses an evolutionary search algorithm such as GA, then it is still unpractical to use CFD to evaluate large numbers of combustor designs as required in multiple generations of the GA (Despierre et al., 1997).

Thus, the combustor design strategy represented in Figure 2.5 is infeasible and very time-consuming, particularly when unsteady CFD simulations are performed at each stage of the search algorithm.

2.4 Combustor design using response surface model and CFD simulations

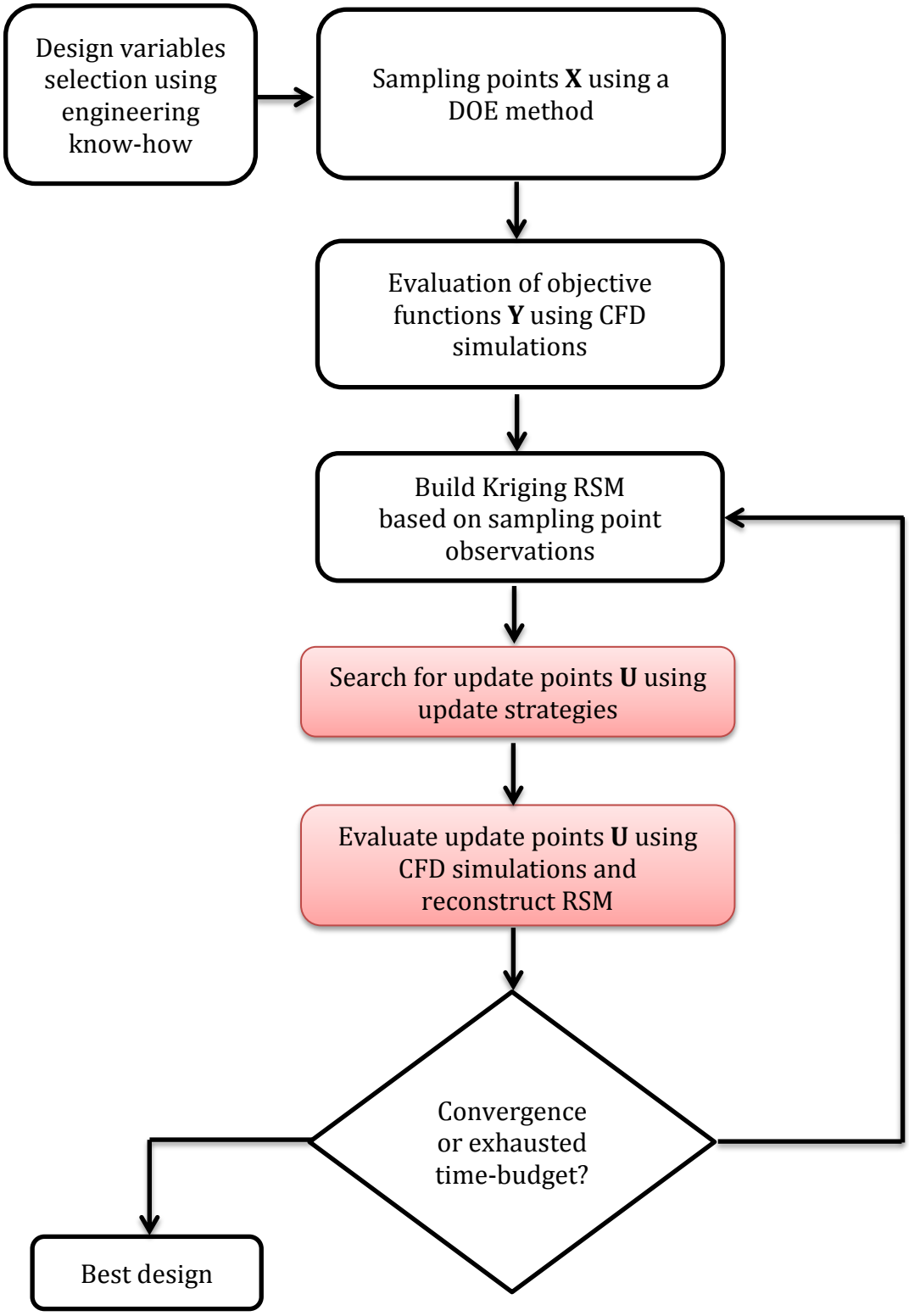

Fig. 2.6 Combustor design strategy based on Kriging response surface modeling (RSM) and CFD simulations (Keane and Nair, 2005)

To make the direct design strategy in Figure 2.5 more efficient and practical in the context of combustor design, it requires a methodology where the search algorithm is not coupled directly to expensive CFD simulations. Figure 2.6 represents such a strategy for combustor design; where pre-defined set of combustor CFD simulations within the target design space can be represented by an intermediate approximate model on which a global search is performed. The intermediate model is referred to as surrogate or response surface model (RSM).

Response surface modelling is essentially used to develop surrogates for time-consuming expensive experiments or computational simulations. It provides a tool to perform investigative experimentation in the design cycle, without having to perform expensive unsteady CFD simulations of all the possible design configurations explicitly. The objective or target functions evaluations are replaced by simpler functions, which are fitted carefully to the CFD evaluation data obtained on pre-defined design points within the design space. From a design optimisation perspective, it is widely used for a quick understanding of how the engineering function behaves in different coordinate (or variable) directions.

The existing methodologies that use response surfaces for design optimisation can be classified on the basis of the type of response surface and the method that is used to search for the update points. Jones (2001) provides an excellent description of various types of response surface methods that are currently used. The main two types of response surface methods are non-interpolating and interpolating methods. The non-interpolating methods such as fitting quadratic polynomial surfaces are unreliable as they fails to capture the true underlying function shape (c.f. Jones, 2001). The interpolating types perform better than non-interpolating ones in terms of capturing the shape of function being modelled. They are further classified in two types: one which has no statistics involved with fixed basis functions e.g. thin-plate spline, multi-quadric etc. and others which has statistical interpretation i.e. realization of a stochastic process having tuned basis function parameters e.g. Kriging.

Further classification of the methodology in Figure 2.6 is based on update point search strategy used to increase the accuracy of the response surface. The different search methods that are currently used for updating the constructed response surface are listed in Appendix B. For detailed description on these various response surface and search point methods, refer to Jones (2001).

The Kriging response surface method and its update strategies are discussed briefly here, as they form the part of the Kriging based design optimisation strategy used late in this thesis for combustor design. The main steps in this process are outlined next.

2.4.1 Design space sampling plan

Once the variables to be optimized are selected, a set of observational data **Y** is collected at sample points **X** in the design space. Clearly, the location of the points **X** in this set can have a significant impact on the accuracy of the surrogate model constructed. The design space is usually defined as a hypercube (a multi-dimensional cube) with vertices at the maxima and minima of the design variables. The number and distribution of sample points, known as a design of experiment (DOE), has an impact on both the time needed to build an approximate model and its accuracy.

The simplest form of DOE that can be used is a full factorial design which samples the design space on a uniform grid. A 2^k factorial design samples each variable at its upper and lower limit whereas a 3^k factorial design includes a point at the center of the range of each variable. This type of DoE requires a large number of points to effectively fill a design space with many variables. Hence fractional factorial designs are often used (Myers and Montgomery, 1995).

Another method of DOE is Latin hypercube design (Mackay et al., 1979). This method reduces the number of points needed to fill the design space effectively by never sampling the same value of a variable twice. Further optimizing the Latin hypercube design, by maximizing the minimum distance between points, yields a space filling design whilst retaining the Latin hypercube sampling criterion (Morris and Mitchell, 1995). Also, an LP_τ array (Statnikov and Matusov, 1995; Sobol, 1979) method is an attractive DoE method. It is based on the uniformly distributed sequences in space. An important feature of LP_τ sampling is that it provides a way to add more points to the initially sampled points whilst maintaining the same uniformity characteristics.

2.4.2 Kriging response surface model

Whilst the RSM constructed from a finite number of DOE points may not be as accurate as the individual simulations of all possible points, it provides almost instantaneous predictions of all points thus facilitating exhaustive global search (Sacks et al., 1989, Jones, 2001).

Amongst several possible surrogate model building methods, the Kriging surrogate model is widely used in aerospace design. The Kriging interpolation method was first developed by Daniel Krige (Krige, 1951) as a geostatistical technique to estimate unknown values from data observed at known locations. Given two vectors of variables $\mathbf{X^i}$ and $\mathbf{X^j}$, each of length $\boldsymbol{l}$, the objective function values $\mathbf{Y}(\mathbf{X^i})$ and $\mathbf{Y}(\mathbf{X^j})$, is assumed to depend on the distance between $\mathbf{X^i}$and $\mathbf{X^j}$. The function values will tend to be small if the distance $\left\|\mathbf{X^i} - \mathbf{X^j}\right\|$ is small.

This can be statistically modeled by assuming the correlation between the two objective function values, $\mathbf{Y}(\mathbf{X^i})$ and $\mathbf{Y}(\mathbf{X^j})$, to be given by

$$\text{Corr}[\mathbf{Y}(\mathbf{X^i})\ \mathbf{Y}(\mathbf{X^j})] = \exp\left[-\sum_{k=1}^{l} \boldsymbol{\theta}_k \left\|\mathbf{X^i}_k - \mathbf{X^j}_k\right\|^{\boldsymbol{p}_k}\right] \qquad \text{Eq. (2.1)}$$

If $\mathbf{X^i} = \mathbf{X^j}$, the correlation is 1 and if $\left\|\mathbf{X^i} - \mathbf{X^j}\right\| \to \infty$, the correlation tends to zero. $\boldsymbol{\theta}_k$ and $\boldsymbol{p}_k$ are the hyper-parameters of the Kriging model, which are tuned to the response**,** in order to make new prediction $\widehat{\mathbf{Y}}(\mathbf{X})$. $\boldsymbol{\theta}$ is the width parameter which affects how far the influence of a sample point extends. Also known as the 'activity parameter', it helps in high-dimensional problems to identify the most important variables by determining its relative size. $\boldsymbol{p}$ determines the degree of smoothness of the Kriging model. Also Kriging allows these hyper-parameters to vary with each dimension. Hence, due to reduced numbers of assumptions in the Kriging method, as to the nature of the design space, the Kriging surrogate model can be more robust and accurate compared to others; see Jones (2001), Forrester et al. (2008) for more details.

2.4.3 Kriging RSM update points strategies

After evaluation of an initial sample and construction of the response surface model, the next step is to refine the response surface model with additional data using update or infill points. These update points can be obtained by exploiting the surrogate using best predicted point search or by exploring the surrogate model by using kriging prediction error. Another advanced method is to use the balanced exploitation/exploration method of expected improvement (Forrester et al., 2008).

2.4.3.1 Best Kriging prediction search

A natural way to refine the surrogate model surface is to compute a new simulation at the optimum point predicted by the RSM (Forrester et al., 2004) and add it to the database of observations to re-construct the surrogate model. Once the Kriging model hyper parameters (Eq. 2.1) are tuned to the initial sample observations, a Kriging prediction of the objective function value at some new point $\mathbf{X}^*$ is given by (see Sacks et al. (1989), Jones (2001) for more details);

$$\widehat{\mathbf{Y}}(\mathbf{X}^*) = \hat{\mu} + \mathbf{r}^{\boldsymbol{T}}\mathbf{R}^{-1}(\mathbf{Y} - \mathbf{1}\hat{\mu}) \qquad \text{Eq. (2.2)}$$

Where, $\hat{\mu}$ is the estimated value of the mean, **r** is the vector given by *corr*[**Y**(**X***)**Y**(**X**^{i})] for **i** =1…,n; **R** is the correlation matrix whose elements are given by Eq. (2.1), **1** is the n x 1 vector of ones and **Y** is the vector consisting of all objective function values. A search is carried out on the Kriging prediction response surface to find regions of optimal design configurations. For this process, a global optimizer (e.g. GA) is used as it can return multiple regions of local optima (Toal et al. 2008). This result is further exploited using dynamic hill climbing search algorithm to find the exact location of the optimal design (Song and Keane, 2005, Toal et al., 2008).

2.4.3.2 Kriging prediction error

The accuracy of the Kriging prediction depends largely on the distance between the prediction point location and the observed data point location. The Kriging process also provides the ability to estimate the error in the predictions made. This is given by

$$s^2(\mathbf{X}^*) = \hat{\sigma}^2 \left[1 - \boldsymbol{r}^T \boldsymbol{R}^{-1} \boldsymbol{r} + \frac{(1 - \mathbf{1}^T \boldsymbol{R}^{-1} \boldsymbol{r})^2}{\mathbf{1}^T \boldsymbol{R}^{-1} \boldsymbol{r}}\right] \qquad \text{Eq. (2.3)}$$

where, $s^2(\mathbf{X}^*)$ is the error estimate in the Kriging prediction at point $\mathbf{X}^*$ and $\hat{\sigma}^2$ is the variance.

The Kriging prediction error estimate can be used as an exploration based update criterion, by seeking points of maximum predicted error, to improve the accuracy of the surrogate model (Forrester et al., 2008).

2.4.3.3 Expected improvement

The expected improvement update criterion is a balanced surrogate model exploration and exploitation method (Forrester et al., 2008). With prediction provided by Eq. (2.2) and estimated error using Eq. (2.3), the prediction uncertainty about the function's value at a point **X** can be modeled as the realization of a normally distributed random variable **Y**(**X**) with mean $\widehat{\mathbf{Y}}(\mathbf{X})$, standard deviation $\hat{s}(\mathbf{X})$ and a probability density function given by

$$\frac{1}{\hat{s}(\mathbf{X})\sqrt{2\pi}} \exp - \left[\frac{1}{2}\left(\frac{\mathbf{Y}(\mathbf{X}) - \widehat{\mathbf{Y}}(\mathbf{X})}{\hat{s}(\mathbf{X})}\right)^2\right] \qquad \text{Eq. (2.4)}$$

The most acceptable value at $\mathbf{X}$ is $\widehat{\mathbf{Y}}(\mathbf{X})$, however since there is uncertainty in its value with probability decreasing as $\mathbf{Y}(\mathbf{X})$ moves away from $\widehat{\mathbf{Y}}(\mathbf{X})$, we can compute the expectation of an improvement, $\mathbf{I}$ on the best value so far.

With $\widehat{\mathbf{Y}}(\mathbf{X})$ as the prediction at $\mathbf{X}$, the amount of improvement, $\mathbf{I}$

$$\mathbf{I}\left(\widehat{\mathbf{Y}}, \boldsymbol{f_{min}}\right) = \max\left\{\boldsymbol{f_{min}} - \widehat{\mathbf{Y}}, 0\right\} \qquad \text{Eq. (2.5)}$$

obtained with respect to the best currently known objective function value $\boldsymbol{f_{min}}$ could be maximized (Wagner et al. 2011). The expected improvement criterion is then given as

$$\mathbf{E}[\mathbf{I}(\mathbf{X})] = \int_{-\infty}^{\infty} \max(\boldsymbol{f_{min}} - \mathbf{Y}(\mathbf{X}), \mathbf{0}) \emptyset\left(\mathbf{Y}(\mathbf{X})\right) \mathbf{dY} \qquad \text{Eq. (2.6)}$$

$$= \begin{cases} \left[\boldsymbol{f_{min}} - \widehat{\mathbf{Y}}(\mathbf{X})\right] \boldsymbol{\Phi}\left(\dfrac{\boldsymbol{f_{min}} - \widehat{\mathbf{Y}}(\mathbf{X})}{\hat{s}(\mathbf{X})}\right) + \hat{s}\, \emptyset\left(\dfrac{\boldsymbol{f_{min}} - \widehat{\mathbf{Y}}(\mathbf{X})}{\hat{s}(\mathbf{X})}\right) & if\ \hat{s} > 0 \\ 0, & if\ \hat{s} = 0 \end{cases}$$

where $\boldsymbol{\Phi}(.)$ is the normal cumulative distribution function and $\emptyset(.)$ is the normal probability distribution function. If $\hat{s} = 0$, $\mathbf{E}[\mathbf{I}(\mathbf{X})] = 0$ and thus there is no expectation of further improvement at previously sampled point. For maximizing the expected improvement, $\boldsymbol{f_{min}} - \widehat{\mathbf{Y}}$ should be replaced by $\widehat{\mathbf{Y}} - \boldsymbol{f_{min}}$, to treat it as a minimization problem with minimization of the negative of the data. As proved by Locatelli (1997), with increasing number of updates based on maximum $\mathbf{E}[\mathbf{I}(\mathbf{X})]$, the design space would be populated densely enough to find the global optimum (Forrester et al., 2008).

The Kriging model based design strategy using these update criteria (c.f. Figure 2.6) has been previously applied successfully for combustor design. Jeong et al. (2006) reported 95% saving in the total design cycle cost using a Kriging strategy compared to using only evolutionary search algorithm based strategy (c. f. Figure 2.5). The study concluded that this method is a practical approach for real-world combustor design problems. Duchaine et al. (2009) also demonstrated a multi-objective combustor design optimisation study using a Kriging model based design strategy and proved it to be a feasible tool with manageable computational resource and time.

2.5 Summary

This chapter provided an overview of combustor design evolution stages and key flow features of the combustor from design point of view. Attention was drawn on multiple vortex mechanisms present inside the combustor and the flame/vortex interaction process. The combustor flow evaluation during the design stages evolved over time in terms of semi-empirical/analytical methods to more accurate network flow solvers, and recently with advanced 3D CFD evaluations.

With combustor flow evaluation obtained, the early days 'cut and trial' design strategy to find optimal design was replaced by integrated search algorithms and recently by response surface model (e.g. Kriging) based strategies. The current state-of-the-art in the context of combustor design and optimisation is the use of CFD based Kriging design strategy with addition of update points to improve its accuracy for finding optimal design.

Chapter 3

Combustor flow modelling - theory

3.1 Introduction

Combustor flow is turbulent, reacting and consists of many complex coupled physical-chemical phenomena (Kuo, 1986; Peters, 2000). As discussed in the previous chapter, semi-empirical, analytical and network methods are not accurate enough for real world combustor development. The current state-of-the-art CFD techniques allow for the use of more sophisticated models of fluid flow, turbulence, combustion and turbulence-chemistry interactions. Also, higher combustor flow resolution using more computational cells is possible enabling complex geometries of real combustors to be adequately represented. This chapter discusses the conservative equations used for modeling reacting combustor flow using commercial CFD software ANSYS FLUENT™ version 12.1. The governing equations are discussed without treating their derivations.

3.2 Governing equations of reacting fluid flow

Reacting flow differs from non-reacting flow, mainly due to reacting gas being a non-isothermal mixture of many species, each requiring individual tracking. Also, compared to classical aerodynamics, a complex set of thermodynamic data is required as the heat capacities in reacting gases change significantly with temperature and composition (Kuo, 1986; Peters, 2000). In reacting gas flow, the species react chemically through multiple chemical reactions and the rate at which reactions occur requires specific modeling. Indeed, Navier-Stokes non-reacting fluid flow equations need to be adapted for such a multi-species and multi-reaction gas flow (Peters, 2000; Poinsot and Veynante, 2005).

Consider a reacting gas mixture consisting of N species, each characterized by their mass fraction

$$Y_k = {}^{m_k}/_{m} \qquad (k = 1 \text{ to N}) \qquad \text{Eq. (3.1)}$$

where, m_k is the mass of species k present in a given volume v and m is the total mass of gas in this volume. The primitive variables for a three dimensional compressible reacting flow are (Peters, 2000; Poinsot and Veynante, 2005; Echekki, 2011);

- Density $\rho = m / v$
- Three dimensional velocity field u_i
- Energy (or enthalpy or temperature T)
- Pressure
- Mass fraction Y_k of the N reacting species

Hence, compared to six variables in non-reacting flow solutions, $N + 6$ variables are needed to be solved in a reacting flow. Thus, significant extra computational effort is required to solve the full set of conservation equations, including separate equations for each species.

3.2.1 Conservation of mass and species

The mass conservation equation for the total reacting mixture with N species is given as (Poinsot and Veynante, 2005):

$$\frac{\partial \rho}{\partial t} + \frac{\partial \rho u_i}{\partial x_i} = 0 \qquad \text{Eq. (3.2)}$$

Compared to the non-reacting case, the mass conservation equation is unchanged as the combustion processes do not generate any mass.

For species k, the mass conservation equation with diffusion velocities is given by (k = 1, N):

$$\frac{\partial}{\partial t}(\rho Y_k) + \frac{\partial}{\partial x_i}(\rho(u_i + V_{k,i})Y_k) = \dot{\omega}_k \qquad \text{Eq. (3.3)}$$

where, $V_{k,i}$ is the i^{th} component of the diffusion velocity V_k of species k, $\dot{\omega}_k$ is the reaction rate of species k, and

$$\sum_{k=1}^{N} Y_k V_{k,i} = 0 \qquad \text{Eq. (3.4a)}$$

$$\sum_{k=1}^{N} \dot{\omega}_k = 0 \qquad \text{Eq. (3.4b)}$$

The different species in a diffusing mixture move at different velocities. In a reacting flow system, one is more interested in the velocity of a given species with respect to the local mass-average velocity **v** rather than with respect to stationary coordinates (Kuo, 1986). For a mixture of N species, the local mass-average velocity **v** is defined as:

$$\mathbf{v} = \frac{\sum_{i=1}^{N} \boldsymbol{\rho}_i \mathbf{v}_i}{\sum_{i=1}^{N} \boldsymbol{\rho}_i} \qquad \text{Eq. (3.5)}$$

where $\mathbf{v_i}$ denotes the velocity of the i^{th} species with respect to stationary coordinate axes. Hence, mass diffusion velocity (V_i) for a species is given by:

$$V_i = \mathbf{v_i} - \mathbf{v} \qquad \text{Eq. (3.6)}$$

The diffusion velocity indicates the relative motion of component i to the local motion of the reacting fluid (Kuo, 1986). According to Williams (1985), it is mathematically difficult to solve for diffusion velocities using Eq. (3.3). Hence, most combustion codes currently employ a simplified approach based on Hirschfelder's law (see Hirschfelder et al., 1954) or Fick's law of diffusion (see Kuo 1986) which provides convenient approximations for diffusion velocities of reacting species. Hence, to maintain global mass conservation, two methods can be employed. The first method involves solving for Eq. (3.3) initially with only N-1 species equations. The last species mass fraction is obtained from

$$Y_N = 1 - \sum_{k=1}^{N-1} Y_k \qquad \text{Eq. (3.7)}$$

This method is, however, not very accurate and must be used only for strongly diluted flames (Poinsot and Veynante, 2005). A more accurate method consists of solving for a modified species equation using Hirschfelder and Curtiss approximation and written as

$$\frac{\partial}{\partial t}(\rho Y_k) + \frac{\partial}{\partial x_i}(\rho(u_i + V_i^c)Y_k) = \frac{\partial}{\partial x_i}\left(\rho D_k \frac{W_k}{W}\frac{\partial X_k}{\partial x_i}\right) + \dot{\omega}_k \qquad \text{Eq. (3.8)}$$

where V_i^c is the correction velocity added to the convective velocity u_i to ensure global mass conservation. In unsteady flow calculations, as each time step, this correction velocity is computed and added to the convective velocity field thus ensuring the compatibility of the species and mass conservation equations (Kuo, 1986; Poinsot and Veynante, 2005).

3.2.2 Conservation of momentum

The equations for conservation of momentum in reacting flow are similar to non-reacting flow and given by (Poinsot and Veynante, 2005):

$$\frac{\partial}{\partial t}(\rho u_j) + \frac{\partial}{\partial x_i}(\rho u_i u_j) = -\frac{\partial p}{\partial x_j} + \frac{\partial \tau_{ij}}{\partial x_i} + \rho \sum_{k=1}^{N} Y_k f_{k,j} \qquad \text{Eq. (3.9a)}$$

where

p is the static pressure

Eq. (3.9b)

$$\tau_{ij} = -\frac{2}{3}\mu \frac{\partial u_k}{\partial x_k}\delta_{ij} + \mu\left(\frac{\partial u_i}{\partial x_j} + \frac{\partial u_j}{\partial x_j}\right)$$

is the viscous stress tensor with the first term associated with volume dilatation

$f_{k,j}$ is the volume force acting on the species k in direction j.

μ is the dynamic viscosity

Even though the momentum equation is similar for reacting and non-reacting flow, the physics and behaviour of the flow is entirely different. The combustion process, through multiple chemical reactions modifies the flow greatly due to the temperature gradients it introduces in the flow field (Peters, 2000). The dynamic viscosity changes significantly because of the temperature variations and also density variations occur in the ratio of 1:8 to 1:10 (Poinsot and Veynante, 2005). The dilatation through the flame front increases all the speeds thus increasing the local Reynolds number of the reacting gases. This causes great variation in the local Reynolds number, which is not the case in non-reacting flow, thus making it more challenging to solve (Lewis and Von Elbe, 1987).

3.2.3 Conservation of energy

The energy conservation equation for reacting flow, in the form of sensible enthalpy h_s, is given as (Poinsot and Veynante, 2005)

$$\frac{\partial}{\partial t}(\rho h_s) + \frac{\partial}{\partial x_i}(\rho u_i h_s) = \dot{\omega}_T + \frac{Dp}{Dt} + \frac{\partial q_i}{\partial x_i} + \tau_{ij}\frac{\partial u_i}{\partial x_j} + \dot{Q} \qquad \text{Eq.(3.10a)}$$

where

$$\dot{\omega}_T = -\sum_{k=1}^{N} \Delta h_{f,k}^{o} \dot{\omega}_k \qquad \text{Eq.(3.10b)}$$

is the chemical term and is associated with heat released due to combustion

$\dot{Q}$ is the external heat source term and not due to combustion

$$q_i = -\lambda \frac{\partial T}{\partial x_i} + \rho \sum_{k=1}^{N} h_{s,k} Y_k V_{k,i} \qquad \text{Eq. (3.10c)}$$

is the heat flux term in which first term is a heat diffusion term expressed by Fourier's Law and second term is associated with the diffusion of species with different enthalpies

Various simplified forms of the energy equation commonly used in reacting flow CFD are constant pressure flames, equal heat capacities for all species and constant heat capacity for a mixture (see Poinsot and Veynante (2005) for more detailed discussion).

3.3 Turbulent combustion modelling

Turbulence, even in isothermal fluid dynamics, is complex and difficult to simulate (Pope, 2000). Similarly combustion without turbulence is a fundamentally complex process involving varied chemical time and length scales. It consists of hundreds of species and thousands of chemical reactions, thus making it very difficult to solve numerically (Kuo, 1986; Peters, 2000; Poinsot and Veynante, 2005). Thus, simulation of turbulent combustion concerns with two-way interaction of two complex disciplines of turbulence and combustion.

The current state-of-the-art in CFD simulation of turbulent combustion can be classified by three levels of computational accuracy; (1) Reynolds-averaged Navier-Stokes (RANS) (2) Large eddy simulations (LES) and (3) Direct numerical simulations (DNS).

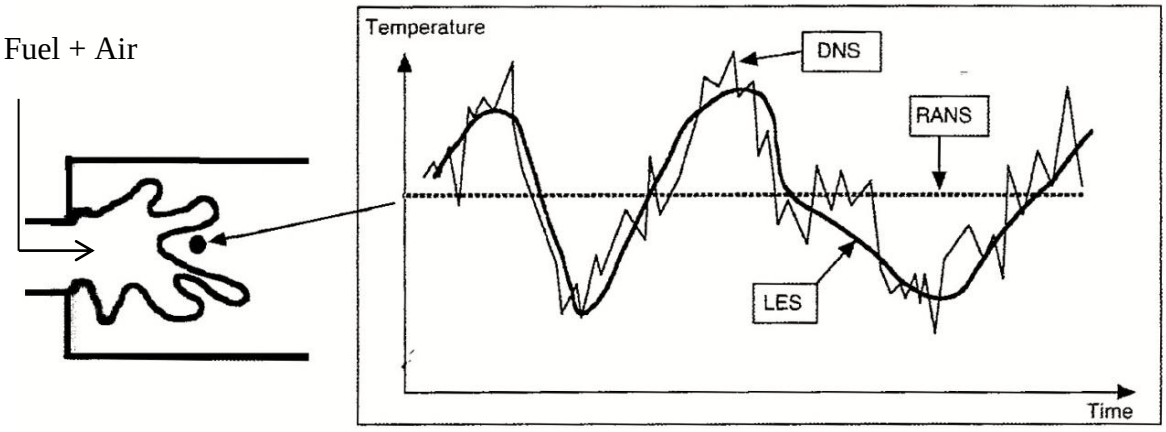

Fig. 3.1 Temperature fluctuations as computed by RANS, LES and DNS methods in a turbulent flame brush (Poinsot and Veynante, 2005)

Figure 3.1 shows how these methods capture the temperature fluctuations in a turbulent flame brush. The most accurate solution of time-averaged Navier-Stokes equations can be obtained using direct numerical simulations (DNS) which predicts all time-variations of temperature (c.f. Fig. 3.1). In DNS, all the length and time scales of turbulence are directly resolved and the effect on combustion is determined without any model for turbulent fluctuations (Malalasekera, 1995; Peters, 2000; Poinsot, 2005). However, the computing requirement for DNS is very high and is currently impossible to be employed for real-world combustor flows. In contrast, although LES explicitly calculates the large scale turbulent scales of motion and can compute the large scale flame-front, it employs a sub-grid model to compute the effect of small scale turbulent motion on combustion (Malalasekera, 1995). LES captures only the low-frequency variations of temperature (c.f. Fig 3.1). Even though small scale turbulent motions are

modelled to reduce the computational cost, LES is still unpractical for combustor simulations, especially from a design point of view where many CFD evaluations are required for different designs. Given the significant computing cost of DNS and LES, the RANS based approach is the most practical one for combustor simulations. RANS equations govern the transport of the averaged flow quantities, with all the scales of turbulent motion being modelled. Using RANS, the temperature predicted at a point is a constant corresponding to the mean temperature at this point (c.f. Fig. 3.1).

Since a RANS based CFD approach is used in this thesis to model the combustor flow, it is discussed in more detail in Appendix B. Also, the partially premixed combustion model and NOx pollutant model are described briefly in Appendix B, as these are applied later in the thesis to solve reactive combustor flow.

3.4 Summary

This chapter provided a mathematical overview of the governing equations used for modelling combustor reacting flow using ANSYS Fluent 12.1 without treating their derivations explicitly and discussed briefly the turbulent combustion modelling methods.

Based on this, the Rolls-Royce three-dimensional lean burn combustor and a two-dimensional test combustor are modelled and analyzed in chapters 4 and 5 respectively.

Chapter 4

Rolls-Royce lean burn combustor flow analysis

In this chapter, a gas turbine lean burn combustion system, using complex fuel injector geometry with multiple inlet swirlers developed at Rolls-Royce PLC., has been investigated with an objective of understanding its key flow features and its influence on the combustor flow-field. A URANS method using the Reynolds Stress Model (RSM) is used to analyze the combustor flow-field and predict its behaviour over a long period of physical flow-time under partially premixed combustion conditions. The findings on swirl-induced instabilities in the vicinity of the air blast atomizer of the fuel injector and their effect on heat release and flow-field fluctuations in the combustor are also presented. An investigation is presented on the effect of time-step size on the prediction of temperature variation in the flow-field. The mass-weighted average temperature variation is monitored so as to identify its relation to the PVC behaviour under combusting conditions. Flame-vortex interaction and combustion induced vortex breakdown phenomena causing PVC suppression and hence flame flashback into the injector, are captured and analyzed using axial velocity plots. (Note that flame flashback here and further in this report refers to upstream propagation of the flame in to the injector's premixing zone).

4.1 Computational model

The numerical prediction of swirl flow instabilities is computationally expensive; it is three-dimensional and time dependent, and has therefore been attempted only recently (Fokaides et al., 2009 and Dunham et al., 2009). Figure 4.1 shows the complete computational domain used for URANS analysis indicating locations where inlet and outlet boundary conditions were specified. The swirler vanes are not included in this model. Instead, the configuration uses appropriate boundary conditions derived from a through-the-swirlers model solution run earlier.

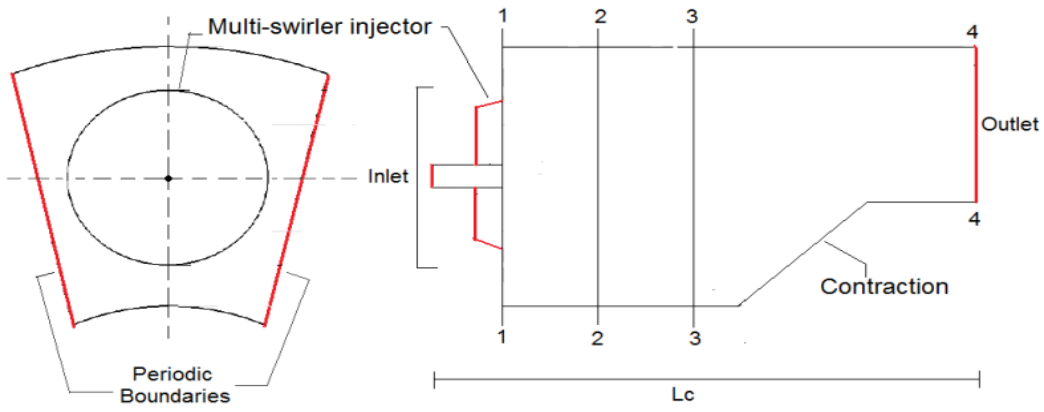

Fig. 4.1 Computational domain consisting of a section of an annular combustor (left) and a meridional plane view (right)

The inlet velocity is specified as the boundary condition at swirler inlets and outflow is specified as the boundary condition at the outlet. It consists of a section of annular combustor with periodic boundary conditions on both sides and part of the fuel injector geometry downstream of the swirler blades. The fuel injector consists of a multiple inlet swirlers arranged co-axially. All of the air, except for cooling, enters the combustor through the swirlers and fuel is introduced in the high velocity stream of air in the injector as a liquid film for atomization and mixing. The combustion processes take place in the combustor along its length and hot gases with products exit from the outlet.

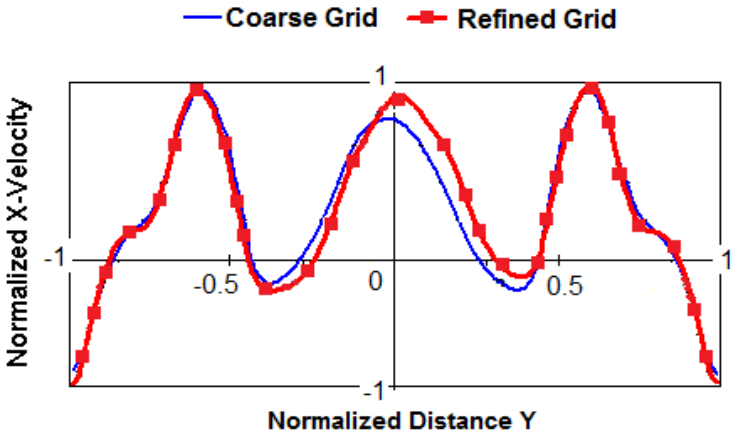

Fig. 4.2 Normalized x-velocity profiles for a coarse and refined grid near the injector exit

Figure 4.2 shows the comparison between the predictions by a coarse and fine mesh in terms of normalized x-velocity profiles captured near the injector exit at isothermal conditions. The mesh is constructed using ICEM CFD meshing tool. The coarse mesh is a multi-block structured mesh with 0.95 million hexahedral cells, whereas the fine mesh has approximately 2.7 million cells, concentrated mainly in the injector region.

Table 4.1: Key 3D Unsteady CFD setup parameters for FLUENT 6.3	
Solver	Pressure Based
Space	3D
Time	Unsteady 2nd order implicit
Energy	Yes
Turbulence Model	Reynolds Stress (standard wall functions)
Transport and Reaction	
Species	Partially Premixed Combustion
PDF Options	Inlet Diffusion: Yes
Mixture Properties	PDF-mixture
Boundary Conditions	
Main and pilot swirl inlet	Velocity-inlet
Inlet (Momentum)	X, Y, Z velocity profiles (obtained from isothermal run)
Inlet (Temperature)	870 K
Inlet (Species)	Progress variable = 0
	Mean mixture fraction = 0
	Mixture fraction variance = 0
Discrete phase BC type	escape
Outlet	Outflow
Operating Conditions	
Pressure(pa)	1361305
Solution Controls	
Pressure-Velocity Coupling	SIMPLE
Discretization:	
Pressure	Standard
Momentum	Third-Order MUSCL
Turbulent Kinetic Energy	First Order Upwind
Turbulent Dissipation Rate	First Order Upwind
Reynolds Stresses	Third-Order MUSCL
Energy	Third-Order MUSCL
Progress Variable	Third-Order MUSCL
Mean Mixture Fraction	First order upwind
Mixture Fraction Variance	First order upwind

As seen in Figure 4.2, the agreement between the meshes is very good away from the axis of the injector. In the region near the axis of the injector, a difference in predictions is observed, however the averaged x-velocity value over the profile for the two meshes is fairly similar. Though the mesh-independence of the solution is not 100% conclusive, both the profiles are found to compare favourably with the measured experimental profiles (not published due to confidentiality reasons), reassuring that the solution is robust, at least from a time-averaged viewpoint. Additionally, due to the computational expense of the simulation under reactive conditions, and with an objective to develop an engineering solution to the problem which will be of more industrial value, the coarse mesh with 0.95 million hexahedral cells is used for the CFD analysis under reactive conditions.

Table 4.1 highlights some of the key unsteady CFD setup parameters. The CFD package Fluent™ version 6.3 is used for solving the unsteady Reynolds-averaged Navier-Stokes (URANS) equations in three-dimensions with time dependence. The solver used is pressure based and has a second order implicit unsteady formulation for time. The Reynolds stress model (RSM) is used for turbulence modeling due to its known capability to accurately predict complex swirling flows. The SIMPLE pressure-correction method is used for pressure-velocity coupling. The combusting simulations discussed in this report were run at a high pressure of 1.36 MPa and the inlet air temperature is 870 K. Fluent's Zimont partially premixed combustion model is used as the species model. The model solves a transport equation for the mean reaction progress variable $\bar{C}$, (to determine the position of the flame front), as well as the mean mixture fraction $\bar{f}$, and the mixture fraction variance $\overline{f'^2}$. Ahead of the flame ($\bar{C}$ = 0), the fuel and oxidizer are mixed but unburnt, and behind the flame ($\bar{C}$ = 1), the mixture is burnt (User Guide, Fluent 6.3). Overall, the computational model used is representative of a lean burn combustor.

4.2 Analysis methodology

With reference to Figure 4.1, planes 1-1, 2-2 and 3-3 are set up inside the combustor at increasing distances from the injector end. Plane 4-4 is the exit plane of the combustor. Mass weighted average temperature and axial velocity variation is analyzed over 40ms of flow time, which represents more than four combustor flow residence times.

Initially, the reactive simulation was run iteratively without time stepping to allow the flow-field to develop and obtain sensible initialization for subsequent unsteady run. The unsteady model was then switched on, and the time-dependent flow-field evolved with the anticipated features. The precessing vortex core formation, its unstable behaviour and suppression were all observed using the visualisation tools EnSight 9.0. The effect on unsteady heat release is analyzed using temperature plots.

The unsteady reactive simulation was initially run at different time-step sizes, from 10^{-2} s being the coarsest to 10^{-5} s as the finest, in order to understand its effect on temperature and flow-field instabilities. Temperature fluctuations at the exit plane predicted by different time-step size simulations over 40 ms flow-time were compared. Although the PVC was captured reasonably well in the coarsest time-step size computations, it was unable to even qualitatively capture the phenomena of CIVB and PVC suppression. Hence, the finest time-step size of 10^{-5} s was used to capture the PVC formation, its evolution over time and its suppression due to CIVB, and also to analyze its effect on temperature fluctuations in the combustor. The reactive simulation was run upto 0.1s of flow time to account for any further instability effects, changes in the heat release pattern and to understand the periodic pattern of unsteadiness in the combustor. The run time required to simulate 0.1s of flow time with 10^{-5}s time-step size was approximately three months, using 8 processes in parallel on a cluster using Intel quad core processors with 2.8GHz clock rate.

4.3 Vortex breakdown and precessing vortex core

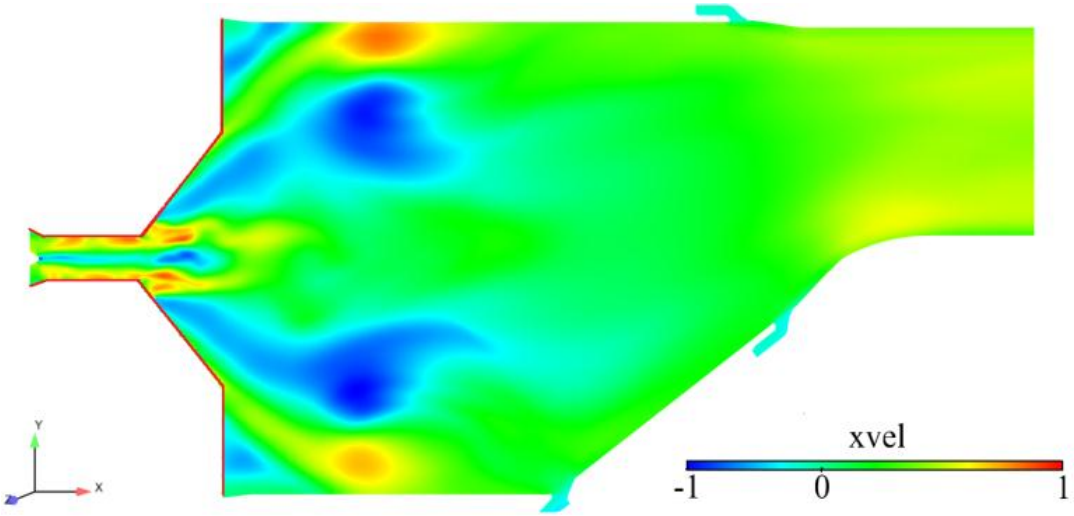

Fig. 4.3 Instantaneous axial velocity (xvel) flow field

In the current setup, a swirling jet at high swirl number (S>0.6) is introduced in the combustion chamber through an injector consisting of multiple swirler blades arranged co-axially, under reactive conditions. Figure 4.3 shows an instantaneous axial velocity flow field. The vortex breakdown takes the form of an axi-symmetric bubble of recirculating fluid. This bubble then travels downstream, later forming a large central recirculation flow zone (RFZ). This type of bubble mode breakdown usually prevails at a high swirl number (Lucca-Negro and O'Doherty, 2001). Due to the rotating motion of the flow, there exists a tangential velocity component in addition to the axial and radial components which induces the flow to change its direction and establish a spiral motion

(Alecci et al., 2005). A low pressure zone in the central core of this spiral is created as seen in Figure 4.4.

Figure 4.4 shows the central vortex core structure inside the air-blast atomizer of the injector. This low pressure structure was initially aligned with the axis of the injector inside the air-blast atomizer, but then later breaks down at a point downstream and starts to precess about the axis of the injector. Hence, it is a precessing vortex core, which is also rotating at the same time, about the axis of the injector (and the combustor). This identification is in agreement with the topology of the PVC by Poinsot et al. (Poinsot and Veynante, 2005).

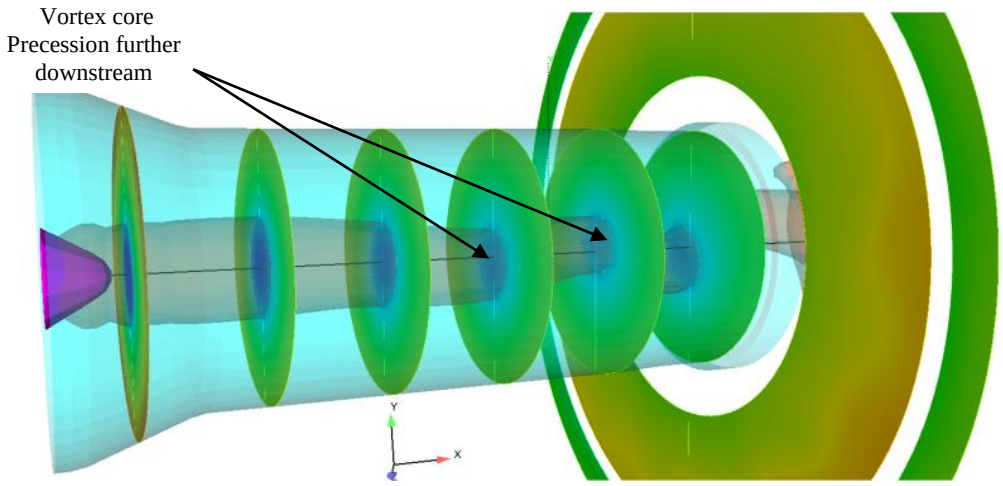

Fig. 4.4 Precessing nature of the vortex core structure

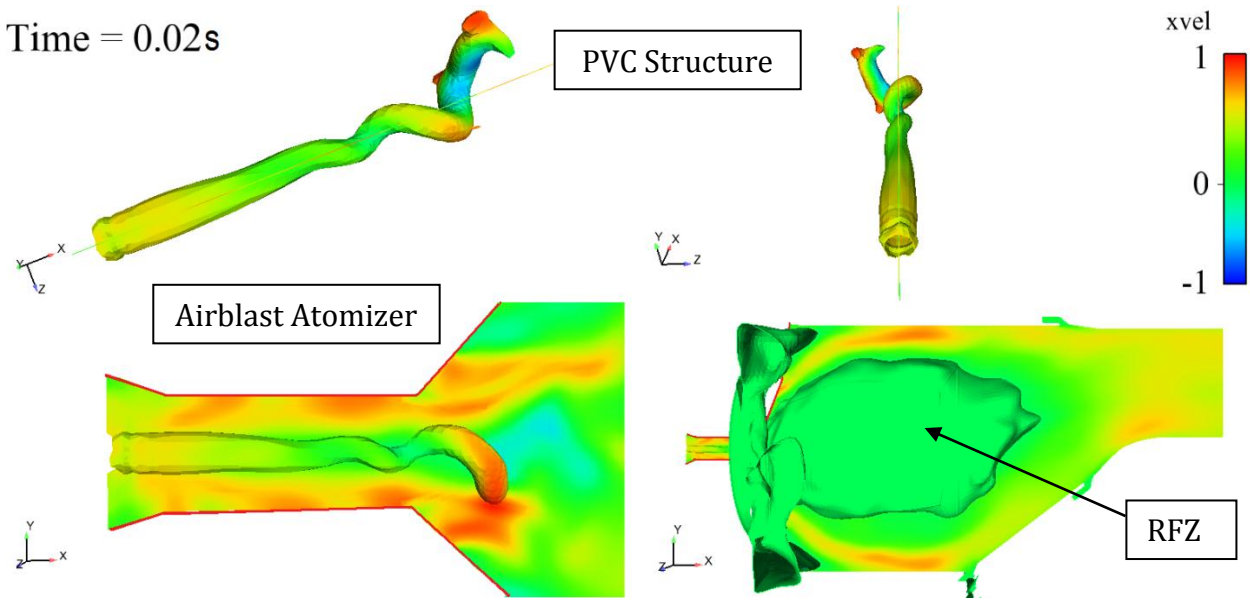

Fig. 4.5 Axial velocity field with PVC structure and RFZ at T = 0.02s

Figure 4.5 depicts the axial velocity flow field after 0.02s of flow time. It clearly shows the existence of PVC in the vicinity of the air blast atomizer flow field. The PVC structure has a clockwise winding sense but the whole structure rotates in an anti-clockwise sense and has a periodic motion. In the present injector configuration, the PVC resides only within the injector and extends in length up to the end face of the injector. The PVC is captured using a pressure iso-surface at a low pressure value of -40 KP4. This PVC resembles the PVC structure observed by Wang et al. (2007), who simulated gas-turbine injector flow using LES under reacting conditions.

In Figure 4.5, the low-pressure core which is initially aligned with the X-axis, is then driven away from the centerline flow, and extended downstream spirally. The PVC structure as a whole follows the main flow. The RFZ formed downstream is also shown using an iso-surface of zero axial velocity. These findings are in agreement with the findings of Fick et al. (1997) and Froud et al. (1995), who used experimental methods for identifying the PVC, its precessing nature and its interaction with RFZ downstream in swirl induced flows. These findings are also in agreement with the findings on Fokaides et al. (2009) which reported the existence of the PVC in the vicinity of an air blast atomizer.

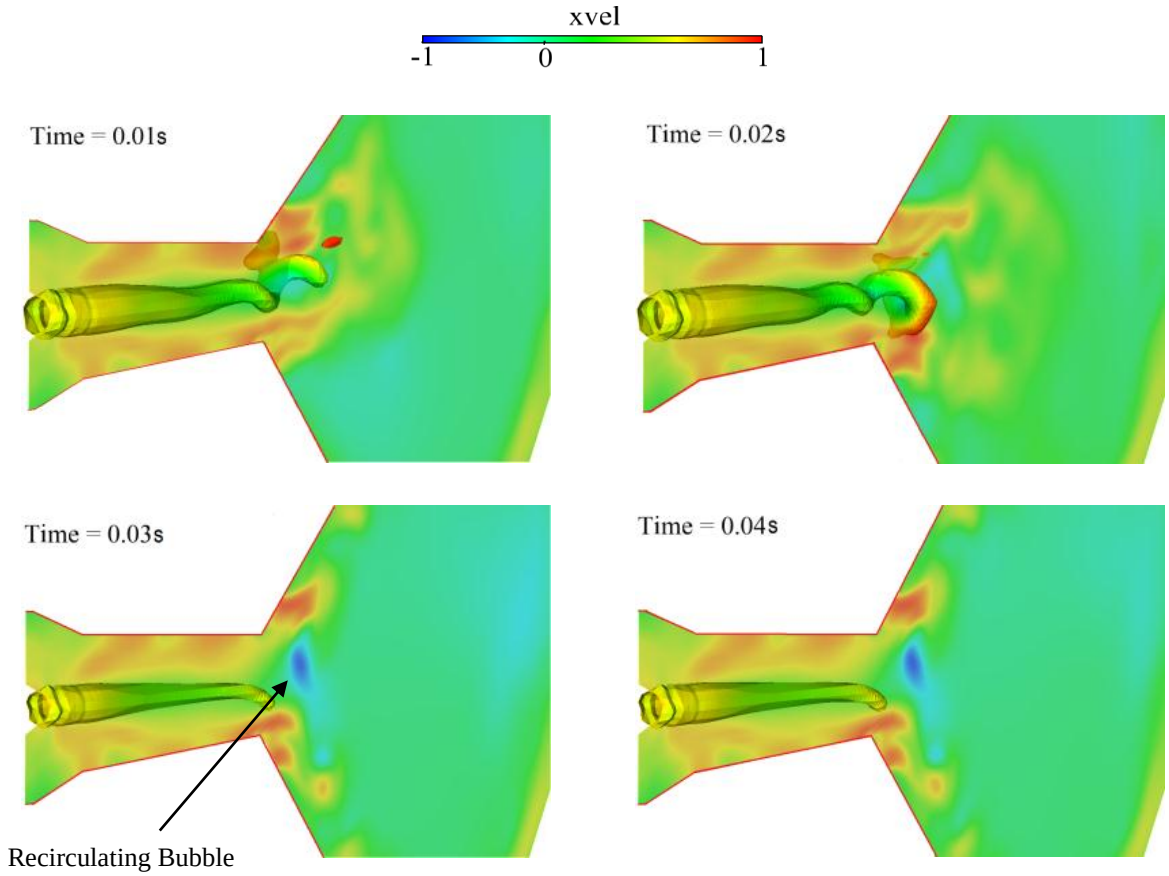

Fig. 4.6 Structure of the precessing vortex core at denoted flow times

Figure 4.6 shows the time evolution of the PVC in the vicinity of the air blast atomizer over 40ms of flow-time. Four different instants are shown to give a clearer understanding about the structural evolution of the PVC. The PVC develops and forms into a spiral structure during the first 10ms of flow-time. It then sustains its motion and grows in strength from 10ms to 20ms. After T = 20ms, the PVC structure is suppressed as seen at T = 30ms of Figure 4.6. The PVC still rotates in an anti-clockwise sense but has now reduced in size and strength. A recirculating bubble is seen to have formed at the exit of the pilot jet after T = 30ms in Figure 4.6.

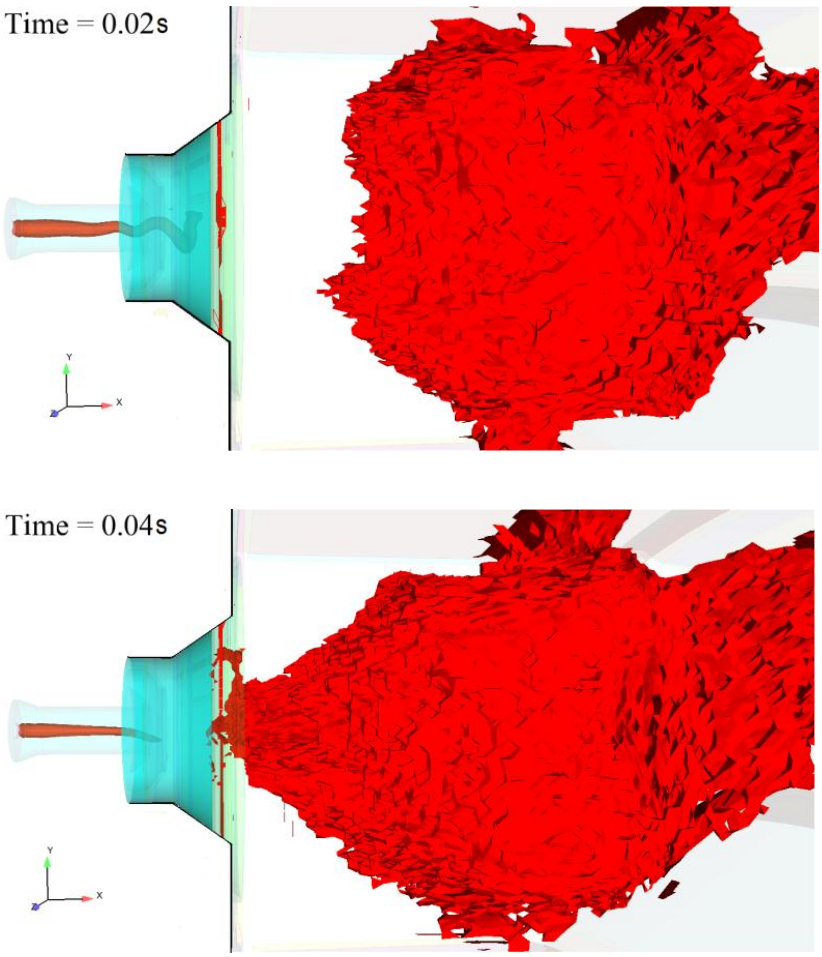

Fig. 4.7 Iso-contours of mean progress variable $\bar{C}$ = 1 showing CIVB

Figure 4.7 shows the combustion induced vortex breakdown (CIVB) phenomen4. It shows iso-contours of mean progress variable, $\bar{C}$ = 1, downstream from the injector's exit in the combustor indicating that the mixture is completely burnt. At T = 0.02s, the completely burnt mixture occurs further downstream away from the injector's premixing zone due to the existence of the PVC and high axial momentum in the vortex core. At T = 0.04s, the PVC structure breaks down due to expansion of hot gases in the RFZ downstream, leading to flame flashback into the injector's pre-mixing zone as the mixture with $\bar{C}$ = 1 propagates upstream near the injector. This process is referred to as combustion induced vortex breakdown (CIVB) (Fritz et al., 2004 and Tangermann et al.,

2009). Figure 4.8 shows the position of the flame-front near the injector's exit at the denoted flow times. At T = 0.02s, due to PVC existence, the flame-front is established away from the premixing zone of the injector. At T = 0.04s, the flame front moves upstream and this clearly shows the occurrence of the flashback mechanism into the premixing zone of the injector. These findings related to the flashback mechanism due to CIVB are in agreement with experimental findings of Fritz et al. (2004) which showed that CIVB is the dominating mechanism of flashback. Numerical findings of Tangermann et al. (2009) have also reported flashback observations due to CIVB using URANS method on a quasi-2D model of a simplified geometry.

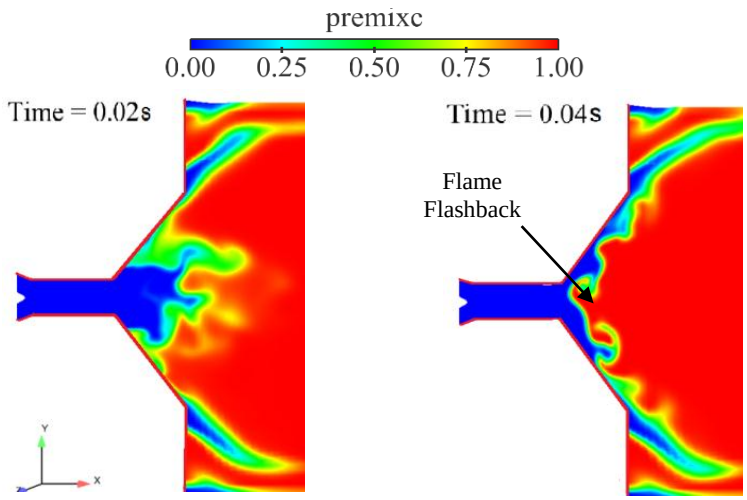

Fig. 4.8 Position of the flame-front near injector exit as seen in the meridional plane

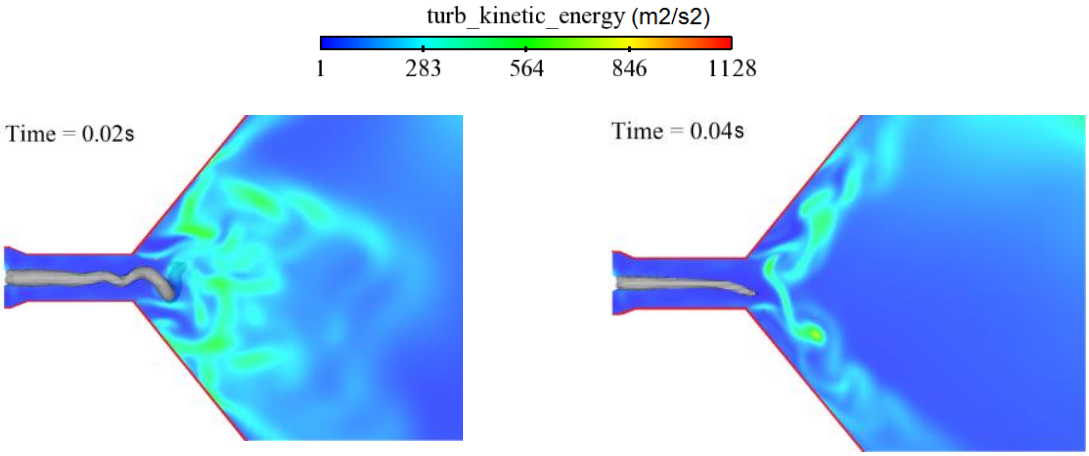

Fig. 4.9 Distribution of turbulence kinetic energy levels at denoted flow times

Figure 4.9 shows the distribution of turbulence kinetic energy in the vicinity of the air-blast atomizer before (left) and after (right) the suppression of the precessing vortex core (PVC). To achieve low-emission combustion, complete evaporation of liquid fuel droplets and thorough mixing of fuel and air within a short distance is desirable [15].

The existence of the PVC at T = 0.02s produces high levels of turbulence in the vicinity of the air blast atomizer end. The existence of the PVC at T = 0.02s produces high levels of turbulence in the vicinity of the air blast atomizer end. It facilitates the breakup of the liquid fuel into droplets and also enhances the fuel/air mixing process (Patel and Menon, 2008). Due to PVC suppression, as seen at T = 0.04s, the turbulence kinetic energy level is reduced compared to T = 0.02s, which may affect the liquid fuel breakup process resulting in inefficient fuel/air mixing. As the flow expands from the injector exit and evolves downstream, strong shear layers develop, due to the velocity difference between the jet flow and the ambient fluid. Large-scale coherent structures are generated in the shear layer regions, and shed downstream sequentially (Durham et al., 2009). As vortices move downstream, they merge and increase the shear layer spread.

Figure 4.10 shows velocity vectors at plane 1-1 which is located downstream of the injector-end close to the exit of the injector and it clearly reveals the near injector-end flow field aerodynamics before and after the PVC suppression.

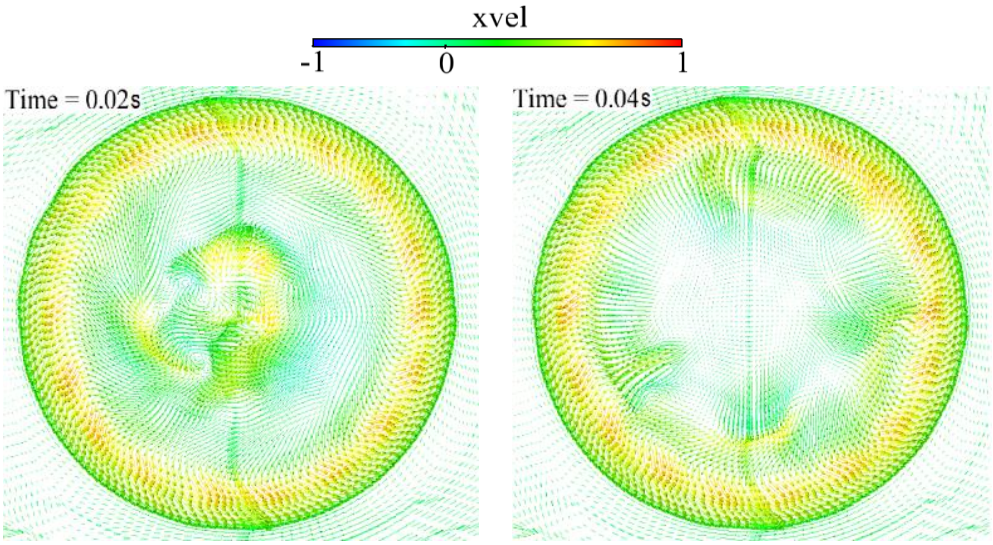

Fig. 4.10 Vortices near injector-end flow field (plane 1-1) at denoted flow-times colored by axial velocity

As seen in the Figure 4.10, at the denoted flow times, the velocity vectors show the existence of multiple vortices which emanate from the centre, precess around the centre, diverge and then continue to revolve around the centre. At T = 0.02s, the vortices are seen to precess around the geometric centre of the injector end due to the existence of the PVC structure. However after PVC suppression, these vortices move away from the centre and precess far away from the geometric centre. This behaviour of the vortices is expected to be greatly influenced by the upstream injector geometry. The presence of these vortices distorts the streamline pattern in the downstream direction. These vortices exert a significant influence on the combustion process by modulating the mixing processes among incoming fuel, air and hot combustion products.

4.4 Temperature fluctuation

One of the main objectives of this study is to understand the effect of the PVC on the heat release pattern inside the combustor and the impact of combustion on the PVC itself. For this purpose, the URANS simulation was run at different time-step sizes in order to understand the effect of simulation time-step size on temperature prediction patterns. Figure 4.11 shows the variation of mass-weighted average temperature (T_{ma}) captured by different time-step size simulations at the exit plane 4-4 (c.f. Figure 4.1) of the combustor. The Y-axis is normalized against a reference temperature. The average value of T_{ma} captured by all time-step size simulations remains similar though the coarser time-step sizes are not able to capture small time-scale fluctuations in the flow-field.

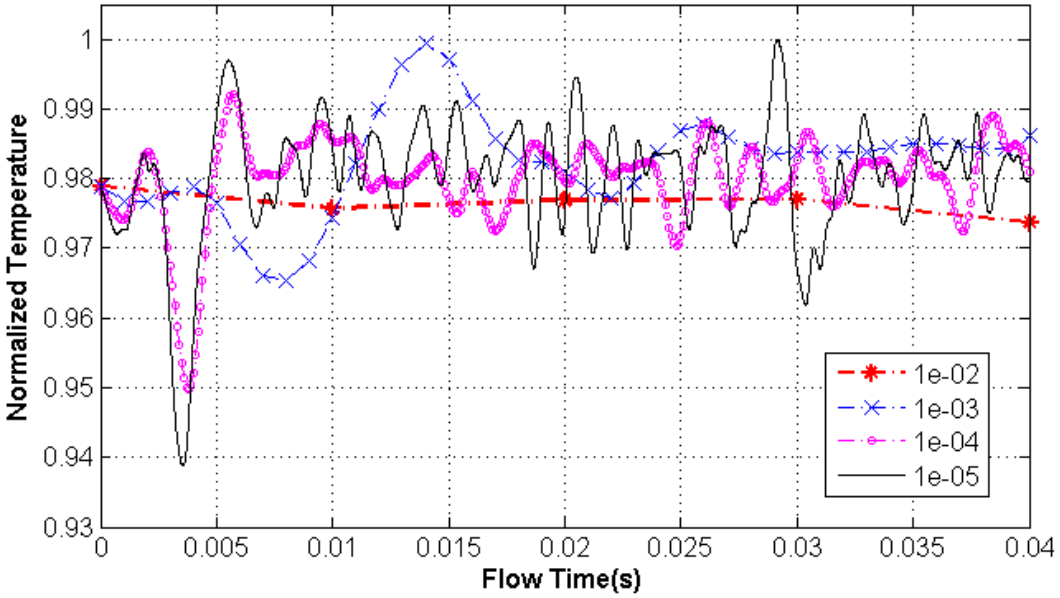

Fig. 4.11 Mass-weighted average temperature (T_{ma}) variations at exit plane captured by different time-step size simulations

Figure 4.12 depicts the temperature field at the denoted flow times for the simulation with 1e-05s time-step size. The existence of the PVC at T = 0.02s is responsible for relatively cooler temperatures close to the injector. This is seen more clearly in Figure 4.13, which shows the temperature profile at plane 1-1. As seen in Figure 4.9, the PVC in the vicinity of the air blast atomizer causes intense turbulence generation and rapid mixing of the fuel and air. Assisted by multiple vortex structures in this zone (c.f. Figure 4.10) the PVC structure helps to keep the flame away from the injector assembly itself (c.f. Figure 4.8) thus allowing homogenous mixing of air and fuel before the mixture reaches the combustion zone. As seen in Figure 4.13 at T = 0.04s, due to flashback (c.f. Figure 4.8) there is an intense temperature rise in the premixing zone of the injector. The PVC structure, which reduces both in size and strength (c.f. Figure 4.6) after suppression, ceases to exist in the vicinity of the air blast atomizer. This results in relatively less turbulence generation leading to inefficient mixing of fuel and air in the

near injector-end flow field. This leads to the formation of fuel rich pockets and hence the appearance of hot-spots and a sudden rise in flow-field temperature. Hot-spots of high temperature are clearly visible in plane 1-1 in Figure 4.13. This may lead to increased production of NOx and also cause damage to the injector assembly, which is not designed to operate at these high temperatures.

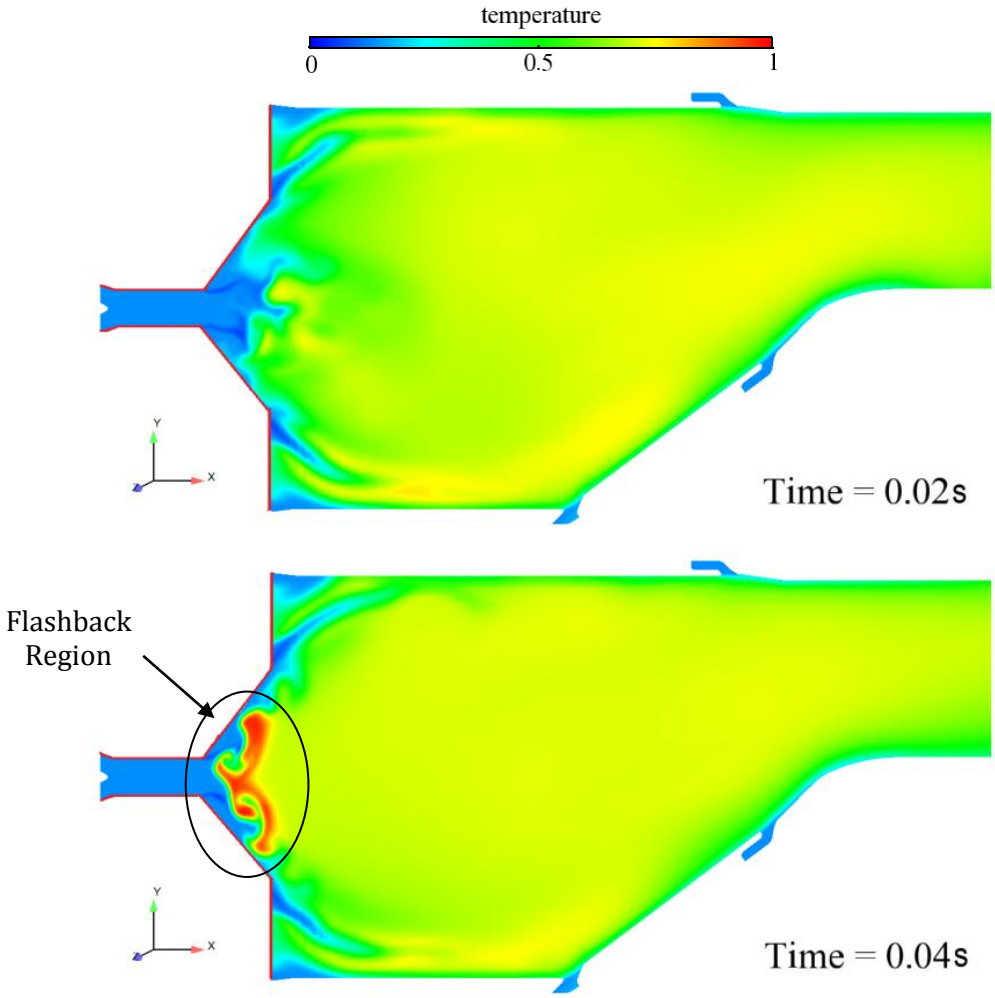

Fig. 4.12 Temperature field in the meridional plane at denoted flow times

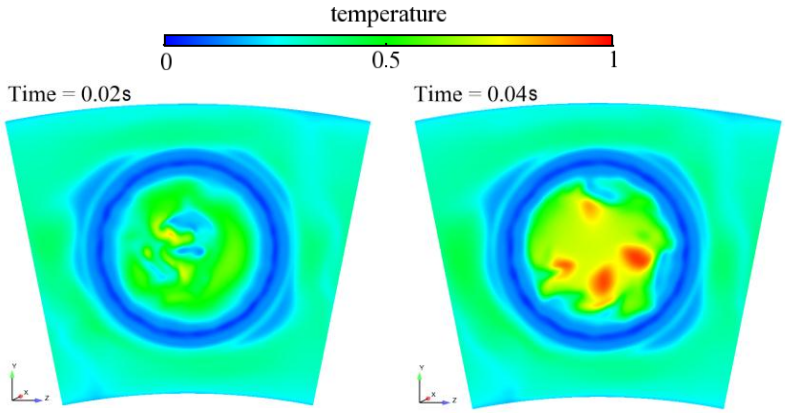

Fig. 4.13 Plane 1-1 temperature field at denoted flow times

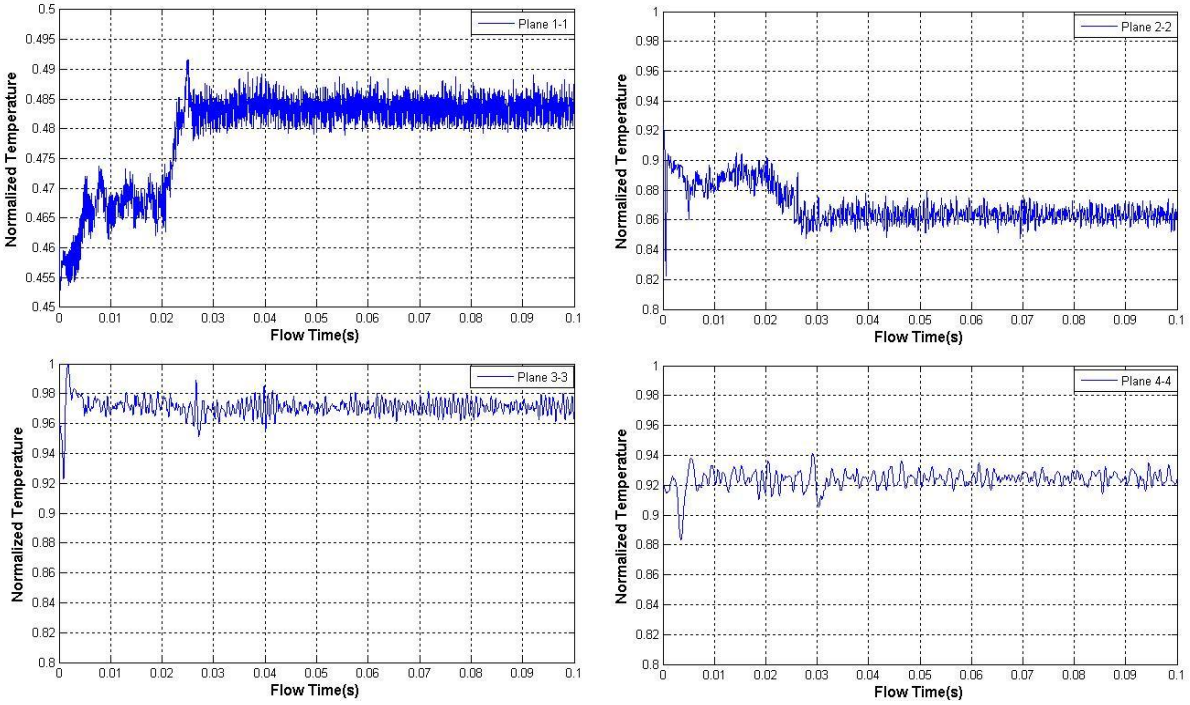

Fig. 4.14 Mass-weighted average temperature (T_{ma}) variation at each plane in the combustor

Figure 4.14 shows the variation of mass weighted average temperature (T_{ma}) over 0.1s of flow-time across all four monitoring planes setup in the combustor (c.f. Figure 4.1). The graphs are normalized against a reference temperature. Plane 1-1 is the closest to the injector-end and lies in the most turbulent zone. Planes 2-2 and 3-3 lie further downstream of plane 1-1 at increasing distances. The effect of the PVC evolution (c.f. Figure 4.6) and multiple precessing vortices (c.f. Figure 4.10) is seen on the temperature profiles, especially of plane 1-1 and 2-4. On planes 1-1 and 2-2 in Figure 4.14, an initial transient is seen for the first 0.01s of flow-time. This coincides with the period of PVC formation in the vicinity of the air blast atomizer of the injector. From 0.01s to 0.02s, the PVC structure sustains in the swirling flow generating high turbulence and oscillations, whose effect is seen on the heat release pattern (i.e. temperature variation) on planes 1-1 and 2-4. Also along with PVC, multiple vortices which precess around the PVC (c.f. Figure 4.10) are periodically shed downstream from the injector. Hence, high frequency oscillation of temperature is seen at these planes. The frequency of oscillation of temperature at these planes is related to frequency of PVC precession and frequency at which the vortices are shed downstream. The effect is strongest on plane 1-1 compared to plane 2-2, as it is very close to the injector-end face.

Ahead of flow-time T = 0.02s, the PVC is suppressed due to expansion of hot gases in the RFZ formed downstream of the injector. Due to this suppression the PVC reduces in size and strength and a sudden rise is seen in the temperature profile on plane 1-1. At the same time, a temperature drop is seen in plane 2-2 between T = 0.02s and T = 0.03s due to expansion of the flame upstream in the injector. Further ahead of T = 0.03s, the flow-

field is settled with fluctuating temperature at high frequency in the absence of the PVC. At planes 3-3 and 4-4, an oscillating behaviour of temperature variation is seen over the entire 0.1s of flow-time, but the frequency of oscillations is less compared to plane 1-1 and plane 2-2, as they are further away from the PVC structure. This suggests that the PVC oscillations have relatively less effect on the heat release pattern on planes 3-3 and 4-4. Plane 3-3 has maximum heat release and thus has peak temperature compared to the other planes. Plane 4-4, being the exit plane, is the farthest from the PVC, and has the lowest frequency of temperature oscillation. Plane 3-3 has maximum heat release and thus has peak temperature compared to other planes.

The average of the mass-weighted average temperatures (T_{ama}) over 0.1s of flow-time on plane 4-4 is also less compared to plane 3-3 due to cooling effects. The amplitude and frequency of temperature oscillation at exit plane 4-4 is the result of all instabilities including the PVC, RFZ and other vortices which precess around the PVC (c.f. Figure 4.10) and shed downstream in the combustor. This is in agreement with experimental evidence of Fokaides et al. (2009) who performed frequency analysis of spontaneous emission near and downstream of the instability and showed that the frequency of fluctuation decreases further downstream from the nozzle vicinity and concluded that periodic heat release would not be evidenced downstream of the instability regime. The temperature fluctuation pattern depicted in Figure 4.14 also shows that the PVC instability has more effect near the injector and the effect decreases downstream.

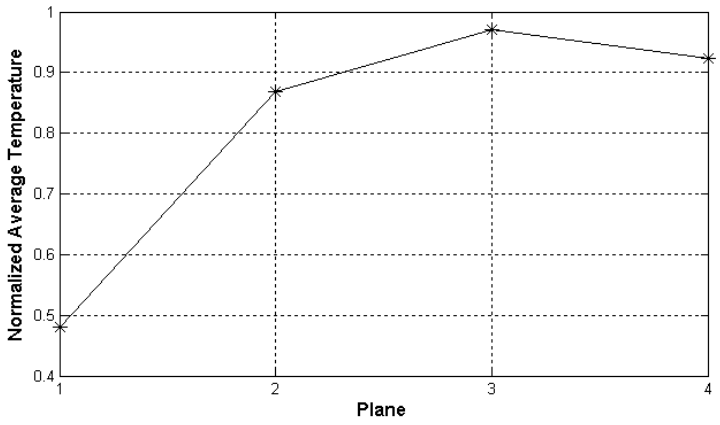

Fig. 4.15 Average of mass-weighted average temperature (T_{ama}) inside the combustor (Normalized)

Figure 4.15 shows the variation of the average of mass-weighted average temperatures (T_{ama}) over 0.1s of flow-time inside the combustor, along its length at all four planes. This average is the average of mass-weighted average temperatures recorded over 0.1s of flow time at each plane. The first plane is naturally cooler due to its closeness to the injector exit plane and existence of the low pressure zone. The temperature rises through plane 2 and 3 as they lie in the recirculation flow zone (RFZ) which is also the main reaction zone and contains the flame. A drop in exit plane temperature is seen relative to plane 3-3 due to the cooling effect of the air intake near the exit.

4.5 Velocity fluctuation

Figure 4.16 shows the variation of X-velocity along the axis of the injector and combustor at the denoted flow-times. Position along the axis is normalized against maximum length until combustor contraction section (c.f. Figure 4.1). The PVC structure (c.f. Figure 4.5) resides only within the injector, after which it is destroyed. Evidence elsewhere suggests that the structure is destroyed by turbulence near the exit of the injector (Poinsot and Veynante, 2005). However, its existence and suppression has a clear effect on the velocity flow-field downstream the injector exit.

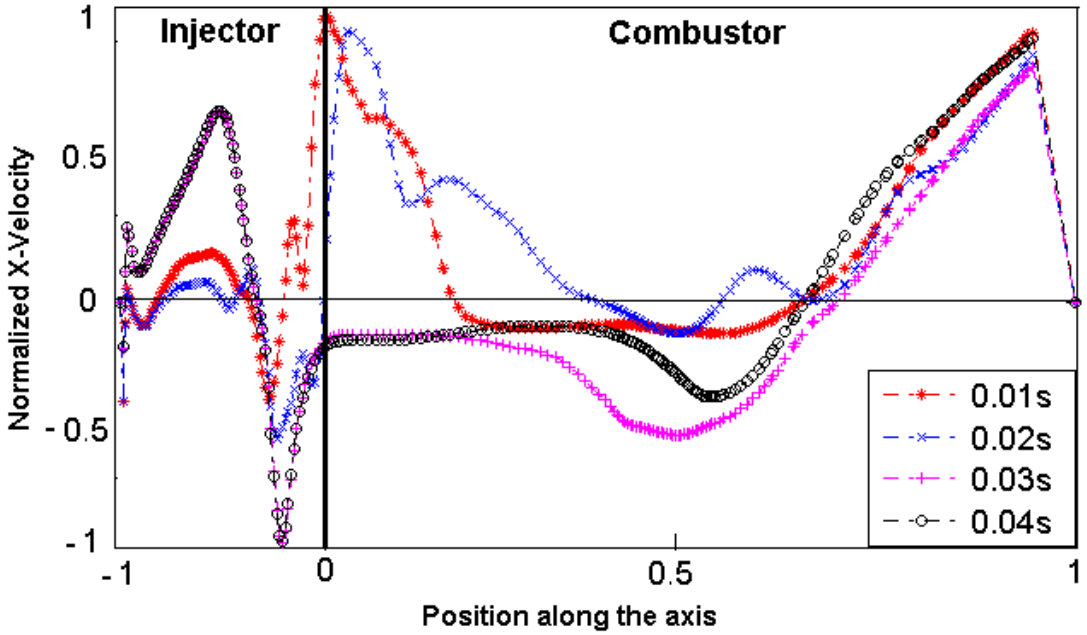

Fig. 4.16 Variation of X-velocity along the axis of the injector and combustor at denoted flow-times

As seen in Figure 4.16, at flow-time T = 0.01s, the PVC exists but in the formation stage (c.f. Figure 4.6). Nevertheless, it clearly has a strong effect on the velocity field downstream the injector. The existence of the PVC generates high turbulence kinetic energy (c.f. Figure 4.9) and causes an acceleration of the flow along the axis of the combustor, especially near the injector exit. At flow-time T = 0.02s, due to strengthening of the PVC, the flow has higher axial momentum near the injector exit which causes the 'push forward' effect on the flow-field downstream the injector, pushing the flame-front forward (c.f. Figures 4.7 and 4.8).

At flow-time T = 0.03s, the PVC structure is suppressed in size and strength as shown in Figure 4.6. Due to this suppression, a decrease in the level of turbulence kinetic energy near the injector exit region was discussed above (c.f. Figure 4.9). The X-velocity variation at T = 0.03s in Figure 4.16, shows the effect of PVC suppression. Along the axis of the combustor, negative X-velocity is seen in the near-injector exit flow-field as the

RFZ enters the injector's premixing zone. The suppression of the PVC from the vicinity of the air blast atomizer end creates a 'pull backward' effect. This causes upstream propagation of the flame-front (c.f. Figure 4.8) into the injector's premixing zone and an intense temperature rise (c.f. Figure 4.12) and hot-spots (c.f. Figure 4.13) in the premixing zone of the injector. This variation of axial velocity along the axis, due to damping of PVC in combustion, is also evidenced by Roux et al. (2005). This vortex breakdown phenomena induced by combustion and discovered as CIVB by Fritz et al. (2004) in an experimental setup is captured here by the URANS method. At flow-time T = 0.04s, the PVC structure remains suppressed. In Figure 4.16, at T = 0.04s, the near injector flow-field shows no change in X-velocity variation, compared to T = 0.03s, while a distinct change is observed further downstream the injector exit.

4.6 Summary

URANS simulations of a modern lean burn combustor geometry using a complex fuel injector system for gas turbine propulsion applications have been performed in this chapter. The simulation was run for a total of 0.1s of flow-time, with mass-weighted average temperature fluctuations monitored across different planes. However, after 40ms of flow time, no further change in the flow-field behaviour was observed which represents more than four combustor flow through times, using a time-step size of 10^{-5} s.. The run time required to simulate 0.1s of flow time with 10^{-5}s time-step size was approximately three months, using 8 processes in parallel on a cluster using Intel quad core processors with 2.8GHz clock rate.

An axisymmetric bubble type vortex breakdown is captured which then develops downstream in to a central recirculation flow zone (RFZ) which holds the flame and combustion processes. A start-up precessing vortex core (PVC) showing complex dynamical behaviour over the first 20ms of flow-time is also captured in the vicinity of the air blast atomizer. In addition to this PVC, multiple vortices are seen emanating from the centre and precessing around the central axis influencing the near injector flow field dynamics. Later, PVC suppression, a phenomenon caused due to the expansion of hot gases and combustion processes downstream of the injector is captured. The analysis performed using the URANS method on a complete 3D geometry predicts the PVC suppression and flashback phenomenon. Due to PVC suppression, hot-spots with very high temperatures near the injector exit are observed. Such hot-spots are undesirable as they can produce higher NOx and cause possible damage to the injector assembly itself.

Since the computational analysis cost of Rolls-Royce combustor simulations is very high and unpractical for developing new design strategies, a two-dimensional test combustor problem with similar flow features (e.g. recirculation flow zone, flame-vortex interaction etc.) and unsteady reactive dynamics is described and analyzed in chapter 5.

Chapter 5

Two-dimensional combustor flow in spatio-temporal domain

5.1 Introduction

As discussed in chapter 2, vortices are present naturally in many reacting flows of technological interest e.g. in continuous combustors, where their production is related to the streams injected into the chamber and to the turbulent motion of the flow. In general, concentrated vorticity constitutes the large-scale structure of the turbulent shear flows found in combustion systems. The elementary interaction between a vortex and a flame thus appears as a key process in the description of turbulent reactive flows (Renard et al., 2000). Flame-vortex interaction is one of the most significant instability mechanisms in large-scale gas turbine combustors (Venkataraman et al., 1999 and Bernier et al., 2004). The vortex roll-up often governs the transport of fresh reactants into the burning regions and this process determines the rate of the reaction in the flow and the amplitude of the pressure pulse associated with the vortex burn out. This view of practical devices and modes of operation clearly indicates that vortices and the accompanying dynamical interaction with combustion are of great importance.

In this chapter, flame-vortex dynamics in a 2D lean burn combustor is analyzed. A numerical study of steady and unsteady turbulent reactive processes behind a profiled backward-facing step is presented. Although the 2D combustor geometry is simplified the flame-vortex behaviour is representative of that seen in more complex system†.
Flame-vortex dynamics behind a backward-facing step has been examined experimentally and numerically previously (Poinsot et al., 1987; Venkataraman et al., 1999; Keller et al., 1982; Cohen et al., 1996; Paschareit et al., 1998, Yu et al., 1991). However, definitive conclusions regarding the essential mechanisms or conditions under which flame-vortex dynamics may arise have not been reached yet. In most cases, it has been observed that under unstable operating conditions, as determined by the

† See Chapter 4

mixture equivalence ratio and Reynolds number, one or more large vortices periodically convolute the flame front during part of the instability cycle. It has been suggested that the periodic convolution of the flame leads to oscillations in the heat release rate that may couple with the pressure field. To close the loop, pressure must also drive the vortex formation and flame convolution in a way that ensures positive feedback. In a study by Ghoniem et al. (2005), experimental evidence supporting the role of unsteady vortex shedding and flame-vortex interactions in sustaining the combustion instability was provided.

The interaction of a premixed flame with the transient vortical structures in a turbulent flow can have a profound effect on the flame. Time dependent effects of stretch and strain can alter chemical pathways and may result in flame quenching. Combustion instability governed primarily by the turbulent mixing zone behind the trailing edge of a bluff-body flame holder, and by the recirculation zone immediately behind its base has been highlighted in studies by Mellor et al. (1976), Spadaccini (1974) and Lefebvre (1977). The effect of the recirculation zone on combustion instability under laminar as well as turbulent conditions has been studied by Huck and Marek (1978), using an axisymmetric combustion chamber with a sudden increase in cross-section area at the inlet port. When the size of the port was decreased, prolonging the residence time of the gases in its vicinity, a marked improvement in combustion stability was noted, indicating the influence of the size of the recirculation zone in this respect.

5.2 Experimental combustor test rig of Keller et al.

The combustor modeled for the study is the one used by Keller et al. (c.f. Figure 5.1) in an experimental study of mechanisms of instabilities in turbulent combustion leading to flashback. The combustion chamber had an oblong rectangular cross section to model the essential features of planar flow and was provided with a profiled backward-facing step acting as the flame holder. Premixed propane/air mixture was used as the working fluid.

Upon experimental investigation, Keller et al. observed three modes of instabilities in the combustion chamber under highly turbulent conditions: 1) humming – a significant increase in the amplitude of the vortex pattern in the turbulent mixing zone; 2) buzzing – a large-scale oscillation of the flame up and down across the test section, eventually obliterating the vortex pattern of the mixing zone; 3) chucking – a cyclic formation of the flame that appears as if it were periodically spilled over the edge of the step. The mechanism of these phenomena is ascribed to the action of the vortices in the recirculation zone, and their interactions with the trailing vortex pattern of the turbulent mixing layer behind the step.

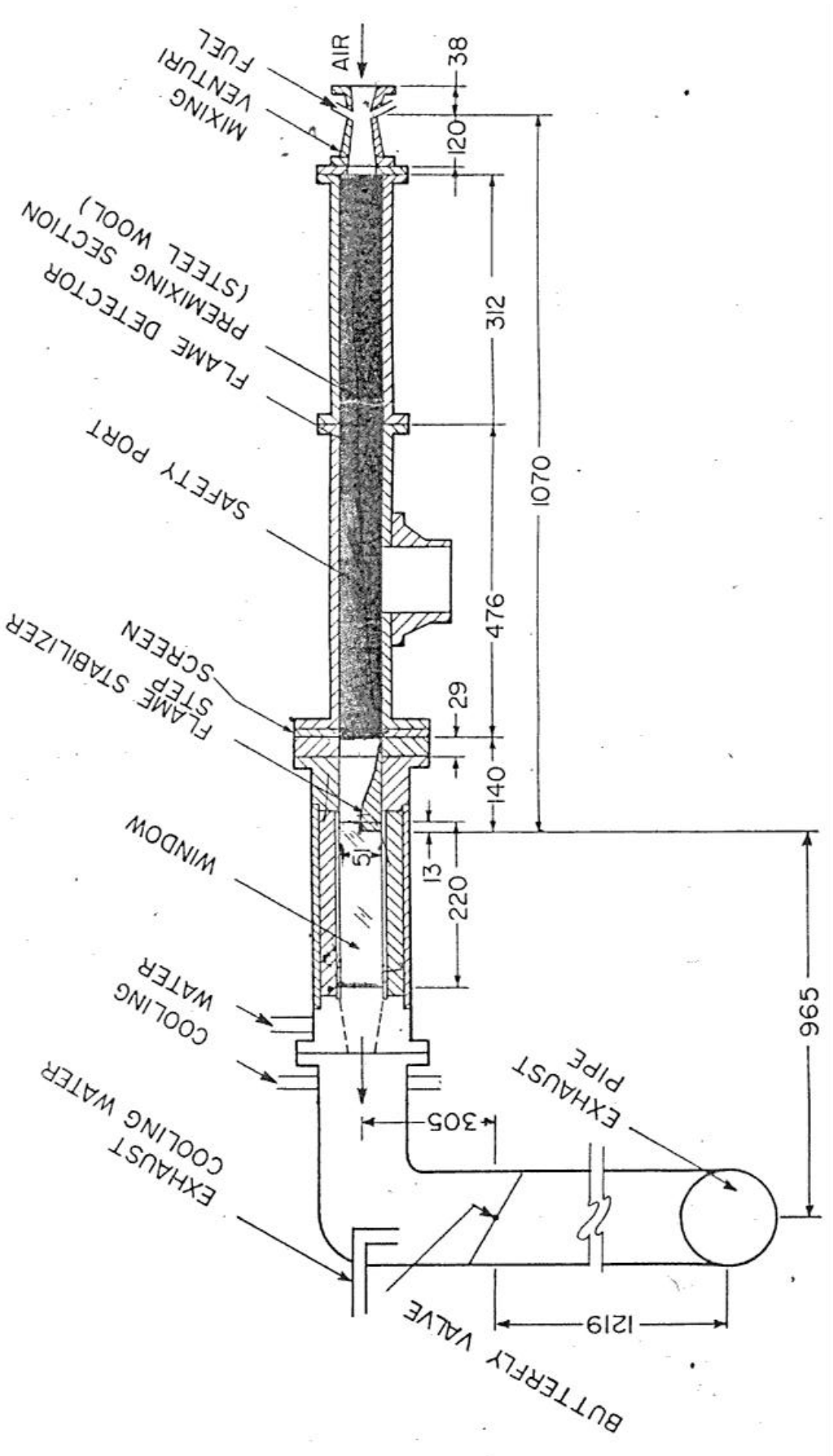

Fig. 5.1 Cross section of the combustion chamber experimental setup as used by Keller et al., 1982 and Ganji et al. (1980) (All dimensions in mm)

5.2.1 Flame/vortex interaction process – a physical understanding

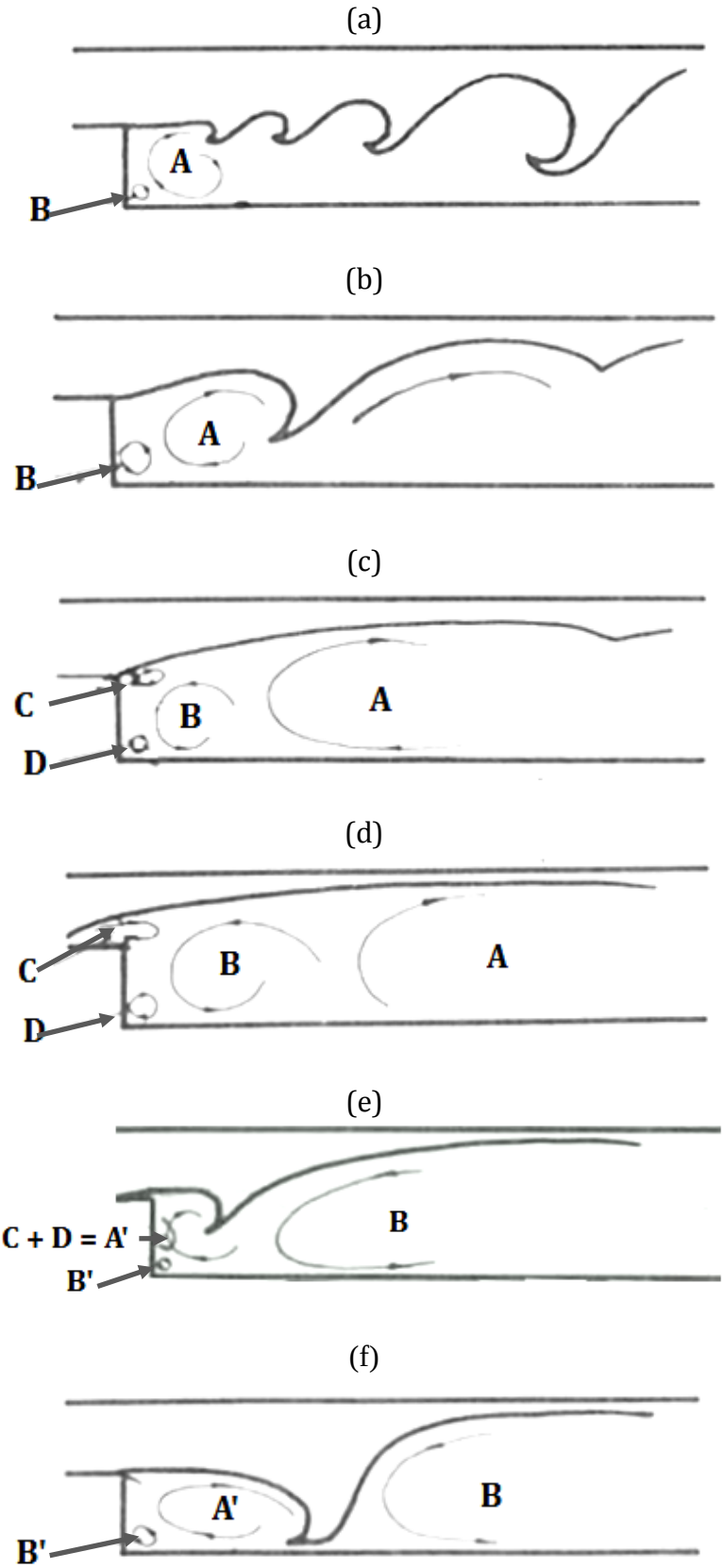

Fig. 5.2 Interaction between flame front and trailing vortices behind the step (Keller et al., 1982)

The instabilities in turbulent combustion of premixed gases stabilized by the base flow behind a bluff body are intimately related to the large-scale structures of turbulent shear flow. Its prominent features have been described by Roshko (1976) while those pertaining to the base flow behind a step, including in particular the recirculation zone, were investigated experimentally earlier by Kim et al. (1978) and recently by Ghoniem et al. (2005) and Altay et al. (2009).

Figure 5.2(a) shows a trailing vortex pattern downstream of the step. According to Keller et al. (1982), the flame front delineates the outer edges of the mixing layer at the contour of the interface between the burned gases and the fresh charge. The recirculation vortex A lies below, as a rule, established behind the step, irrespective of whether the flow-field is associated with combustion or not. This gives rise to the counter rotating vortex B. Figure 5.2(b) shows that under the presence of combustion, when burned gases are produced both of these vortices (A and B) grow. As the recirculation vortex of the burned gases grows, it causes the vortex A to be pushed downstream (c.f. Figure 5.2(c)), while the size of vortex B increases. As a consequence of the counterclockwise circulation of this vortex, it gives rise to vortices C and D, as required by compatibility with flow of the fresh charge. When vortex B becomes larger (c.f. Figure 5.2(d)), vortex C may be forced upstream, causing a flow reversal on the top of the step, tripping the boundary layer, and pushing the flame upstream. This is the characteristic feature of the turbulent flashback observed by Keller et al. (1982). The flame front is attached at its upstream edge of the boundary layer, but behind it is lifted from the wall by the action of vortex C.

Further as vortex B still grows, it is convected downstream, while vortex C pairs with vortex D to form a new vortex A', and also a new corner vortex B' is formed (c.f. Figure 5.2(e)). Finally, vortex A' grows to a size which is comparable to that of vortex A and B' to B (c.f. Figure 5.2(b)). At the same time, vortex B is convected further downstream and the combined action of vortex A' and B causes the flame to acquire a practically vertical orientation, extending across the full height of the combustor (c.f. Figure 5.2(f)).

Figure 5.2(b) illustrates the forming of the first vortex of the so-called humming cycle, the instability of high frequency oscillation. According to Keller et al. (1982), this occurs evidently due to pairing of the recirculation vortex A with the first component of the set of trailing vortices. The next vortex downstream is the result of the growth of vortex A in the course of its convection. In this study, a premixed reacting flow under steady and unsteady conditions is simulated at high Reynolds number in a representative of the geometry as shown in Figure 5.1.

The fundamental focus here is to capture flow dynamics coupled with flame motion, but not considering acoustic modelling of the upstream and downstream elements.

5.3 Geometric model

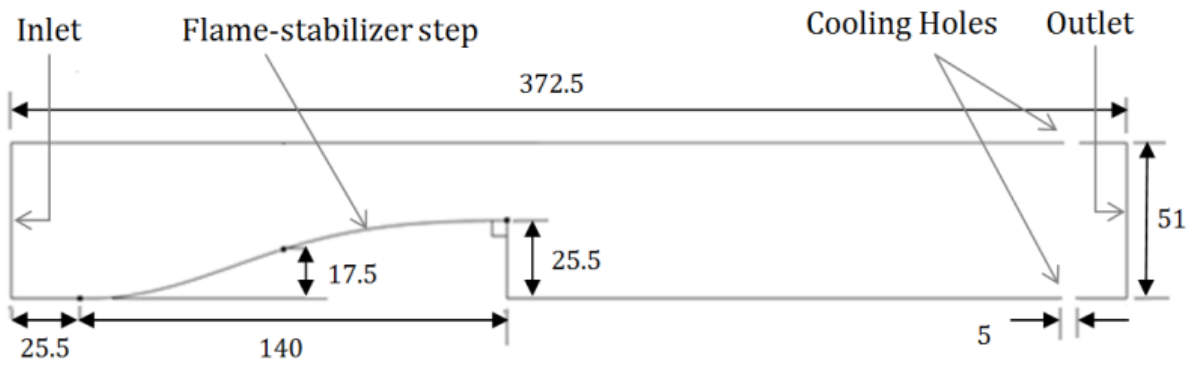

Fig. 5.3. Computational domain of the combustor with a flame-stabilizer step (All dimensions in mm)

Numerical simulations have often been used for investigation of flame/vortex interactions. Figure 5.3 shows the complete computational domain used for steady and unsteady RANS analysis indicating locations where inlet and outlet boundary conditions were specified. Important factors considered in the design of the system (c.f. Figure 5.1) by Keller et al. (1982), and previously by Ganji et al. (1980), were thorough mixing of propane and air before entering the test section and uniform velocity (flat inlet velocity profile) at the entrance to the test section (i.e. combustion chamber). Referring to the experimental setup of Keller et al., (1982) (c.f. Figure 5.1), the premixing tube is not included in the computational model. Instead of this, the configuration uses appropriate boundary conditions at the inlet and outlet of the system. In a realistic combustor, the desired outlet temperature profile is far from flat; instead, it has a profile that peaks above the mid-height of the blade. The objective is to provide lower temperatures at the turbine blade root, where mechanical stresses are highest, and at the tip of the blade which is the most difficult to cool (Lefebvre, 1983). Hence, cooling is provided near the outlet of the combustor, both at the upper and the lower wall for representing a realistic combustor outlet flow condition. The width of the cooling hole is 5 mm and is at a distance of 22mm from the outlet of the combustor. The combustion processes take place in the combustor at atmospheric pressure along its length and hot gases with products exit from the outlet.

5.4 Boundary conditions

Appropriate inlet and outlet boundary conditions are necessary for the simulation of instability processes (Najm et al., 1994). To explore the flame/vortex dynamics in the combustor in an unsteady turbulent flow, a sinusoidal function (Table 5.1) is imposed at the inlet velocity boundary condition. This technique is indeed an easy way to represent the effect of an acoustic resonance in the reaction region (Thibaut et al., 1998). The

amplitude of the forcing fluctuation is 50% of the inlet velocity at a frequency of 175 Hz, which corresponds to the frequency of the humming cycle as reported by Keller et al (1982). Table 5.1 lists the key CFD parameters employed in the commercial CFD package ANSYS FLUENT™ version 12.1. The solver used is pressure based and has a second order implicit unsteady formulation for time. The standard k - ε model is used for turbulence modeling, with standard wall functions. The SIMPLE pressure-correction method is used for pressure-velocity coupling. Combustion takes place at a lean equivalence ratio of 0.86. Fluent's partially premixed combustion model is used as the species model. The model solves a transport equation for the mean reaction progress variable $\bar{C}$, (to determine the position of the flame front), as well as the mean mixture fraction $\bar{f}$, and the mixture fraction variance $\overline{f'^2}$. Ahead of the flame ($\bar{C}$ = 0), the fuel and oxidizer are mixed but unburnt, and behind the flame ($\bar{C}$ = 1), the mixture is fully burnt (Theory Guide, ANSYS FLUENT™ Version 12.1, 2009).

Table 5.1. Key CFD analysis parameters for Ansys Fluent 12.1

Solver:	Pressure based
Space:	2D
Time:	Unsteady second order implicit
Energy equation:	Yes
Turbulence model:	*k* - *ε* (standard wall functions)
Transport and reaction:	
Species	Partially premixed combustion
Mixture properties	PDF-mixture (propane + air)
Equivalence ratio	0.86
Boundary conditions:	
Inlet	Velocity-inlet
Inlet (Momentum)	For steady RANS; V_{in} = 13.3 m/s
	For unsteady RANS; User defined function with forced sinusoidal fluctuation at inlet, with frequency = 175 Hz and amplitude = 50% of inlet velocity V_{in} = 13.3 + 6.65*sin(1099.55*t) *(t = time-step size)*
Inlet (Temperature):	300 K
Outlet:	Outflow
Cooling inlet:	Velocity inlet; V_{in} = 13.3 m/s
Reynolds number:	2.06 * 10^4 (based on step height)
Operating pressure:	101325 Pa
Convergence criteria:	1e-06 (for residuals of continuity, x-velocity and y-velocity)

5.5 Computational grid

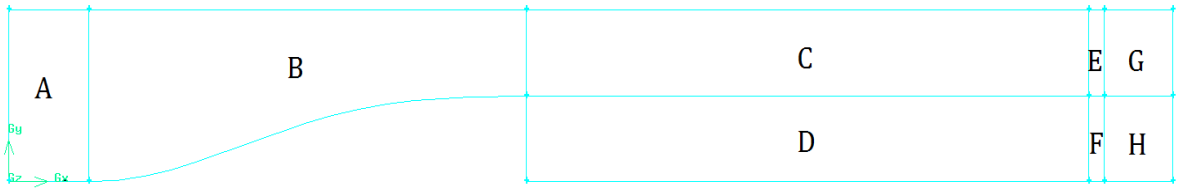

Fig. 5.4 Multi-block structured hexahedral computational grid strategy

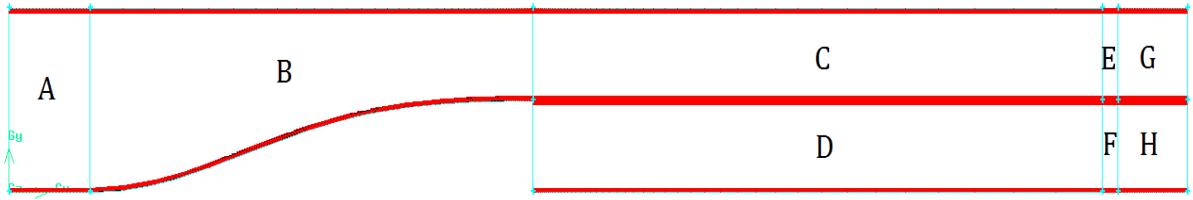

Fig. 5.5 Locations of boundary layer mesh in the 2D combustor

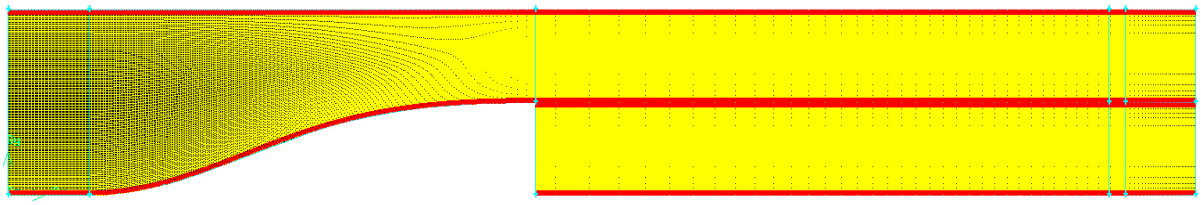

Fig. 5.6 Overall view of a structured hexahedral mesh across the 2D combustor

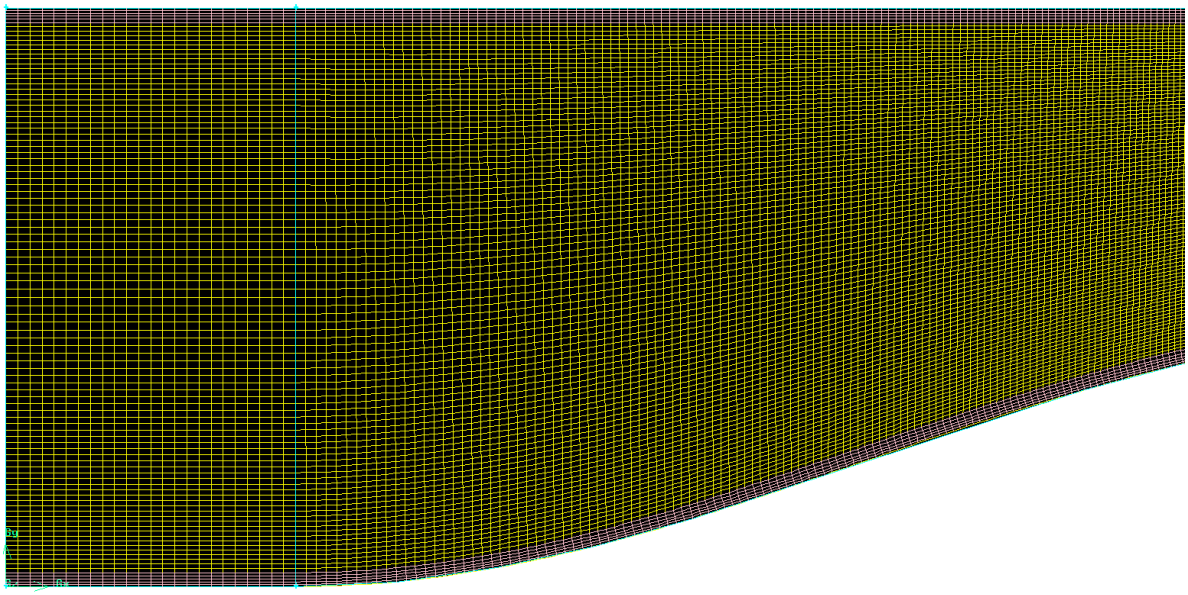

Fig. 5.7a Closer view of the mesh near the inlet

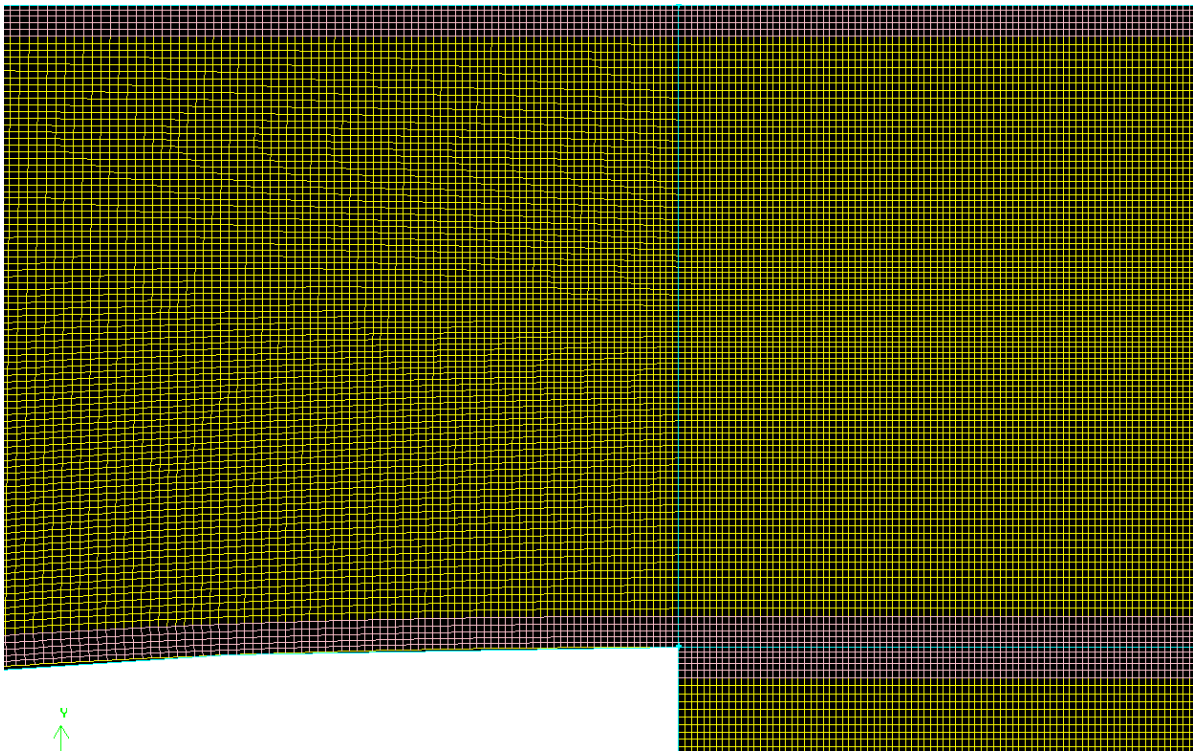

Fig. 5.7b Closer view of the mesh near the end of the step

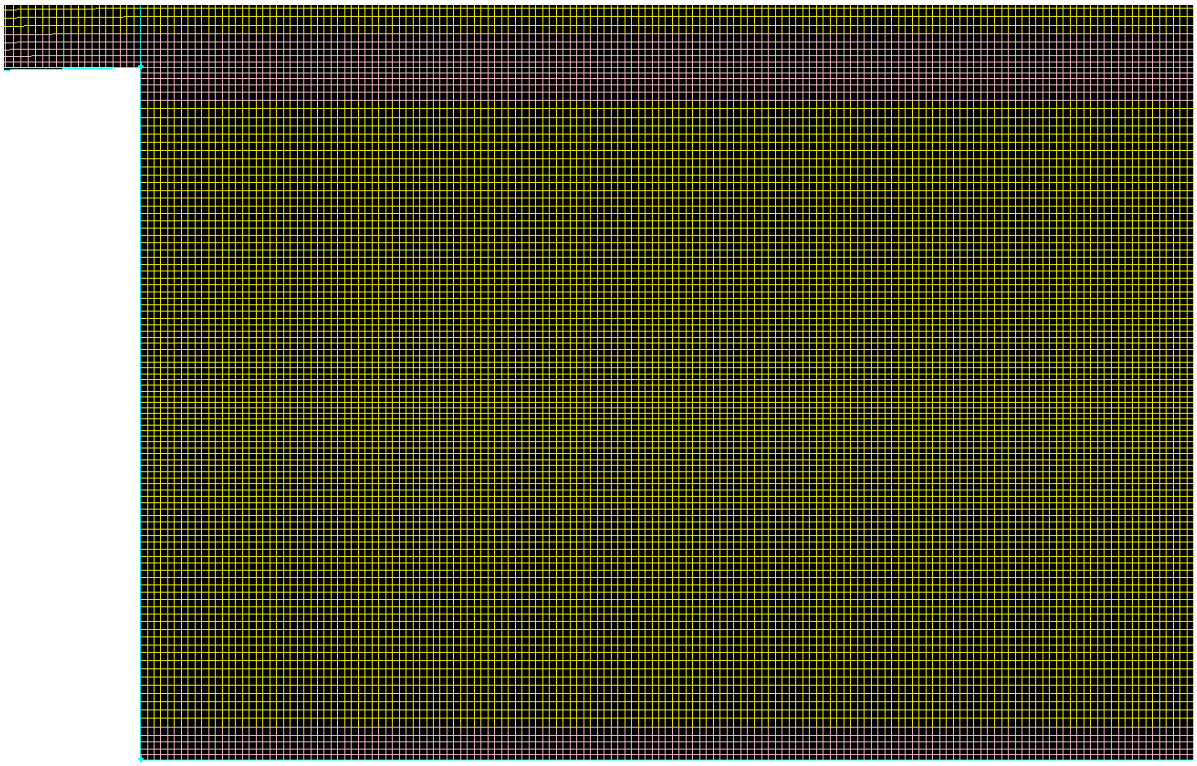

Fig. 5.8a Closer view of the mesh behind the step

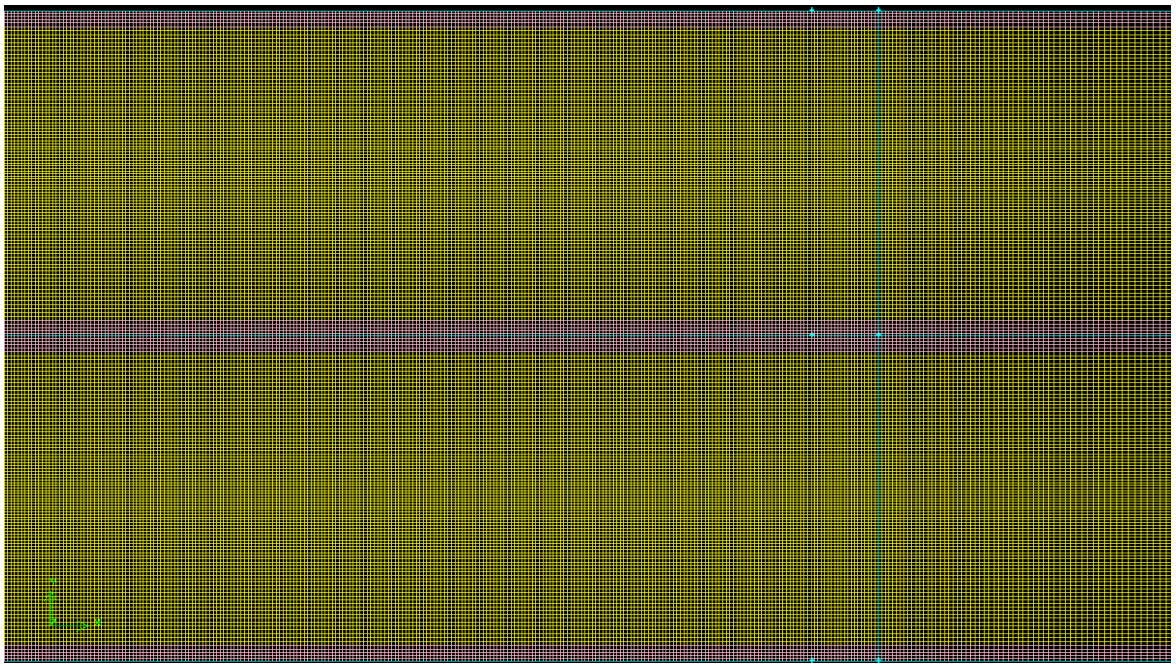

Fig. 5.8b Closer view of the mesh near the outlet

A multi-block structured hexahedral approach is used for meshing the 2D combustor geometry. Figure 5.4 shows the 2D combustor geometry divided into 8 blocks for structured meshing. Blocks A and B make up the incoming zone of the premixed propane/air mixture flow. Blocks C and D consist of flow expansion and recirculation vortex zones behind the 2D flame-stabilizer step and require high mesh resolution. Blocks E and F consist of inlets for cooling air streams, which mixes with hot reacting gases flowing towards the outlet. Blocks G and H consist of the near-outlet flow zone.
Since the reacting flow inside the 2D combustor is turbulent in nature, it is affected by the presence of the walls. Hence, the near-wall region flow determines successful prediction of wall-bounded turbulent reacting flow. As mentioned in section 4.4, standard wall functions in the $k - \varepsilon$ turbulence model are utilized for modelling the viscosity affected near wall region flow. Figure 5.5 shows the distribution of boundary layer meshes at the walls inside the combustor. The boundary layer mesh is extended along the center line of the combustor to maintain the finer resolution (to capture flame-front established near the combustor center line) and cell size growth. Figure 5.6 shows the complete structured mesh utilized for RANS and URANS analysis of the combustor. Figure 5.7a shows a closer view of the mesh near the inlet, whereas; Figures 5.7b and 5.8a shows the mesh near the end of the step and just behind the step respectively. The mesh is finer near and behind the flame stabilizer step compared to the near inlet zone. Figure 5.8b shows a closer view of the mesh near the outlet.

5.5.1 Spatial grid sensitivity

For determining the effect of mesh size on the CFD solution for the configuration shown in Figure 5.3, five multi-block structured meshes of increasing cell counts were

constructed using GAMBIT™ version 2.3. A Y+ value of ~30 is maintained for meshes 1 and 2, but for meshes 3, 4 and 5 the Y+ value is less than five as a result of a finer resolution expected to be needed to capture complex combustion processes. Table 5.2 lists the cell counts of all meshes along with the computation time and iterations required to evaluate a converged reactive steady RANS solution using eight processes in parallel on a cluster using Intel quad core processors with 2.8GHz clock rate.

Table 5.2. Mesh size and steady RANS analysis details

Mesh	~ Cell count	~ Run-time (mins)	~ No. of iterations for convergence
1	11000	12	4000
2	46000	40	6500
3	190000	120	13000
4	420000	880	28000
5	800000	1900	40000

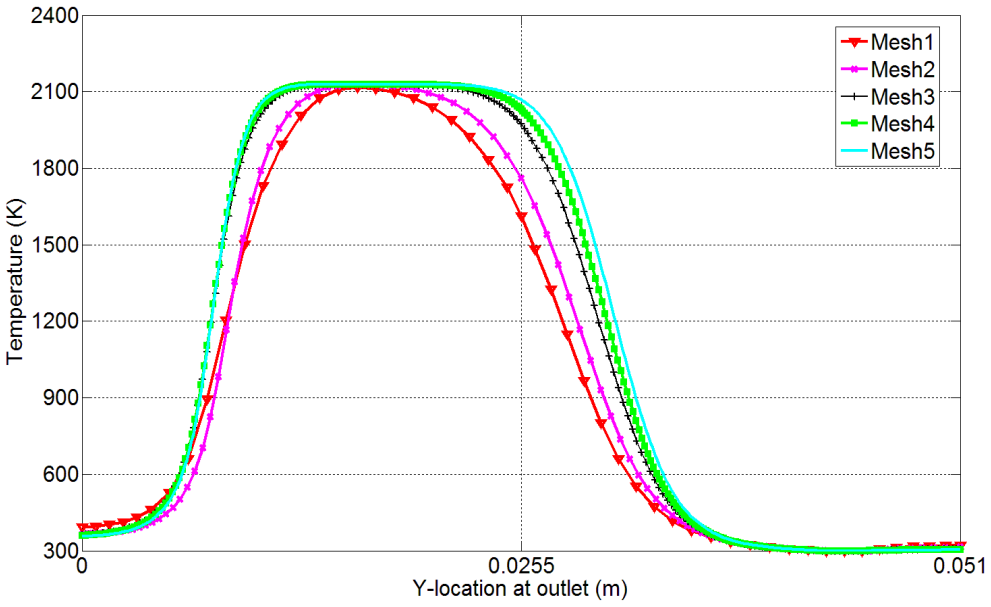

Fig. 5.9 Outlet temperature profiles as captured by different mesh sizes using steady RANS

Figure 5.9 shows the comparison between the predictions obtained from the five different meshes (c.f. Table 5.2) in terms of temperature profiles at the outlet plane of the combustor. As seen in Figure 5.9 the agreement between meshes is good near the walls. Away from the walls, grid independence is approached by mesh 3, though it is not 100 % conclusive near the centerline of the combustor. Due to the significant increase

in the computational expense produced by refining the mesh further (c.f. Table 5.2) and from an engineering point of view of design optimisation, mesh 3 is deemed suitable for further CFD analysis and design optimisation.

5.5.2 Temporal grid sensitivity

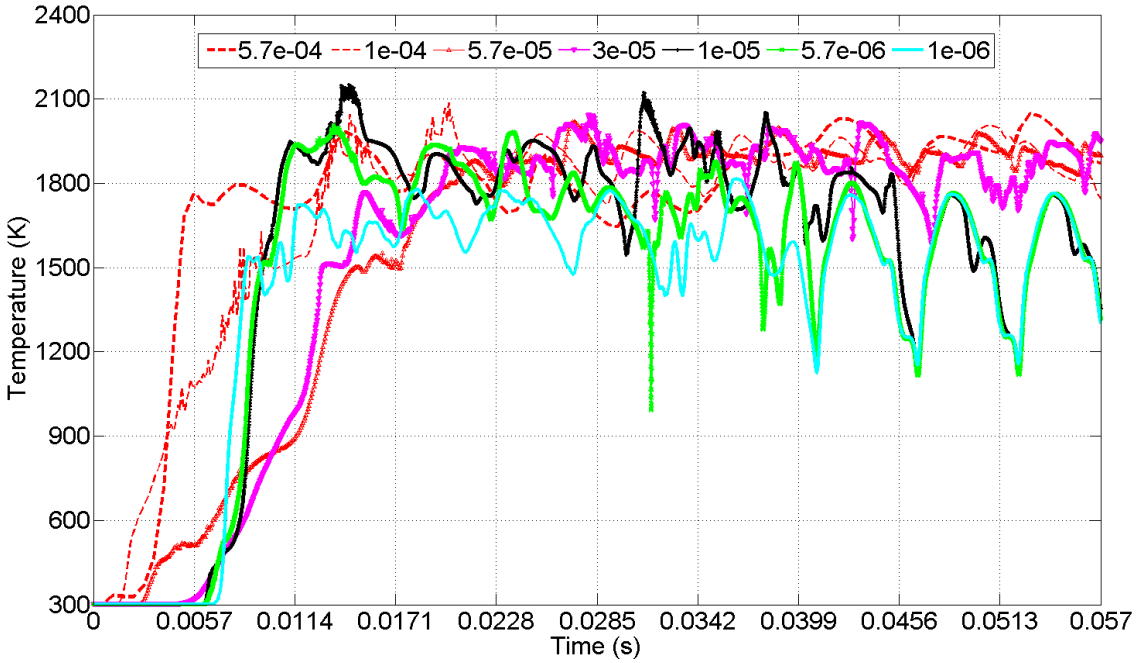

Fig. 5.10 Area-weighted average temperature (T_a) fluctuations at the outlet as captured by different time-step size URANS simulations

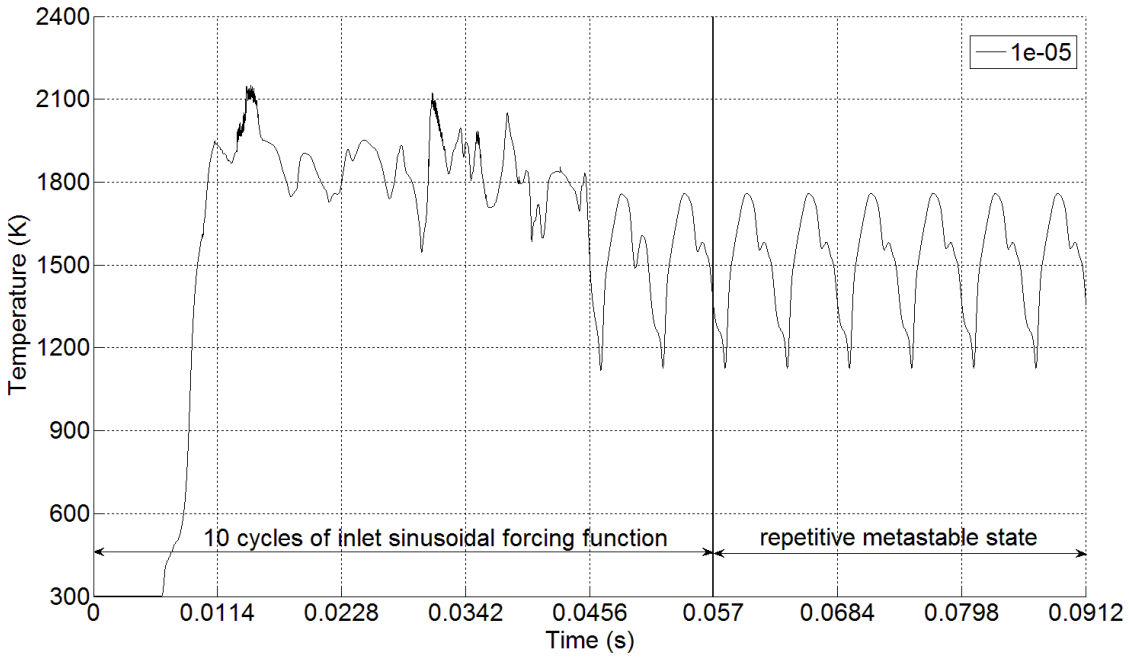

Fig. 5.11 Reactive flow-field settlement into meta-stable state as captured by time-step size 1e-05 URANS simulation

After investigating the effect of different mesh sizes on the outlet temperature profile using steady RANS, the combustor with cooling holes (c.f. Figure 5.3) is investigated using URANS on mesh 3, with the sinusoidal velocity variation at the inlet. The URANS simulation is run using different time-step sizes for 10 cycles of the sinusoidal forcing function in order to understand the effect of simulation time-step sizes on the average outlet temperature prediction patterns.

Figure 5.10 shows the variation of area-weighted average temperature (T_a), as captured by different time-step size URANS simulations, at the outlet of the combustor. The coarser time-step size simulations are not able to capture the humming instability cycle in the reactive flow-field. The coarsest time-step size at which the URANS simulation successfully captures the humming cycle is 1e-05s.

As shown in Figure 5.11, after the initial transient, the flow-field settles in to a repetitive cycle of temperature fluctuations by the end of the ninth inlet velocity cycle, with a peak temperature of ~ 1800K and minimum of ~ 1200 K. The URANS simulation is further run with finer time-step sizes of 5.7e-06s and 1e-06s, and these results agree closely with the simulation results for 1e-05s in the tenth cycle. Thus, the average outlet temperature variation predicted by URANS is deemed to become sufficiently insensitive of the simulation time-step size at 1e-05s. Hence, a simulation time-step size of 1e-05s is used for further URANS analysis.

5.6 Combustor flow dynamics in spatial and temporal domains

The aim of this analysis is to develop an understanding of flame/vortex dynamics behind the flame-stabilizer step of the 2D lean burn combustor (c.f. Figure 5.3) in both spatial and temporal domains. Initially, both isothermal and reactive steady RANS analysis is presented highlighting the effect of combustion processes on the flow field behind the flame-stabilizer step. Later, reactive URANS analysis is presented focusing on time-dependent behaviour of flame and vortex interaction.

5.6.1 Steady-state isothermal flow-field

Figures 5.12 and 5.13 show the x-velocity flow-field and stream function variation inside the 2D lean burn combustor respectively, obtained after running non-reactive steady RANS simulations to convergence† over 10000 iterations (~40 minutes of wall clock time). As seen in Figure 5.12, as the flow passes over the profiled flame-stabilizer step, the velocity of the flow increases. At the end of the step, flow separation takes place. In the upper part of the combustor the flow largely maintains its momentum, whereas behind the step a recirculating vortex is formed. The flow reattaches along the bottom wall at a certain distance downstream of the step.

† See Appendix C

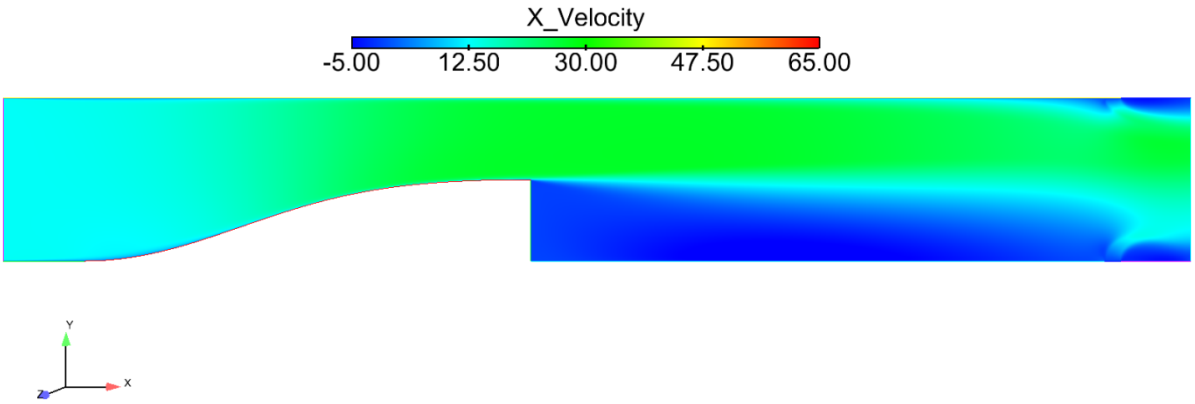

Fig. 5.12 X-velocity flow-field inside the combustor under isothermal conditions

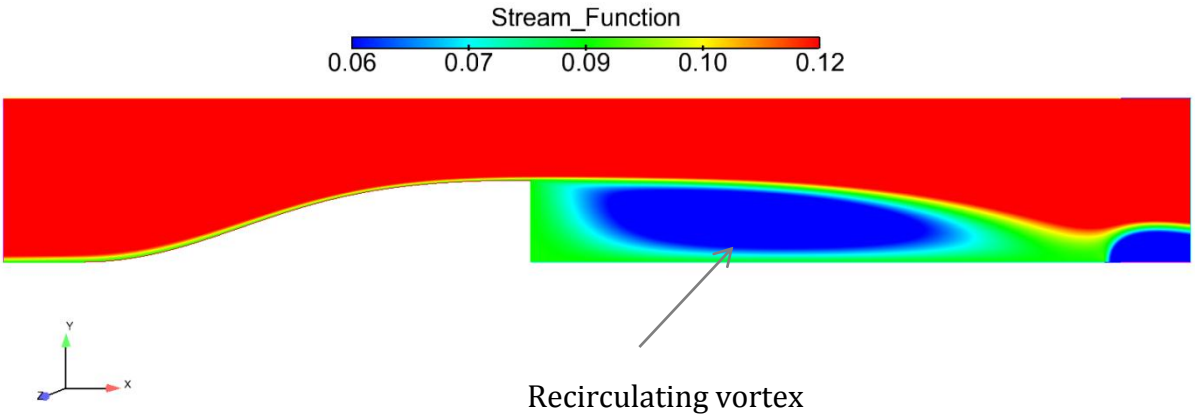

Fig. 5.13 Recirculating vortex behind the step under isothermal conditions

The recirculating vortex behind the step under isothermal conditions is shown in Figure 5.13 using stream function plot.

5.6.2 Steady-state reactive flow-field

Figures 5.14 and 5.15 show the x-velocity flow-field and stream function variation inside the 2D lean burn combustor respectively, obtained after running reactive steady RANS simulations to convergence† over ~13000 iterations (120 mins). Compared to the non-reactive solution, the reactive solution takes longer to converge. Similar to the non-reactive flow, the propane/air mixture accelerates over the profiled flame-stabilizer step and separates at the end. The effect of combustion process on the flow-field is clearly seen in Figure 5.14. Due to the combustion processes, the axial velocity of the flow increases inside the chamber due to thermal expansion.

† See Appendix C

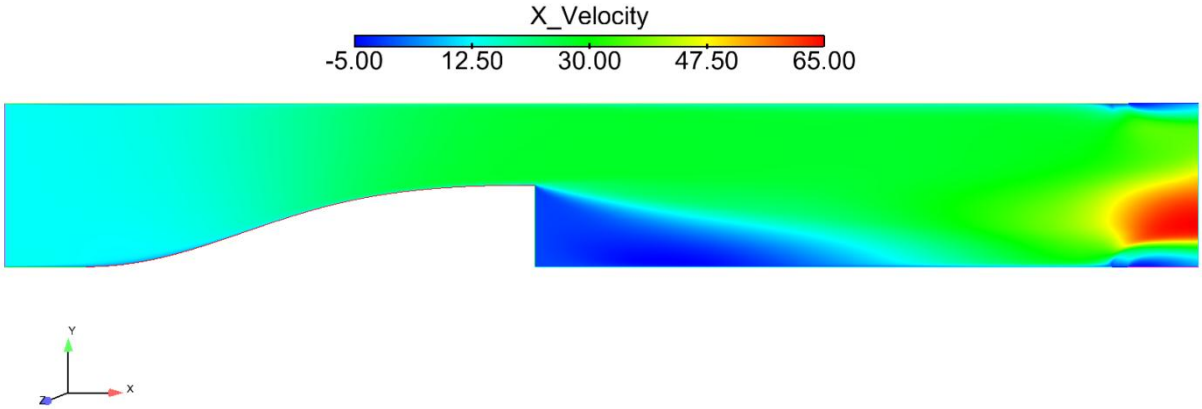

Fig. 5.14 X-velocity flow-field inside the combustor under reactive conditions

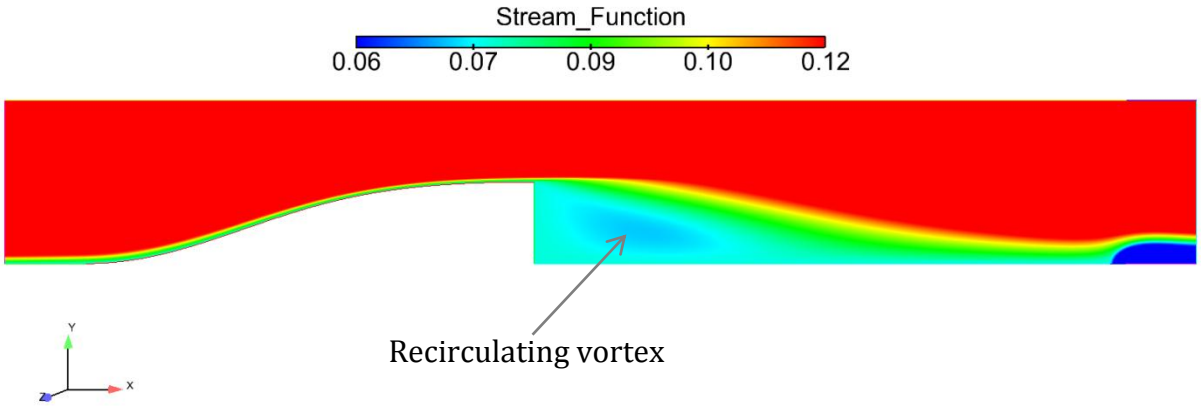

Fig. 5.15 Recirculating vortex behind the step under reactive conditions

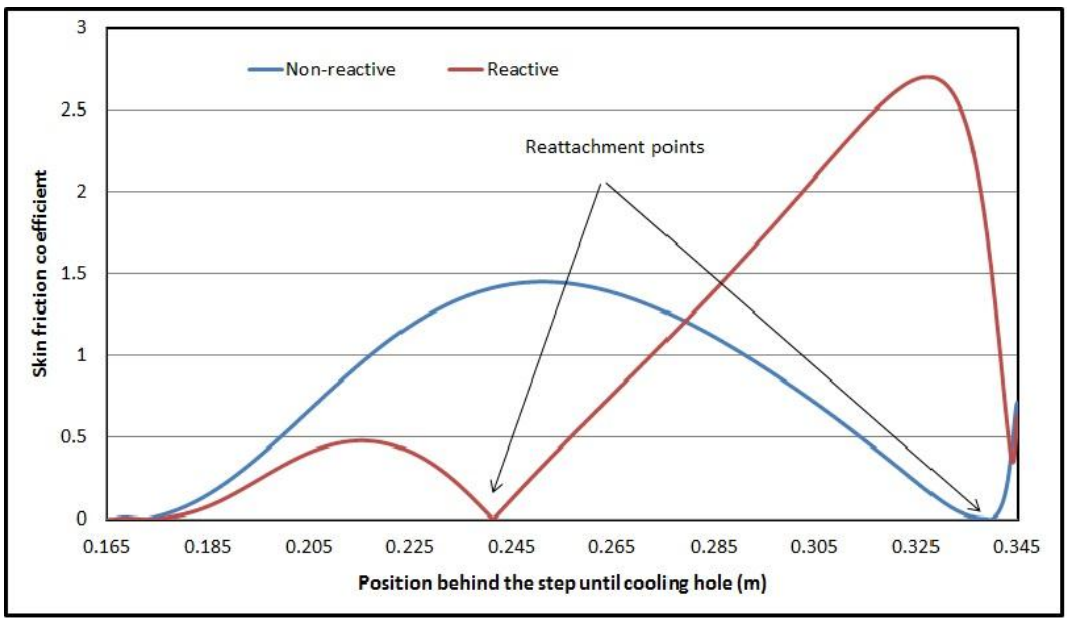

Fig. 5.16 Reattachment length behind step under isothermal and reactive conditions

Just behind the step, the x-velocity is greater in the cold unburnt mixture (c.f. Figure 5.17 for burnt/unburnt mixture in the flow-field), whereas further downstream towards the outlet, the situation is reversed. This observation is in agreement with the observation of Thibaut and Candel (1998).

The primary function of the flame-stabilizer step is to provide a low-velocity region for flame stabilization and allow occurrence of combustion. The recirculating vortex behind the step under reactive conditions is shown in Figure 5.15. The effect of combustion processes on the size of the recirculation vortex is clearly seen in Figure 5.15. The recirculating vortex shrinks in size under reactive conditions compared to the non-reactive condition (c.f. Figure 5.13) under which an expanded vortex exists behind the step. Further due to shrinking of the recirculating vortex behind the step under reactive conditions, the flow reattaches at a smaller distance from the step as compared to the non-reactive condition. Figure 5.16 shows the positions of flow reattachment behind the step under non-reactive and reactive conditions.

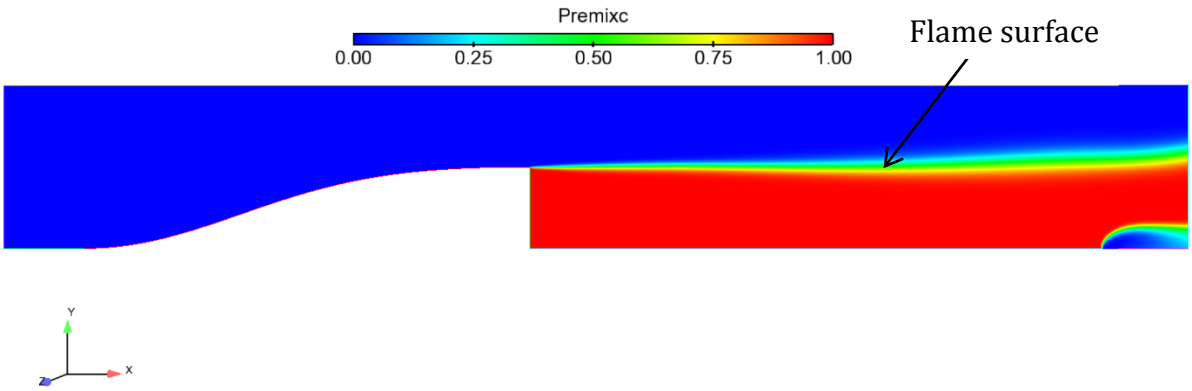

Fig. 5.17 Burnt and unburnt mixture field inside the combustor under reactive conditions

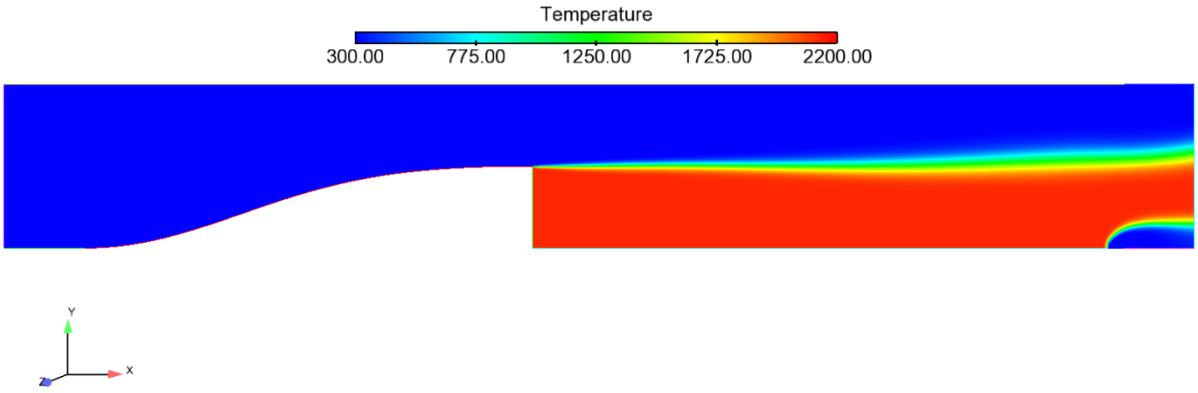

Fig. 5.18 Temperature flow-field inside the combustor under reactive conditions

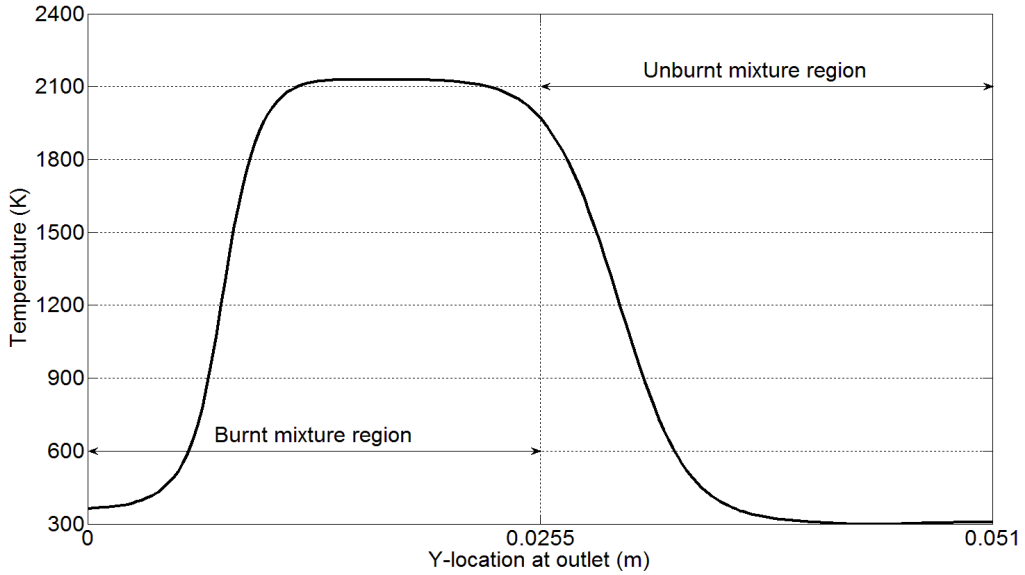

Fig. 5.19 Outlet temperature profile of the combustor (steady RANS)

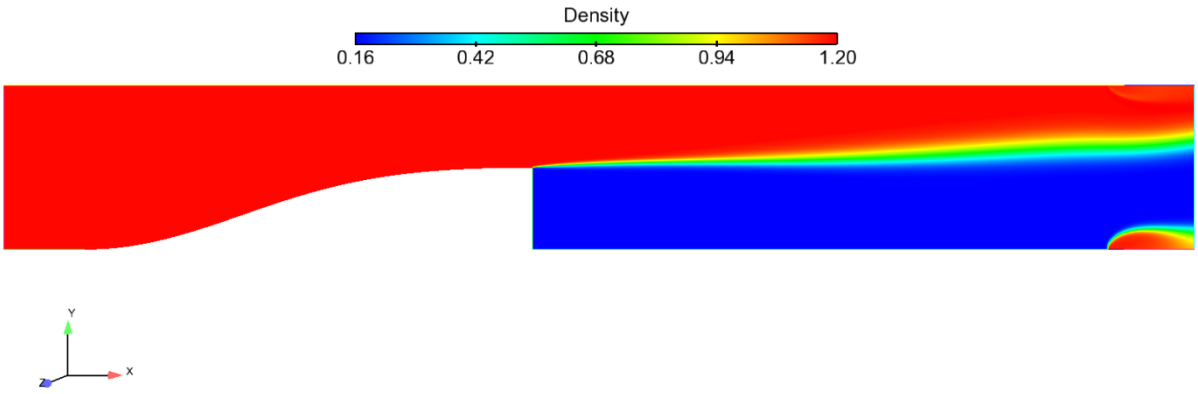

Fig. 5.20 Density field inside the combustor under reactive conditions

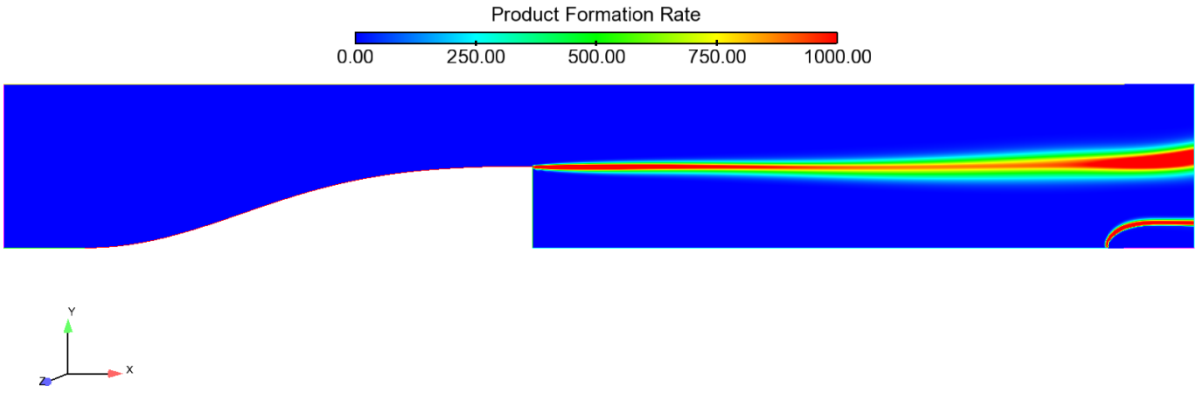

Fig. 5.21 Product formation rate inside the combustor under reactive conditions

The steady turbulent flames require flame stabilization mechanisms (Poinsot and Veynante, 2005). The recirculation zone behind the step (c.f. Figure 5.15) provides the low-speed region necessary for flame stabilization. Figure 5.17 shows the progress variable flow-field and indicates the position of the flame surface (or flame front) inside the chamber. As the Reynolds number of the flow is in the turbulent regime, the mixture burns only in the location where the turbulent flame speed S_T is able to sustain the mixture velocity $\tilde{u}$, i.e. the region behind the step. Therefore the chamber behind the step is separated into unburnt and burnt mixture regions by an interface, where combustion has started but not yet fully established. Above this surface ($\bar{C}$ = 0), the fuel and oxidizer mixture is mixed but unburnt, and below this surface ($\bar{C}$ = 1), the mixture is completely burnt. Thus, due to high mixture velocity in the upper part of the chamber behind the step, much of the mixture escapes unburnt from the combustor.

Figure 5.18 shows the temperature field inside the combustor. The temperature is maximum (~2100 K) in the burnt mixture region, reduces in the interface region and is the lowest in the unburnt mixture region. The temperature of the mixture which escapes unburnt from the combustor remains at the inlet temperature of 300 K. Figure 5.19 shows the outlet temperature profile of the combustor as captured by steady RANS.

As discussed previously in chapter 3, even though the flow is incompressible, density fluctuations exists due to temperature gradients induced by combustion processes, which requires the Favre-averaged Navier Stokes equation to be solved (c.f. section 3.2). Figure 5.20 shows the density field inside the combustor under reactive conditions. Large density variation exists in the combustor due to large temperature gradients. This is particularly very high in the region across the flame-front. Density is lower in the burnt mixture zone.

Figure 5.21 shows the production formation rate inside the combustor. For premixed combustion, the reaction takes place only in the combustion zone (flame front) separating burnt and unburnt mixture (c.f. Figure 5.17). Hence the products are formed primarily in the flame surface zone. Product formation also takes place near the cooling inlet at the bottom wall, due to further reactions between high temperature gases exiting the combustor and the air stream at the cooling inlet.

5.6.3 Time-dependent reactive flow-field

After investigating the steady combustion process behind the step in the combustion chamber, a sinusoidal variation is imposed the inlet velocity condition, which represents the effect of an acoustic resonance produced in the experiment by Keller et al. (1982) with the use of loudspeaker radiating in the flow-field (c.f. Figure 5.1 for details). As mentioned in section 4.1, a sinusoidaly varying inlet velocity is used to

generate a humming instability phenomenon, which is ascribed to the interaction between flame-front and the trailing vortex pattern of the turbulent shear layer behind the step.

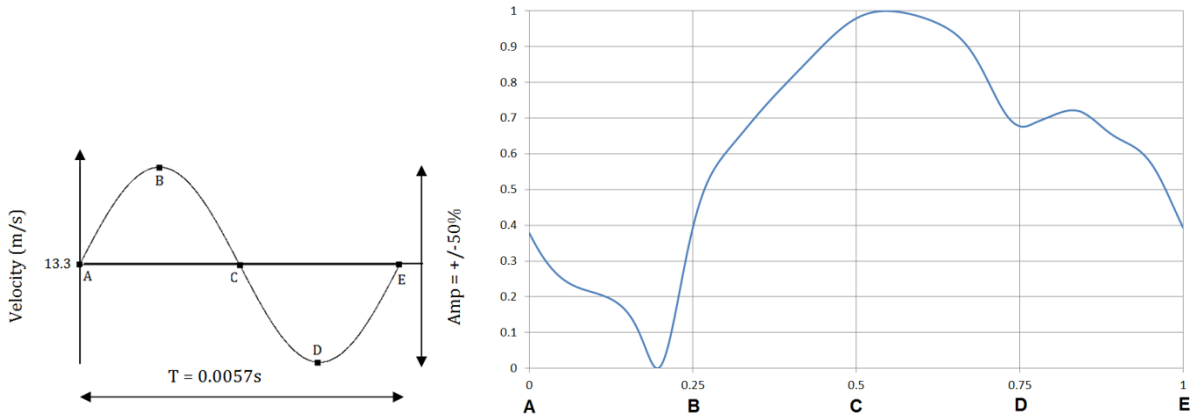

(a) Sinusoidal forcing function

(b) Non-dimensionalized humming cycle temperature variation with time showing corresponding points A-E

Fig. 5.22 A sinusoidal forcing function (a) imposed at the inlet of the combustor and its corresponding outlet temperature variation pattern (b)

Figure 5.22(a) shows the sinusoidal forcing function imposed at the inlet of the 2D combustor and Figure 5.22(b) shows the corresponding location of points A-E on the temperature variation (humming) cycle. The unsteady RANS simulation is started from the converged steady RANS results in order to achieve faster convergence of the solution as compared to unsteady RANS simulation starting from initial conditions†.

Figure 5.23 shows the x-velocity flow-field of the combustor at cycle points A-E corresponding to Figure 5.22. At point A in the cycle, a large low-velocity region exists behind the step with high velocity gases at the outlet. At point B in the cycle, as the inlet velocity reaches its maximum value, the region of low-velocity mixture shrinks with a shorter flow re-attachment length. Also, a larger bubble of high-velocity gases now escapes at the outlet compared to cycle point A. At cycle point C, the low-velocity region behind the step increases in size. At cycle point D, the velocity reaches its minimum value, which creates the biggest low-velocity region in the cycle. Also, the exit velocity of the gases is the lowest. At cycle point E, the inlet velocity rises to its original value, and the state of x-velocity flow field is similar to cycle point A. This cycle continues into a metastable state.

Figure 5.24 shows the axial velocity variation along the length of the combustor (plotted along the combustor centerline) under reactive conditions at different points of the sinusoidal cycle shown in Figure 5.22. It shows an increase in the x-velocity of the burnt mixture (or products) along the length of the combustor. This is the effect of the

† See Appendix C

combustion process which accelerates the products and increases their flow velocity compared to unburnt gases.

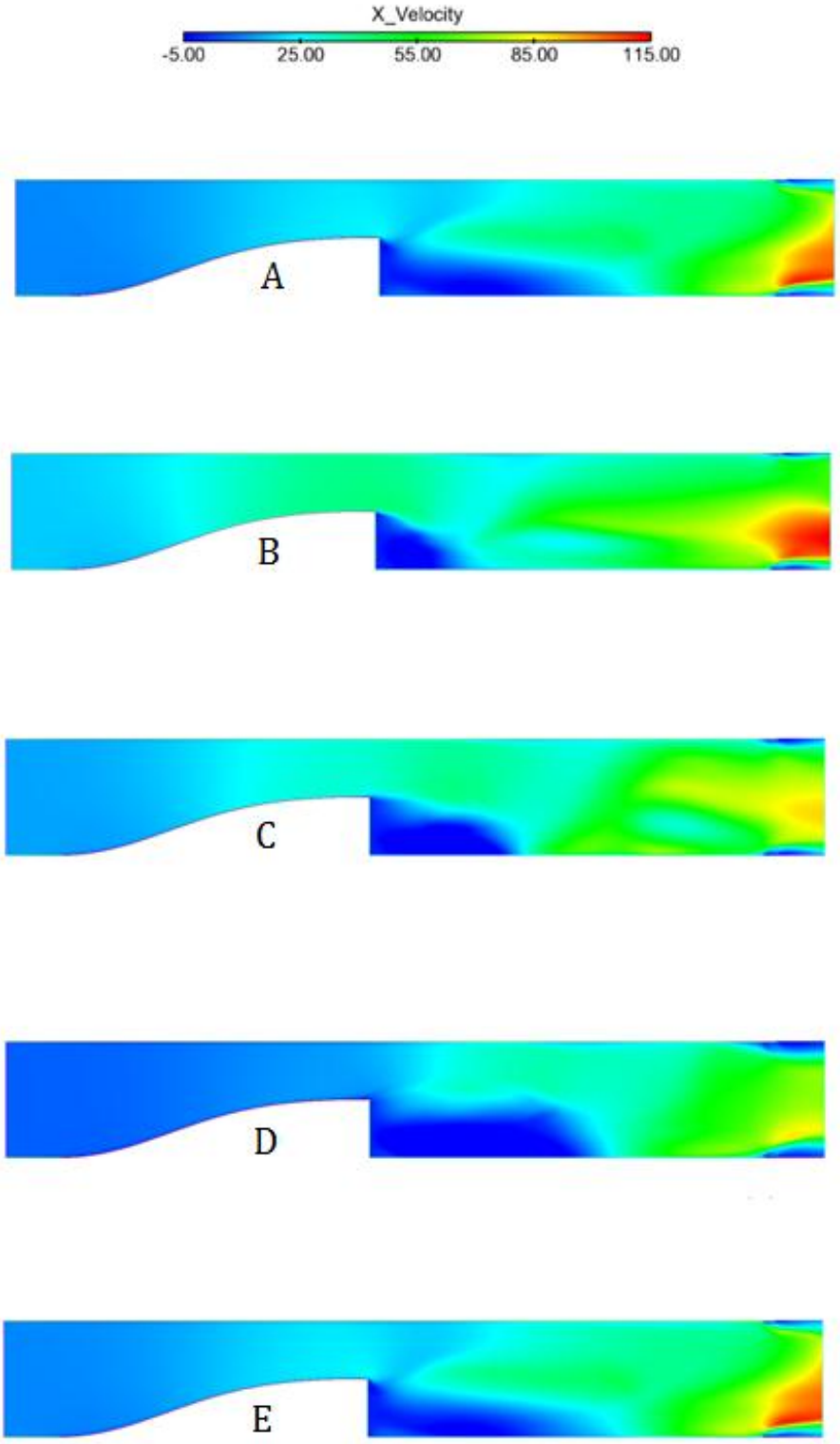

Fig. 5.23 Time-dependent x-velocity flow-field inside the combustor under reactive conditions at points corresponding to Figure 5.22

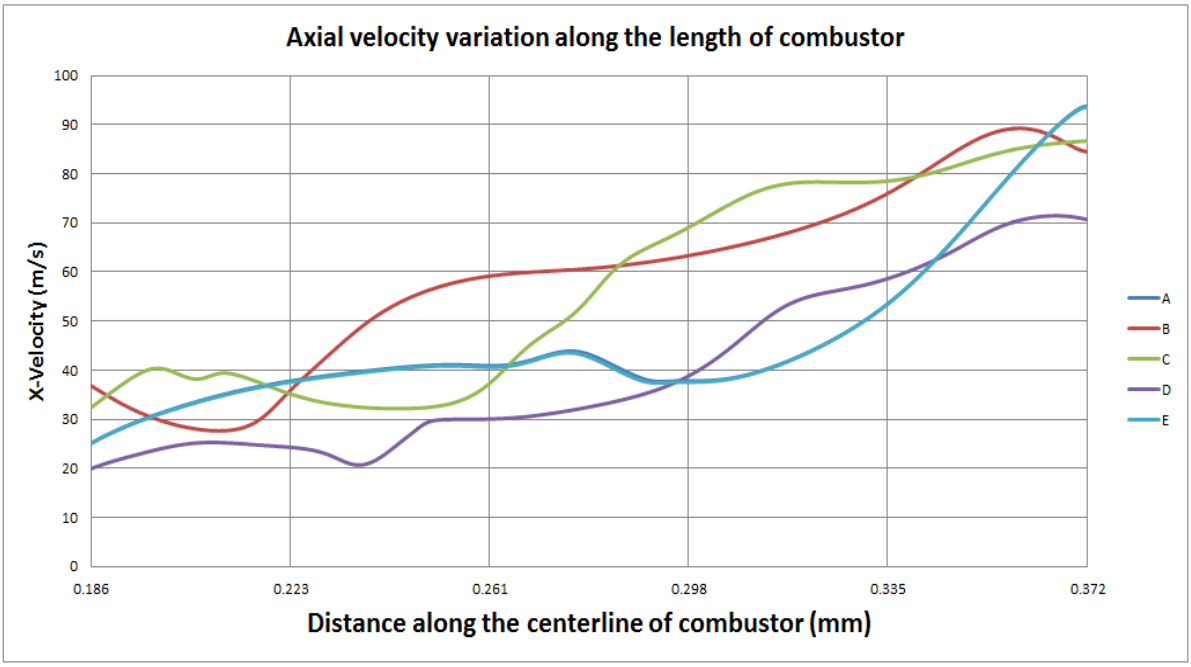

Fig. 5.24 Axial velocity variation along the length of the combustor under reactive conditions

Figure 5.25 shows the reaction progress variable flow field inside the combustor at points A to E in the cycle.. The imposed inlet sinusoidal pulsation creates organized structures behind the step.

At point A in the cycle, the formation of wake vortex V_2 occurs near the edge of the step, which wrinkles the flame. Downstream, the previous wake vortex V_1 as shown in Figure 5.25A is moving near the outlet which convolutes the flame around it. Near the upper cooling hole, trapped burnt mixture is seen due to the earlier interaction between the incoming cooling jet and moving flame front.

As the velocity reaches its maximum at cycle point B, the growing recirculation vortex V_2 of the burned gases causes the previous vortex V_1 (as shown in Figure 5.25A) to be pushed downstream, while vortex V_2 increases in size. As the flame front convolutes now around vortex V_2, the flame front ahead of vortex V_2 reaches the wall of the combustor, burning more of the mixture before reaching the outlet.

At cycle point C, as the velocity decreases from its maximum value, vortex V_2 continues to grow in size as it moves downstream. The flame advances in to the combustor forming two fronts, a leading vertical front that accelerates forward on the top half of the combustor, and a horizontal front that extends back to the step. Vortex V_2 pushes the unburnt mixture trapped between the convoluted fold of the flame surrounding it and the leading curved flame front moving ahead of it vertically as shown in Figure 5.25C.

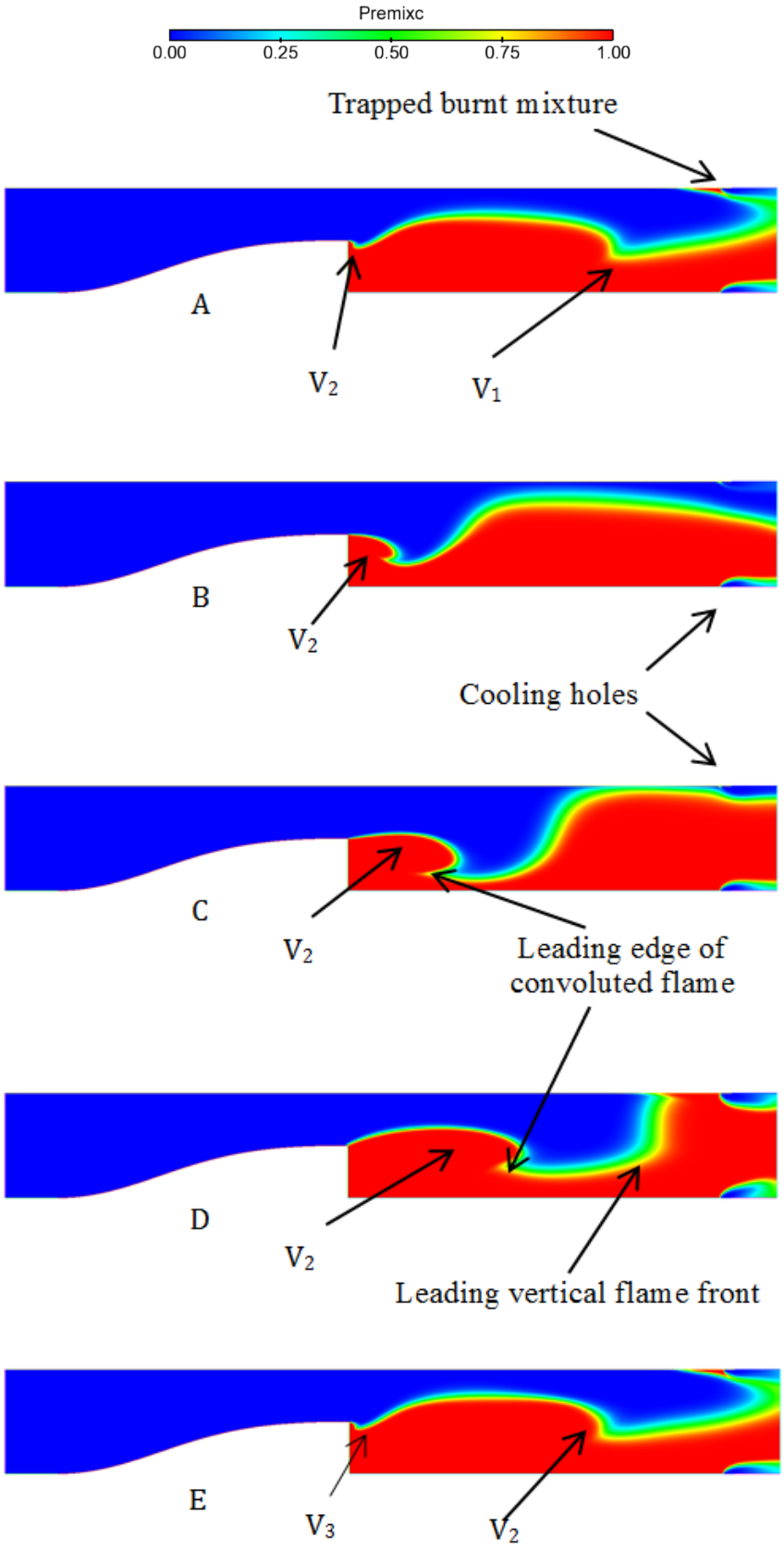

Fig. 5.25 Pulsed flame inside the chamber (V_{in} = 13.3 m/s, T_{in} = 300 K, ϕ = 0.86, excitation amplitude = 50%, frequency = 175 Hz). Corresponding phases are indicated on sinusoidal velocity variation graph

At point D, *t*he velocity reaches its minimum value, due to which the flame front is lifted behind the step as vortex V_2 grows and stretches further downstream with its leading edge folded more as compared to cycle point C. Due to the reduced velocity of the mixture; the flame propagates upwards near the wall of the combustor. The leading vertical flame front is pushed further downstream as it reaches the upper wall, burning all the mixture leaving the combustor. At cycle point E, the velocity rises again to its original value. A new vortex V_3 is again formed at the step edge with the previous vortex V_2 convecting further downstream. Again, near the upper cooling hole, trapped burnt mixture is observed due to the interaction between the incoming cooling jet and moving flame front. This marks the end of the humming cycle which is then sustained in a meta-stable mode. The average outlet temperature variation (c.f. Figure 5.11) is synchronized with this humming cycle.

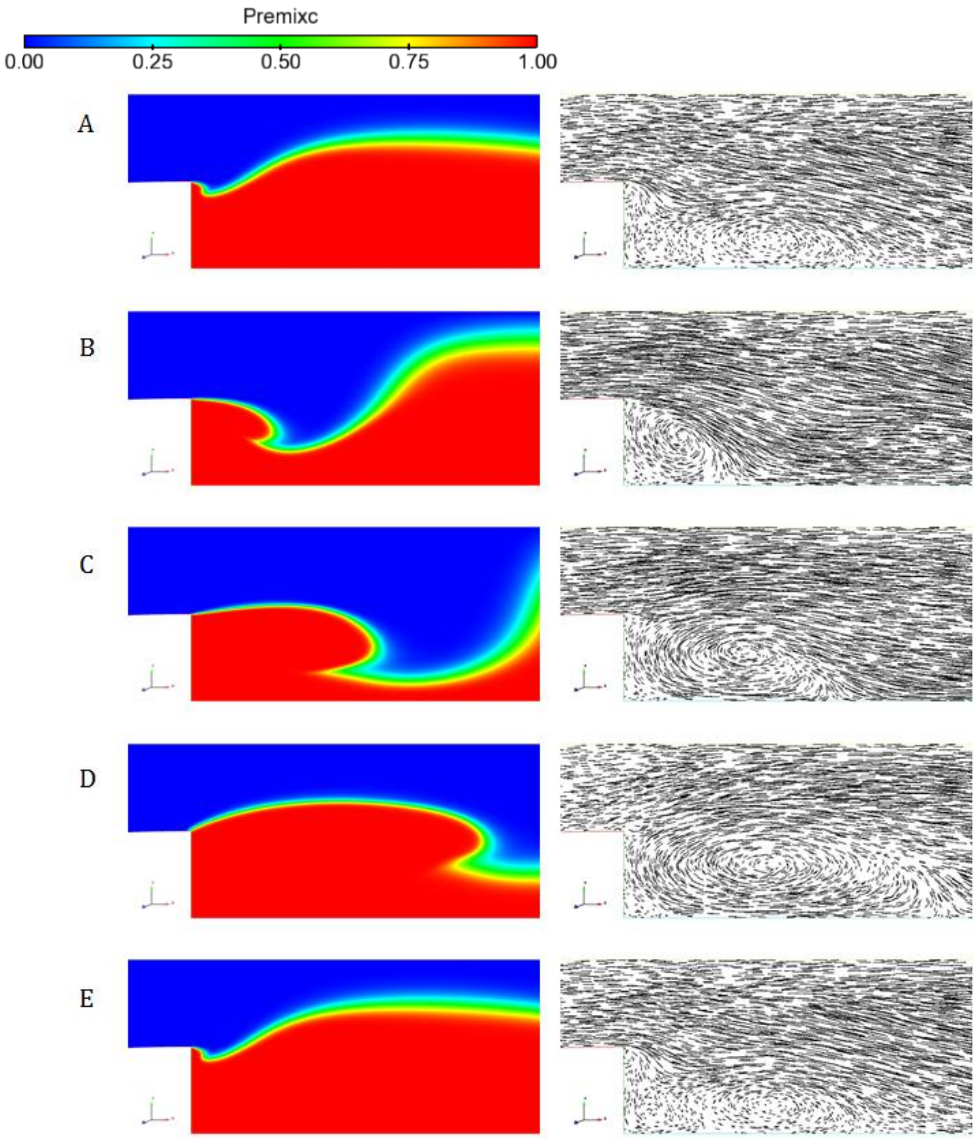

Fig. 5.26 Near-step vortex shedding and flame convolution during the humming cycle

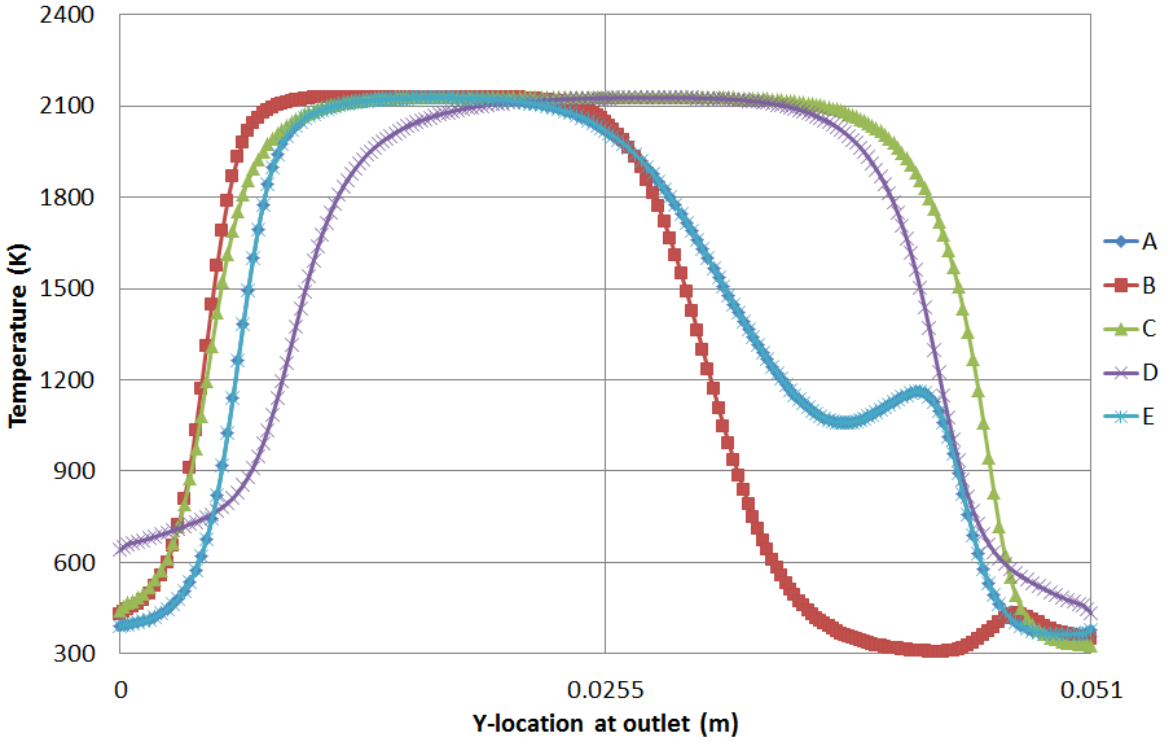

Fig. 5.27 Outlet temperature profile variation during the humming cycle

Figure 5.26 shows the process of flame convolution around the vortex which sheds behind the flame stabilizer step over the humming cycle. The five images shown correspond to the different time instances A-E as shown in Figure 5.22. The recirculating and downstream moving vortex behind the step controls the behaviour and movement of the flame-front throughout the humming cycle.

Figure 5.27 shows the outlet temperature profile variation at points A-E in Figure 5.22. At point A (start of the humming cycle), most of the mixture escaping from the lower half of the combustor is completely burnt and is at high temperature ~2100 K, whereas, in the upper part, the mixture is mostly partially burned, and at a lower temperature. At cycle point B, due to high velocity, most of the mixture escapes unburnt from the upper part of the combustor which explains the sudden drop in the temperature profile in the upper part. At point C, due to the vertically lifted flame front, the incoming mixture is completely burnt before reaching the outlet, hence resulting in a relatively uniform temperature profile at the outlet across the centerline. At cycle point D, the vertical flame front moves forward but due to a lower inlet velocity, the cooling jet bubble flows further away from the combustor wall reducing the amount of burnt mixture leaving the outlet, thus reducing the outlet temperature near the upper and lower walls. At cycle point E, the inlet velocity increases, pushing the vertical flame front ahead and suppressing the cooling jet bubble flow. The temperature profile for cycle point E matches with temperature profile at cycle point A.

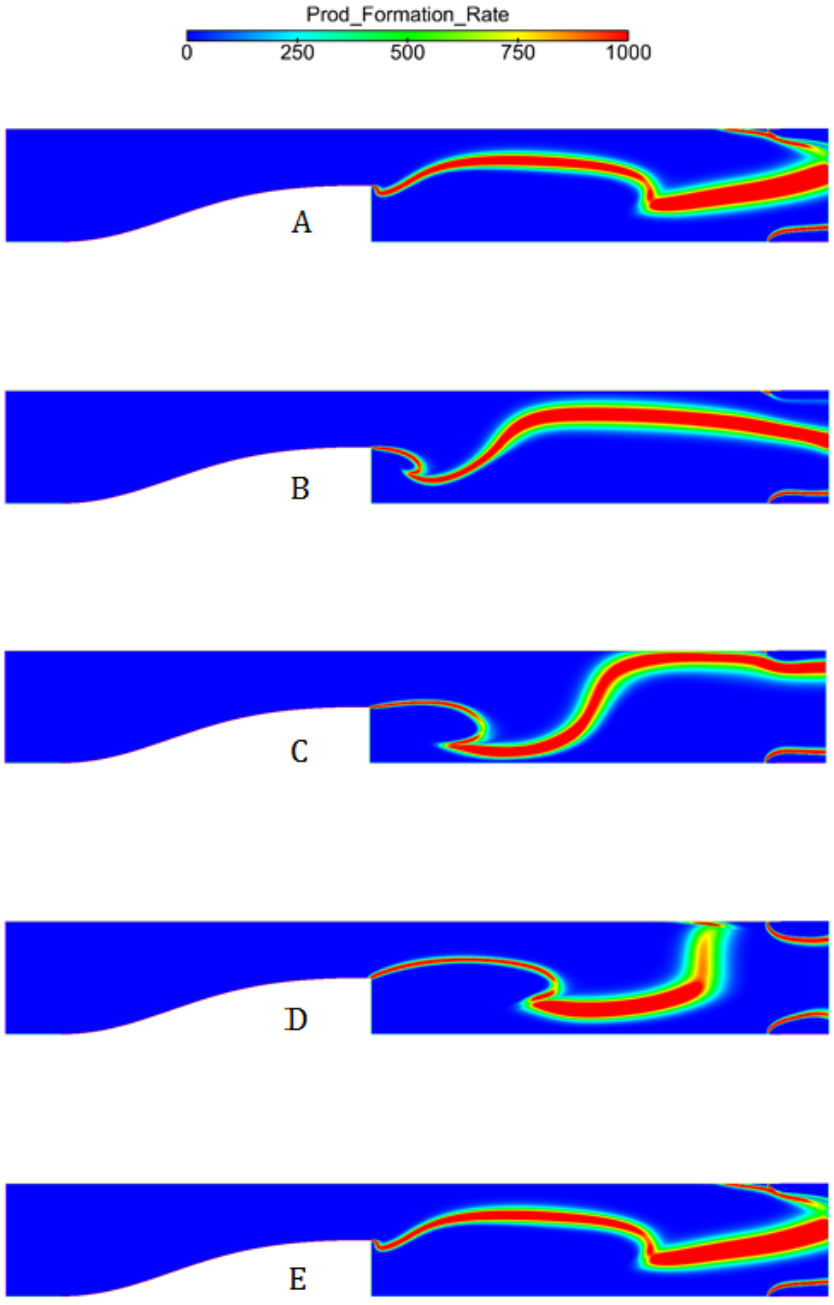

Fig. 5.28 Product formation rate during the humming cycle

Figure 5.28 shows the product formation rate inside the combustor over the humming cycle. As the reaction takes place at the flame surface, converting the reactant into products, the product formation rate is high in the vicinity of the flame-front. The variation in its behaviour is directly linked with the variation of the flame front position over the humming cycle.

5.6.4 Comparison against experimental results of Keller et al. (1982)

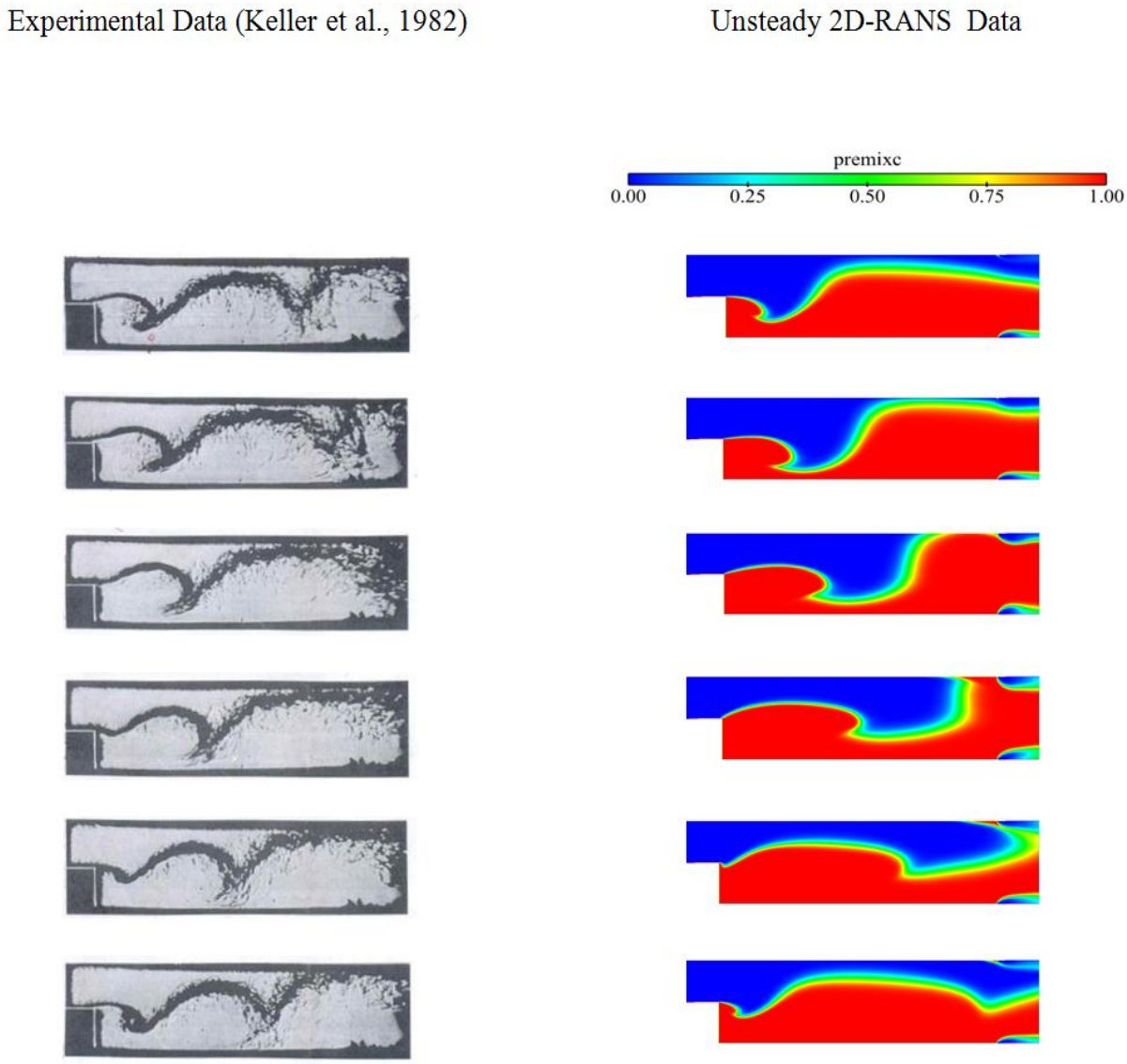

Fig. 5.29 Humming cycle captured by unsteady RANS in comparison with experimental data of Keller et al. (1982) [Time interval between frames: 1ms]

Figure 5.29 shows the comparison of the URANS prediction with the experimental data of Keller et al. (1982) (c.f. Figure 5.1). The results are in good agreement, qualitatively, in the near step region where the wake vortex is formed and periodical flame convolution occurs. Away from the step, the flame structure is less accurately captured as the URANS averages instantaneous flame front fluctuations and shows only the mean value. Also, the mesh size used for the reactive URANS simulation is not fine enough to accurately capture the flame front with all its detail. An appropriate large eddy simulation (LES) on a fine mesh is required in order to capture all details of the flame front propagation and fluctuations, and is not within the scope of the current analysis.

5.6.5 Comparison against experimental results of Altay et al. (2009)

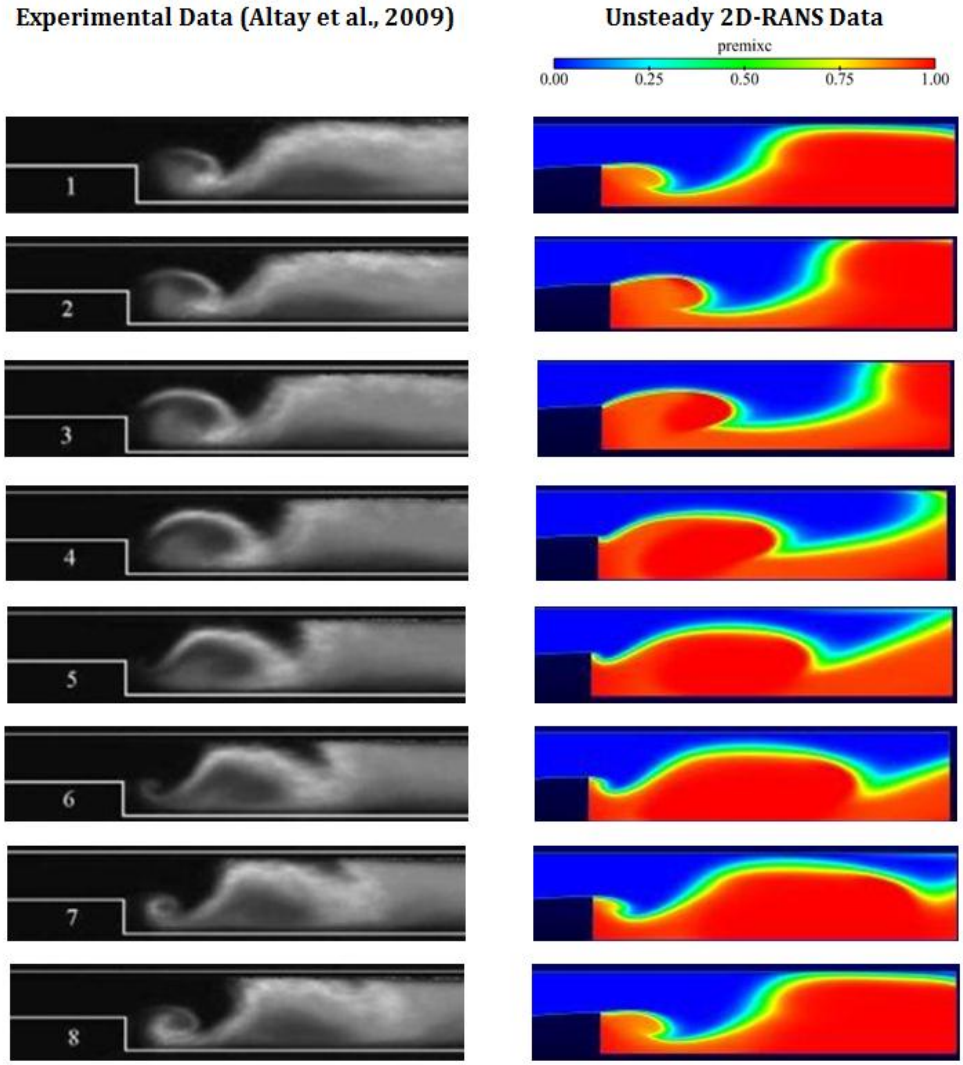

Fig. 5.30 Flame/Recirculation zone interaction captured by unsteady RANS compared with experimental data of Altay et al., 2009 on a different geometrical configuration, (Time interval between frames: 1.1 ms)

Figure 5.30 shows the comparison of flame/recirculation zone interaction results as captured by URANS and the experimental setup of Altay et al. (2009). The flame/vortex interaction process behind the step captured by the URANS simulation is in good qualitative agreement with the experimental data of Altay et al. (2009), who studied combustion dynamics behind the step but on a different geometrical configuration. Nevertheless, the qualitative agreement of URANS results regarding the flame/vortex interaction process is encouraging. This imparts confidence into the reactive URANS model used for capturing the flame/vortex dynamics, at least from an averaged solution point of view, if not in all its details.

5.7 Combustor thermal NOx formation in spatial and temporal domains

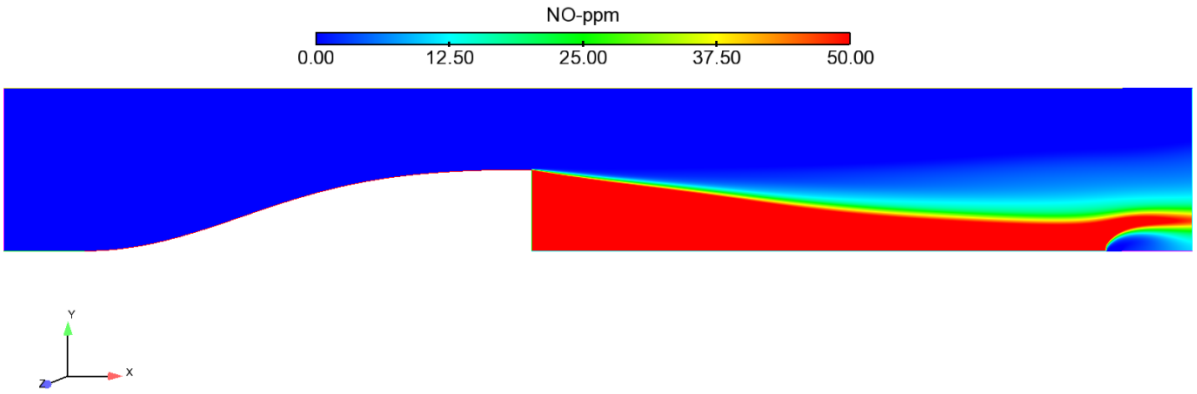

Fig. 5.31 Steady-state NOx flow-field

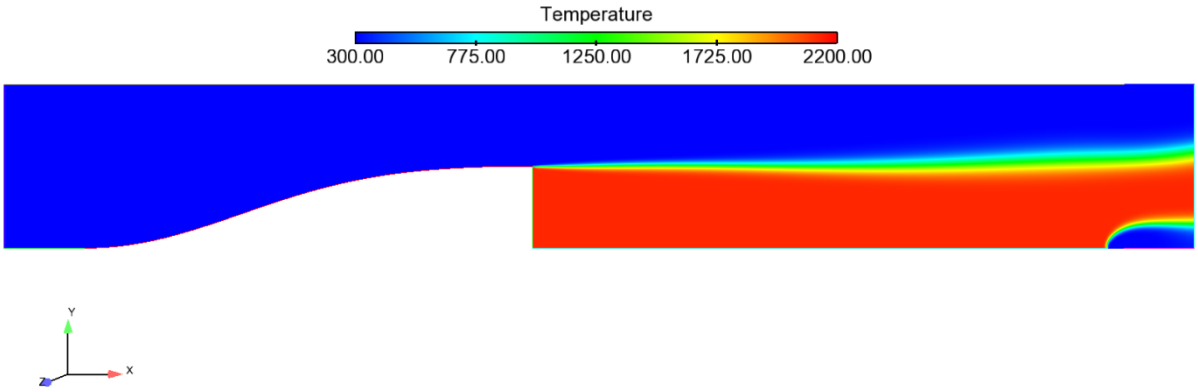

Fig. 5.32 Temperature flow-field inside the combustor under reactive conditions

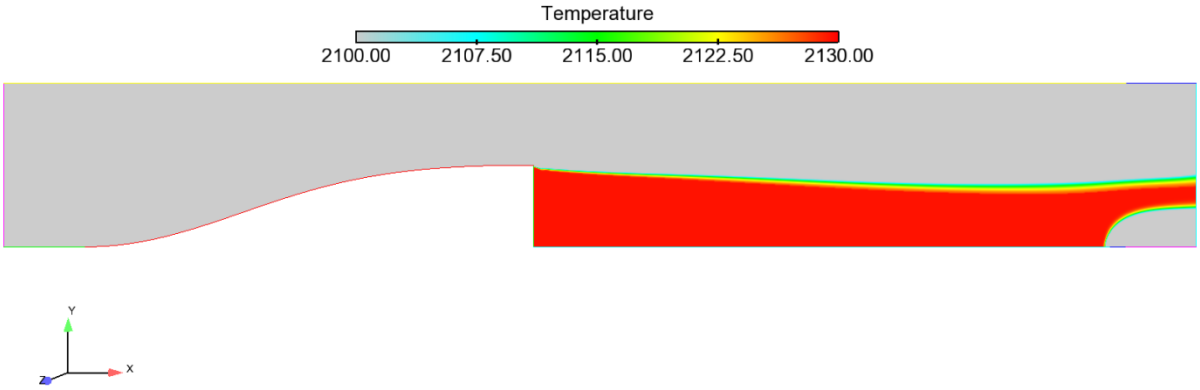

Fig. 5.33 Temperature flow-field inside the combustor above 2100 K

NOx modelling is complex as it requires accurate capturing of chemical kinetics, combustion reaction time and length scales and associated fluid dynamics and turbulent motions. This necessitates a very fine resolution of the computational domain in space and time, making the simulations very expensive. Hence, in this section, modelling of NOx formation in the 2D lean burn combustor is presented only from a qualitative point of view with no experimental validation. The steady and unsteady NOx solution is developed with an aim of constructing a preliminary understanding of the correlation between combustion temperature and thermal NO levels in both spatial and temperature domains. NOx as well as temperature is used as an objective function in later combustor design studies.

5.7.1 Steady-state thermal NOx

The NOx analysis in the spatial domain is performed by post-processing the previous reactive flow solution. With combustion and fluid dynamics model turned off, only the NOx model is run until thermal NO residual convergence†. Total computation wall clock time for converged thermal NO solution is ~90 minutes.

Figure 5.31 shows the NOx flow-field as captured by the steady RANS simulation. It shows significant thermal NO production behind the flame stabilizer step due to the occurrence of reaction processes at very high temperatures (c.f. Figure 5.32).This is in agreement with the Zeldovich mechanism of thermal NO formation (Malte, 1974, Hill and Smoot, 2000). Figure 5.33 shows the part of the reactive flow-field where the temperature is the highest (>2100K) which correlates to the high thermal NO concentration zone in Figure 5.31.

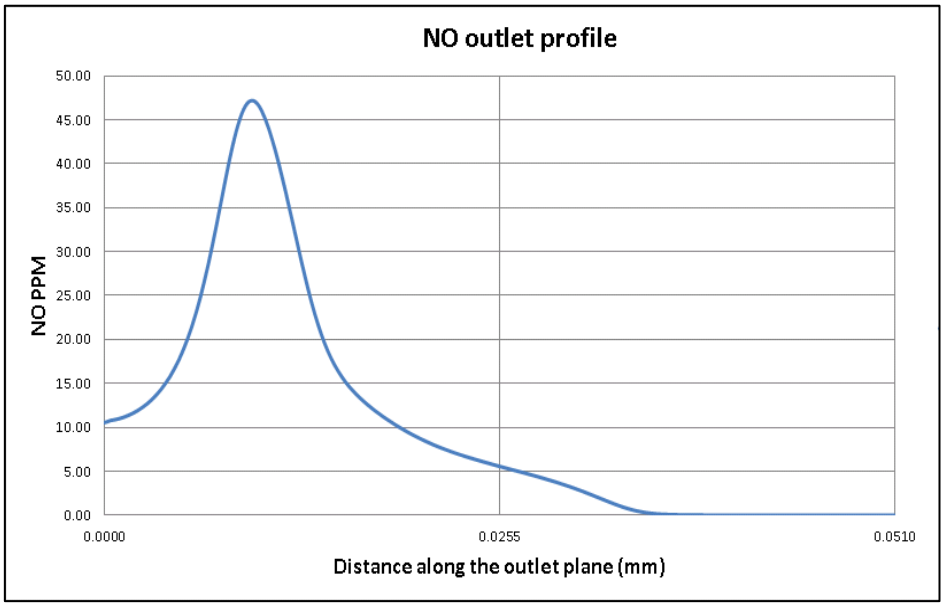

Fig. 5.34 Outlet thermal NO profile in parts per million (ppm)

† See Appendix C

Figure 5.34 shows the thermal NO outlet profile. High levels of thermal NO escapes from the combustor outlet near the lower wall. The outlet thermal NO level reduces towards the upper wall, with almost no thermal NO detection in the upper half of the combustor due to the flow being largely non-reactive.

5.7.2 Time-dependent thermal NOx

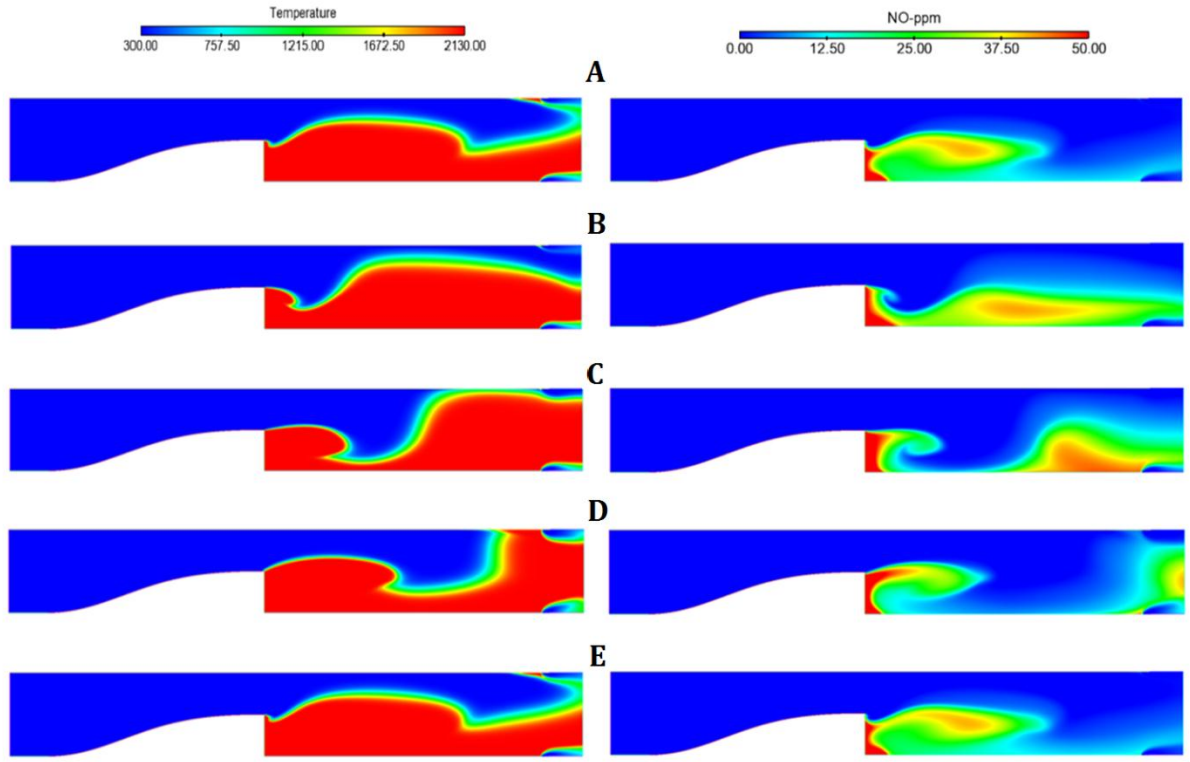

Fig. 5.35 Thermal NO production and transport during the humming cycle corresponding to high temperature regions inside the combustor

For NOx analysis in the temporal domain, the NOx formation is computed simultaneously with combustion reaction at every time step of URANS, as the flame-vortex dynamics affects thermal NO formation and its transport.

Figure 5.35 shows the time-dependent NOx flow-field in correlation with high temperature zones of the combustor as captured by URANS. As discussed in section 5.6.3, the inlet sinusoidal pulsation creates organized vortex structures behind the step which drives the flame/vortex instability. Thermal NO formation, which is directly linked with high temperature zones, also varies according to the flame/vortex motion downstream of the step. Referring to different instances of the humming cycle (c.f. Figures 5.22 and 5.35), at cycle point A, the existence of high temperature wake vortex behind the step leads to high thermal NO concentration. The extent of high thermal NO concentration is until the leading edge of downstream flame as shown in Figure 5.35. At

cycle point B, a new high temperature vortex grows in size behind the step entraining thermal NO. Downstream the step, a diffusion of thermal NO concentration is seen, with high amount of thermal NO escaping at the outlet of the combustor.

At cycle point C, thermal NO concentration is high in two areas of the combustor. One is in the growing vortex behind the step and other behind the curved vertical flame moving towards the outlet. At cycle point D, due to low inlet velocity and lifting of the flame behind the step, the thermal NO concentration follows the flame dynamics with further diffusion in the stretched vortex. The highest amount of thermal NO escapes at the outlet during this instance of the humming cycle, as the curved vertical flame is pushed near the exit reaching the upper wall of the combustor (c.f. Figure 5.35). At cycle point E, the inlet velocity rises again to its original value marking the end of the humming cycle. The thermal NO concentration in the combustor matches to cycle point A. This process is sustained in a meta-stable state.

Overall the thermal NO concentration is observed to be higher in high temperature regions and is entrained by the vortices shedding behind the step during the humming cycle.

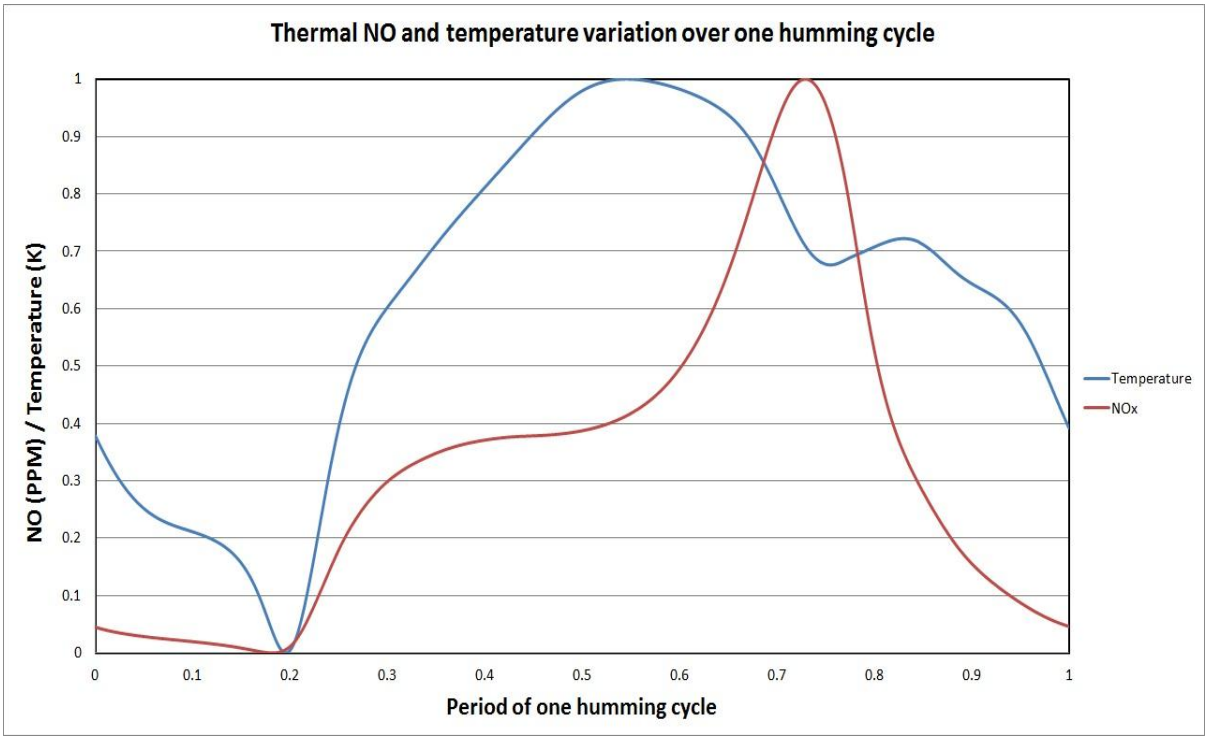

Fig. 5.36 Area-weighted average thermal NO variation at the outlet of the combustor in correlation with area-weighted average temperature over one humming cycle

Figure 5.36 shows the variation of area-weighted average thermal NO in direct correlation to area-weighted average temperature. Both variables are non-dimensionalized with respect to the peak values of outlet thermal NO and temperature

respectively. As seen in Figure 5.36, the peak of thermal NO levels at the outlet arrives later in time compared to the peak of average temperature. This is because the time-scales of NOx formation are considerably longer than the time-scales of the main combustion reactions (Barths et al, 1998). Hence, the NO pollutant formation moves more slowly towards the outlet in comparison to high temperature combustion reaction products which adjust rapidly downstream during the humming cycle. This is consistent with the observations of Barths et al. (1998).

5.8 Summary

This chapter presented an analysis of 2D isothermal and lean burn reactive flow-fields, along with thermal NO pollutant formation. Both steady and unsteady RANS based computational reactive fluid dynamics of the combustor were discussed. Based on this analysis, in the next chapters, various design strategies are developed for flame-stabilizer step design to influence the flame/vortex dynamics downstream. The objective functions used for design optimisation are the outlet temperature profile and area-weighted thermal NO in the spatial domain. For design strategies in the temporal domain, the objective function is humming cycle averaged outlet area-weighted thermal NO and temperature.

Chapter 6

Kriging based high-fidelity strategy for combustor design

6.1 Introduction

Based on the description of the Kriging response surface method in Chapter 2 and 2D combustor steady and unsteady CFD analyses in Chapter 5, a Kriging based high-fidelity design optimisation strategy is applied to combustor design in this chapter. Using multiple initial sampling plans a standard Kriging strategy is used to optimize the inlet flame-stabilizer step design (c.f. Figure 5.1).

The optimisation problem is set-up for two geometry variables (defining the shape of the flame stabilizer step) and two single-objectives, outlet temperature and NOx, as they are of current interest to the combustor design community. A reasonably accurate representation of the design space is first evaluated on a 10x10 design matrix for the two variable study.

To test the effectiveness of the standard Kriging strategy, the total number of high-fidelity CFD evaluations used in the optimization is limited to only 10. With this fixed computational budget and a number of different starting sampling plans, the Kriging design strategy is assessed for its performance in terms of its statistical mean and variance and confidence interval level.

6.2 Kriging based design optimisation strategy

Figure 6.1 shows the traditional Kriging based design optimisation strategy. The three key stages of the strategy includes: (1) Initial sampling using DOE (2) Constructing Kriging response surface and (3) Update points search strategies for increasing Kriging prediction accuracy.

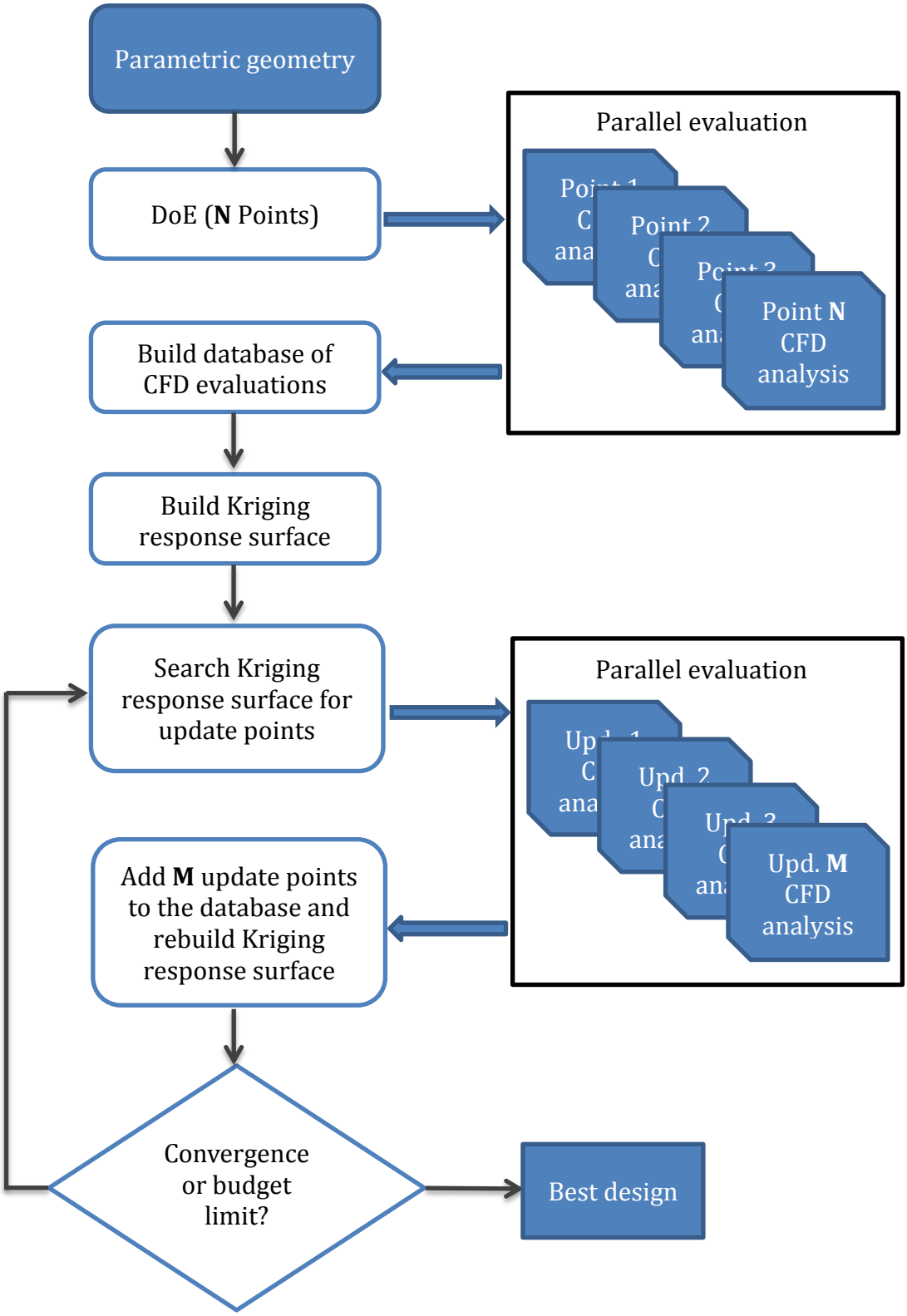

Fig. 6.1 Kriging design optimisation strategy employing a DOE sampling plan and update points methodology

Identifying the effects of variables or parameters within a design space, a space filling design of experiments (DOE) method is used to generate an initial sample of evaluation points. These DOE points are evaluated in parallel using CFD analysis. A database of objective function values at sample points obtained using CFD evaluations is built. Further, a Kriging response surface model is constructed based on the observations at few sample points within the design space. This surface provides a glimpse of the variation of objective function values in the design space. As the response surface model accuracy is limited due to a relatively small initial sample, the accuracy of the model is increased by adding further update points. The update points are found using a genetic algorithm followed by dynamic hill climbing algorithm, which provides a combination of global and local search strategy to find the exact location of the predicted optimum configuration. The resulting update points are again evaluated in parallel using CFD analysis and added to the database to update the Kriging model. This process is continued until the RSM is converged or the given computational budget gets exhausted.

6.3 Problem setup

6.3.1 Parametric geometry model

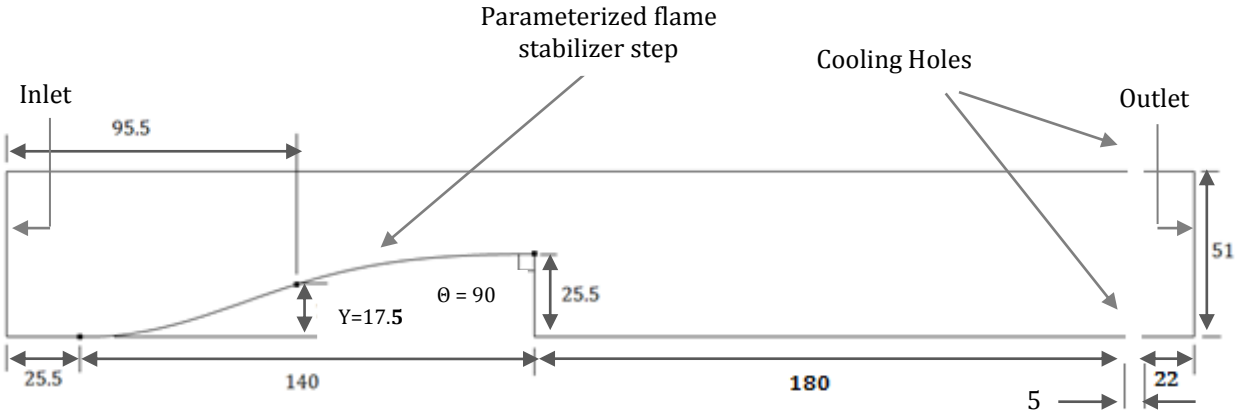

Fig. 6.2 Computational domain of the combustor consisting of a parameterized flame stabilizer step (All dimensions in mm)

The construction of the 2D profiled backward-facing step combustor is carried out using the CAD package CATIA (Computer Aided Three Dimensional Interactive Application) version V5R18. CATIA is a multi-platform CAD/CAM/CAE commercial software suite developed by the French company Dassault Systemes. Figure 6.2 shows the computational domain of the combustor consisting of a parameterized flame stabilizer step. The flame stabilizer step is constructed and parameterized using a cubic spline in CATIA.

Parameterization using cubic spline:

A cubic spline is a spline constructed of piecewise third-order polynomials which passes through a set of control points. Consider a 1-dimensional spline for a set of $n+1$ points (y_0, y_1 … y_n) with n intervals between them. There is a separate cubic polynomial for each interval, each with its own coefficients

$$Y_i(x) = a_i + b_i x + c_i x^2 + d_i x^3 \qquad \text{Eq. (6.1)}$$

Together, these polynomial segments are denoted as $Y(x)$, the spline, as shown in Equation 6.1, where, x is a parameter $x \in [x_i, x_{i+1}]$ and $i = 0, \ldots n$. a_i, b_i, c_i *and* d_i are the constraints.

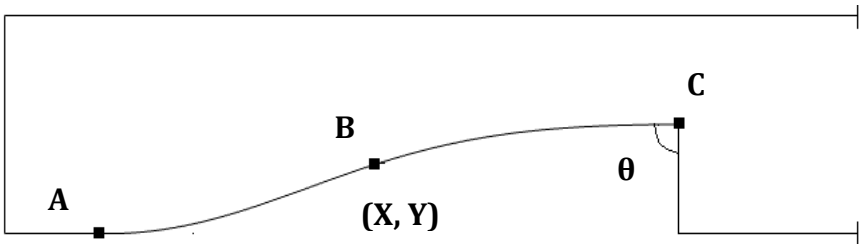

Fig. 6.3 Flame-stabilizer step design parameterization using spline control points

Figure 6.3 shows a closer view of the flame stabilizer step (A-B-C) baseline geometry. Points A, B and Care connected by a spline curve of which control point A and C are fixed. However, the angle θ at point C is free. At control point B, the x-coordinate is fixed at a distance of 95.5mm from the inlet and the y-coordinate is variable. Thus, two variables [Y and θ] are used to change the shape of the flame-stabilizer step and thus influence flame/vortex interaction processes downstream. A baseline spline is defined by Y = 17.5mm and θ = 90 degrees.

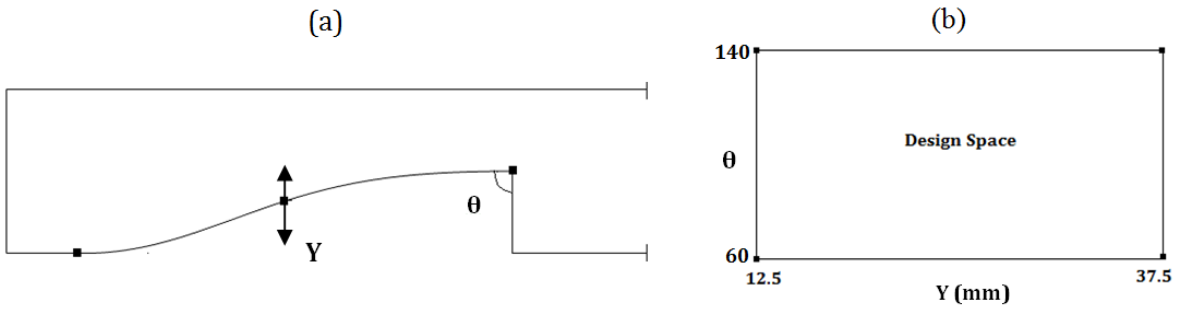

Fig. 6.4 (a) Two design variables under consideration and
(b) design space with lower and upper bounds

Figure 6.4(a) shows the two design variables of the flame stabilizer step that is considered for the optimization process. Figure 6.4(b) shows the two-dimensional design space that is considered for the design study indicating the upper and lower limits of the variable values.

6.3.2 Modified meshing strategy

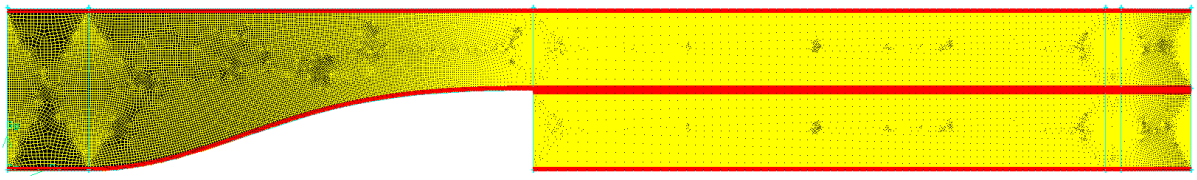

Fig. 6.5 A paved quadrilateral mesh using quad-pave meshing scheme in Gambit

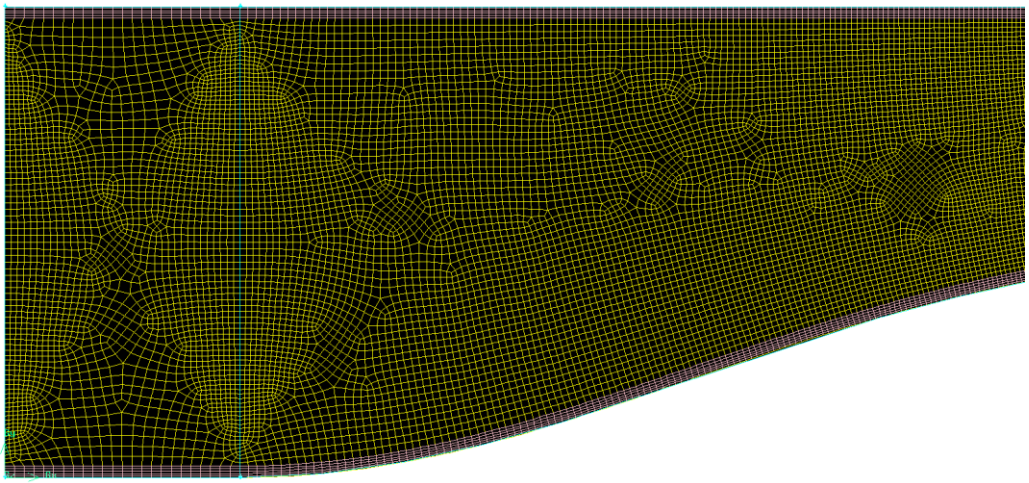

Fig. 6.6a Closer view of the modified mesh near the inlet of the combustor

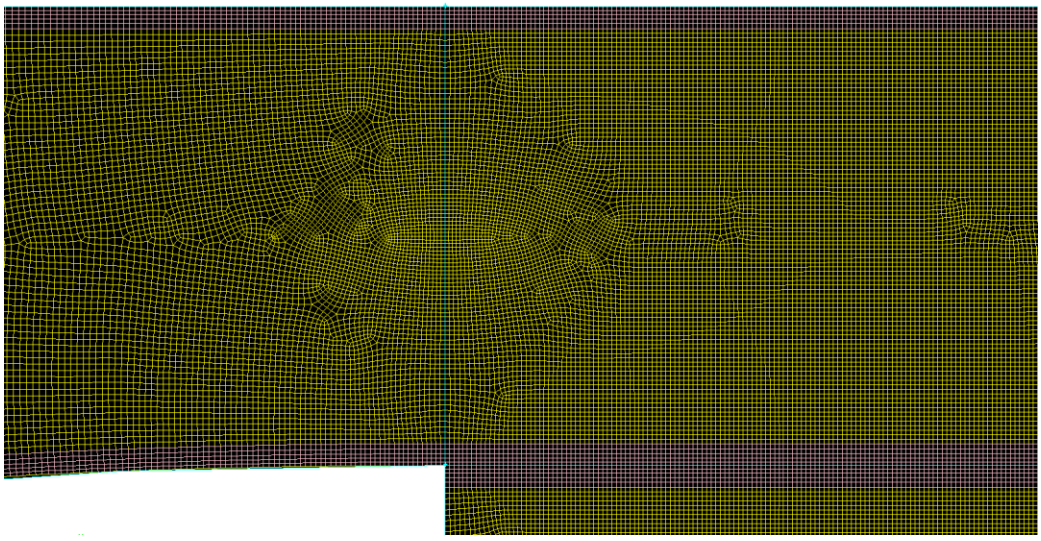

Fig. 6.6b Closer view of the modified mesh near the flame-stabilizer step exit

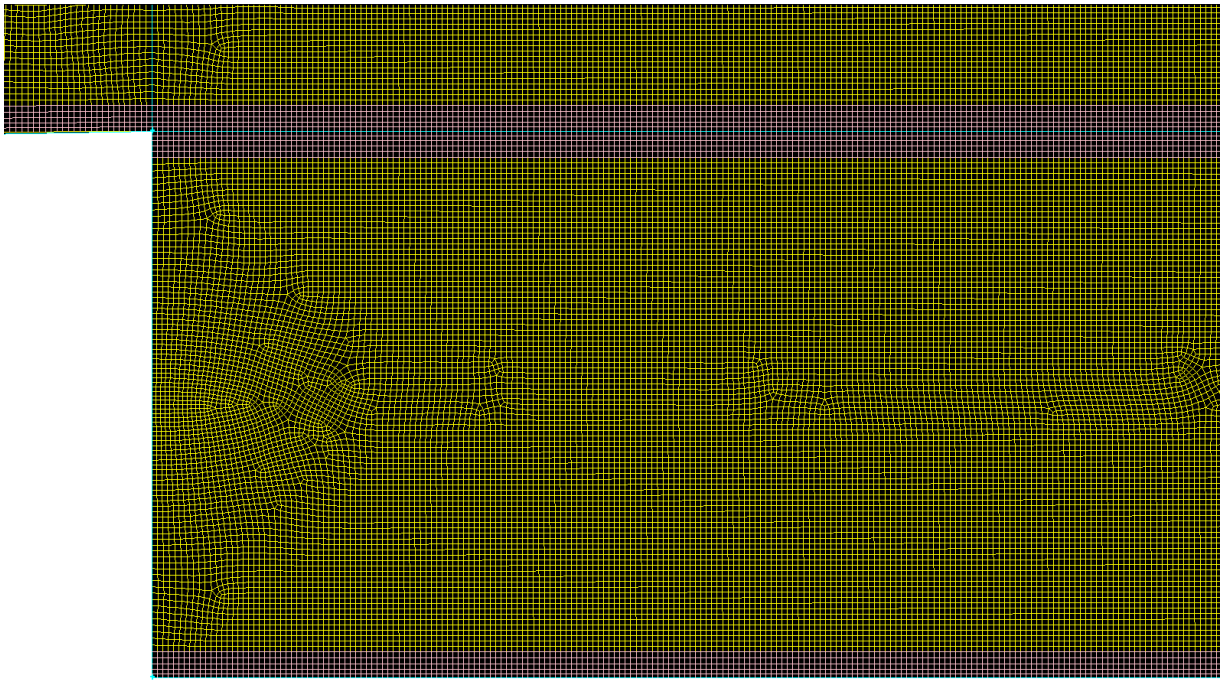

Fig. 6.7a Closer view of the modified mesh behind the flame-stabilizer step

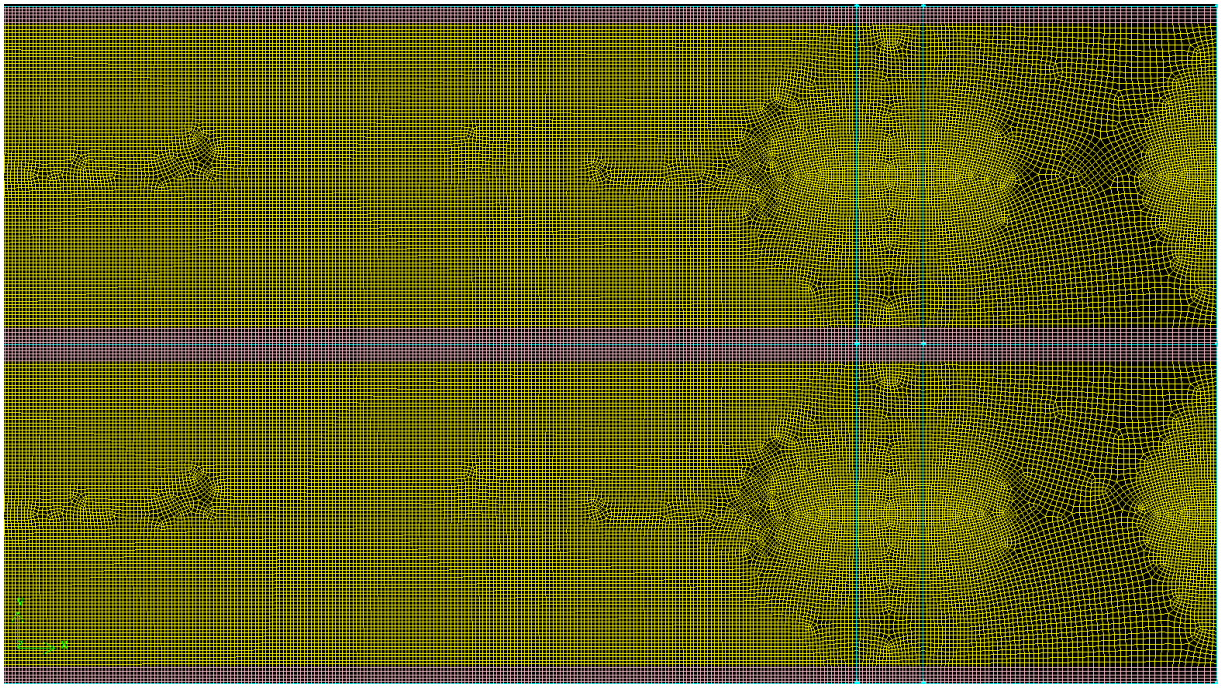

Fig. 6.7b Closer view of the modified mesh near the exit of the combustor

Section 6.5 in Chapter 5 presented a hexahedral meshing strategy for the 2D combustor on the baseline geometry. Since the profile of the flame-stabilizer step is smooth in the baseline configuration, the hexahedral scheme is the best way to mesh the geometry. However, during the design study the shape of the flame-stabilizer step varies between extreme values, which might not be suitable for a structured hexahedral mesh approach. At high values of θ, the hexahedral mesh tend to be very skewed which could

lead to mesh quality and CFD solution convergence issues. Thus, a quadrilateral-paved (quad-paved) meshing approach is applied to the 2D combustor. The mesh 3 configuration (c.f. Table 5.2), which is selected in the mesh sensitivity analysis, is re-meshed using quad-pave meshing scheme in Gambit 2.3.16. With this scheme Gambit creates an unstructured face mesh consisting of quadrilateral mesh elements. The boundary layer scheme is retained as previously used in mesh 3.

Figure 6.5 shows an overall view of the quad-pave mesh in the 2D combustor. Figures 6.6a and 6.6b shows a closer view of the modified mesh near the inlet and flame-stabilizer step exit respectively; whereas Figures 6.7a and 6.7b shows a closer view of the modified mesh behind the flame-stabilizer step and near the combustor exit respectively. A relatively coarser mesh is built near the inlet and the outlet of the combustor, with finer mesh near the step exit and behind the step zone. The total cell count in this scheme is ~ 180,000 as compared to ~190,000 in the structured hexahedral approach.

To understand the effect of the quad-pave meshing scheme on the CFD solution, a reactive CFD analysis using steady RANS is carried out. The outlet temperature profile is measured and compared to the profile obtained using the hexahedral mesh. Figure 6.8 shows the comparison of the outlet temperature profiles predicted using these two different meshing strategies.

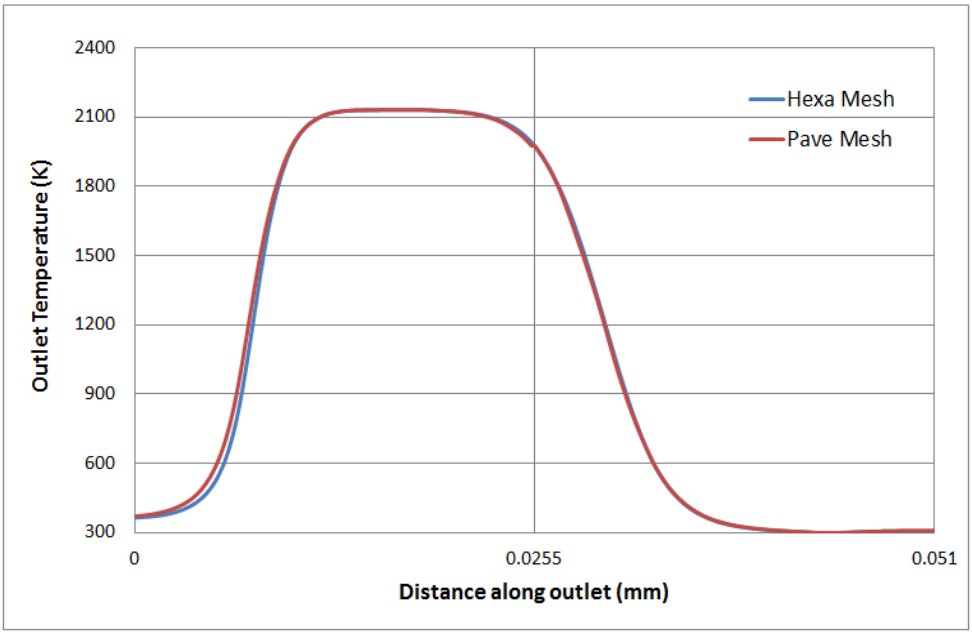

Fig. 6.8 Outlet temperature profile as predicted by hexahedral and quad-pave meshing

As shown in Figure 6.8, only a small difference in the outlet temperature profile is noticed in the burning mixture zone of the combustor. However, overall the solution remains largely unaffected. Thus, for the purpose of a design optimisation study, the modified mesh is used without any further changes.

6.4 Experiment design

6.4.1 100 point detailed prediction surfaces

With the combustor design parameters, design space and meshing strategy defined, a reasonably accurate representation of the design space is evaluated on a 10x10 regular grid of design points for outlet temperature and thermal NO objective functions, both in spatial and temporal domains.

6.4.1.1 Spatial domain (using steady RANS)

(A) Outlet temperature profile

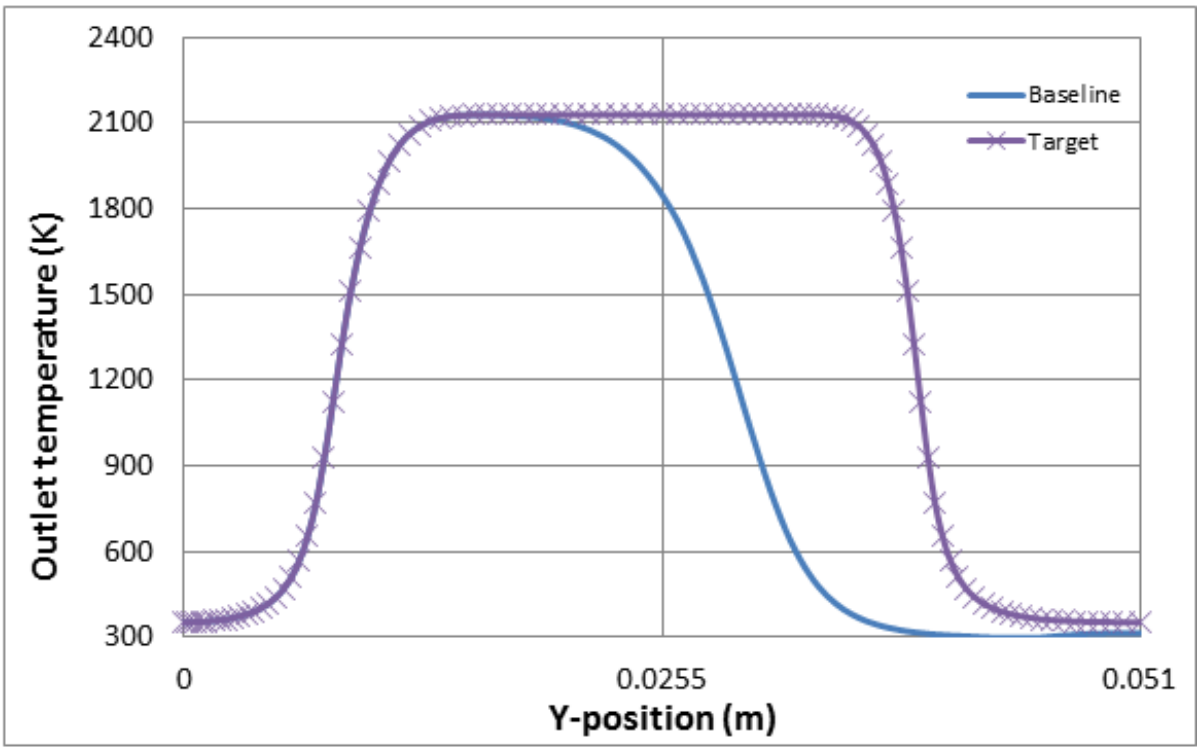

Fig. 6.9 Comparison between baseline geometry outlet temperature profile and target outlet temperature profile

Figure 6.9 shows the comparison between the outlet temperature profile of the baseline step geometry and the developed target outlet temperature profile. The target outlet temperature profile is developed such that it is more symmetrical about the centerline of the combustor, which represents an approximate position of the flame front inside the chamber, above which the mixture is unburnt and below which the mixture is burnt.

The aim of the optimization process is to minimize the difference between the design and target profiles. This is done by changing the shape of the flame-stabilizer step i.e.

changing the design variables Y and θ until a design is found that minimises the root mean square deviation (RMSD) of the difference between the design outlet temperature profile and the target outlet temperature profile. If vector P represents points on an individual design outlet temperature profile and vector T represents points on the target outlet temperature profile, then:

For, $T = [T_1, T_2, T_3 \ldots\ldots T_n]$ and $P = [P_1, P_2, P_3 \ldots\ldots P_n]$;

where, n = number of points in the profile;

$$\text{RMSD}\ (T, P) = \sqrt{MSE(T, P)} = \sqrt{\frac{\sum_{i=1}^{n}(T_i - P_i)^2}{n}} \qquad \text{Eq. (6.2)}$$

The value of the RMSD is used as the objective function for outlet temperature optimisation.

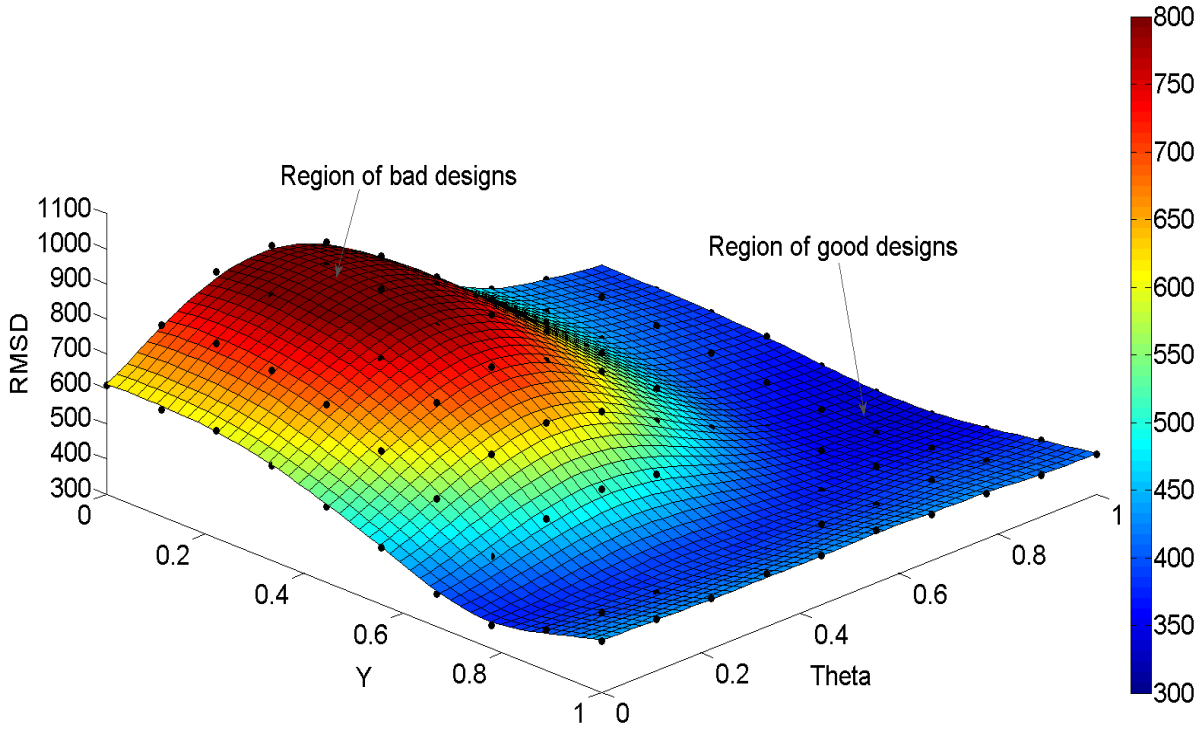

Fig. 6.10 Kriging response surface for steady outlet temperature generated using 10x10 regular grid CFD data

Figure 6.10 shows the steady outlet temperature Kriging RSM constructed using 100 CFD runs based on 10x10 regular grid data points. As shown in Figure 6.10, the Kriging response surface fits smoothly over the evaluated 10x10 grid of CFD data points indicating a low level of numerical noise in the data. It shows a hill of high objective

function values at lower design parameter values of Y and θ, signifying a region of bad designs. The region with good designs consists of a valley surrounding the hill at higher values of Y and θ. This region becomes the area of attention when applying a Kriging design optimisation strategy for outlet temperature.

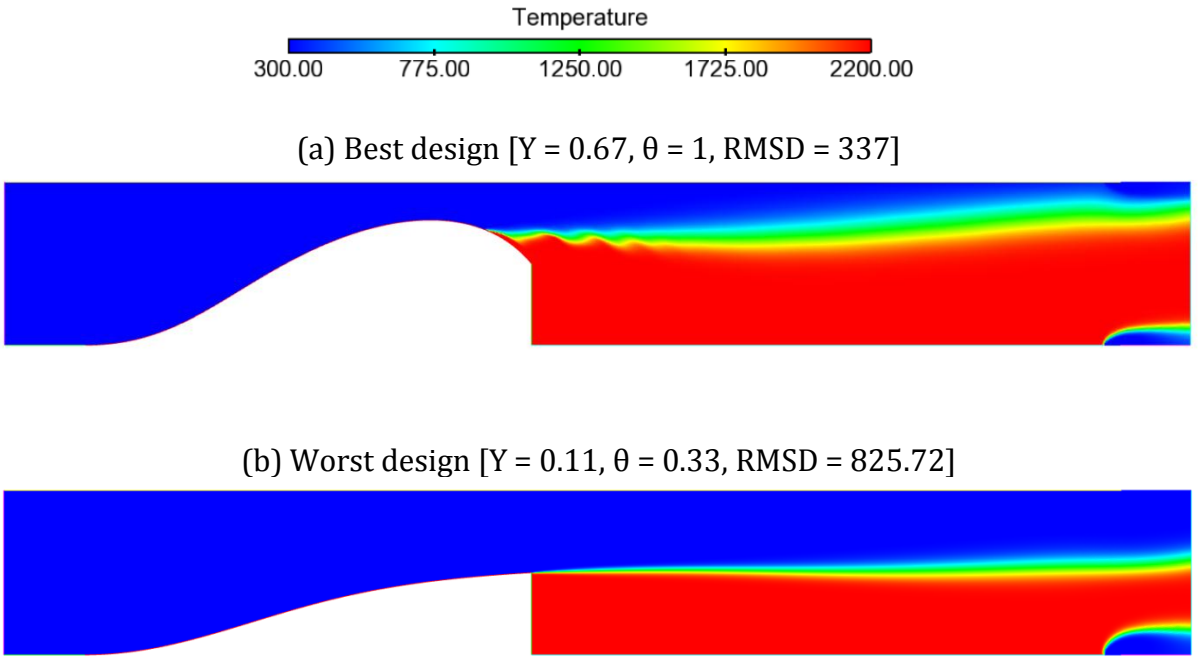

(a) Best design [Y = 0.67, θ = 1, RMSD = 337]

(b) Worst design [Y = 0.11, θ = 0.33, RMSD = 825.72]

Fig. 6.11 Best and worst designs for outlet temperature profile obtained using 10x10 regular grid CFD evaluations

(a) Best design (b) Worst design

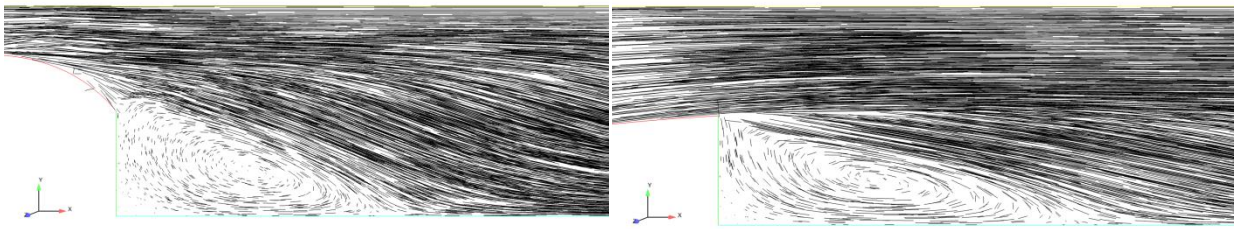

Fig. 6.12 Vortex behind the best and worst step designs for outlet temperature profile

Figure 6.11 shows the best and worst step designs temperature flow-field obtained using 10x10 regular grid CFD evaluation. At higher values of Y and θ [c.f. Figure 6.11(a)], the incoming mixture velocity is reduced due to the contraction leading to higher amount of mixture burning in the combustor downstream. Figure 6.12(a) shows the flow separating near the end of the step, which leads to a wrinkled flame effect near the step as captured in Figure 6.11(a) with a recirculating vortex behind the step.

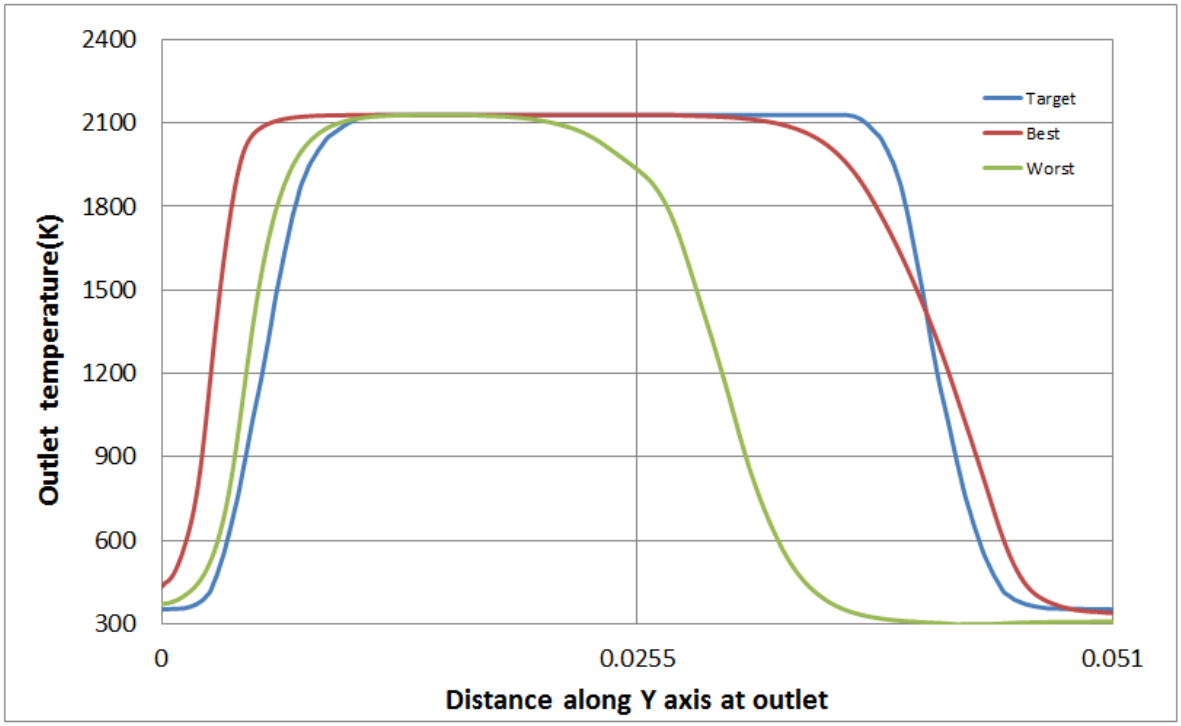

Fig. 6.13 Comparison between baseline geometry outlet temperature profile and target outlet temperature profile

At lower values of Y and θ [c.f. Figure 6.11(b)] the incoming mixture velocity continues to be higher in the upper part of the combustor leading to high amount of unburnt mixture at the combustor exit. Figure 6.12 (b) shows the stretched vortex behind the worst step design. Hence, predominantly, a reduction in incoming mixture velocity favors a good design for outlet temperature profile. Figure 6.13 shows the comparison between the outlet temperature profiles of the best and worst designs against the target outlet temperature profile.

(B) Outlet thermal NO

The objective function for combustor outlet NOx is concerned with thermal NO concentration in parts per million (ppm) at the outlet plane. For this prediction a custom field function in Fluent 12.1 is setup which computes NO ppm from the following equation (Ansys Fluent theory guide, 2009):

$$\text{NO ppm} = \frac{\text{NO mole fraction x } 10^6}{1 - \text{H}_2\text{O mole fraction}} \qquad \text{Eq. (6.3)}$$

An area-weighted average of the thermal NO in ppm at the outlet plane is considered as the objective function to be minimized in the optimisation process.

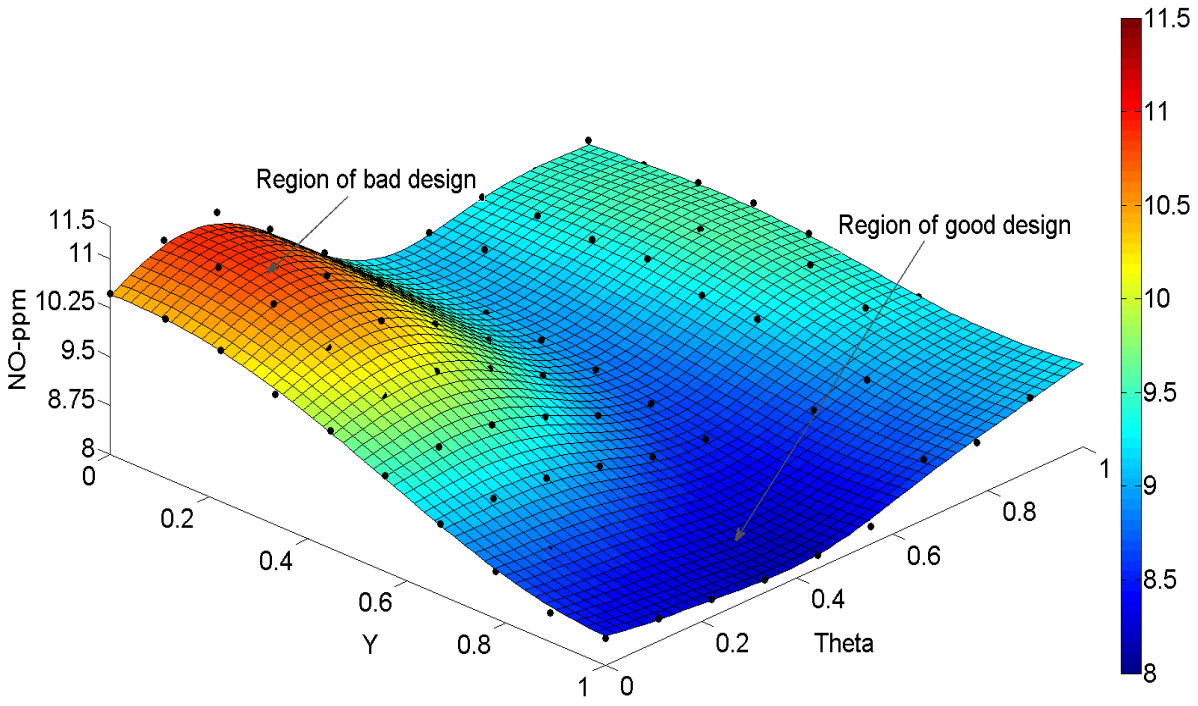

Fig. 6.14 Kriging response surface for steady outlet thermal NO generated using 10x10 regular grid CFD data

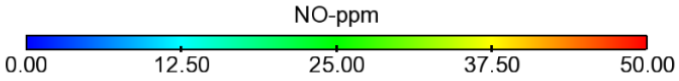

(a) Best design [Y = 0.89, θ = 0.44, NO = 8.17 ppm]

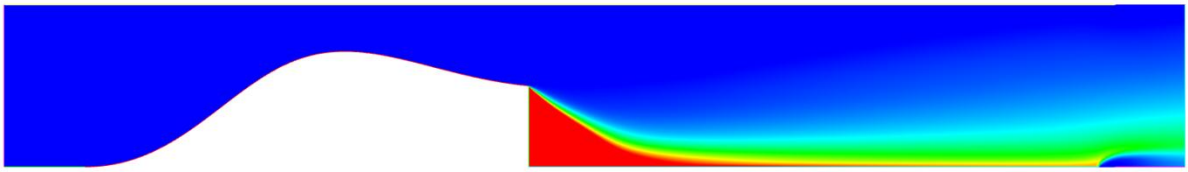

(b) Worst design [Y = 0, θ = 0.22, NO = 10.98 ppm]

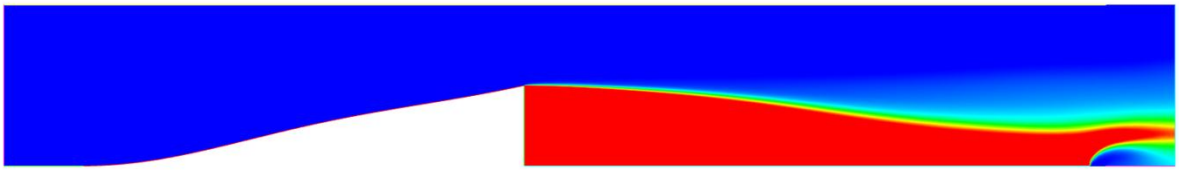

Fig. 6.15 Best and worst designs for outlet thermal NO obtained using 10x10 regular grid CFD evaluations

(a) Best design (b) Worst design

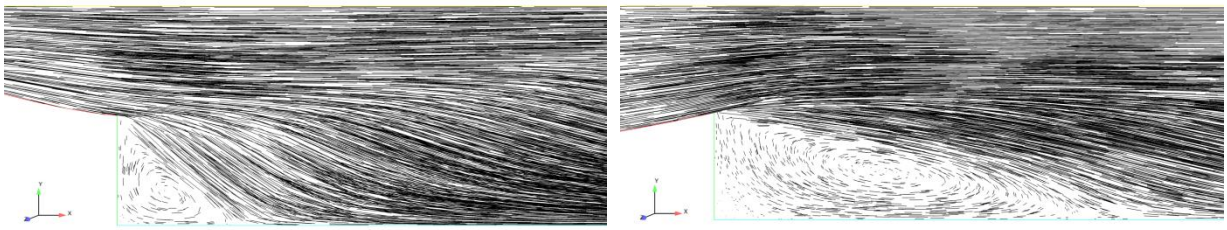

Fig. 6.16 Vortex behind the best and worst step designs for outlet temperature profile

Figure 6.14 shows the steady outlet NO Kriging RSM constructed using 10x10 regular grid CFD evaluations.A hill of high objective function values is observed at lower design parameter values of Y and θ, indicating a region of bad designs. This is similar to the observation in outlet temperature profile RSM (c.f. Figure 6.10). However, the region of good designs exists at high values of Y and intermediate values of θ. This region becomes the area of attention when applying Kriging optimisation strategy for steady outlet NO.

Figure 6.15 shows the best and worst designs for outlet thermal NO objective function using 10x10 regular grid CFD evaluations. The best design [c.f. Figure 6.15(a)] is obtained at high value of Y and intermediate value of θ. The amount of thermal NO produced is low mainly due to the small recirculation zone behind the step [c.f. Figure 6.15(a)] and is entrapped. Hence, low amount of thermal NO is transported towards the outlet. Whereas, in the case of worst design [c.f. Figure 6.15(b)], the thermal NO production is larger due to bigger recirculation vortex behind the step [c.f. Figure 6.16(b)].

Hence, a smaller recirculation vortex behind the step majorly favors good designs with lower thermal NO.

6.4.1.2 Temporal domain (using URANS)

(A) Time-averaged outlet temperature profile

Figure 6.17 shows the variation of combustor area-weighted outlet temperature T_a over time for the baseline configuration. This unsteady RANS computation is started from the converged steady RANS solution. The simulation settles into a meta-stable state after four cycles of inlet sinusoidal fluctuation. Over the 4^{th} cycle of fluctuation, the outlet area-weighted average temperature at each time-step is recorded leading to a time-averaged area-weighted average temperature

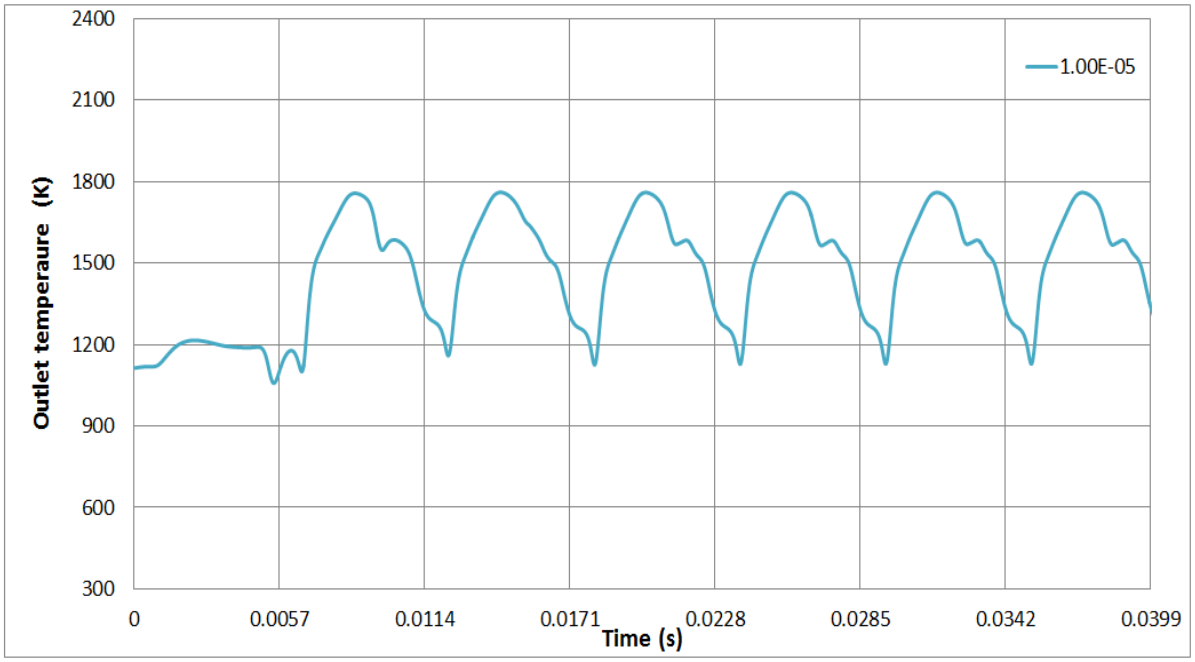

Fig. 6.17 Variation of area-weighted outlet temperature (T_a) over time (URANS solution started from converged steady RANS solution)

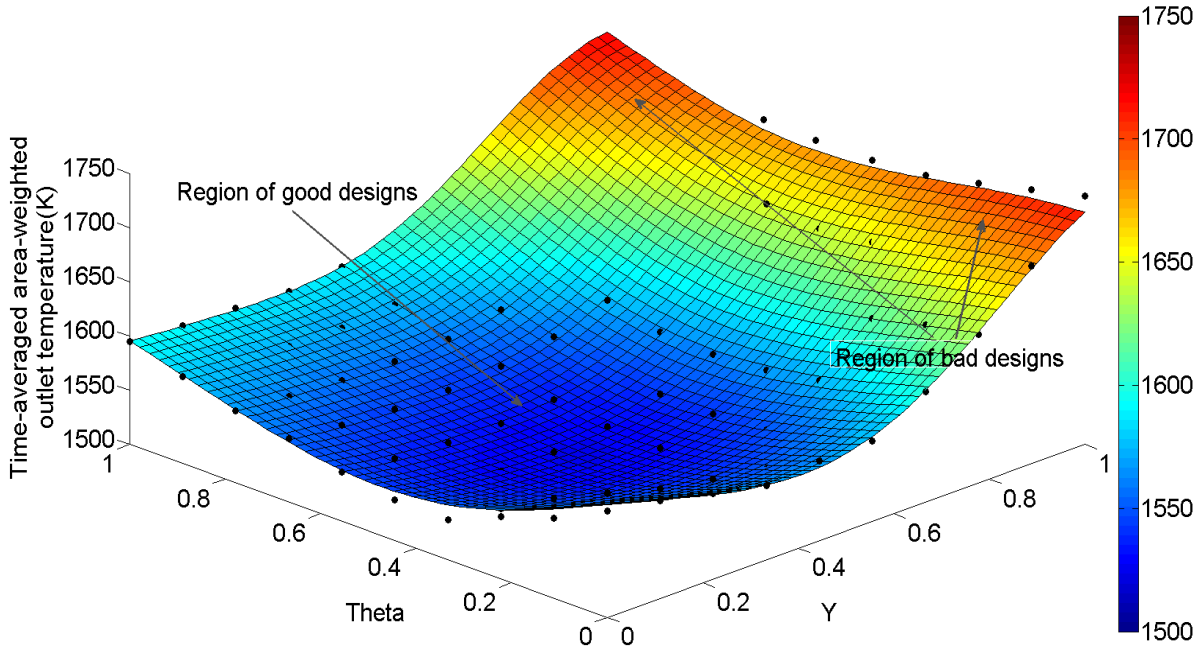

Fig. 6.18 Kriging response surface for time-averaged area-weighted outlet temperature obtained using 10x10 regular grid CFD data

$$\overline{T_a} = \frac{\sum_{i=1}^{t} T_a^i}{N_t} \qquad \text{Eq. (6.4)}$$

N_t = number of time-steps

which is taken as the objective function to be minimized in the Kriging design optimisation process for area-weighted outlet temperature in temporal domain.

Figure 6.18 shows the Kriging RSM constructed for time-averaged outlet temperature using 100 CFD runs based on 10x10 regular grid data points.Compared to the RSM of steady outlet temperature (c.f. Figure 6.10), a different picture of the objective function landscape is observed. The region of good designs in steady outlet temperature RSM is no longer the best for the time-averaged outlet temperature objective function. As seen in Figure 6.18, a valley of low objective function values exists at intermediate values of Y and θ. This region becomes the focus of attention when applying the Kriging design strategy for time-averaged outlet temperature. Interestingly, this regions design parameters value are close to the baseline design parameter values.

(a) Best design
[Y = 0.22, θ = 0.33, $\overline{T_a}$ = 1525 K]

(b) Worst design
[Y = 0.89, θ = 1, $\overline{T_a}$ = 1927.5 K]

Fig. 6.19 Flame stabilizer step best and worst designs for time-averaged area-weighted outlet temperature (K)

Figure 6.19 shows the comparison between the best and worst designs of the flame-stabilizer step. Since the objective is to obtain a design with minimum time-averaged area-weighted outlet temperature, a contraction at higher values of Y and θ [c.f. Figure 6.19(b)] has an adverse effect. Due to the reduced velocity, almost all of the mixture in the combustor downstream is burnt over the humming cycle. Whereas, with designs at intermediate values of Y and θ [c.f. Figure 6.19(a)], the mixture content at the outlet consists of both burnt and unburnt species over the unsteady humming cycle, leading to a reduction in area weighted outlet temperature. Figure 6.20 shows the effect of the best and worst step designs on the area-weighted outlet temperature variation over the humming cycle. For the worst design, the temperature variation is almost consistent around high value of 1900 K, whereas the temperature fluctuation range for best design is in between 1200 K to 1800 K. Hence, a smooth step profile with intermediate values of Y and θ favors a good design for time-averaged area-weighted outlet temperature.

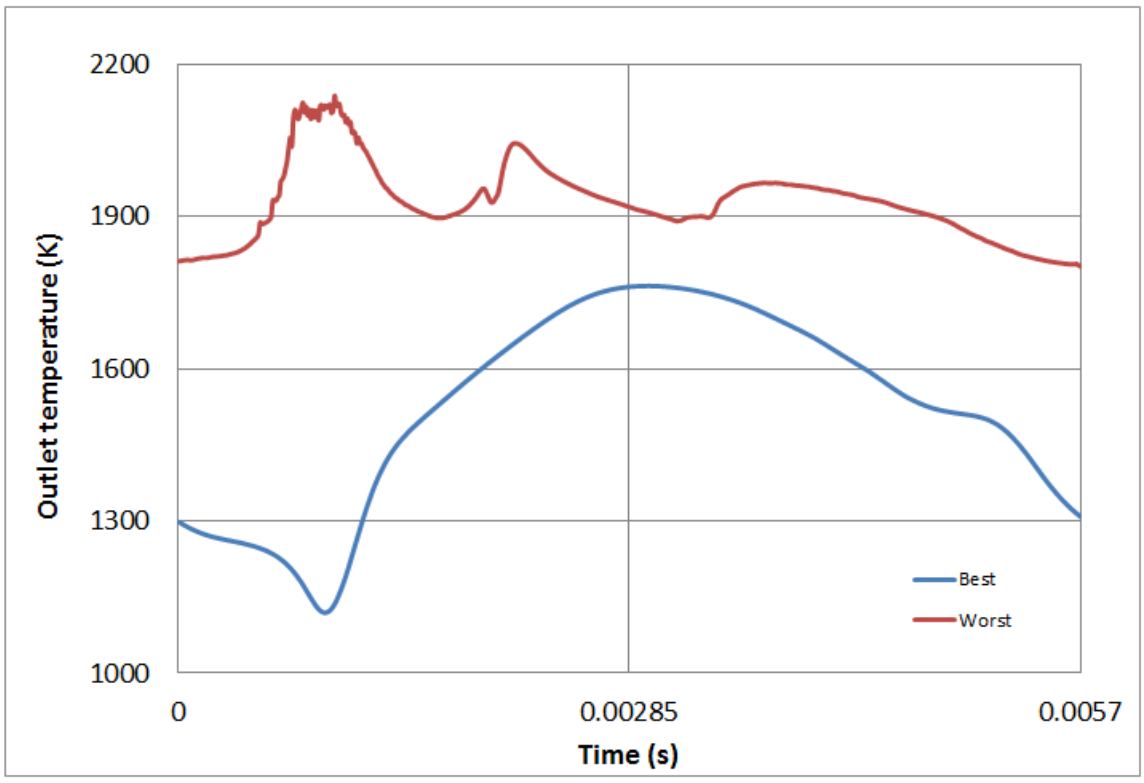

Fig. 6.20 Best and worst designs area-weighted outlet temperature fluctuation over humming cycle

(B) Time-averaged outlet thermal NO

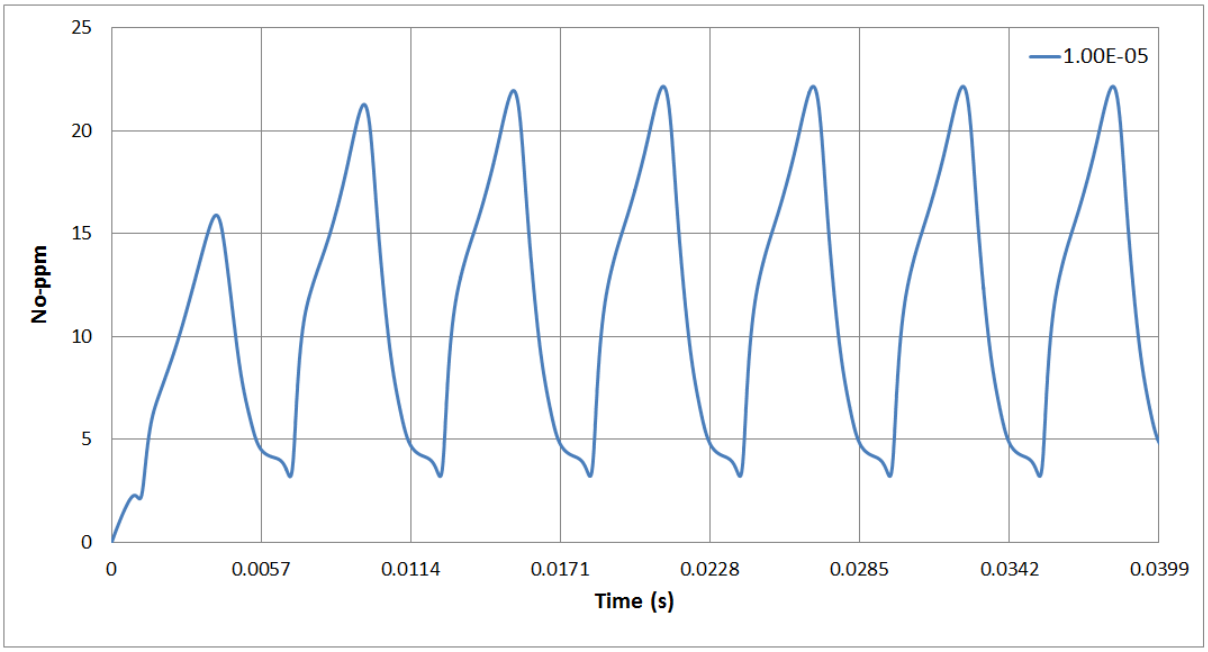

Fig. 6.21 Variation of area-weighted outlet thermal NO (NO_a) as captured by URANS over time

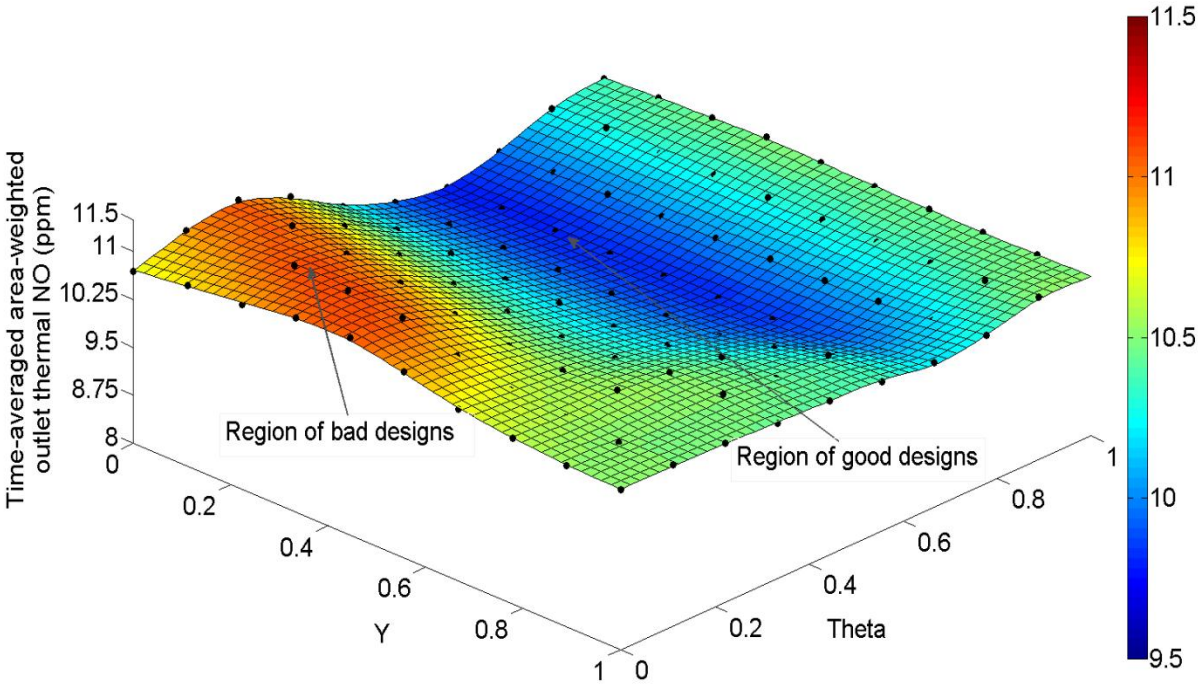

Fig. 6.22 Kriging response surface for time-averaged area-weighted outlet thermal NO obtained using 10x10 regular grid CFD data

Figure 6.21 shows the variation of area-weighted outlet thermal NO (ppm) over time for the baseline configuration. The unsteady RANS thermal NO computation, which is started from the converged steady RANS reactive solution, settles to a meta-stable state after four cycles of fluctuations. This agrees with the unsteady outlet temperature fluctuation cycle (c.f. Figure 6.17).

Thermal NO in parts per million is computed as per Equation 6.3 at each time-step of unsteady RANS. Over the 4th cycle of fluctuation, the outlet area-weighted average thermal NO (ppm) is time-averaged according to

$$\overline{NO_a} = \frac{\sum_{i=1}^{t} NO_a^i}{N_t} \qquad \text{Eq. (6.5)}$$

N_t = number of time-steps

This value of NO is taken as the objective function to be minimized in the Kriging design optimisation process for thermal NO in the temporal domain.

Figure 6.22 shows the Kriging RSM for time-averaged area-weighted outlet thermal NO constructed using 100 CFD runs based on 10x10 regular grid data points.The Kriging response surface fits smoothly over the evaluated 10x10 grid of CFD data points

indicating a low level of numerical noise in the data. A hill of high objective function values at lower design parameter values of Y and θ indicates a region of bad designs. It shows as a valley of good designs at values of θ between 0.4 and 0.8 and values of Y between 0 and 0.6 which becomes the focus of attention.

(a) Best design
[Y = 0, θ = 0.67, $\overline{NO}_a$ = 9.775 ppm]

(b) Worst design
[Y = 0.22, θ = 0.11, $\overline{NO}_a$ = 11.12 ppm]

Fig. 6.23 Flame stabilizer step best and worst designs for time-averaged area-weighted outlet thermal NO (ppm)

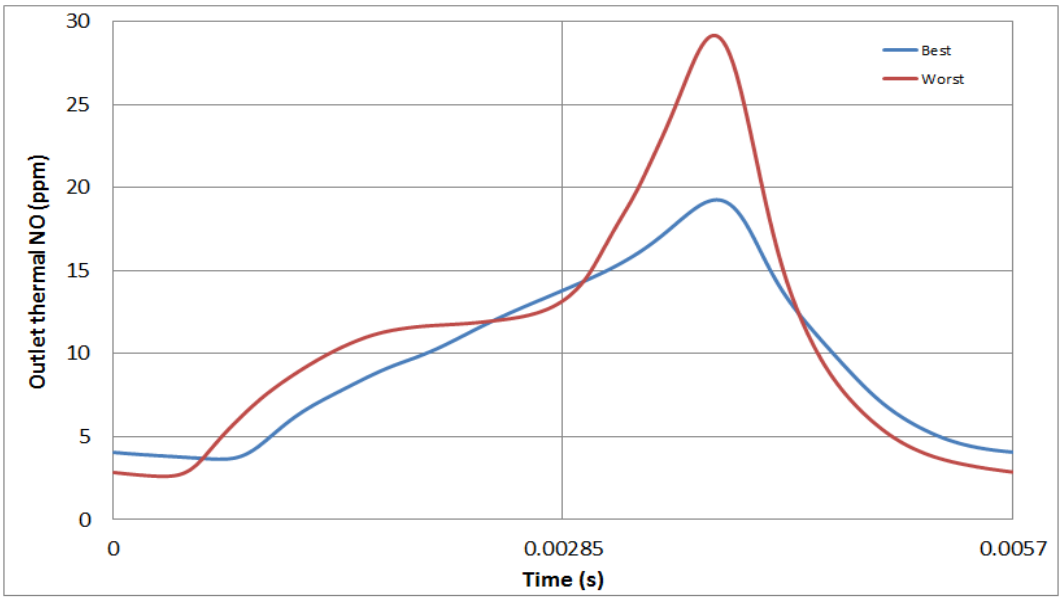

Fig. 6.24 Best and worst designs area-weighted outlet thermal NO fluctuation over humming cycle

Figure 6.23 shows the comparison between the best and worst step profiles for time-averaged area-weighted outlet thermal NO (ppm). The intermediate to higher values of θ (between 0.4 and 0.8) causes the recirculation vortex size behind the step to be relatively smaller. Also, at lower values of Y, the higher mixture velocity leads to a reduction of total amount of burnt mixture and hence high temperatures zone in the combustor. This combination favors a good design from time-averaged area-weighted thermal NO point of view, which predominantly depends on recirculation vortex size and high temperature zones. Figure 6.24 shows the comparison between the best and worst designs area-weighted outlet thermal NO (ppm) over the humming cycle.

6.4.2 Sampling plan using DOE

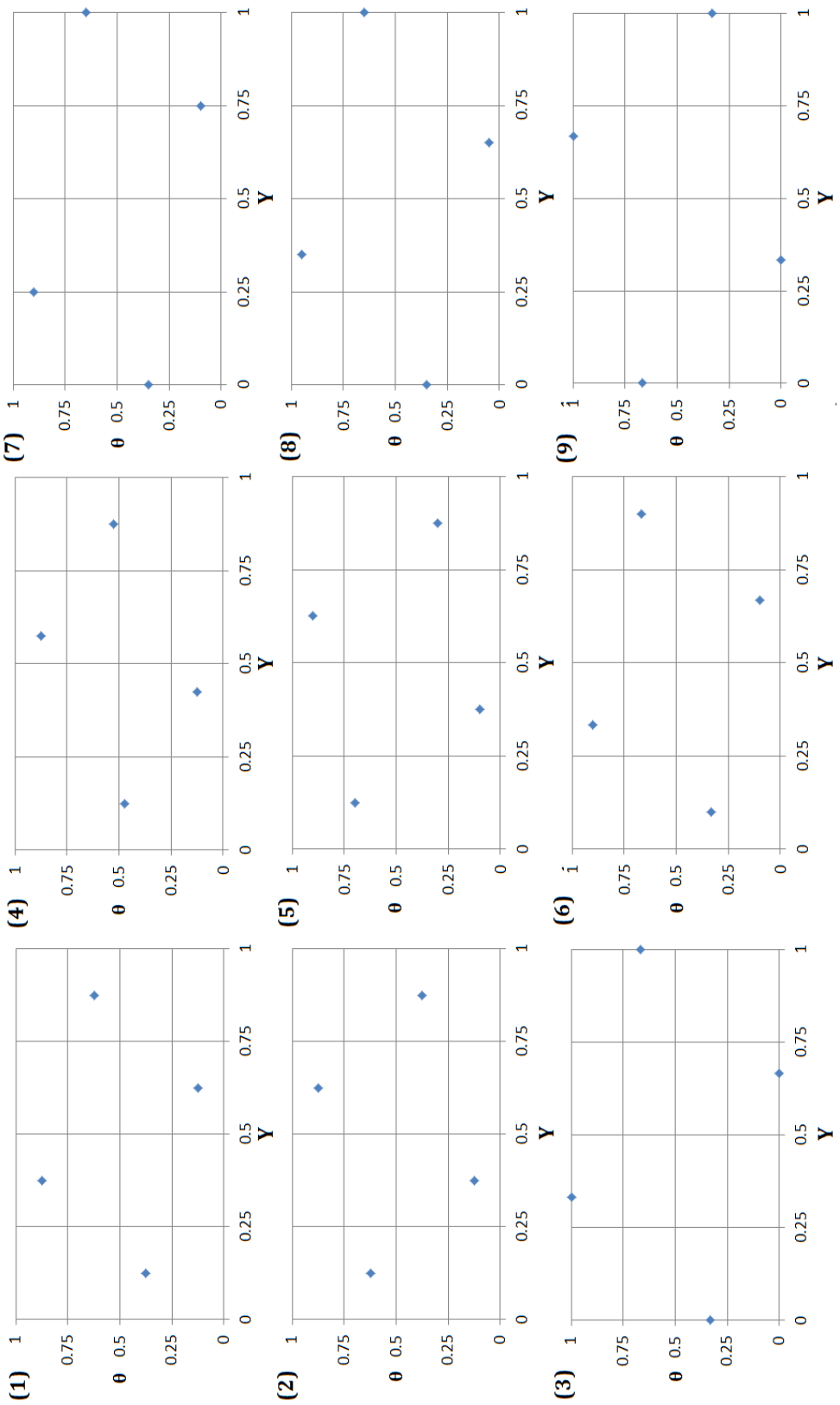

Fig. 6.25 Different optimal Latin-Hypercube samples (LHS)

Since using 100 points to sample the design space is very expensive, attention is now turned to using small initial sample plans followed by an update strategy to locate the best design.

For initializing the design study, 4 space-filling sample points are generated using optimal Latin-Hypercube sampling (LHS). Figure 6.25 shows nine different samples of space-filling points in two dimensions. The two variables are Y and θ (c.f. Figure 6.3). The Kriging design optimisation strategy is applied on all 9 starting samples to investigate their effect on the strategy's ability to find optimum design configuration within the given computational budget of 10 high-fidelity runs.

6.4.3 Update point strategy

After constructing the Kriging surface, based on the observations from DOE points (c.f. Figure 6.2), two update points are generated per update cycle in this design study. One is obtained using best Kriging prediction in the response surface and other is obtained using the expected improvement criteria (Both methods are explained in more detail in Section 2.4.4). Thus a balanced exploration and exploitation approach is used to update the Kriging response surface model.

6.5 Results and discussion

6.5.1 Design optimisation in spatial domain

Figures 6.26 and 6.27 shows the optimisation search histories for Kriging based design strategy using 9 different DOE samples (c.f. Figure 6.25) over a fixed computational budget of 10 high-fidelity CFD runs for outlet temperature profile RMSD and outlet thermal NO respectively. They also show the respective mean performances over all the search histories.

The DOE evaluation consists of 4 sample points with 3 update cycles, each consisting of 2 update points. The different initial samples have an effect on the way the optimisation process progresses over the cycle. This is because different initial samples lead to different information being available at the DOE stage with altered Kriging model convergence behaviour. Hence, each optimisation cycle leads to a different optimal design in Figures 6.26 and 6.27.

A spread, or variation, in the search histories convergence is also shown in Figures 6.26 and 6.27.

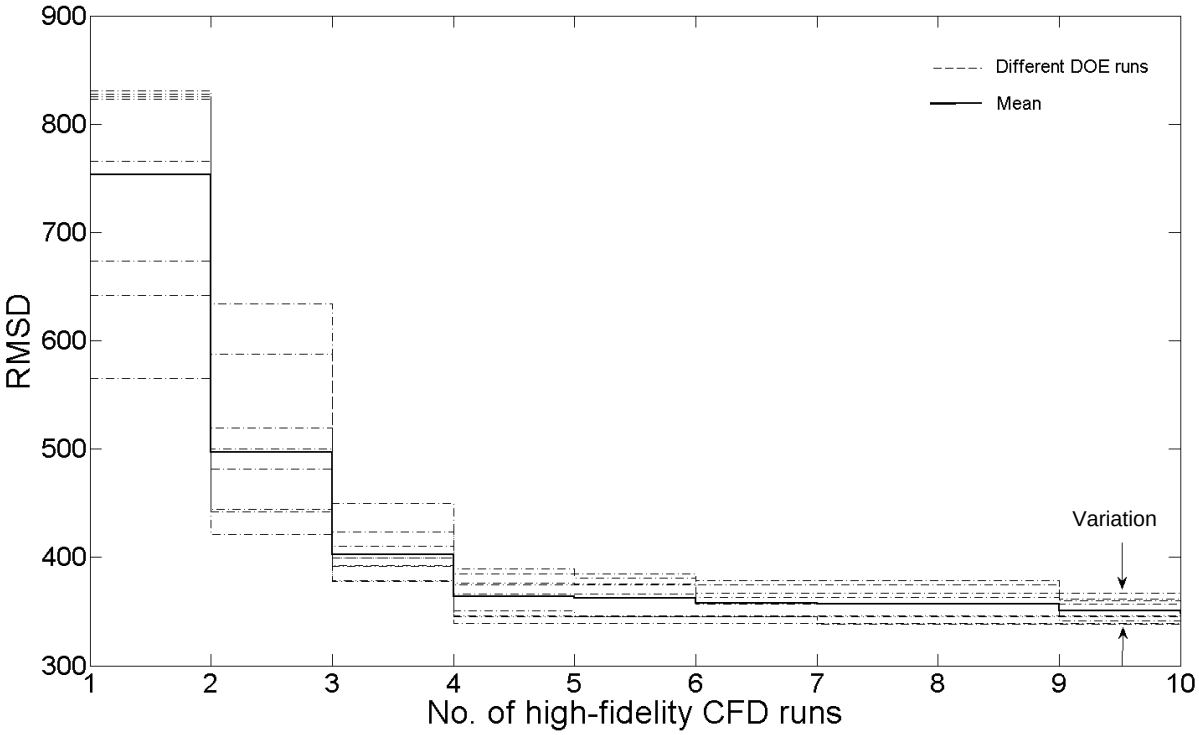

Fig. 6.26 Steady outlet temperature profile RMSD optimisation search histories over a fixed computational budget of 10 high-fidelity CFD runs (4 in initial sample + 6 updates)

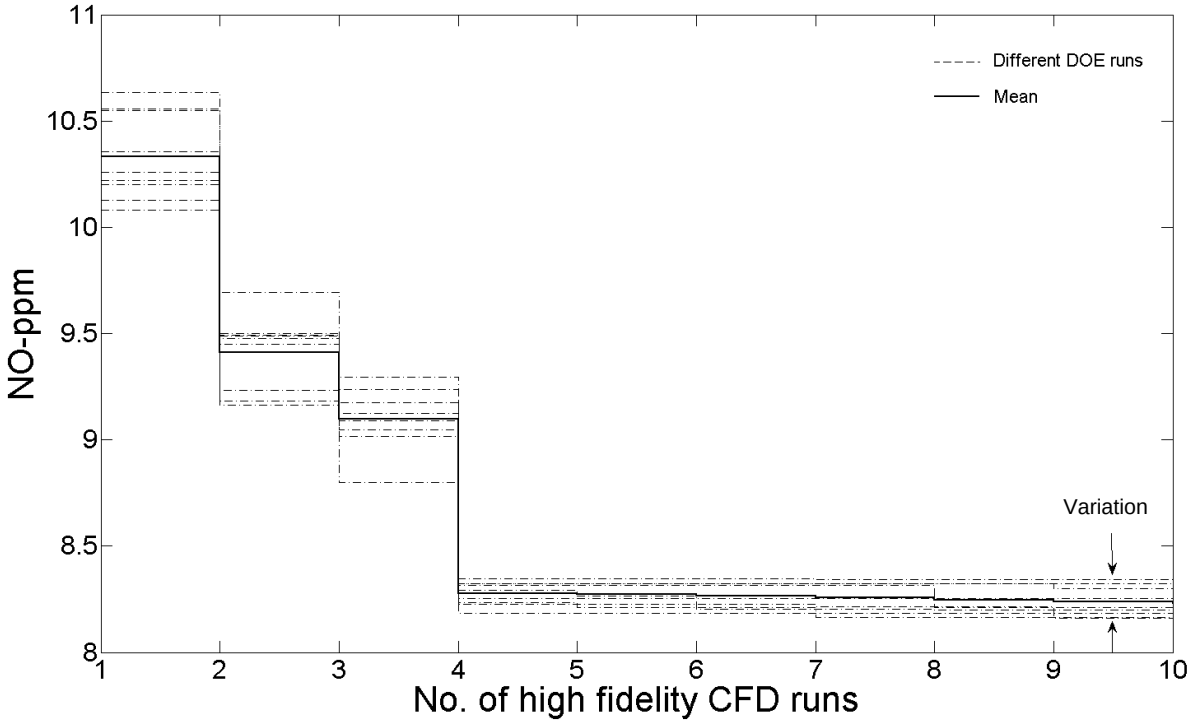

Fig. 6.27 Steady outlet thermal NO optimisation search histories over a fixed computational budget of 10 high-fidelity CFD runs (4 in initial sample + 6 updates)

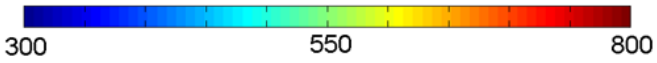

Kriging response surface using DOE sample no. 4 with best optimal design

(1) After DOE

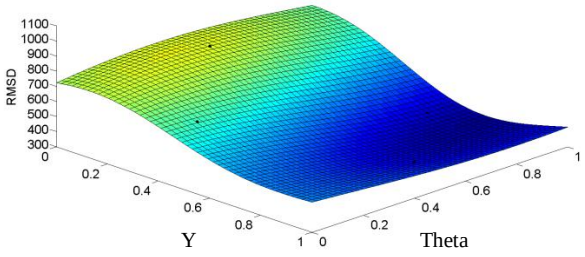

(2) After DOE + Updates

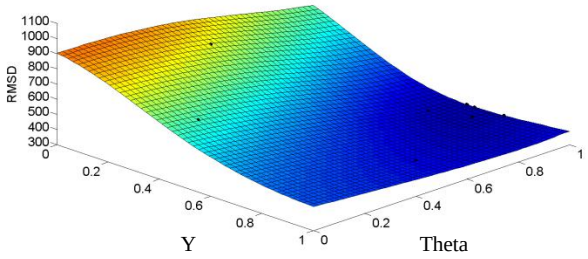

Kriging response surface using DOE sample no. 7 with worst optimal design

(3) After DOE

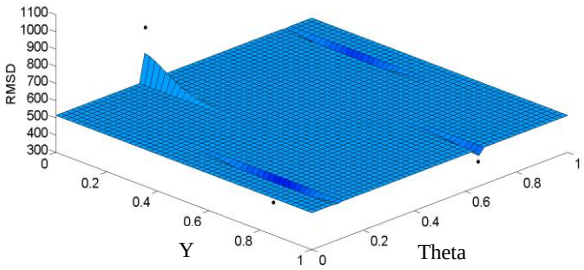

(4) After DOE + Updates

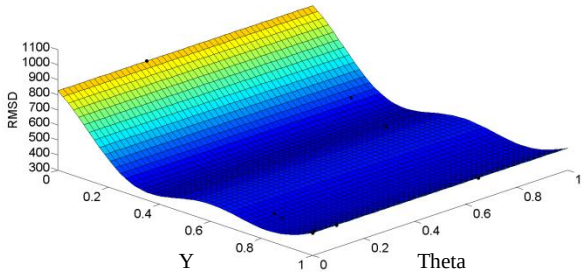

Fig. 6.28 Kriging response surfaces consisting of best and worst optimal designs for steady outlet temperature profile

Figure 6.28 shows the Kriging response surfaces consisting of best and worst optimal designs for steady outlet temperature profile RMSD after the DOE stage and end of the optimisation cycle stage (c.f. Figure 6.26). The ranking of the DOE samples based on the final outlet temperature RMSD values is listed in Appendix E.

In comparison to the shape of the response captured using 10x10 grid CFD evaluations (c.f. Figure 6.10), the response surface of experiment four captures the good and bad design regions within the given fixed computational budget. Whereas, the response surface of experiment seven fails to capture the shape of the response within the given budget. This difference is clearly due to the quality of the information available at the DOE stage which subsequently effects convergence and finding the optimal design with a limited budget. This observation is consistent with one of the possible pitfalls associated with Kriging mentioned by Jones (2001).

Similarly, Figure 6.29 shows the Kriging response surfaces consisting of best and worst optimal designs for outlet thermal NO. (Refer Appendix E for the ranking of the DOE

samples based on the final outlet thermal NO values). The response surface of experiment four captures the good and bad design regions within the fixed computation budget compared to the Kriging surface constructed using 10x10 grid CFD evaluations (c.f. Figure 6.14). The response surface of experiment three fails to capture the correct shape of the response within the fixed computational budget.

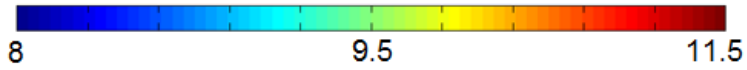

Kriging response surface using DOE sample no. 4 with best optimal design

(1) After DOE (2) After DOE + Updates

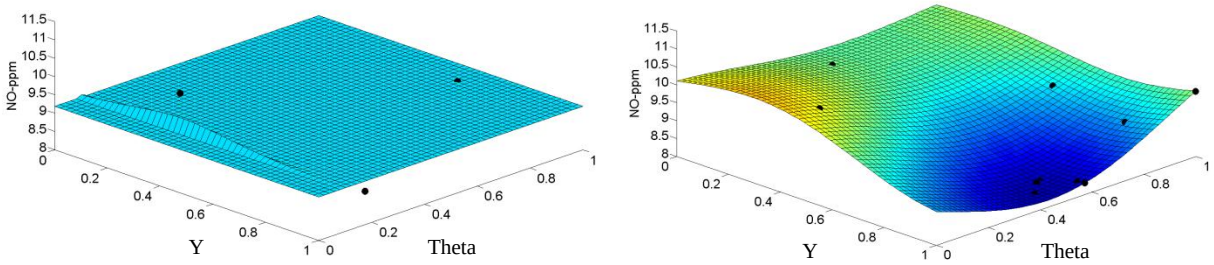

Kriging response surface using DOE sample no. 3 with worst optimal design

(3) After DOE (4) After DOE + Updates

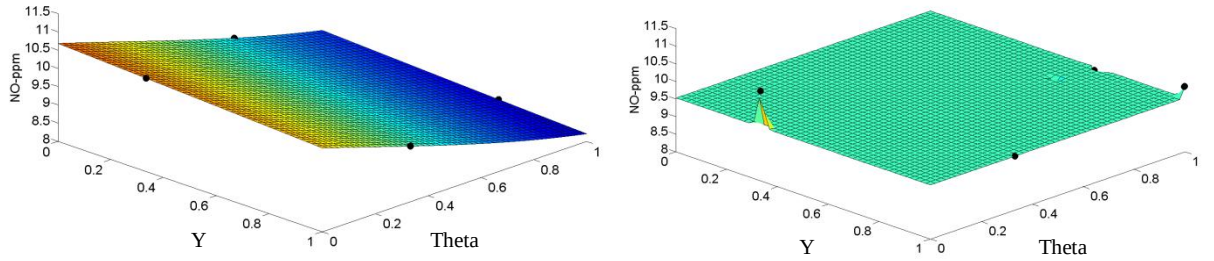

Fig. 6.29 Kriging response surfaces consisting of best and worst optimal designs for steady outlet thermal NO (ppm)

Figures 6.30 and 6.31 shows the optimal flame-stabilizer step designs obtained using Kriging design optimisation strategy for steady outlet temperature RMSD and thermal NO respectively. The shapes of the best optimal designs agree closely with that of the optimal designs found using 10x10 grid CFD evaluations (c.f. Figure 6.11 for outlet temperature RMSD and Figure 6.15 for thermal NO).

This highlights that this approach can obtain good design with ten times less effort than the full grid sampling plan.

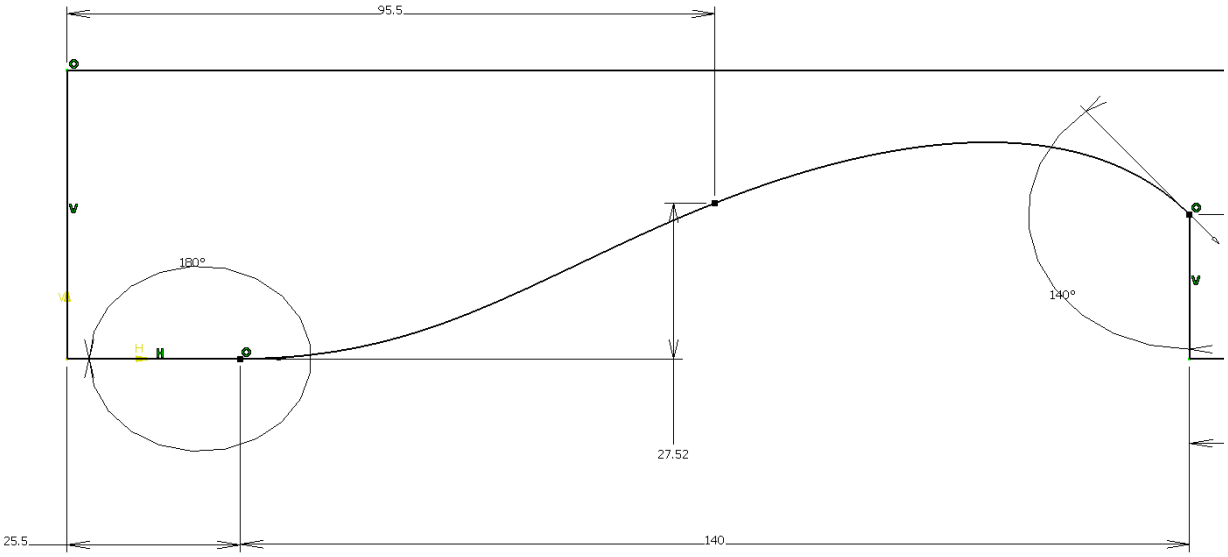

Fig. 6.30 Optimal flame-stabilizer step for steady outlet temperature profile RMSD optimisation at Y = 0.6 (27.52mm) and θ = 1 (140 degrees)

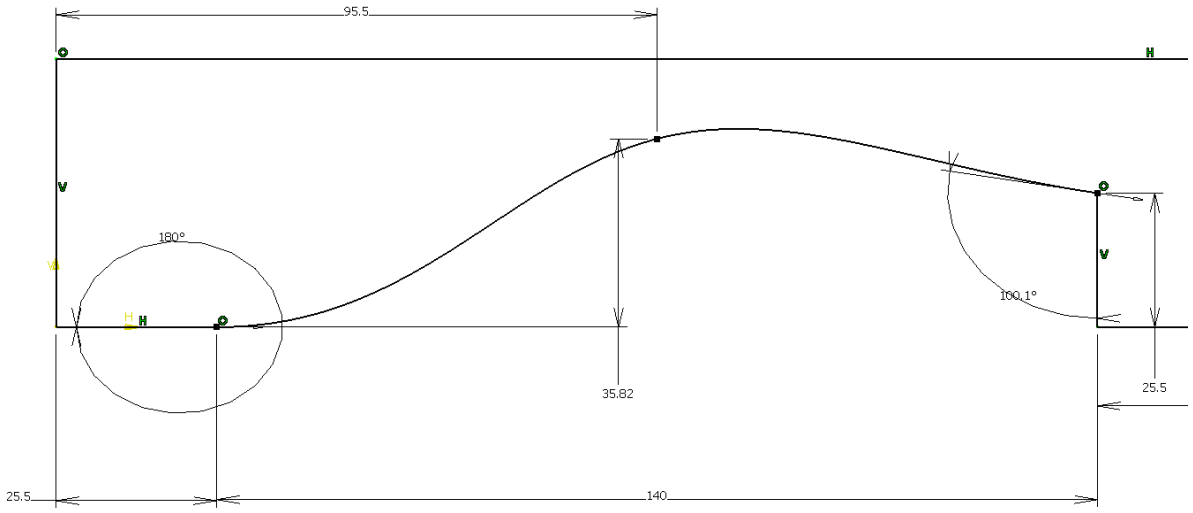

Fig. 6.31 Optimal flame-stabilizer step for steady outlet thermal NO obtained by Kriging design strategy at Y = 0.933 (35.82mm) and θ = 0.446 (100.1 degrees)

6.5.2 Design optimisation in temporal domain

After the investigation of the Kriging strategy for combustor design in the spatial domain using steady RANS, combustor design optimisation in the temporal domain using the Kriging strategy and URANS is performed in the following section. A time-averaged objective function is of main interest for design optimisation in the temporal domain.

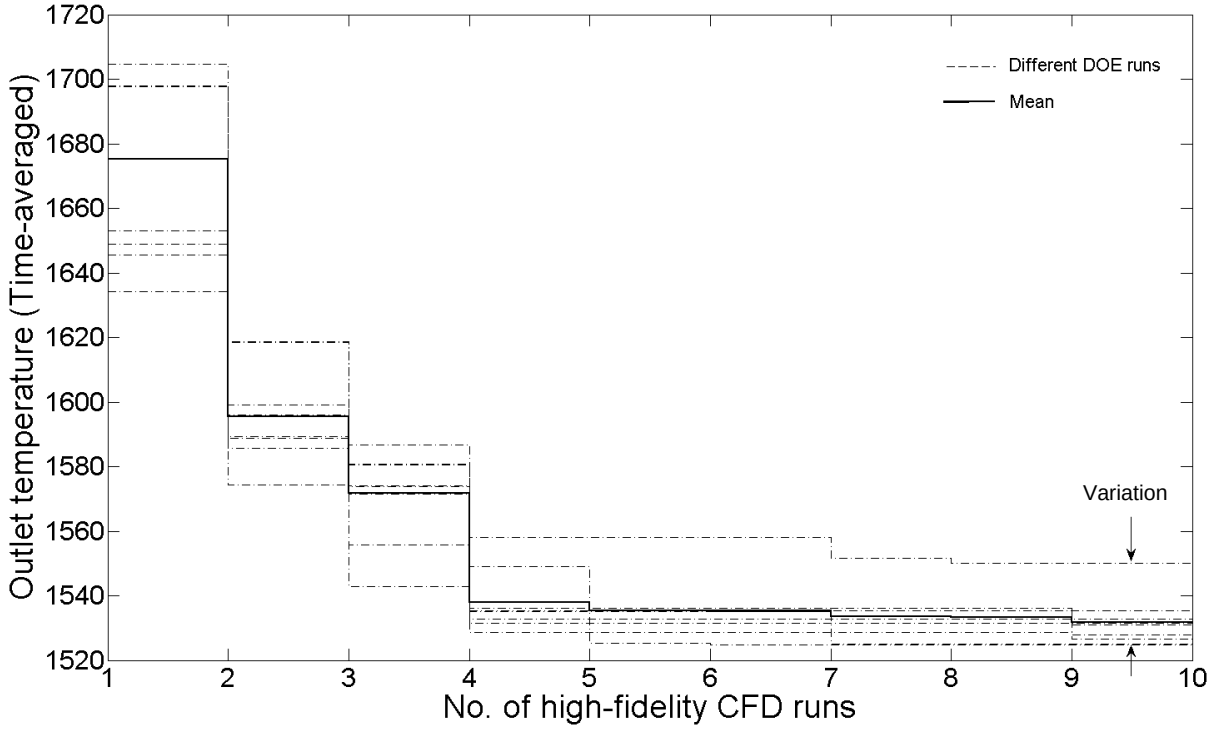

Fig. 6.32 Time-averaged area-weighted outlet temperature (K) optimisation search histories over a fixed computational budget of 10 high-fidelity CFD runs (4 in initial sample + 6 updates)

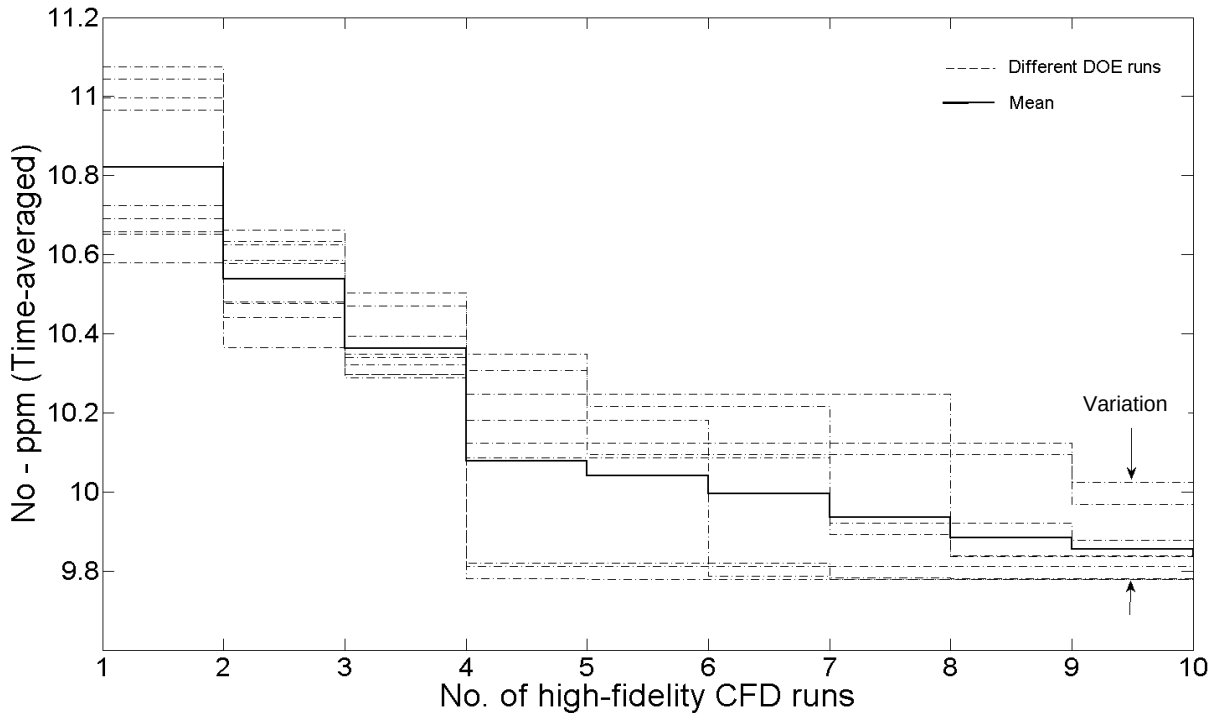

Fig. 6.33 Time-averaged area-weighted outlet thermal NO optimisation search histories over a fixed computational budget of 10 high-fidelity CFD runs (4 in initial sample + 6 updates)

Figures 6.32 and 6.33 shows the optimisation search histories for Kriging based design strategy using 9 different DOE samples (c.f. Figure 6.25) over a fixed computational budget of 10 high-fidelity CFD runs for time-averaged outlet temperature and thermal NO respectively. The mean convergence of all search histories is also shown in Figures 6.32 and 6.33.

Similar to the observation in the spatial domain design search histories (Figures 6.26 and 6.27) different initial samples do have an effect on the way the temporal domain Kriging optimisation process progresses. In Figures 6.32 and 6.33, each optimisation process leads to a different optimal design and a variation in the convergence behaviour of search histories can be seen at the end of the optimisation cycle.

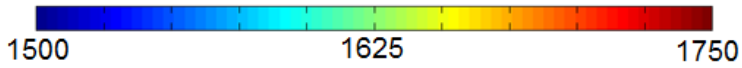

Kriging response surface using DOE sample no. 5 with best optimal design

(1) After DOE

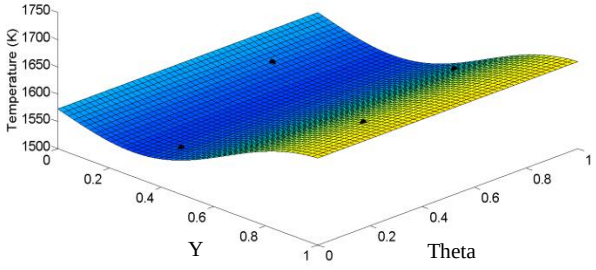

(2) After DOE + Updates

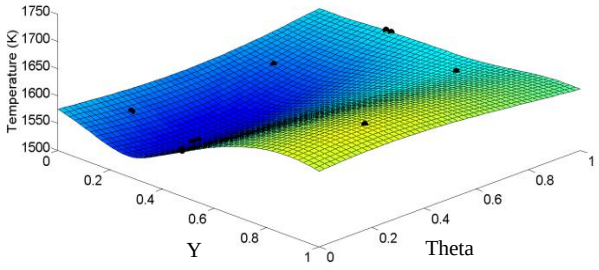

Kriging response surface using DOE sample no. 9 with worst optimal design

(3) After DOE

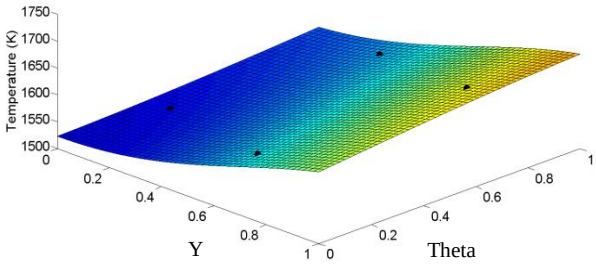

(4) After DOE + Updates

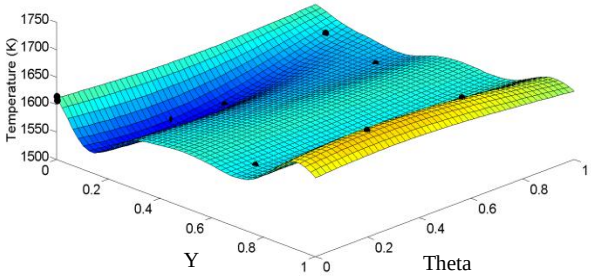

Fig. 6.34 Kriging response surfaces consisting of best and worst optimal designs for time-averaged area-weighted outlet temperature (K)

Figure 6.34 shows the Kriging response surfaces consisting of best and worst optimal designs for time-averaged area-weighted outlet temperature after both DOE stage and end of optimisation cycle. In comparison to 10x10 grid CFD evaluation based Kriging surface (c.f. Figure 6.18), response surface of experiment† 5 is more accurate compared to response surface captured using experiment 9, within fixed computational budget. This is a direct consequence of information available at the DOE stage. Hence, experiment five finds the best optimal design with the lowest objective function value of 1524.87 K.

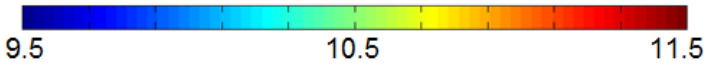

Kriging response surface using DOE sample no. 1 with best optimal design

(1) After DOE

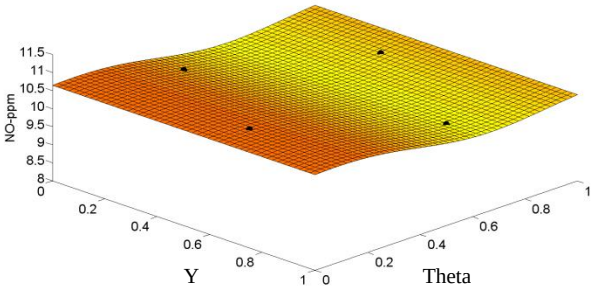

(2) After DOE + Updates

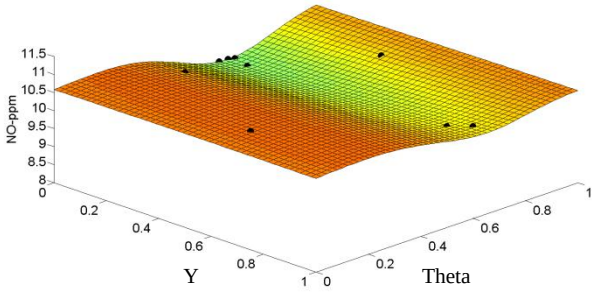

Kriging response surface using DOE sample no. 4 with worst optimal design

(3) After DOE

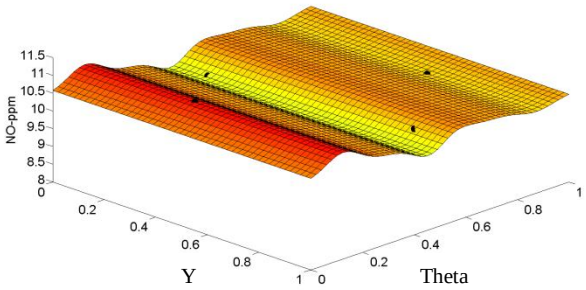

(4) After DOE + Updates

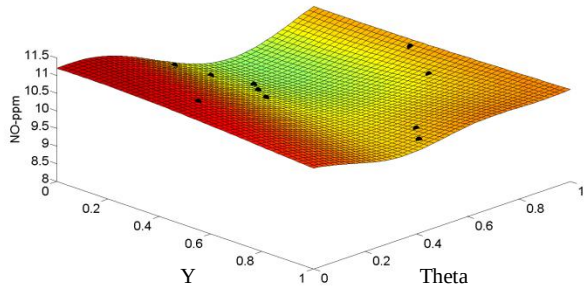

Fig. 6.35 Kriging response surfaces consisting of best and worst optimal designs for time-averaged area-weighted thermal outlet NO

Fig. 6.35 shows the Kriging response surfaces consisting of best and worst optimal designs for time-averaged outlet thermal NO. The response surface of experiment 1 correctly captures the shape of the response within the fixed computation budget compared to the Kriging surface constructed using 10x10 grid CFD evaluations (c.f. Figure 6.22). The response surface of experiment four† fails to capture the correct shape of the response within the fixed computational budget.

† See Appendix D for ranking of the DOE samples based on objective function values

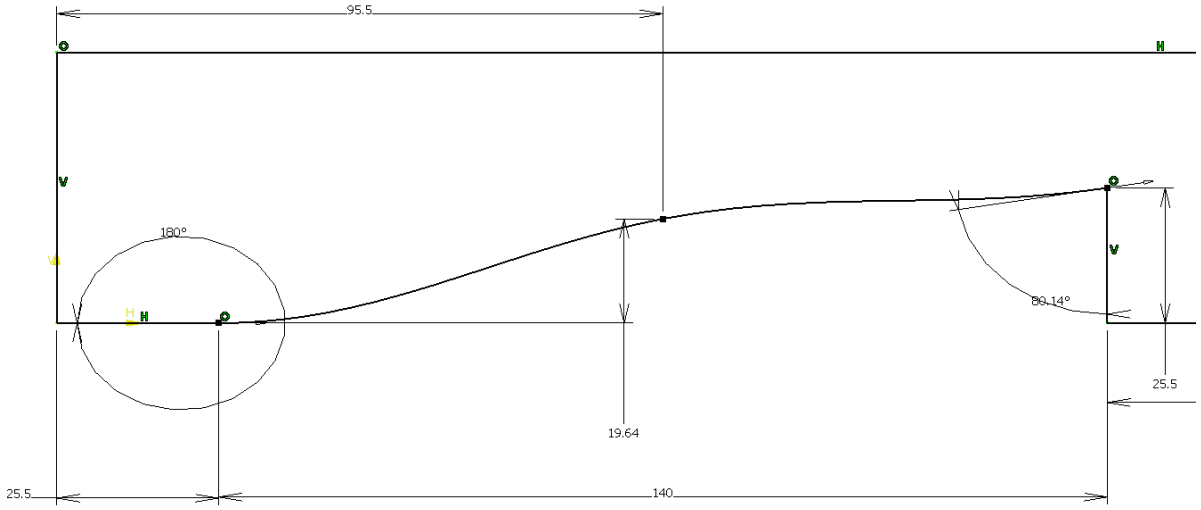

Fig. 6.36 Optimal flame-stabilizer step for time-averaged area-weighted outlet temperature optimisation at Y = 0.285 (19.64mm) and θ = 0.252 (80.14 degrees)

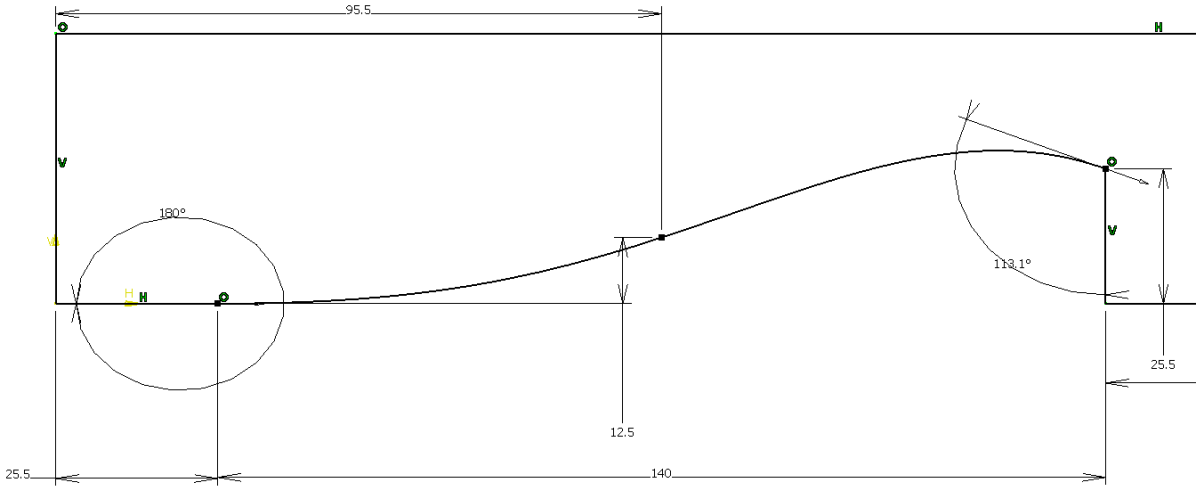

Fig. 6.37 Optimal flame-stabilizer step for time-averaged area-weighted outlet thermal NO optimisation at Y = 0 (12.50mm) and θ = 0.66 (113.1 degrees)

Figures 6.36 and 6.37 shows the optimal flame-stabilizer step designs obtained using Kriging design optimisation strategy in temporal domain for time-averaged area-weighted outlet temperature and thermal NO respectively.

The shapes of the best optimal designs agree closely with that of the optimal designs found using 10x10 grid CFD evaluations (c.f. Figure 6.19 for time-averaged outlet temperature and Figure 6.23 for time-averaged thermal NO).

6.6 Confidence assessment

The Kriging based design strategies, both in spatial and temporal domains, were applied on 9 different DOE samples with mean performance shown in Figures 6.26, 6.27, 6.32 and 6.33. It is the mean performance of different strategies which is of interest in this thesis. This mean is not the true mean (μ) but is an estimated mean (M) as it is based on a small sample of the real (unknown) population and is given by

$$M = \sum_{i=1}^{N} x_i \Big/ N \qquad \text{Eq. (6.6)}$$

where x_i is the individual sample value and N is the total number of samples (nine in this case).

Table 6.1 Relevant statistical estimates for all objective function data in spatial and temporal domains evaluated in section 6.5

Domain	Objective function	Mean (M)	Standard deviation	Standard error
Spatial	Outlet temperature profile RMSD	348.24	10.93	3.64
	Outlet thermal NO (ppm)	8.231	0.07	0.02
Temporal	Time-averaged outlet temperature (K)	1531.44	7.94	2.65
	Time-averaged outlet NO (ppm)	9.837	0.07	0.02

The estimated mean, obtained by Equation 6.6, varies with sample size N. In such a case it is important to estimate the accuracy of the sample or estimated mean (M). This is traditionally given by the estimated standard error (SE). Table 6.1 shows the relevant statistical estimates for all objective function data evaluated in this chapter. Figure 6.38 shows a representative variation in the estimated mean performance of the Kriging strategy for each objective function, over the optimisation cycle with increasing number of samples.

(a) Spatial domain outlet temperature

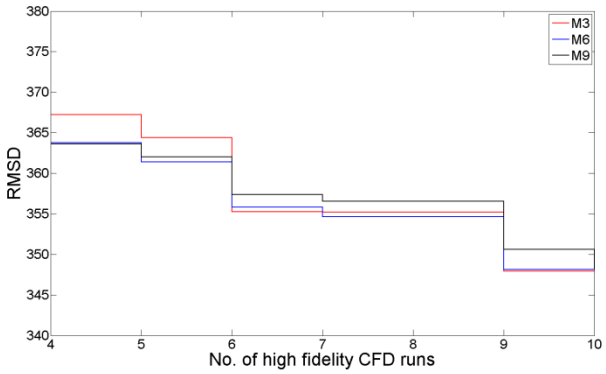

(b) Spatial domain outlet NO

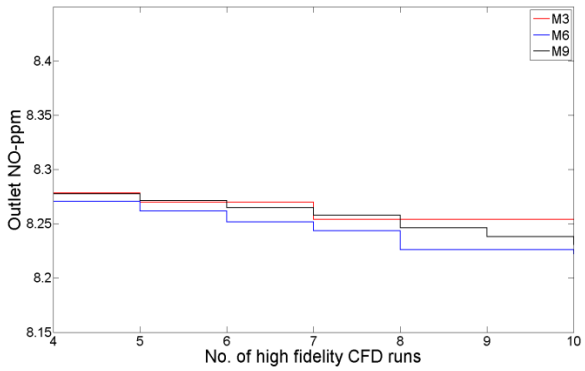

(c) Temporal domain outlet temperature

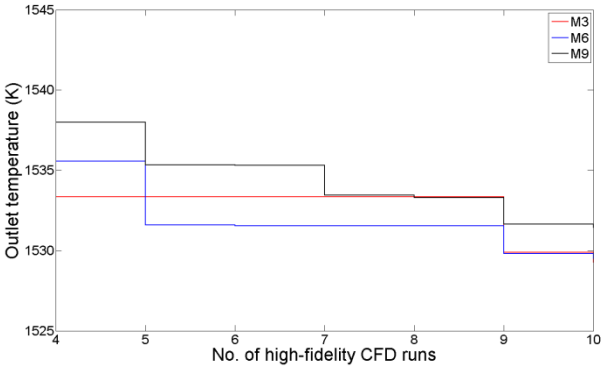

(d) Temporal domain outlet NO

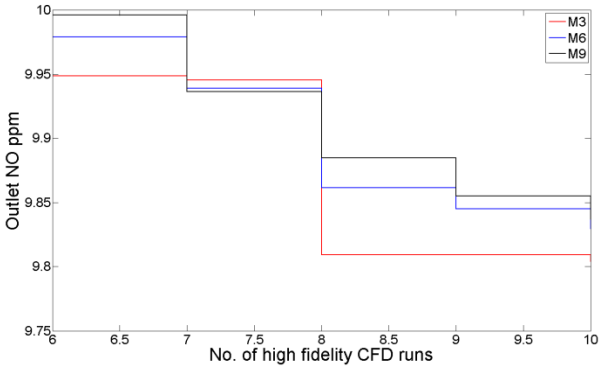

Fig. 6.38 Representative variation in estimated mean (M) due to increased number of samples (n = 3,6 and 9) in the estimation

If the sample size is large and the data is normally distributed around the estimated mean (M), then the standard confidence interval (CI) is (Efron and Tibshirani, 1993)

$$[M - z^{(1-\alpha)} . SE, M - z^{(\alpha)} . SE] \qquad \text{Eq. (6.7a)}$$

where $z^{(\alpha)}$ is the 100 * α (significance level) percentile point of a normal distribution and

$$\text{Confidence level} = 100.(1-2\alpha)\% \qquad \text{Eq. (6.7b)}$$

According to the standard normal table (Efron and Tibshirani, 1993), for 95% confidence level, $z^{(0.975)} = 1.964$ and $z^{(0.025)} = -1.964$.

Thus, 95% standard confidence interval (CI) for a normal distribution data is given by [M – 1.964. SE, M – 1.964. SE]

The use of Equation 6.6 is valid if the sample size is large enough and normally distributed. In this study (section 6.5), the sample size (N) is 9, which may or may not be large enough. More samples can be added to the data to increase the accuracy of estimation of the mean. Also, as the sample size grows the data becomes more normally distributed around the mean. However, adding more samples is expensive as the computation time of the entire design optimisation cycle is high.

Hence, to reduce the uncertainty associated with the accuracy of the estimated mean without adding more samples, the confidence level can be assessed using a bootstrap methodology.

6.6.1 Bootstrapping methodology – an overview

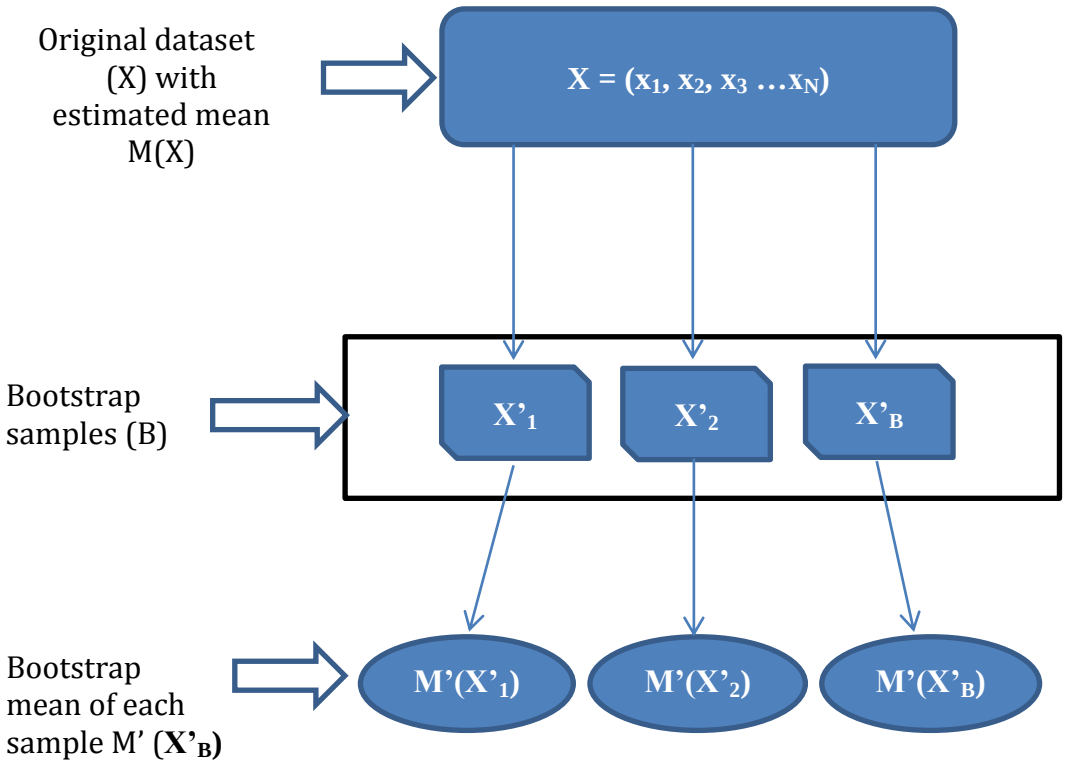

Fig. 6.39 Schematic of a bootstrap method for estimating bootstrap mean

Bootstrapping, originally invented by Efron (1979), is a way of using the current sample or experiment data to simulate what the result might be if the experiment was repeated over and over with new samples. It belongs to the general class of resampling methods.

The core idea of bootstrapping is random sampling-with-replacement from current sample. Figure 6.39 shows the idea behind the bootstrapping method.

Given an initial data set X of independent points $\mathbf{x_1, x_2, x_3 \ldots x_N}$, bootstrap samples B can be drawn at random-with-replacement, each a sample of size N, from N actual observations. For each bootstrap sample B, a bootstrap mean M' is computed. Using these bootstrap replications of mean, true population confidence intervals can be estimated using different bootstrap CI methods as detailed in Efron and Tibshirani (1993) e.g. bootstrap-t, percentile, BCa etc.

Bootstrap confidence intervals are computed in MATLAB version R2010a, which consists of an inbuilt bootstrap confidence interval routine which uses BCa bootstrap CI strategy.

BCa bootstrap stands for Bias-Corrected-and-accelerated bootstrap method. Derivation and more details of this method are given in Efron and Tibshirani (1979). The main reason to prefer this method is its suitability for small sample size data sets. Also, if the bootstrap distribution of sample mean is skewed and not consistent with normal distribution theory, other CI methods are very likely to be inaccurate whereas the BCa bootstrap CI method adjusts for this skewness (Efron and Tibshirani, 1993).

6.6.2 Bootstrapped confidence interval for Kriging based strategy

As the number of bootstrap samples B increases the accuracy of bootstrap computation also increases. Also the time required for this increased computation is much less than computing actual number of increased samples N.

The bootstrap sample size B for computing bootstrapped confidence interval (CI) is obtained from a convergence test. (Refer Appendix D for the results of convergence test for each objective function in spatial and temporal domain).

6.6.2.1 Spatial domain

Figures 6.40 and 6.41 shows the 95% CI on the estimated mean M and the original sample data points (N = 9) for steady outlet temperature profile RMSD and thermal NO respectively.

Using bootstrap CI routine in MATLAB and B = 5000, the 95% confidence interval for steady outlet temperature RMSD is [342.52, 356.15] whereas with B = 1000, the 95% confidence interval for steady outlet thermal NO is [8.19, 8.28].

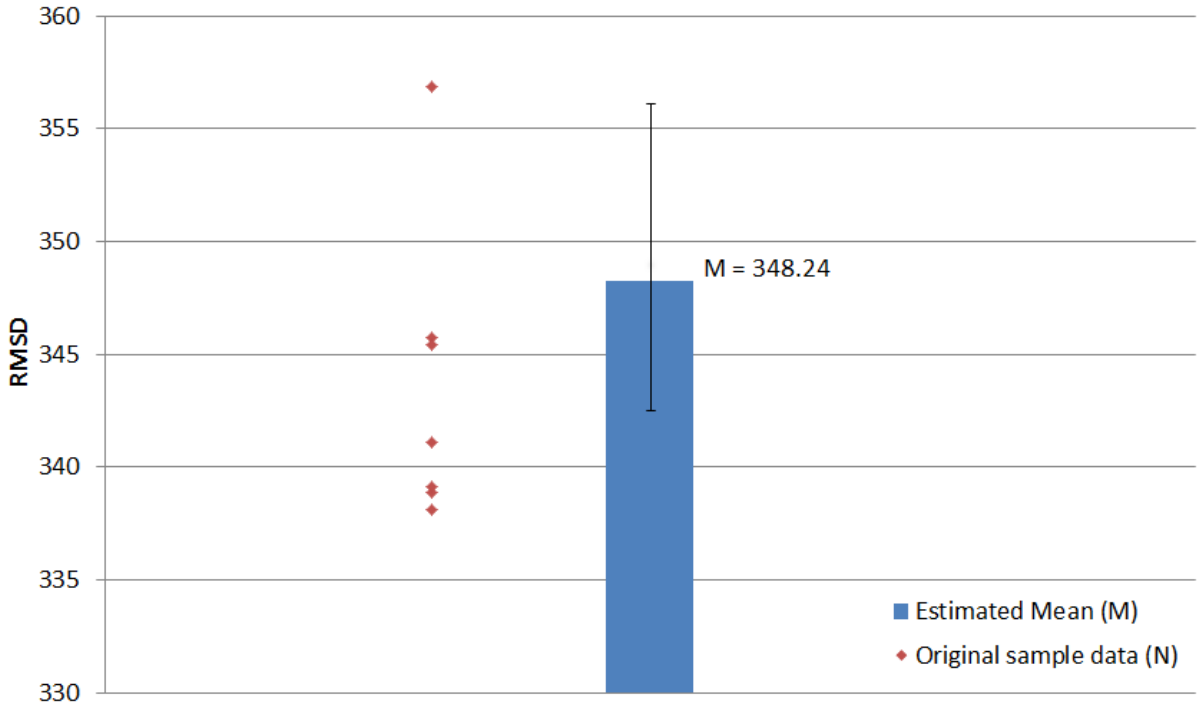

Fig. 6.40 Estimated mean with 95% confidence interval and original sample data points for steady outlet temperature profile RMSD

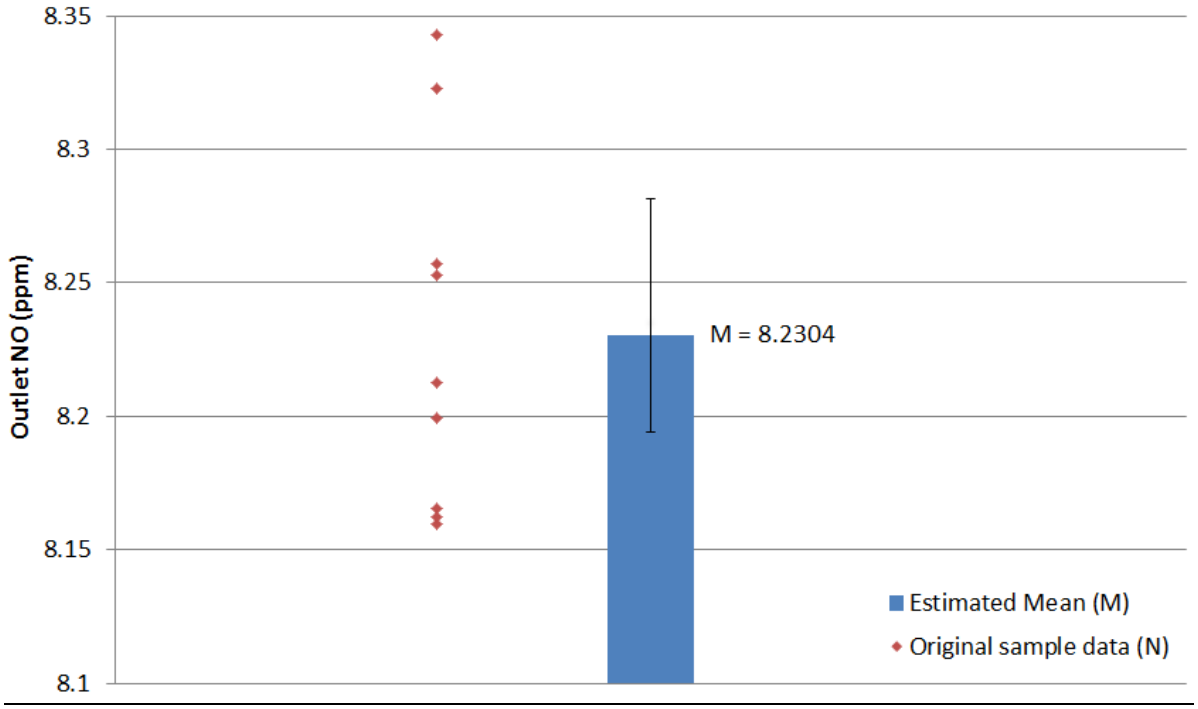

Fig. 6.41 Estimated mean with 95% bootstrapped confidence intervals and original sample data points for steady outlet thermal NO (ppm)

6.6.2.2 Temporal domain

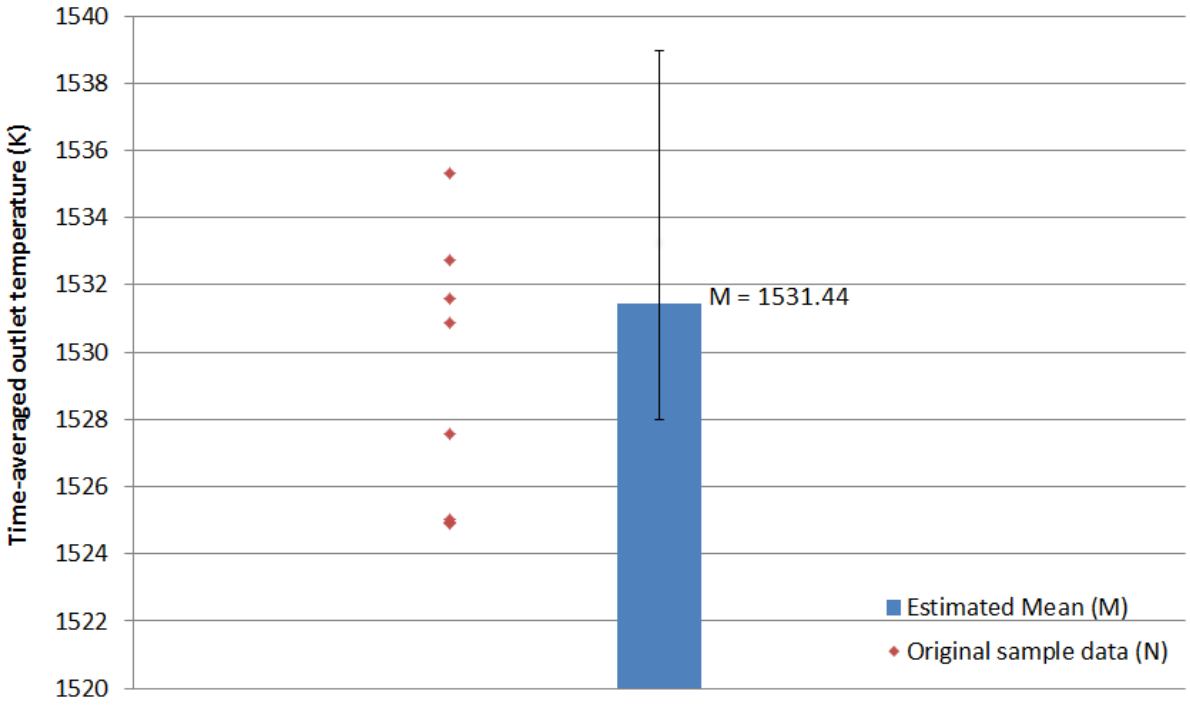

Fig. 6.42 Estimated mean with 95% confidence interval and original sample data points for time-averaged (area-weighted) outlet temperature (K)

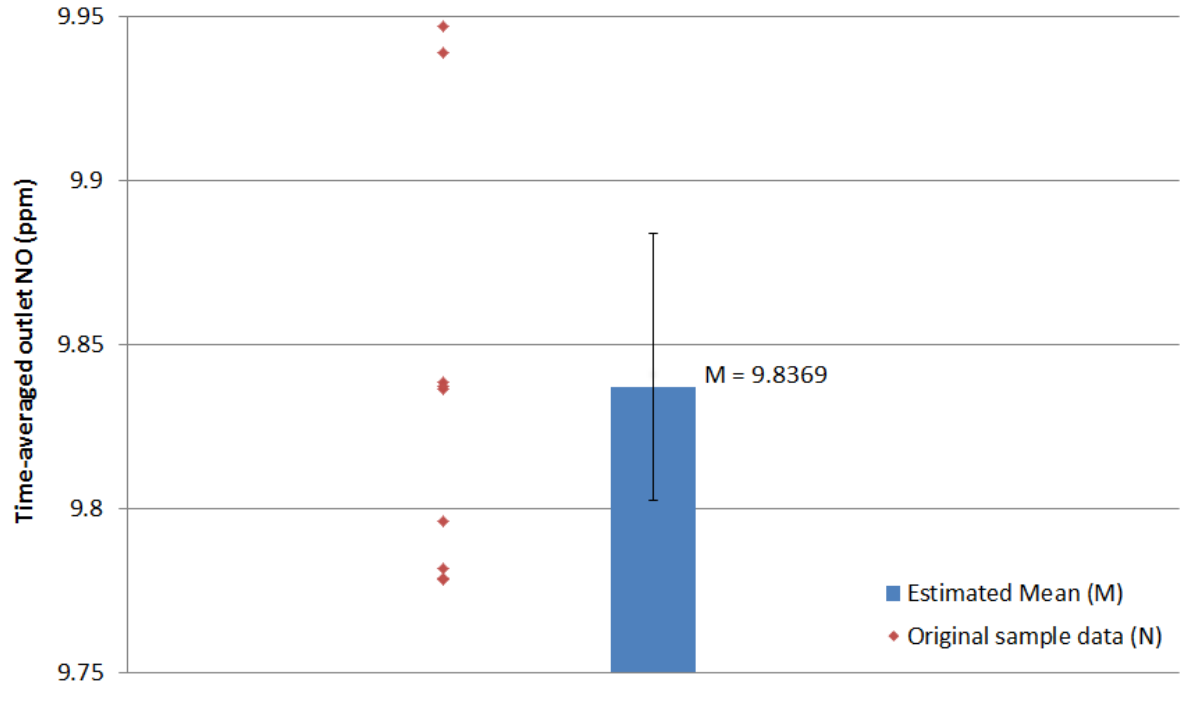

Fig. 6.43 Estimated mean with 95% confidence interval and original sample data points for time-averaged (area-weighted) outlet thermal NO (ppm)

Figures 6.42 and 6.43 shows the 95% CI on the estimated mean M and the original sample data points (N = 9) for time-averaged outlet temperature and thermal NO respectively.

Using bootstrap CI routine in MATLAB and B = 10000, the 95% confidence interval for time averaged outlet temperature is [1528, 1539] whereas with B = 5000, the 95% confidence interval for time-averaged outlet thermal NO is [9.80, 9.88].

6.7 Summary

A Kriging based design optimisation strategy was used to optimize the shape of a flame-stabilizer step in both spatial and temporal domains, using outlet temperature and NOx as the objective functions. The Kriging design strategy optimisation cycle was repeated on 9 different initial samples, which showed how the convergence search history varies, leading to different optimum designs. However, the statistics of interest is the mean performance of the strategy over all the samples. Since the sample size was small, and the mean is only an estimate of the true mean, a confidence assessment was performed on the Kriging design strategy results.

For this purpose, a bootstrap sampling methodology was used to simulate what the true mean might be if the design strategy was repeated over large number of times. Using the bootstrap mean distribution, confidence intervals for all four objective functions were derived. This is summarized in Table 6.2.

Table 6.2 Summary of 95% confidence intervals for Kriging strategy in spatial and temporal domains

Domain	Objective function	Sample mean (N = 9)	95% confidence interval	
			Lower limit	Upper limit
Spatial	Outlet temperature profile RMSD	348.24	342.52	356.15
	Outlet thermal NO (ppm)	8.230	8.19	8.28
Temporal	Time-averaged area-weighted outlet temperature (K)	1531.44	1528	1539
	Time-averaged area-weighted outlet thermal NO ppm	9.837	9.80	9.88

In the next chapter, the Kriging strategy confidence intervals form the basis for performance comparison against the newly developed co-Kriging based multi-fidelity design strategies, both in spatial and temporal domains.

Chapter 7

Co-Kriging based multi-fidelity strategy for combustor design

7.1 Introduction

In this chapter, various multi-fidelity strategies employing a co-Kriging surrogate modeling technique are developed and applied for combustor design in both spatial and temporal domains. In the spatial domain, outlet temperature profile RMSD and thermal NO are used as the objective functions whereas in the temporal domain, time averaged outlet thermal NO (ppm) is used as the objective function. The multi-fidelity strategies consist of two levels of fidelity, a fast but approximate low-fidelity (lo-fi) and an expensive but accurate high-fidelity (hi-fi) combustor solution, which are then used to construct a co-Kriging model. Various low-fidelity models are developed and tested in different combinations with a fixed high-fidelity model leading to the formation of CoTGL strategy in the spatial domain and CoSUS, CoTUS and CoSTUS strategies in the temporal domain. All strategies are run within fixed computational budgets and on multiple initial samples, to collect statistical data with mean convergence behaviour used as a performance indicator. A confidence assessment of the newly developed strategies is also performed and compared against the traditional Kriging based design strategy to identify potential benefits.

7.2 Co-Kriging based design optimisation strategy

Co-Kriging is essentially an extension of the original Kriging methodology (c.f. Section 2.5), and consists of correlating multiple sets of data. CFD simulations can be run at different levels of complexity, e.g. using two different levels of mesh resolution, such that there is a relatively accurate but slow analysis along with a fast but inaccurate analysis.

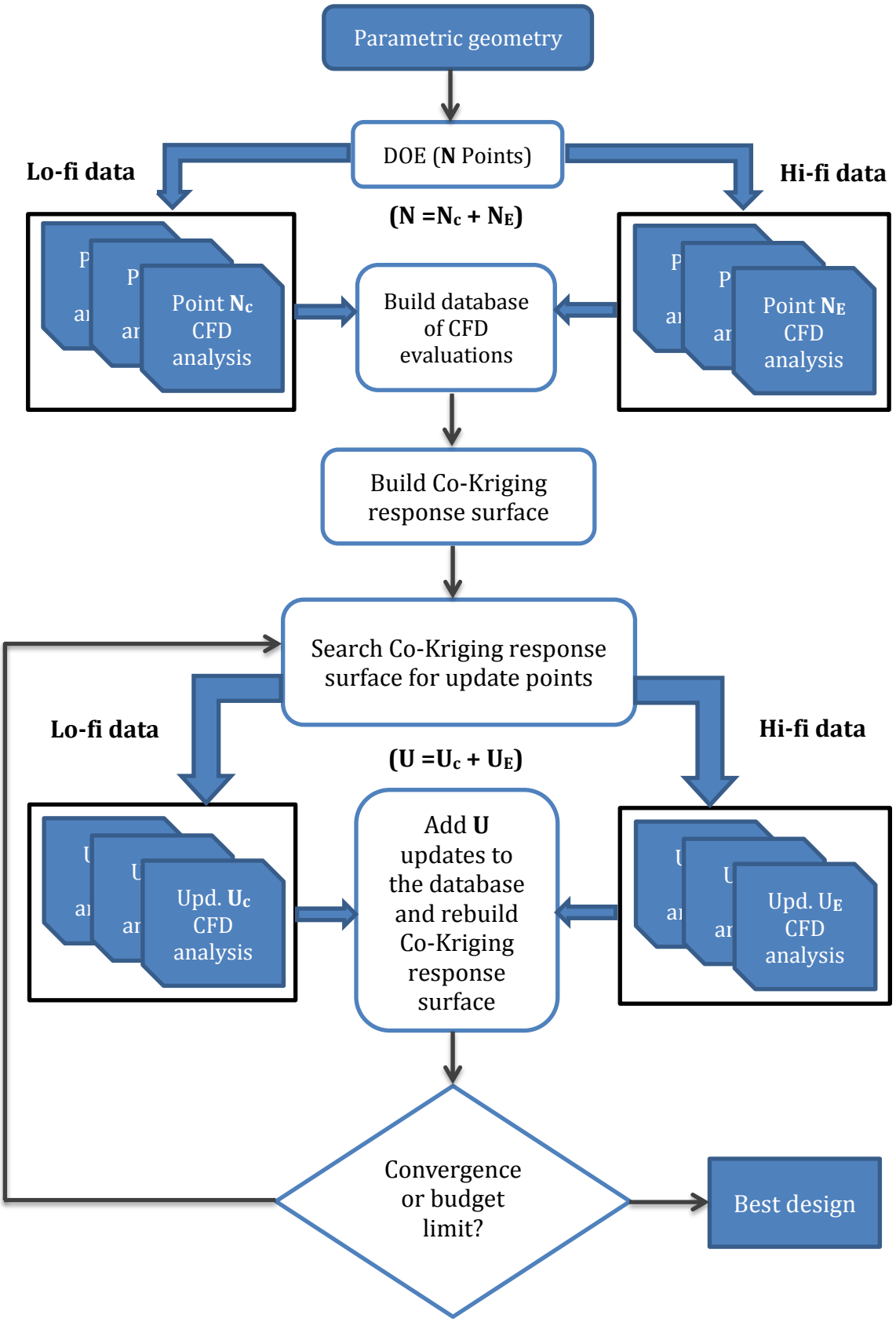

Fig. 7.1 Co-Kriging based multi-fidelity design optimisation strategy employing a DOE sampling plan and update points

However, in the context of design optimisation, these fast approximations, though somewhat inaccurate, may well include important flow-field features and can be used for design search investigation. To improve the efficiency of high-fidelity surrogate based design optimisation systems (c.f. Figure 6.1), a greater quantity of fast (or cheap) analyses can be used in combination with a smaller number of expensive accurate analyses, in a multi-fidelity co-Kriging methodology, to enhance the accuracy of the high-fidelity function surrogate model at a lower computational cost.

Figure 7.1 shows a co-Kriging response surface model based design optimisation strategy with $\mathbf{N_C}$ (cheap) and $\mathbf{N_E}$ (expensive) DOE points and $\mathbf{U_C}$ (cheap) and $\mathbf{U_E}$ (expensive) update points per update cycle, where $\mathbf{N_C} > \mathbf{N_E}$ and $\mathbf{U_C} > \mathbf{U_E}$. $\mathbf{N_E}$ DOE points and $\mathbf{U_E}$ updates are the subsets of $\mathbf{N_C}$ and $\mathbf{U_C}$ respectively. Starting with an initial set of $\mathbf{N_C}$ and $\mathbf{N_E}$ DOE points, a combined database of objective function values is constructed. Based on these observations, a co-Kriging response surface model is built†. Further, to increase the accuracy of the co-Kriging response surface model, update points are selected at either or all locations of the co-Kriging (a) best prediction, (b) maximum prediction error and (c) maximum expected improvement. Also, the update points $\mathbf{U_C}$ and $\mathbf{U_E}$ are evaluated in parallel and the co-Kriging RSM is re-built and searched for optimal designs. This process is iterated until response surface model convergence or the end of a given computational budget.

7.2.1 Spatial domain – Co-Kriging using two different grid levels (CoTGL)

For co-Kriging in the spatial domain, two different levels of grid (or spatial) resolutions are used. The fine grid resolution is used as the expensive high-fidelity model and the coarse grid resolution is used as the cheap low-fidelity model. In order to apply co-Kriging based design optimisation strategy for two different grid levels (CoTGL), the computational cost ratio between the cheap low-fidelity (C) and expensive high-fidelity model (E) is used as the basis for determining the total number of CFD evaluations.

Table 7.1 Relative budget of Kriging and CoTGL strategies for spatial domain outlet temperature profile RMSD and thermal NO optimisation

Strategy	Given budget for high-fidelity CFD runs	Total no. of high-fidelity CFD runs performed	Cost ratio	Total no. of low-fidelity CFD runs performed
Kriging	10	10	-	-
CoTGL	10	7	$E \approx 10C$	30

Table 7.1 shows the details of the CoTGL strategy budget relative to the standard Kriging strategy (applied in Chapter 6) for design optimisation in the spatial domain.

7.2.2 Temporal domain

† See Appendix E

For co-Kriging in the temporal domain, various low-fidelity models in combination with a fixed high-fidelity model are used, leading to multiple co-Kriging based design strategies. These are detailed as follows:

7.2.2.1 CoSUS: Co-Kriging using steady and unsteady RANS simulations: For CoSUS, a low-fidelity model using steady RANS simulations and a high-fidelity model using URANS with Δt = 1e-05s is used. The spatial grid resolution is fixed for both fidelities.

7.2.2.2 CoTUS: Co-Kriging using different time-step sizes of unsteady RANS simulations: For strategy CoTUS, coarse and fine time-step sizes URANS simulations are used as low and high fidelity models respectively, with the same spatial grid resolutions. Two different low-fidelity models are assessed in combination with a fixed high-fidelity model. The two different combinations are:

[a] lo-fi model: URANS with Δt = 5e-05s and hi-fi model: URANS with Δt = 1e-05s
[b] lo-fi model: URANS with Δt = 2e-05s and hi-fi model: URANS with Δt = 1e-05s

7.2.2.3 CoSTUS: Co-Kriging using varying spatio-temporal unsteady RANS simulations: In strategy CoSTUS, a coarse spatial and temporal grid URANS simulation is used as the low-fidelity model. The high-fidelity model is the fine spatial and temporal grid URANS simulation. The different grid sizes are chosen from Table 5.2.

- lo-fi model: URANS with Δt = 1e-04s and grid size of ~11000 cells (mesh 1)
- hi-fi model: URANS with Δt = 1e-05s and grid size of ~180000 cells (mesh 3)

Table 7.2 shows the details of the computational budget for these co-Kriging design strategies in the temporal domain relative to the standard Kriging strategy (applied in Chapter 6) for the time-averaged outlet thermal NO objective function.

Table 7.2 Relative budget of Kriging and various multi-fidelity strategies for time-averaged outlet thermal NO optimisation

	Method	Given budget for high-fidelity CFD runs	Total no. of high-fidelity CFD runs performed	Cost ratio	Total no. of low-fidelity CFD runs performed
	Kriging	10	10	-	-
(1)	**CoSUS**	10	7	E ≈ 5C	15
(2)	**CoTUS** – (a)	10	7	E ≈ 4C	12
(3)	**CoTUS** – (b)	10	7	E ≈ 2C	6
(4)	**CoSTUS**	10	7	E ≈ 18C	54

7.2.3 DOE and update points strategy

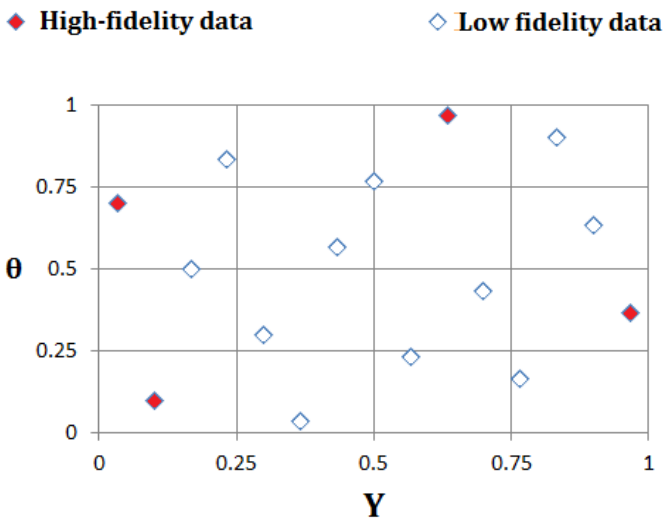

Fig. 7.2 CoTGL strategy sample

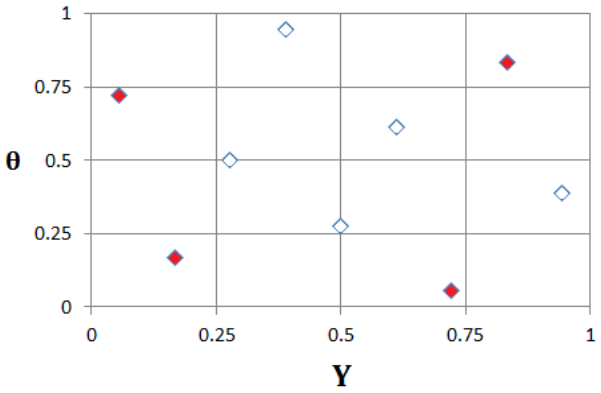

Fig. 7.3 CoSUS strategy sample

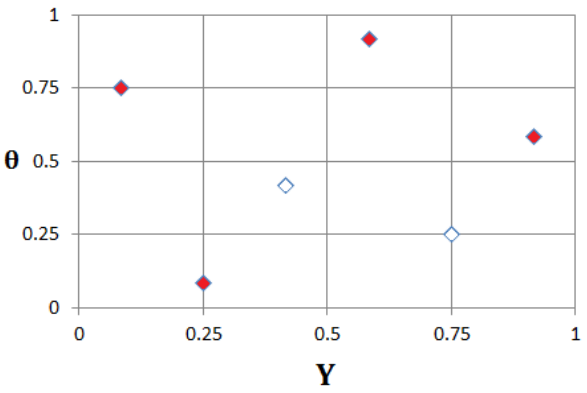

Fig. 7.4 CoTUS-(a) strategy sample

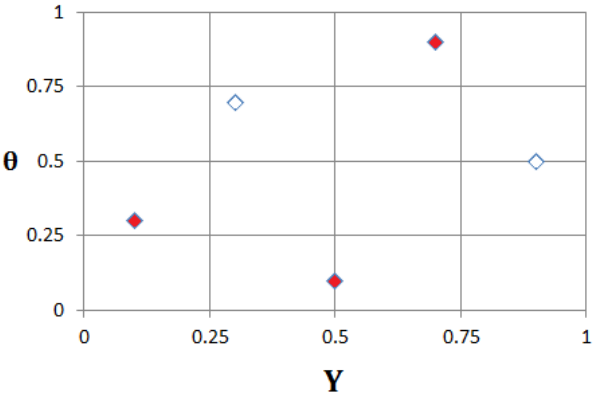

Fig. 7.5 CoTUS-(b) strategy sample

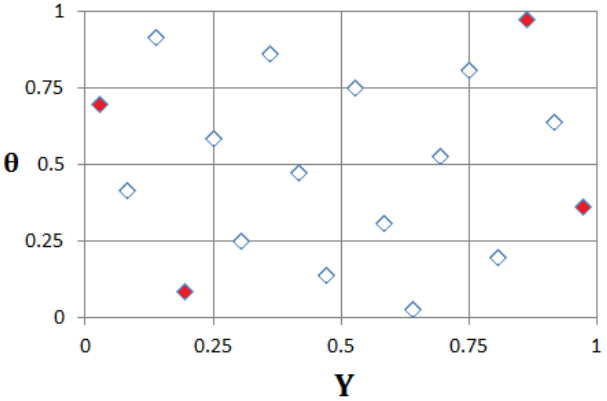

Fig. 7.6 CoSTUS strategy sample

To initialize each design study, DOE sample points are generated using an optimal Latin-Hypercube sampling (LHS) method. As shown in Table 7.2, the total number of high-fidelity CFD runs over the optimisation cycle is limited to seven for all co-Kriging strategies. The remaining three high-fidelity runs are replaced by equivalent number of low-fidelity runs, as determined by the cost ratio between the low and high fidelity model for each co-Kriging strategy.

Table 7.3 High and low fidelity CFD runs budget distribution for different co-Kriging design strategies over DOE and update cycle stage
[Note: N_e and U_e in bold, N_c and U_c in brackets, EI: expected improvement update, BP: best predicted update, ER: maximum error update]

	Method	DOE	Update cycle 1	Update cycle 2	Update cycle 3
	Kriging	**4**	**2**	**2**	**2**
(1)	**CoTGL**	**4**(15)	**1**(5) (1 EI, 2 BP, 2 ER)	**1**(5) (1 EI, 2 BP, 2 ER)	**1**(5) (1 EI, 2 BP, 2 ER)
(2)	**CoSUS**	**4** (9)	**1**(2) (1 EI, 1 BP)	**1**(2) (1 EI, 1BP)	**1**(2) (1 EI, 1BP)
(3)	**CoTUS** – (a)	**4**(6)	**1**(2) (1 EI, 1 BP)	**1**(2) (1 EI, 1 BP)	**1**(2) (1 EI, 1 BP)
(4)	**CoTUS** – (b)	**3**(5)	**1**(1) (1 EI)	**1**(1) (1 EI)	**1**(1) (1 EI)
(5)	**CoSTUS**	**4**(18)	**1**(12) (1 EI, 5 BP, 6 ER)	**1**(12) (1 EI, 5 BP, 6 ER)	**1**(12) (1 EI, 5 BP, 6 ER)

Table 7.3 shows the distribution of total number of high and low fidelity CFD runs over four stages (DOE and three update cycles) for each co-Kriging design strategy. Four high fidelity CFD runs are evaluated at the DOE stage, except for the CoTUS-(b) strategy which consists of three high-fidelity CFD runs. In parallel to these high-fidelity CFD runs, several low-fidelity runs are evaluated (c. f. Table 7.3). Figures 7.2 to 7.6 show the representative DOE samples generated for design strategy CoTGL in spatial domain and strategies CoSUS, CoTUS-(a) and (b) and CoSTUS in temporal domain. Nine such DOE samples for each strategy are generated†. Low-fidelity data is evaluated at all DOE points, whereas the sampling points where high-fidelity data is evaluated are a subset of the full DOE and shown in red. Table 7.3 also gives the details of the update points generated per update cycle. The high fidelity CFD run, per update cycle, is only run at the expected improvement update point.

† See Appendix E for all nine initial samples for each strategy in Table 7.3

7.3 Results and discussions

To test the effectiveness of strategies based on co-Kriging response surface model, initially, strategy CoTGL is applied for combustor design optimisation in the spatial domain for outlet temperature profile RMSD and thermal NO.

Later, strategies CoSUS, CoTUS and CoSTUS are applied to design the combustor in the temporal domain for time-averaged outlet thermal NO. All strategies are applied using a fixed computational budget for low and high fidelity models as listed in Table 7.3. Each strategy is repeated nine times with different initial DOE samples. The results obtained using these multi-fidelity design strategies is also compared against the standard Kriging based design strategy (applied in Chapter 6) to assess their performance.

7.3.1 Co-Kriging based design optimisation in spatial domain using two different grid levels (CoTGL)

7.3.1.1 Outlet temperature profile RMSD

Figure 7.7 shows the steady outlet temperature RMSD optimisation search histories for CoTGL design strategies, using nine different DOE samples, over a fixed computational budget of seven high-fidelity and thirty low-fidelity CFD runs (c.f. Table 7.1). It also shows the mean performance of all the search histories. The DOE evaluation consists of four high-fidelity and fifteen low-fidelity CFD runs. Further, the three update cycles consists of three high-fidelity and fifteen low-fidelity CFD runs in total (c.f. Table 7.3). Similar to the Kriging strategy optimisation histories (c.f. Figure 6.26), the different initial samples lead to different information being available at the DOE stage leading to variations in altered CoTGL model convergence behaviour. Hence, each optimisation cycle leads to a different optimal design. Figure 7.7 also shows the variation in the search histories at the end of the optimisation budget.

Figure 7.8 shows the comparison between the mean of optimisation search histories of Kriging and CoTGL strategies for steady outlet temperature profile RMSD. The CoTGL strategy mean performance is as good as Kriging strategy mean by the end of the fixed computational budget. However, after the DOE stage (four high-fidelity CFD runs), the CoTGL strategy mean is below the Kriging strategy mean, thus demonstrating the potential of the CoTGL strategy to find a good design earlier in the design process.

Figure 7.9 shows the comparison between response surfaces of CoTGL and Kriging strategies, for their respective experiments containing the best optimal designs, after both DOE stage and end of the optimisation cycle stage. The ranking of the DOE samples based on the final outlet temperature RMSD values is listed in Appendix E.

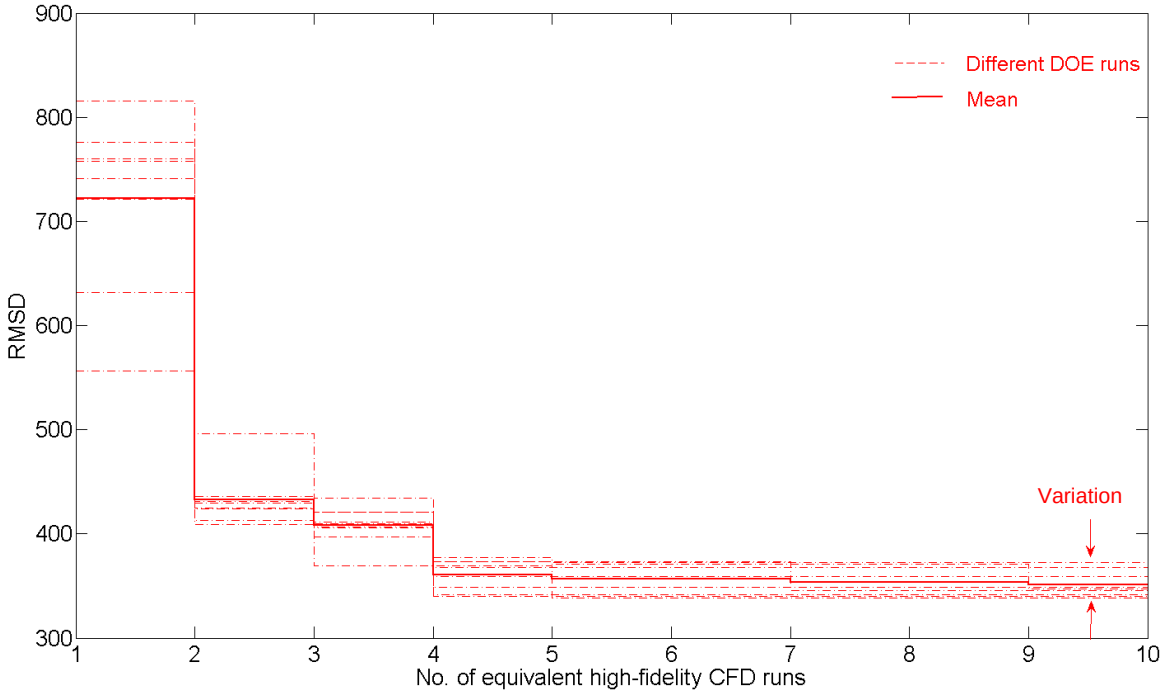

Fig. 7.7 Steady outlet temperature profile RMSD optimisation search histories† using CoTGL over a fixed computational budget (c.f. Table 7.3)

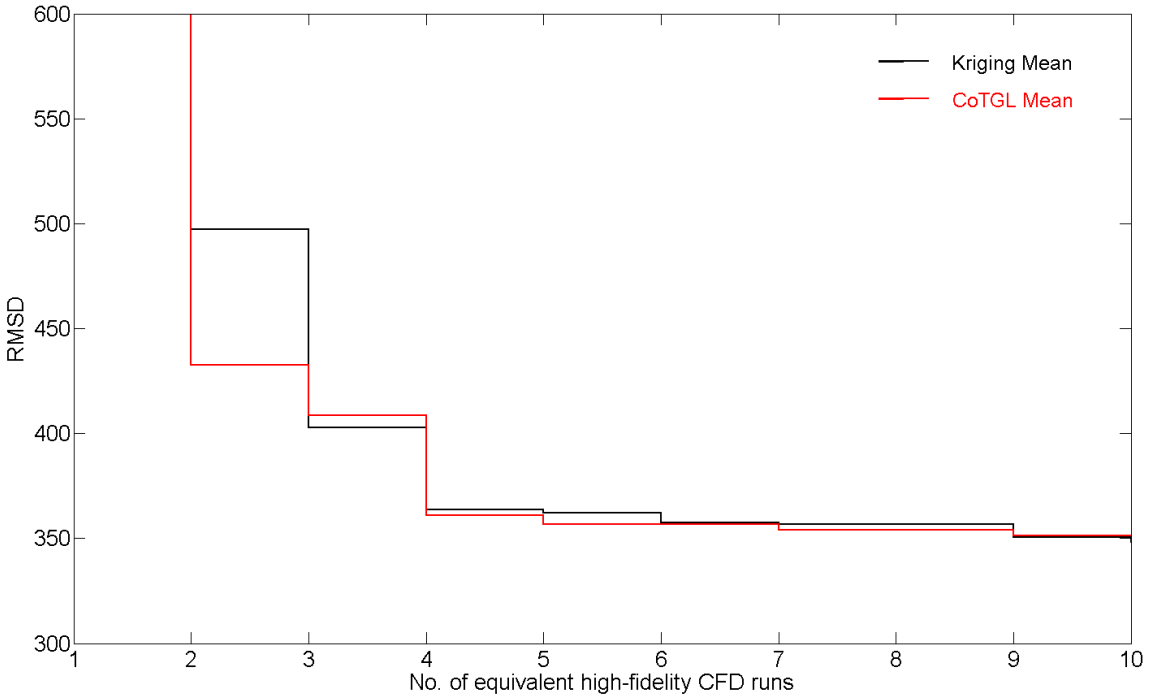

Fig. 7.8 Comparison between mean optimisation search histories of Kriging and CoTGL strategies for steady outlet temperature profile RMSD

† The X-axis, here and in subsequent co-Kriging based strategies, represents the number of equivalent high- fidelity runs, which is seven high-fidelity plus other low-fidelity runs.

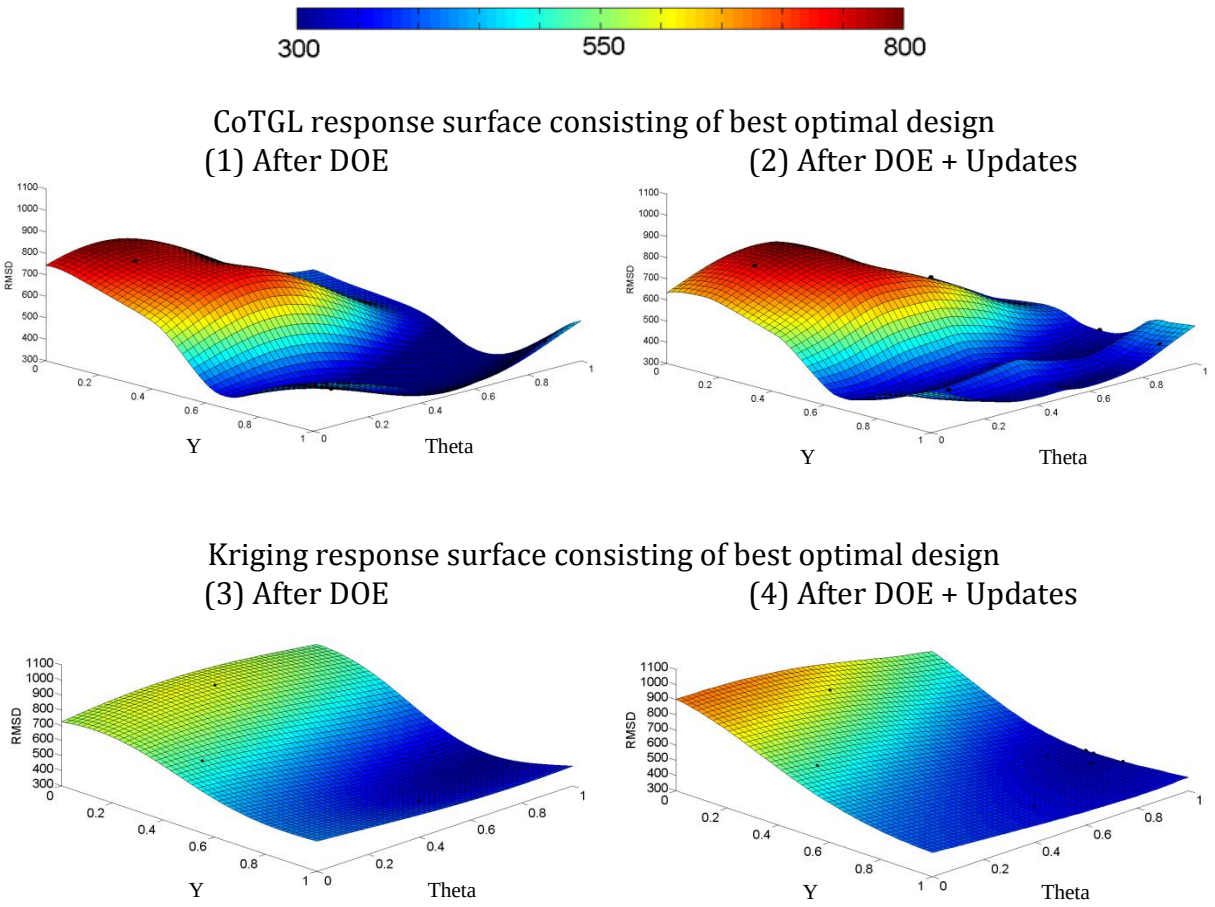

Fig. 7.9 Comparison between CoTGL and Kriging response surfaces consisting of their respective best optimal designs for steady outlet temperature profile RMSD

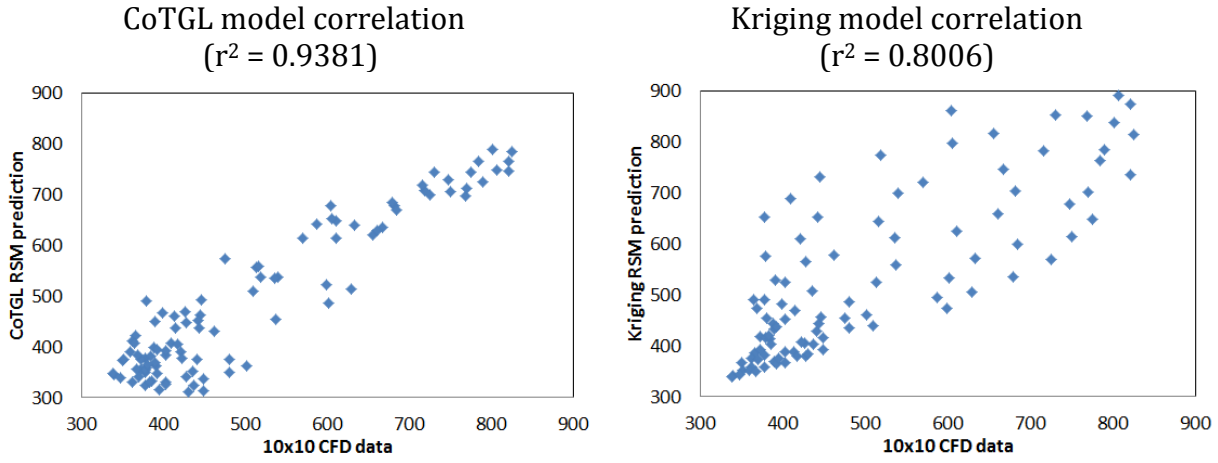

Fig. 7.10 Comparison between CoTGL and Kriging RSM (after DOE + Updates) correlation with 10x10 CFD data for steady outlet temperature profile RMSD

In comparison to the shape of the response surface captured using 10x10 grid CFD evaluations (c.f. Figure 6.10), the CoTGL response surfaces, both after DOE [Figure 7.9(1)] and updates [Figure 7.9(2)] appears more globally accurate, compared to the Kriging response surfaces in Figures 7.9(3) and 7.9(4) respectively. This is because of the availability of a greater quantity of information from the low-fidelity model in CoTGL, which enhances the accuracy of the global response surface.

Figure 7.10 shows the comparison between the correlation of CoTGL and Kriging RSM predictions (at the end of the computational budget) relative to the 10x10 CFD data. As per the scatterplots of Figure 7.10, the CoTGL RSM prediction is more linearly related to the 10x10 CFD data compared to Kriging RSM prediction. The CoTGL model has r^2=0.938 which is higher than Kriging model r^2=0.8. The value of r^2, known as co-efficient of determination, represents a measure of how good the models predictive capabilities are. This quantitatively shows that the CoTGL response surface model is more globally accurate.

Table 7.4 Comparison between the best optimal designs found by Kriging and CoTGL strategies for steady outlet temperature profile RMSD

	Y	Θ	Outlet temperature profile RMSD
Kriging	0.600	1	338.08
CoTGL	0.638	1	338.22

Table 7.4 shows the comparison between the best optimal designs obtained by Kriging and CoTGL strategies within the fixed computational budget. The lowest RMSD value design configuration is found by the Kriging strategy.

7.3.1.2 Outlet thermal NO (ppm)

Figure 7.11 shows the steady outlet thermal NO optimisation search histories for CoTGL design strategies along with the mean performance of all the search histories using nine different DOE samples; over a fixed computational budget of seven high-fidelity and thirty low-fidelity CFD runs (c.f. Table 7.1). Similar to the observations for the CoTGL strategy for steady outlet temperature RMSD, the different initial samples cause variations in CoTGL model convergence due to different information being available at the DOE stage. Hence, different optimal designs are obtained at the end of each optimisation cycle. Figure 7.11 also shows the variation in the convergence across the different experiments at the end of the budget.

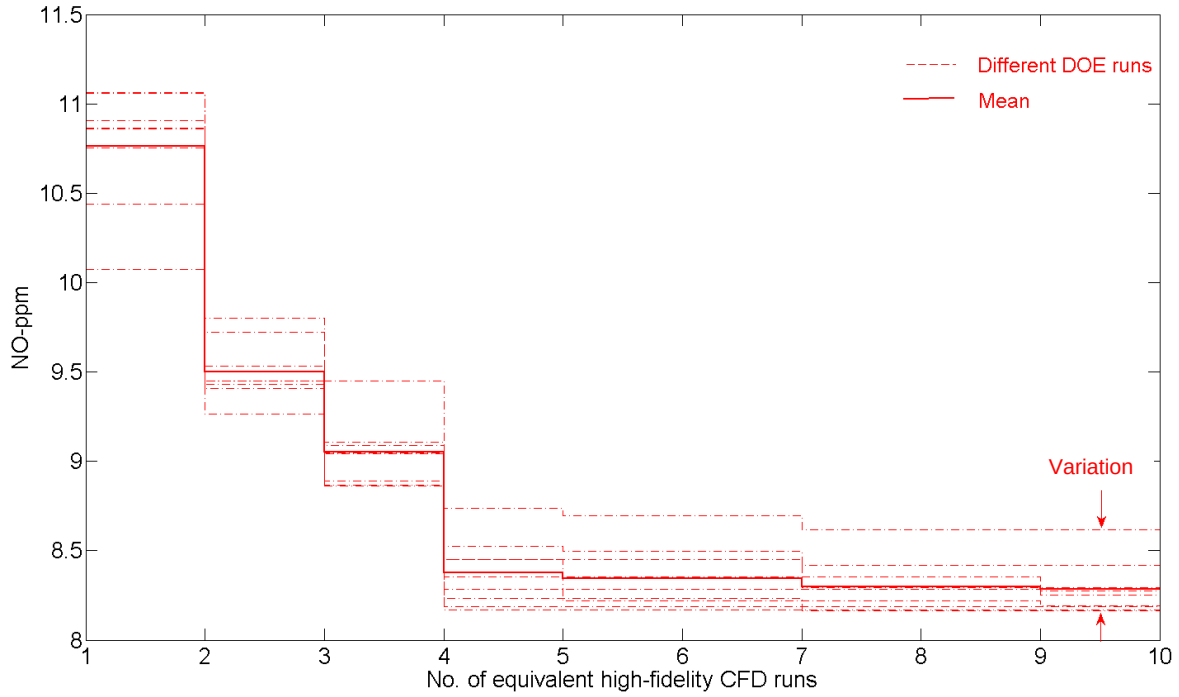

Fig. 7.11 Steady outlet thermal NO optimisation search histories using CoTGL over a fixed computational budget (c.f. Table 7.3)

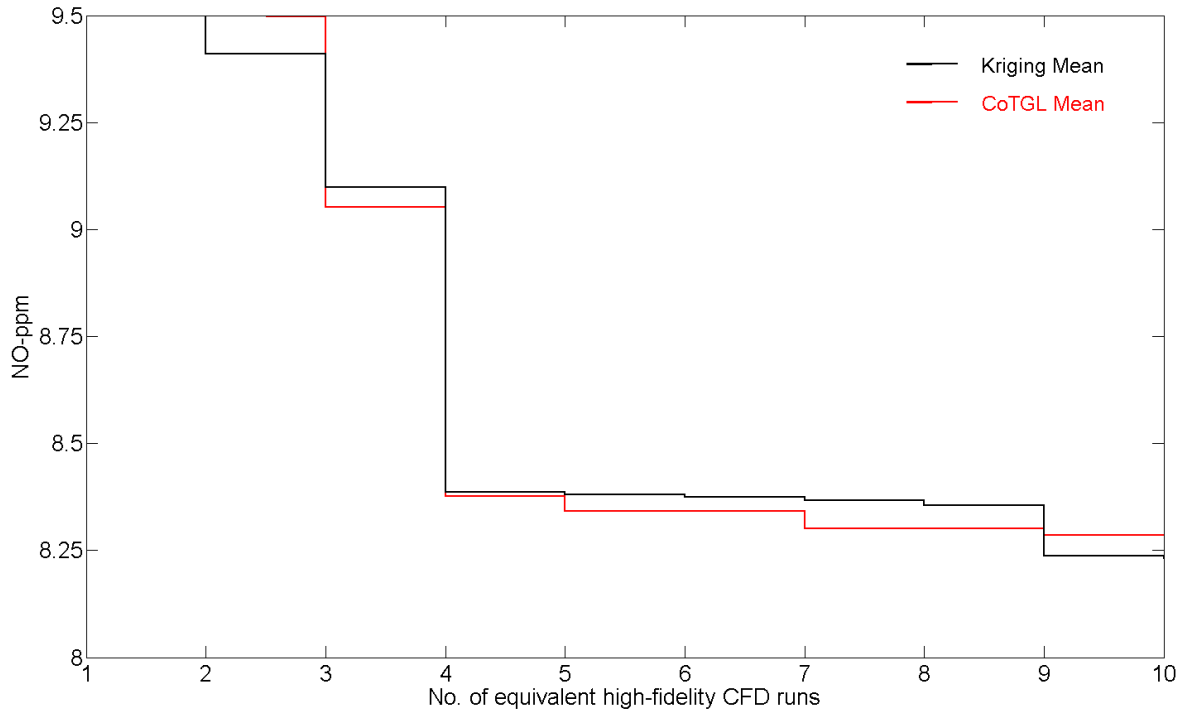

Fig. 7.12 Comparison between mean optimisation search histories of Kriging and CoTGL strategies for steady outlet thermal NO

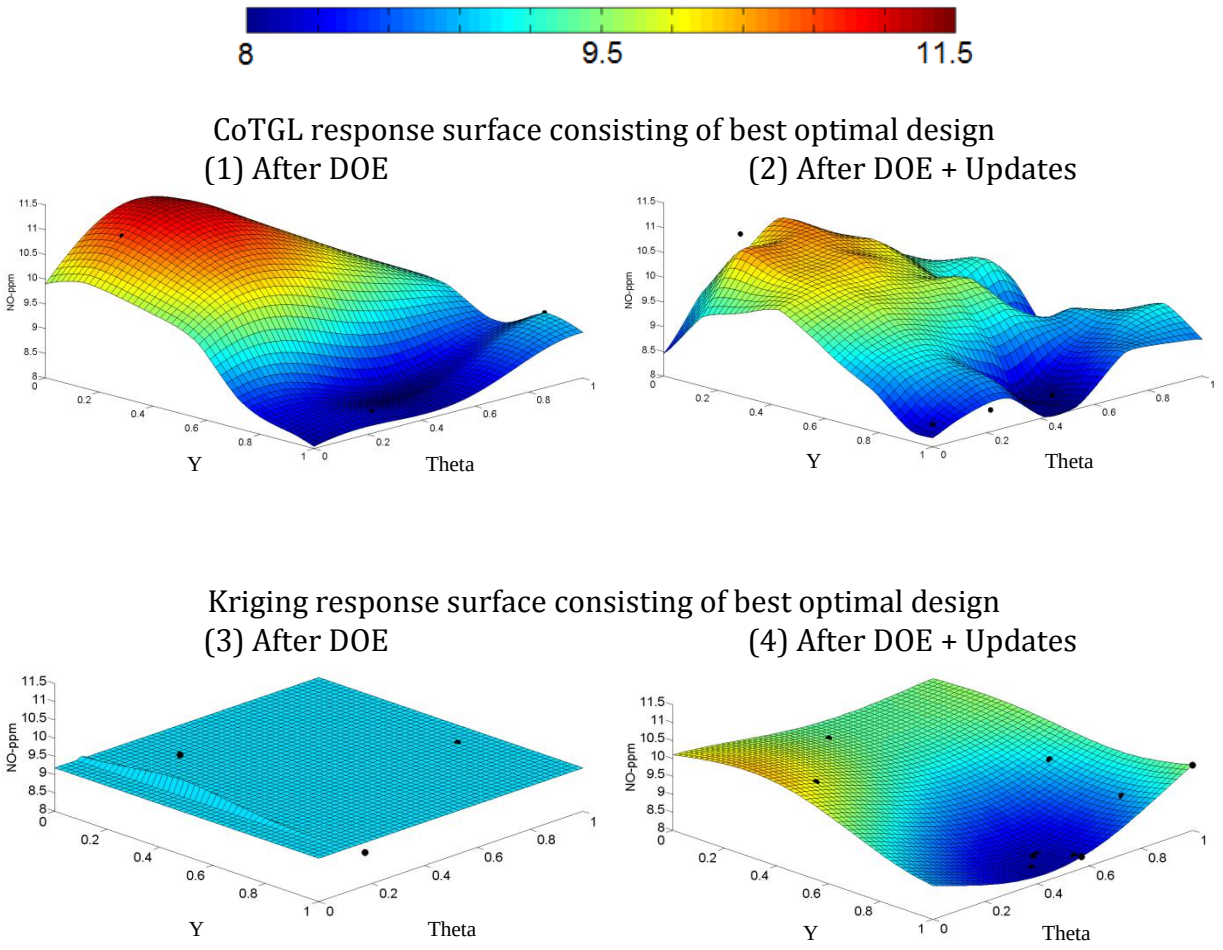

Fig. 7.13 Comparison between CoTGL and Kriging response surfaces consisting of their respective best optimal designs for steady outlet thermal NO (ppm)

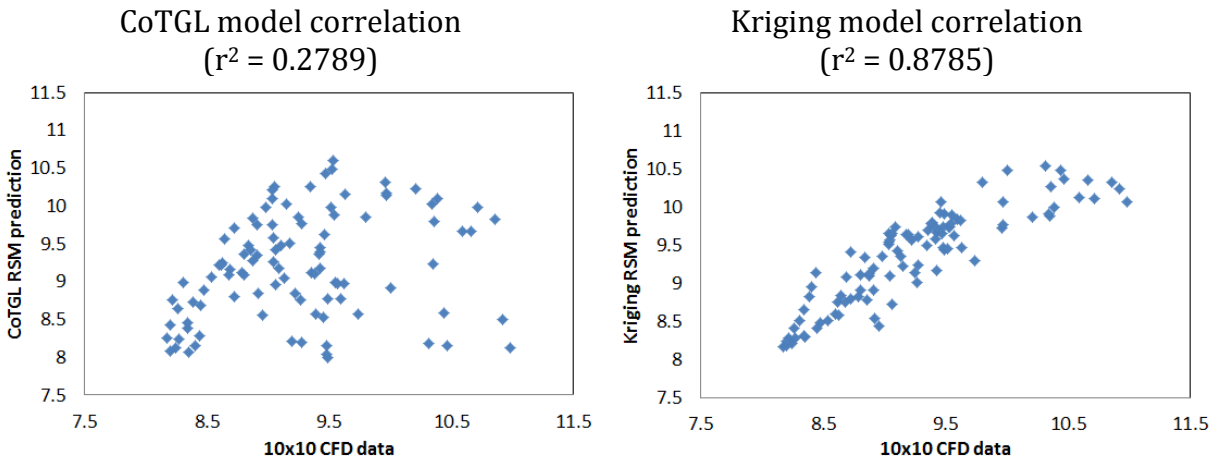

Fig. 7.14a Comparison between correlations of CoTGL and Kriging RSM (after DOE + Updates) predictions with 10x10 CFD data for steady outlet thermal NO (ppm)

Table 7.5 Comparison between the best optimal designs found by Kriging and CoTGL strategies for steady outlet thermal NO

	Y	Θ	Outlet thermal NO (ppm)
Kriging	0.933	0.446	8.159
CoTGL	0.913	0.529	8.164

Figure 7.12 shows the comparison between the mean of optimisation search histories of Kriging and CoTGL strategies for steady outlet thermal NO. The CoTGL strategy does not perform better than the Kriging strategy in terms of mean convergence at the end of the fixed computational budget. However, similar to CoTGL mean for outlet temperature profile RMSD, the CoTGL mean for outlet thermal NO is below the Kriging mean after the DOE stage, thus indicating again the CoTGL strategy's ability to find a good design earlier in the design process.

Figure 7.13 shows the comparison between response surfaces of CoTGL† and Kriging strategies containing best optimal designs for steady outlet thermal NO. In comparison to the shape of the response surface captured using 10x10 grid CFD evaluations (c.f. Figure 6.14), the shape of the CoTGL response surfaces after DOE [Figure 7.13(1)] and updates [Figure 7.13(2)] appear more globally accurate, compared to the Kriging response surfaces [Figure 7.13(3) and (4)] due to the availability of a greater quantity of information from the low-fidelity model.

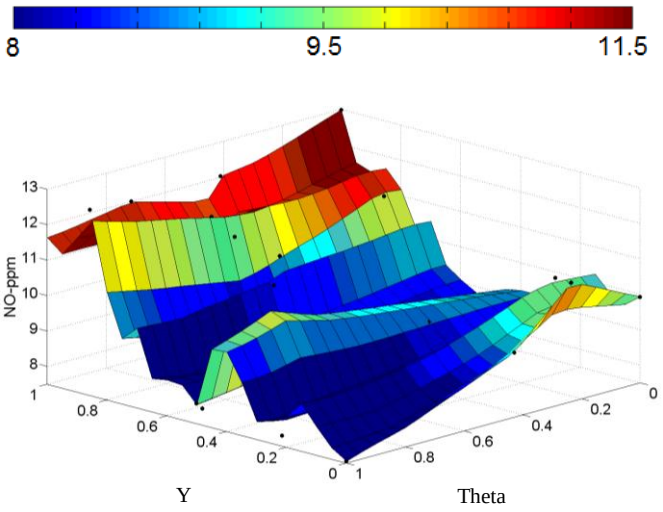

Fig. 7.14b Low-fidelity model of the CoTGL response surface after DOE + Updates

However, the CoTGL response surface at the end of the optimisation cycle [Figure 7.13(2)] appears more distorted due to presence of noise in the low-fidelity model as shown in Figure 7.14b. This noise is regressed in the co-Kriging prediction. Figure 7.14a shows the comparison between the correlation of CoTGL and Kriging RSM predictions (at the end of the computational budget) with 10x10 CFD data. As per the scatterplots of Figure 7.14, the relationship between CoTGL RSM prediction and 10x10 CFD data for outlet thermal NO is more non-linear as compared to the relation between Kriging RSM prediction and 10x10 CFD data. The CoTGL model has r^2=0.278 which is much lower than the Kriging model (r^2=0.878). Even though visually, the shape of the CoTGL RSM appears more accurate, the presence of noise in the prediction again lowers the

† See Appendix E for ranking of CoTGL samples

correlation. Table 7.5 shows the comparison between the best optimal designs obtained by Kriging and CoTGL strategies for outlet thermal NO within fixed computational budget. The best design configuration with lowest thermal NO value is found by Kriging strategy.

7.3.2 Co-Kriging based design optimisation in temporal domain for time-averaged area-weighted outlet thermal NO (ppm)

After the investigation of co-Kriging based design strategies in the spatial domain using steady RANS, combustor design optimisation in temporal domain using various co-Kriging based design strategies - CoSUS, CoTUS and CoSTUS is investigated in this section and compared against traditional Kriging based design strategy within a fixed computational budget (c.f. Table 7.2) for time-averaged outlet thermal NO.

7.3.2.1 Using steady and unsteady RANS simulation (CoSUS)

Figure 7.15 shows the time-averaged area-weighted outlet thermal NO optimisation search histories along with the mean performance of all the search histories using nine different DOE samples; over a fixed computational budget of seven high-fidelity and fifteen low-fidelity CFD runs (c.f. Table 7.2). As shown in Figure 7.15, the variation in convergence behaviour of search histories at the end of the optimisation cycle is higher compared to the variation in the CoTGL strategy for outlet thermal NO (c.f. Figure 7.11).

Figure 7.16 shows the comparison between the mean of optimisation search histories of Kriging and CoSUS strategies for time-averaged area-weighted outlet thermal NO. The CoSUS strategy does not perform better than Kriging strategy in terms of the mean convergence at the end of the fixed computational budget. However, the mean of CoSUS strategy is below the Kriging strategy mean after the DOE stage, thus establishing that strategy CoSUS is able to find a good design earlier in the design process.

Figure 7.17 shows the comparison between the response surfaces of CoSUS† and Kriging strategies containing best optimal designs for time-averaged outlet thermal NO. In comparison to the shape of the response surface captured using 10x10 grid CFD evaluations (c.f. Figure 6.22), the CoSUS strategy captures the correct shape of the response surface after the DOE stage [Figure 7.17(1)] compared to the Kriging response surface [Figure 7.17(3)]. However, at the end of the optimisation cycle, the Kriging response surface [Figure 7.17(4)] appears more accurate as compared to CoSUS strategy response surface [Figure 7.17(2)]. This is established quantitatively in Figure 7.18 which shows the comparison between the correlation of CoSUS and Kriging RSM predictions with 10x10 CFD data. As per the scatterplots of Figure 7.18, the correlation between CoSUS RSM prediction and 10x10 CFD data varies less linearly as compared to correlation between Kriging RSM prediction and 10x10 CFD data. The CoSUS model has r^2=0.7389 which is lower than Kriging model (r^2=0.8855).

† See Appendix E for ranking of CoSUS samples

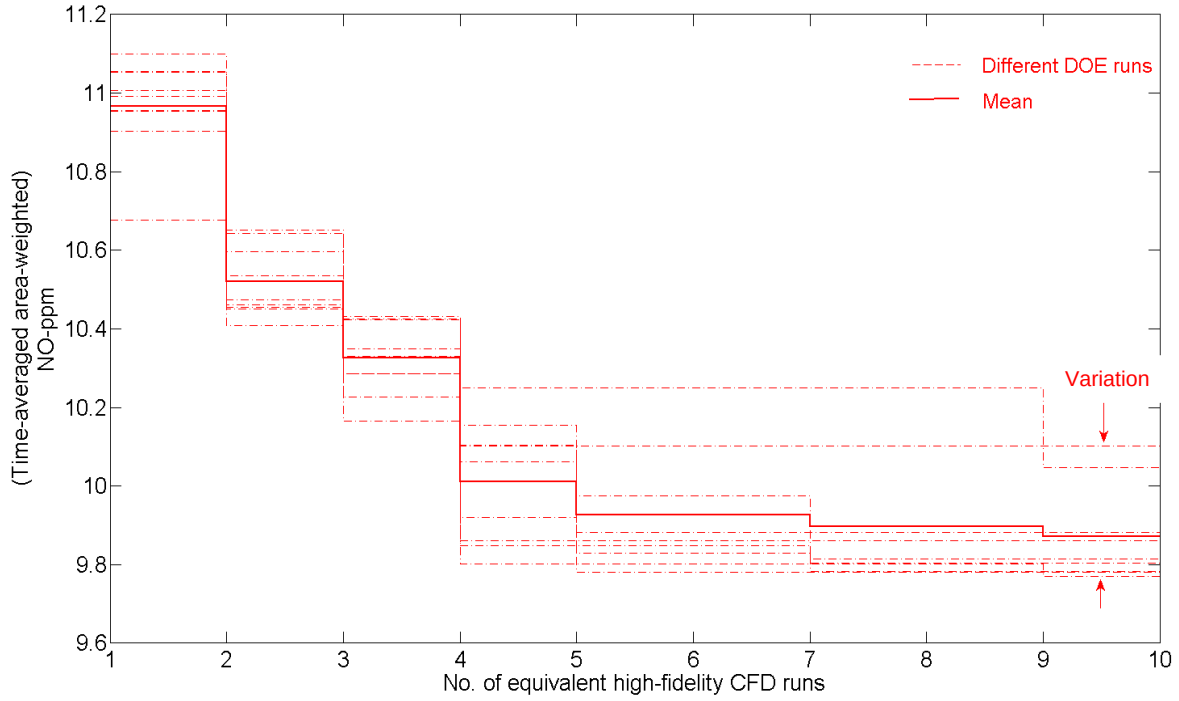

Fig. 7.15 Time-averaged area-weighted outlet thermal NO optimisation search histories using CoSUS over a fixed computational budget (c.f. Table 7.3)

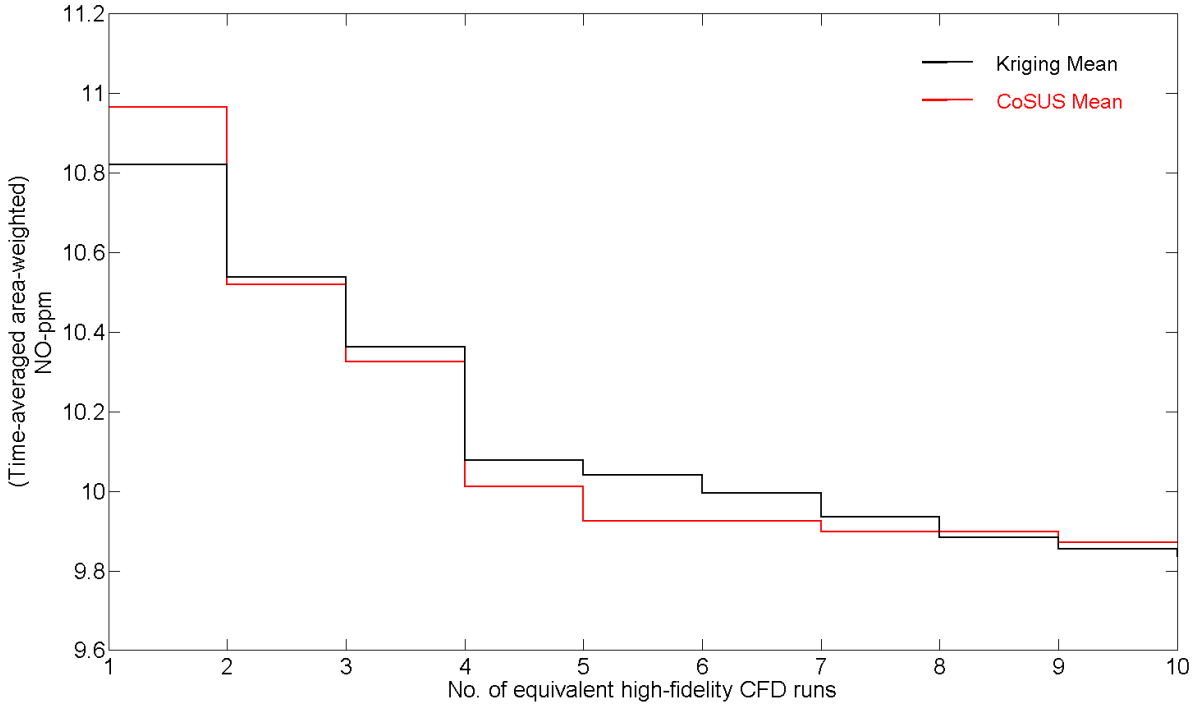

Fig. 7.16 Comparison between mean optimisation search histories of Kriging and CoSUS strategies for time-averaged area-weighted outlet thermal NO

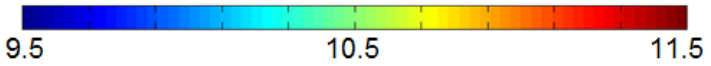

CoSUS response surface consisting of best optimal design

(1) After DOE

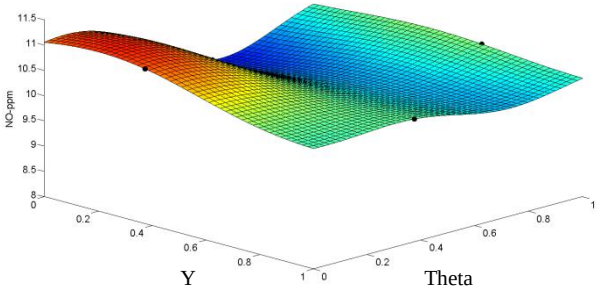

(2) After DOE + Updates

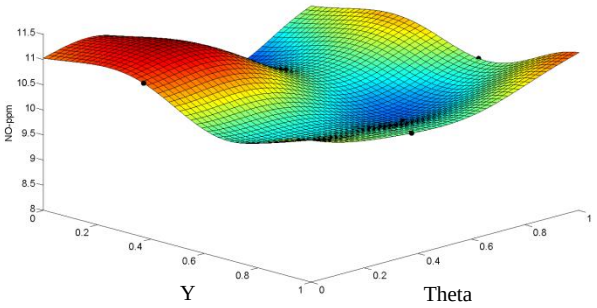

Kriging response surface consisting of best optimal design

(3) After DOE

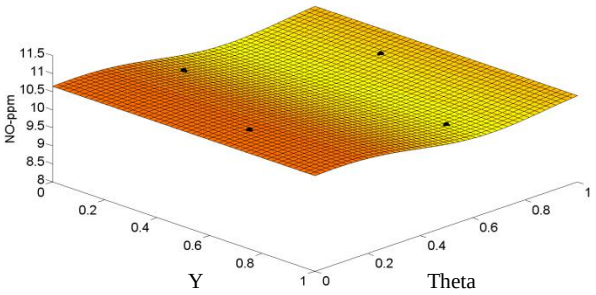

(4) After DOE + Updates

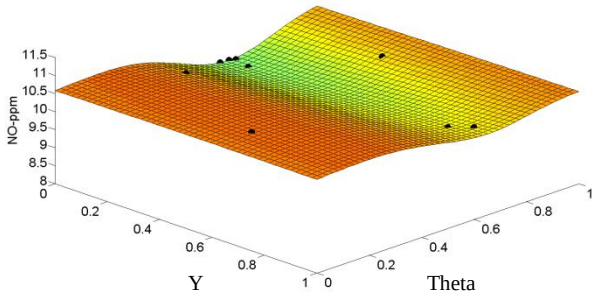

Fig. 7.17 Comparison between CoSUS and Kriging response surfaces consisting of their respective best optimal designs for time-averaged area-weighted outlet thermal NO (ppm)

CoSUS model correlation (r^2 = 0.7389)

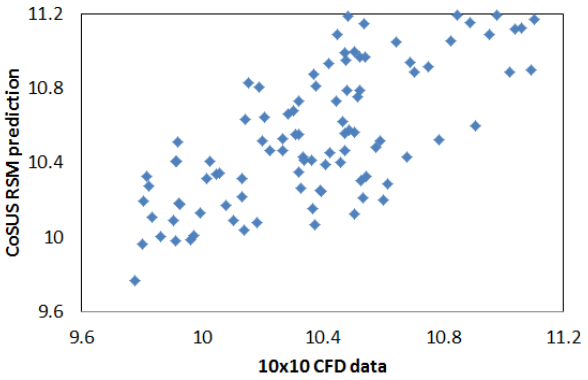

Kriging model correlation (r^2 = 0.8855)

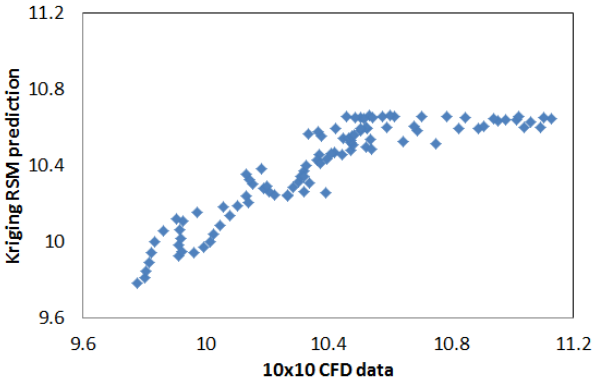

Fig. 7.18 Comparison between correlations of CoSUS and Kriging RSM (after DOE + Updates) predictions with 10x10 CFD data for time-averaged area-weighted outlet thermal NO(ppm)

Table 7.6 Comparison between the best optimal designs amongst all experiments found by Kriging and CoSUS strategies for time-averaged outlet thermal NO			
	Y	**Θ**	**Time-averaged area-weighted outlet thermal NO (ppm)**
Kriging	0	0.660	9.778
CoSUS	0	0.662	9.778

Table 7.6 shows the comparison between the best optimal designs obtained by Kriging and CoSUS strategies for time-averaged outlet thermal NO within fixed computational budget. CoSUS strategy finds similar best optimal design as Kriging strategy.

7.3.2.2 Using different time-step sizes of unsteady RANS simulations

(i) CoTUS-(a)

In CoTUS-(a) strategy the low-fidelity model is URANS with Δt = 5e-05s.

Figure 7.19 shows CoTUS-(a) strategy optimisation search histories and the mean of all the search histories using nine different DOE samples (c.f. Figure 7.4); over a fixed computational budget of seven high-fidelity and twelve low-fidelity CFD runs (c.f. Table 7.2).

Similar to the observation in CoSUS strategy search histories, CoTUS-(a) strategy progresses towards different optimal designs due to different starting samples. However, the variation in convergence of CoTUS-(a) optimisation search histories is higher compared to the variation observed in the CoSUS strategy (c.f. Figure 7.15).

Figure 7.20 shows the comparison between the mean of optimisation search histories of Kriging and CoTUS-(a) strategies for time-averaged area-weighted outlet thermal NO (ppm). Again, the CoTUS-(a) strategy does not perform any better than Kriging strategy in terms of the mean convergence at the end of the fixed computational budget. Also, in contrast to CoSUS strategy, the mean of CoTUS-(a) strategy is above the Kriging strategy mean after the DOE stage and throughout till the end. This shows that CoTUS-(a) strategy fails to improve on the Kriging design process completely.

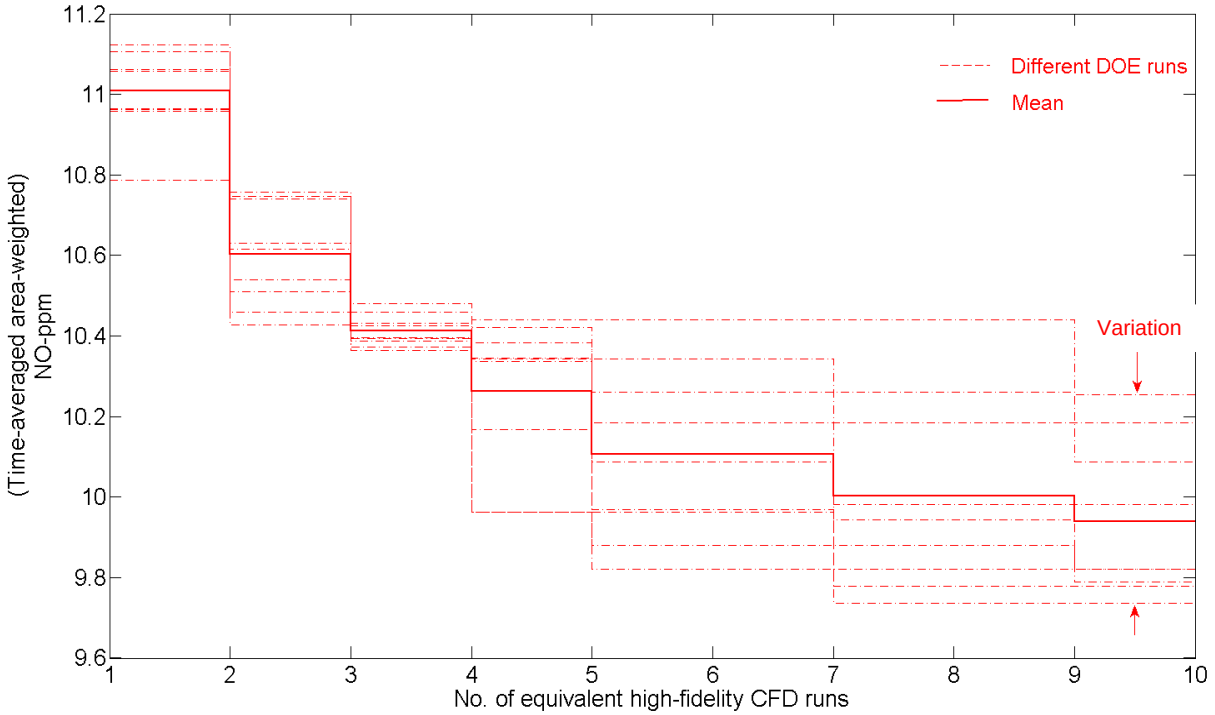

Fig. 7.19 Time-averaged area-weighted outlet thermal NO optimisation search histories using CoTUS-(a) over a fixed computational budget (c.f. Table 7.3)

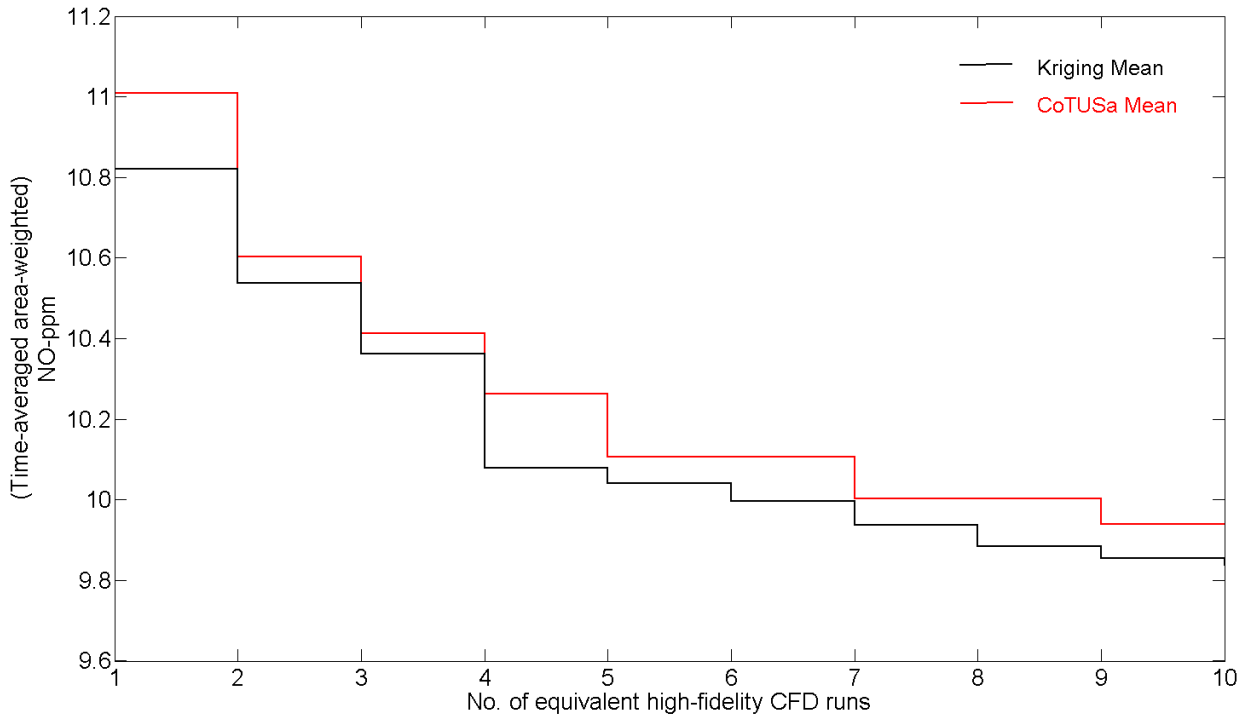

Fig. 7.20 Comparison between mean optimisation search histories of Kriging and CoTUS-(a) strategies for time-averaged area-weighted outlet thermal NO

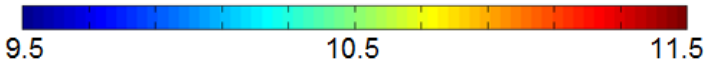

CoTUS-(a) response surface consisting of best optimal design

(1) After DOE

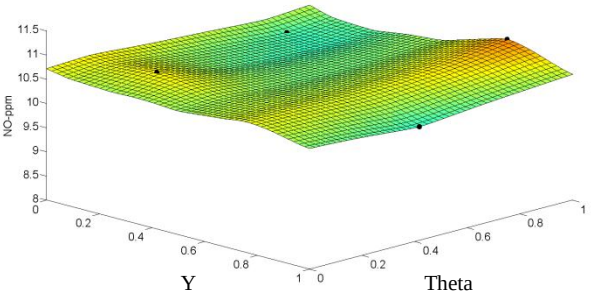

(2) After DOE + Updates

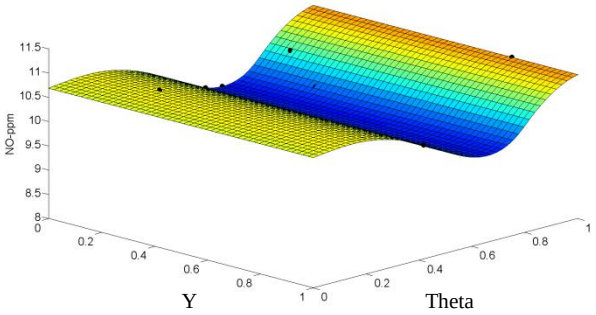

Kriging response surface consisting of worst optimal design

(3) After DOE

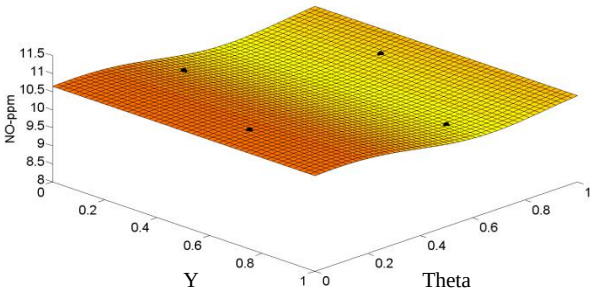

(4) After DOE + Updates

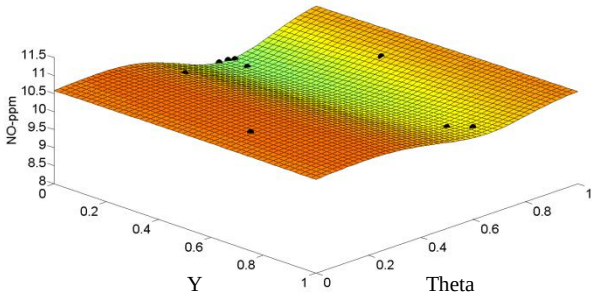

Fig. 7.21 Comparison between CoTUS-(a) and Kriging response surfaces consisting of their respective best optimal designs for time-averaged area-weighted outlet thermal NO

CoTUS-(a) model correlation (r^2 = 0.7723)

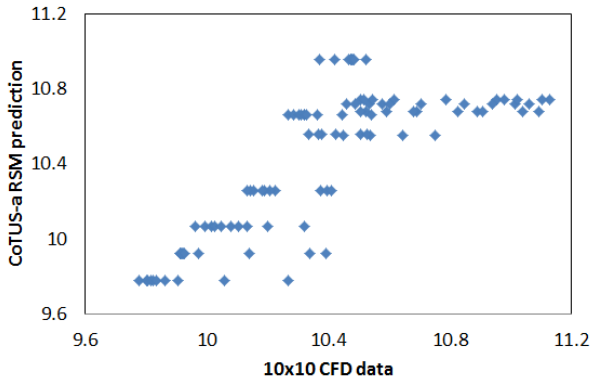

Kriging model correlation (r^2 = 0.8855)

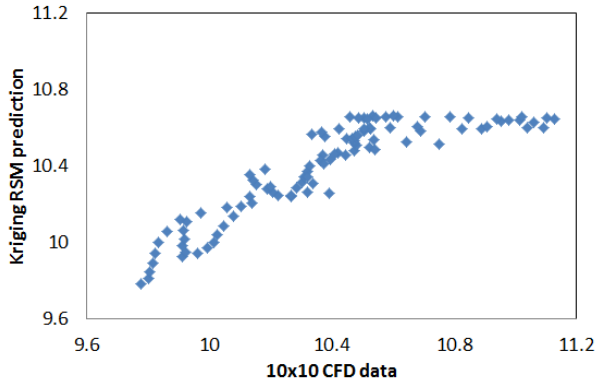

Fig. 7.22 Comparison between correlations of CoTUS-(a) and Kriging RSM (after DOE + Updates) predictions with 10x10 CFD data for time-averaged area-weighted outlet thermal NO

Figure 7.21 shows the comparison between the response surfaces of CoTUS-(a)† and Kriging strategies containing best optimal designs for time-averaged outlet thermal NO (ppm). In comparison to the shape of the response surface captured using 10x10 grid CFD evaluations (c.f. Figure 6.22), the CoTUS-(a) strategy fails to capture the correct shape of the response surface after the DOE or at the end of optimisation cycle stage [Figure 7.17(1) and (2) respectively] compared to the Kriging response surfaces.

Figure 7.22 shows the comparison between the correlation of CoTUS-(a) and Kriging RSM predictions with 10x10 CFD data. Similar to the observation in CoSUS RSM correlation, the scatterplots show that the correlation between CoTUS-(a) RSM prediction and 10x10 CFD data varies less linearly as compared to correlation between Kriging RSM prediction and 10x10 CFD data. However, the CoTUS-(a) model has r^2=0.7723 (which is higher than CoSUS RSM r^2 =0.7389) but lower than Kriging model (r^2=0.8855).

Table 7.7 Comparison between the best optimal designs amongst all experiments found by Kriging and CoTUS-(a) strategies for time-averaged outlet thermal NO

	Y	Θ	Time-averaged area-weighted outlet thermal NO (ppm)
Kriging	0	0.660	9.778
CoTUS-(a)	0	0.656	9.778

Table 7.7 shows the comparison between the best optimal designs obtained by Kriging and CoTUS-(a) strategies for time-averaged outlet thermal NO (ppm) within fixed computational budget. Again, CoTUS-(a) strategy finds similar best optimal design as Kriging strategy.

(ii) CoTUS-(b)

In CoTUS-(b) strategy the low-fidelity model is URANS with Δt = 2e-05s. Figure 7.23 shows the CoTUS-(b) optimisation search histories and the mean of all the search histories using nine different DOE samples; over a fixed computational budget of seven high-fidelity and six low-fidelity CFD runs (c.f. Table 7.2). Similar to the observation in CoTUS-(a) strategy search histories, CoTUS-(b) strategy also progresses towards different optimal designs due to different starting samples. However, the variation in convergence of CoTUS-(b) optimisation search histories is higher compared to the variation observed in the CoSUS and CoTUS-(a) strategies (c.f. Figures 7.15 and 7.19 respectively).

† See Appendix E for ranking of CoTUS-(a) samples

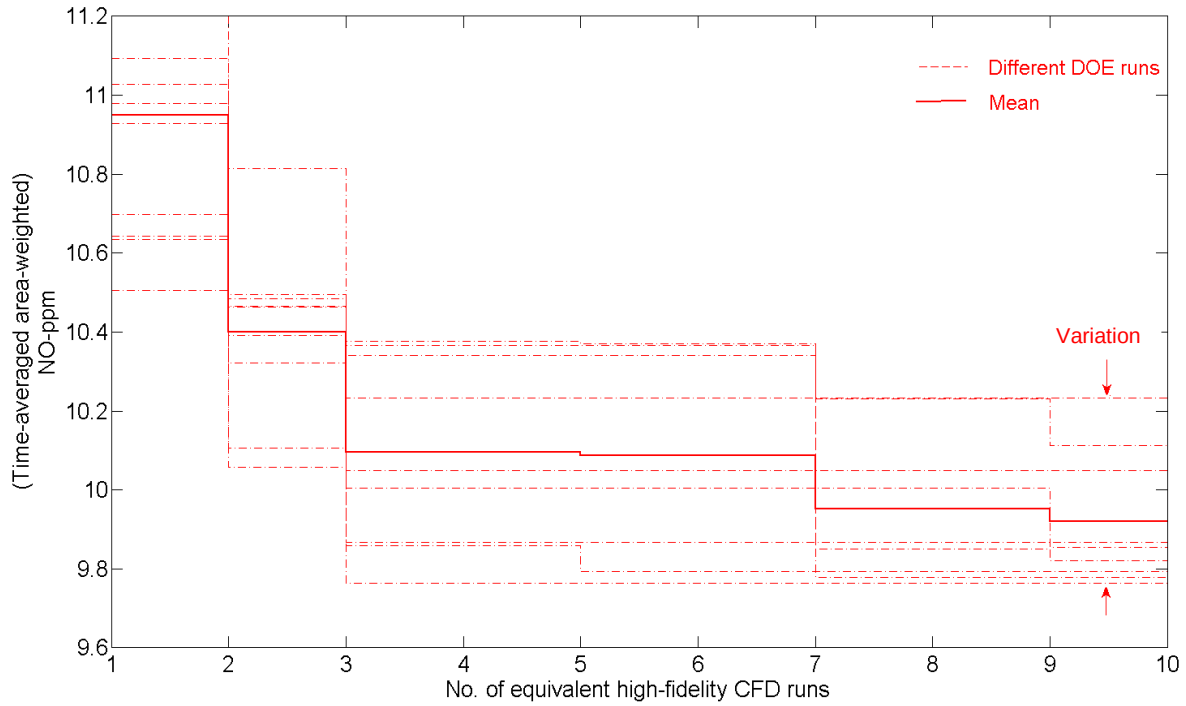

Fig. 7.23 Time-averaged area-weighted outlet thermal NO optimisation search histories using CoTUS-(b) over a fixed computational budget (c.f. Table 7.3)

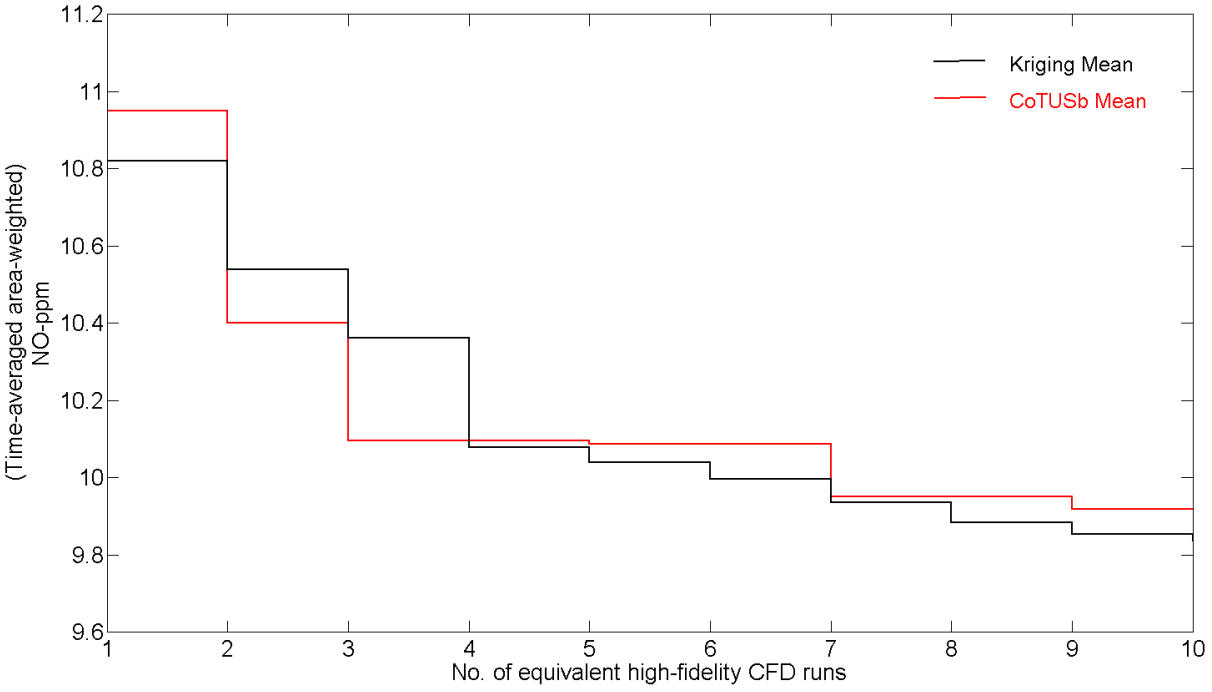

Fig. 7.24 Comparison between mean optimisation search histories of Kriging and CoTUS-(b) strategies for time-averaged area-weighted outlet thermal NO

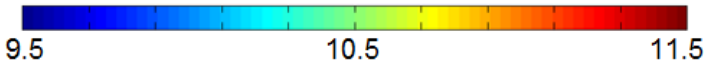

CoTUS-(b) response surface consisting of best optimal design

(1) After DOE

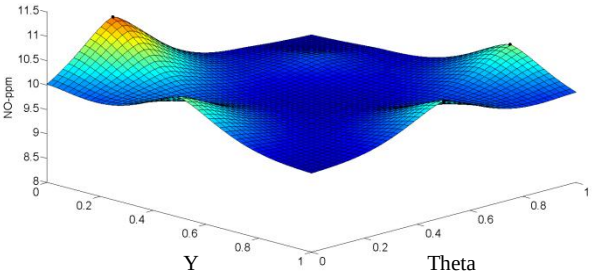

(2) After DOE + Updates

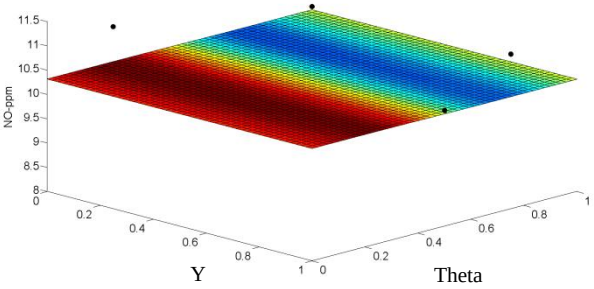

Kriging response surface consisting of best optimal design

(3) After DOE

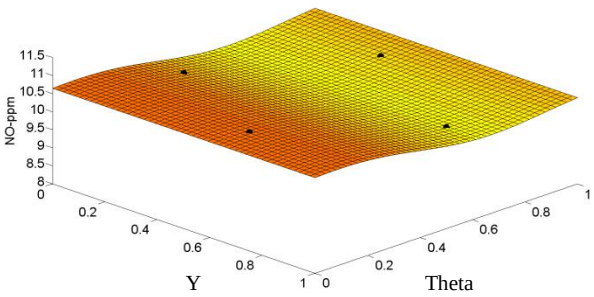

(4) After DOE + Updates

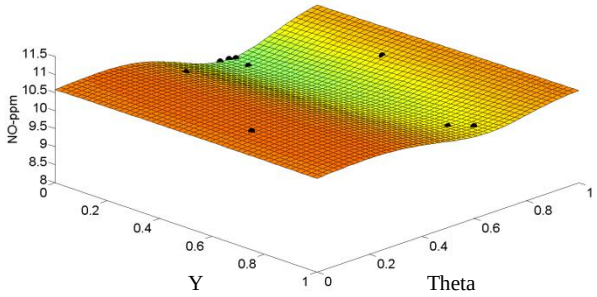

Fig. 7.25 Comparison between CoTUS-(b) and Kriging response surfaces consisting of their respective best optimal designs for time-averaged area-weighted outlet thermal NO

CoTUS-(b) model correlation

(r^2 = 0.8125)

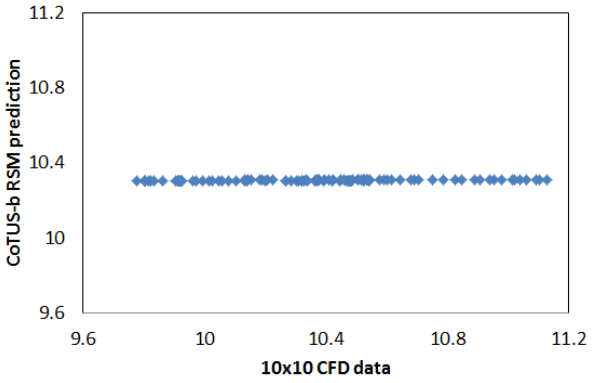

Kriging model correlation

(r^2 = 0.8855)

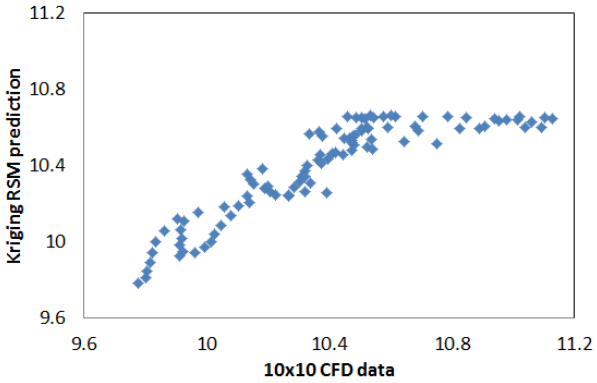

Fig. 7.26 Comparison between correlations of CoTUS-(b) and Kriging RSM (after DOE + Updates) predictions with 10x10 CFD data for time-averaged area-weighted outlet thermal NO

Figure 7.24 shows the comparison between the mean of optimisation search histories of Kriging and CoTUS-(b) strategies. Compared to Kriging strategy, the CoTUS-(b) strategy does not perform better as the mean of the CoTUS-(b) strategy is above the mean of the Kriging strategy after the DOE stage and the end of the optimisation cycle. This shows that similar to CoTUS-(a), CoTUS-(b) strategy also fails to improve on the Kriging design process completely.

Figure 7.25 shows the comparison between the response surfaces of CoTUS-(b)† and Kriging strategies containing best optimal designs for time-averaged outlet thermal NO (ppm). The CoTUS-(b) strategy fails to capture the correct shape of the response surface (c.f. Figure 6.22) after the DOE [Figure 7.25(1)] or at the end of optimisation cycle stage [Figure 7.25(2)] entirely, compared to the Kriging response surfaces. This is due to less number of data points available to build the response surfaces, as the cost ratio between low and high fidelity model of CoTUS-(b) strategy is very low.

Figure 7.26 shows the comparison between the correlation of CoTUS-(b) and Kriging RSM predictions with 10x10 CFD data. The scatterplots show that the CoTUS-(b) RSM prediction have almost no linear correlation with the 10x10 CFD data. However, the CoTUS-(b) model has r^2=0.8125 (which is higher than CoSUS and CoTUS-(a) RSM r^2) but lower than Kriging model r^2=0.8855.

Table 7.8 Comparison between the best optimal designs amongst all experiments found by Kriging and CoTUS-(b) strategies for time-averaged outlet thermal NO (ppm)

	Y	Θ	Time-averaged area-weighted outlet thermal NO (ppm)
Kriging	0	0.660	9.778
CoTUS-(b)	0	0.656	9.778

Table 7.8 shows the comparison between the best optimal designs obtained by Kriging and CoTUS-(b) strategies for time-averaged outlet thermal NO (ppm) within fixed computational budget. As observed previously in CoTUS-(a), strategy CoTUS-(b) also finds similar best optimal design as Kriging strategy.

7.3.2.3 Using different spatio-temporal unsteady RANS simulations (CoSTUS)

Figure 7.27 shows the CoSTUS strategy optimisation search histories with the mean performance of all the search histories using nine different DOE samples; over a fixed computational budget of seven high-fidelity and fifty-four low-fidelity CFD runs (c.f. Table 7.2).

† See Appendix E for ranking of CoTUS-(b) samples

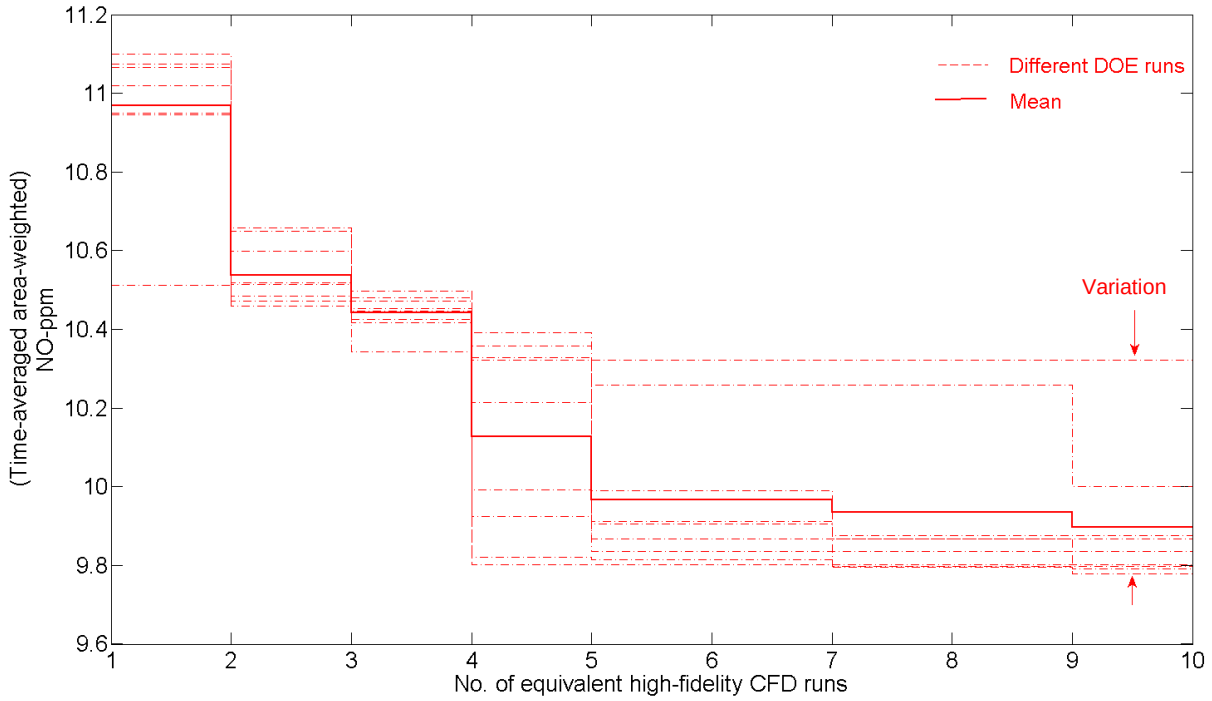

Fig. 7.27 Time-averaged area-weighted outlet thermal NO (ppm) optimisation search histories using CoSTUS over a fixed computational budget (c.f. Table 7.3)

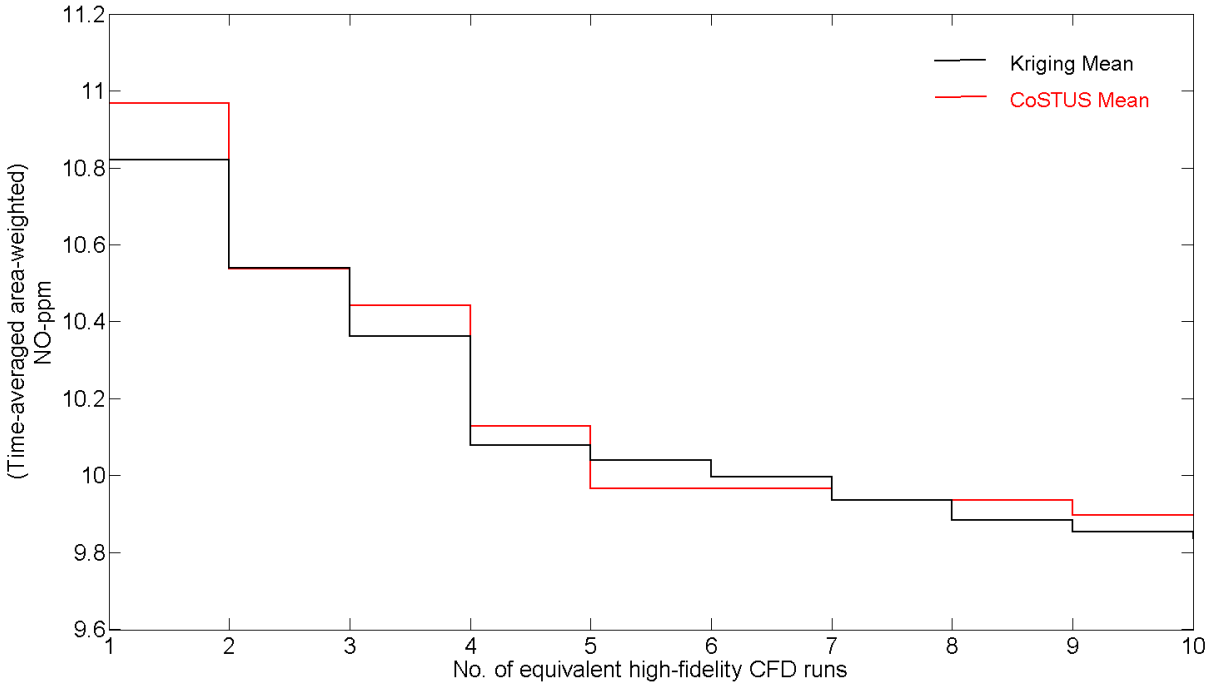

Fig. 7.28 Comparison between mean optimisation search histories of Kriging and CoSTUS strategies for time-averaged area-weighted outlet thermal NO (ppm)

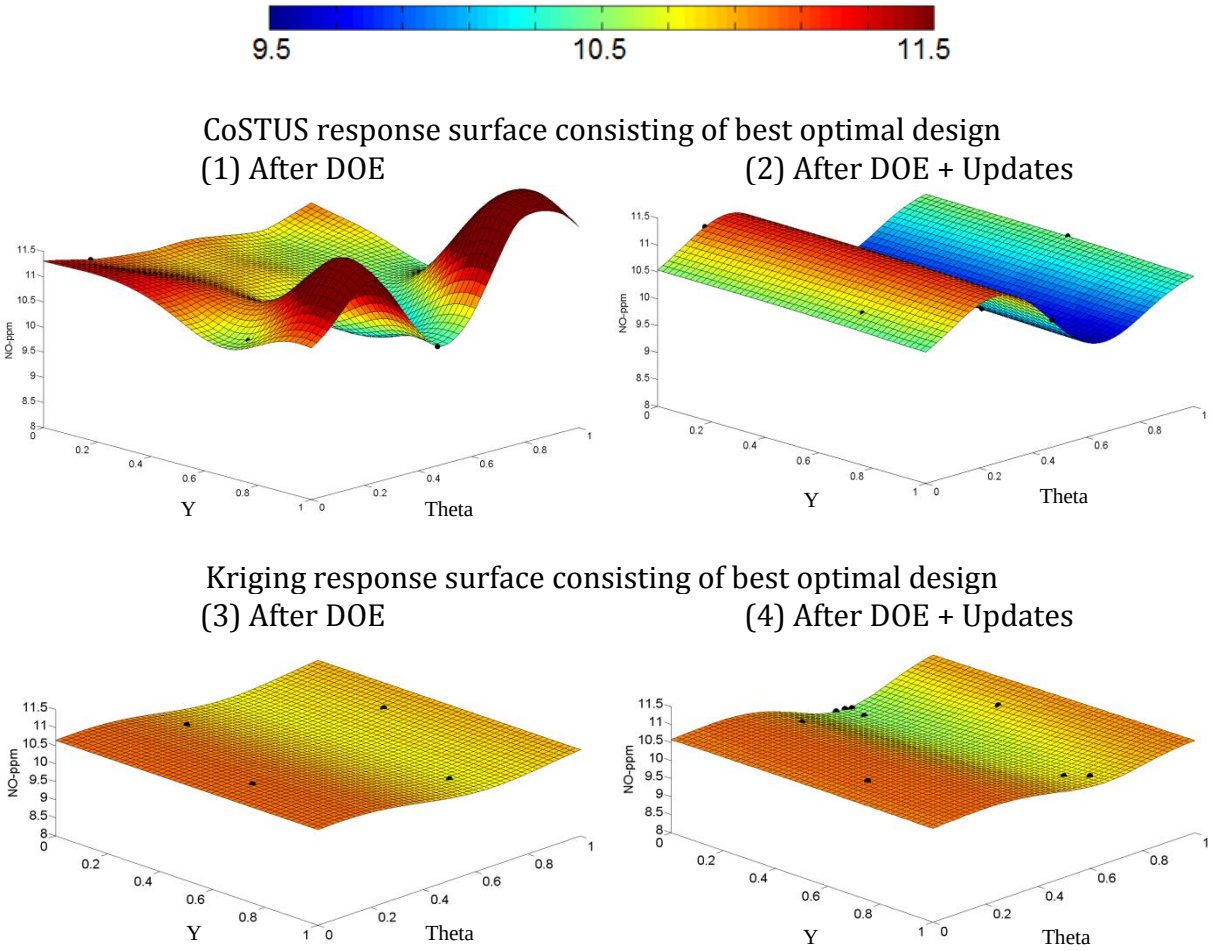

Fig. 7.29 Comparison between CoSTUS and Kriging response surfaces consisting of their respective best optimal designs for time-averaged area-weighted outlet thermal NO (ppm)

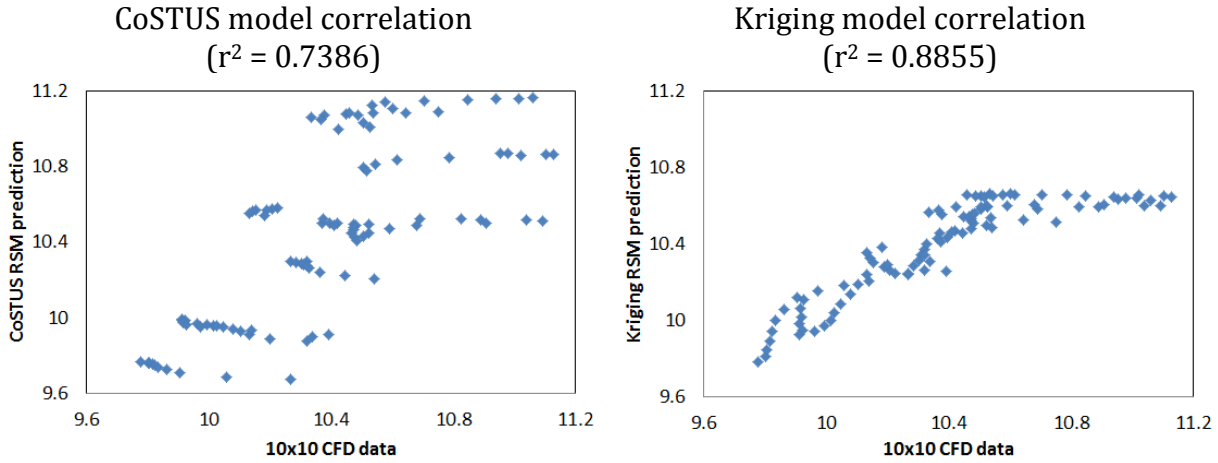

Fig. 7.30 Comparison between correlations of CoSTUS and Kriging RSM (after DOE + Updates) predictions with 10x10 CFD data for time-averaged area-weighted outlet thermal NO(ppm)

Table 7.9 Comparison between the best optimal designs amongst all experiments found by Kriging and CoSTUS strategies within fixed computational budget

	Y	Θ	Time-averaged area-weighted outlet thermal NO (ppm)
Kriging	0	0.660	9.778
CoSTUS	0	0.656	9.778

The CoSTUS strategy has the highest number of low-fidelity runs amongst all the temporal domain co-Kriging strategies. Figure 7.27 also shows the variation in convergence behaviour of search histories at the end of the optimisation cycle.

Figure 7.28 shows the comparison between the mean of optimisation search histories of Kriging and CoSTUS strategies. The CoSTUS strategy does not perform better than Kriging strategy in terms of the mean convergence at the end of the fixed computational budget. However, the mean of CoSTUS strategy is below the Kriging strategy mean after the DOE stage, thus establishing that strategy CoSTUS (similar to CoSUS) is able to find a good design earlier in the design process.

Figure 7.29 shows the comparison between the response surfaces of CoSTUS† and Kriging strategies containing best optimal designs for time-averaged outlet thermal NO (ppm). In comparison to the shape of the response surface captured using 10x10 grid CFD evaluations (c.f. Figure 6.22), the CoSTUS strategy does not capture the correct shape of the response surface after the DOE stage [Figure 7.17(1)] or at end of optimisation stage [Figure 7.17(2)].

Figure 7.30 shows the comparison between the correlation of CoSTUS and Kriging RSM predictions with 10x10 CFD data. The scatterplots show that the CoSTUS RSM prediction has a less linear correlation with the 10x10 CFD data compared to correlation of Kriging RSM with 10x10 CFD data. However, the CoSTUS model has r^2=0.7386 which is lower than Kriging model r^2=0.8855. Table 7.9 shows the comparison between the best optimal designs obtained by Kriging and CoSTUS strategies for time-averaged outlet thermal NO (ppm) within fixed computational budget. As observed previously in CoSUS, CoTUS-(a) and CoTUS-(b), strategy CoSTUS finds the best optimal design similar to Kriging strategy.

7.4 Bootstrapped confidence interval for co-Kriging based strategies

† See Appendix E for ranking of CoSTUS samples

The co-Kriging based multi-fidelity design optimisation strategies, both in spatial and temporal domains, were applied on nine different DOE samples with mean performances shown in Figures 7.7, 7.11, 7.15, 7.19, 7.23 and 7.27. These mean performances were compared against the Kriging strategy mean performances in Figures 7.8, 7.12, 7.16, 7.20, 7.24 and 7.28.

Table 7.10 summarizes the relevant statistical estimates for steady and time-averaged outlet thermal NO (ppm) data evaluated in this chapter, using strategies CoTGL, CoSUS, CoTUS and CoSTUS in comparison with the Kriging strategy in spatial and temporal domains.

Table 7.10 Relevant statistical estimates for all objective function data evaluated using strategies CoTGL, CoSUS, CoTUS and CoSTUS.

	Objective function		Sample mean (M)	Standard deviation	Standard error
Spatial domain	Temperature profile RMSD (K)	Kriging	348.242	10.9274	3.6424
		CoTGL	351.127	12.4281	4.1427
	NO (ppm)	Kriging	8.2305	0.0684	0.0228
		CoTGL	8.2851	0.1484	0.0495
Temporal domain	Time-averaged area-weighted NO (ppm)	Kriging	9.8369	0.0653	0.0218
		CoSUS	9.8727	0.1204	0.0401
		CoTUS-(a)	9.9393	0.1941	0.0647
		CoTUS-b	9.9214	0.1671	0.0557
		CoSTUS	9.8965	0.1731	0.0577

As shown in Table 7.10, in the spatial domain, the Kriging strategy performs better than the CoTGL strategy in terms of sample mean at the end of the optimisation cycle for both objective functions, outlet temperature profile RMSD and thermal NO. The standard deviation of the sample data is also less for the Kriging strategy, which shows that the sample data points are close to the mean, whereas for the CoTGL strategy the variability of data is higher. Hence, the standard error, which is a measure of precision of the sample mean, is lower for Kriging strategy compared to the CoTGL strategy. In the temporal domain, too, the Kriging strategy has lower sample mean and lower standard deviation and error compared to the co-Kriging based strategies CoSUS, CoTUS and CoSTUS.

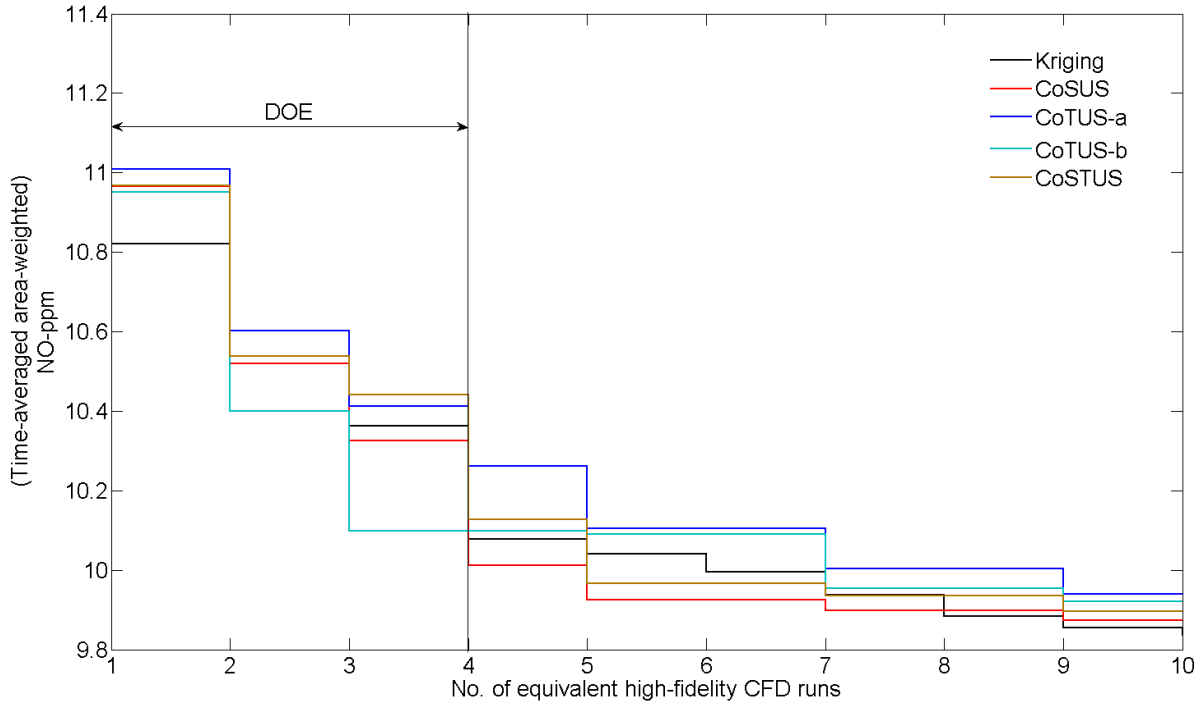

Fig. 7.31 Comparison between sample (N = 9) mean performances of Kriging and various Co-Kriging strategies in temporal domain over the given fixed computational budget (c.f. Table 7.3)

Figure 7.31 shows the comparison between the estimated mean performance (of nine samples) of the Kriging strategy against the CoSUS, CoTUS and CoSTUS strategies over the fixed computational budget. Among all the co-Kriging based strategies, strategy CoSUS performs the best in terms of estimated mean value at the end of the optimisation cycle and also at the end of the DOE stage.

However, the estimated mean is based on a sample size of N = 9. Adding more samples, the estimated mean performances (as presented in Table 7.10 and Figure 7.31) could change leading to a different conclusion. Since this process is expensive, bootstrap based confidence intervals are evaluated giving a range of values where the true mean could be located. Based on these intervals, all co-Kriging based design strategies developed in this chapter are compared against the standard Kriging based strategy.

7.4.1 Spatial domain

The CoTGL design strategy for outlet temperature profile RMSD and thermal NO in the spatial domain is assessed using 95% bootstrapped confidence intervals (CI). A convergence test is initially performed for determining the bootstrap sample size B (see Appendix E) which is then used to construct 95% bootstrap confidence intervals.

(A) Outlet temperature profile RMSD:

Table 7.11 Lower and upper limits of 95% bootstrapped CI for Kriging and CoTGL strategies for steady outlet temperature profile (RMSD)

Strategy	B	Lower limit (K)	Upper limit (K)
Kriging	5000	342.523	356.150
CoTGL	10000	344.728	360.341

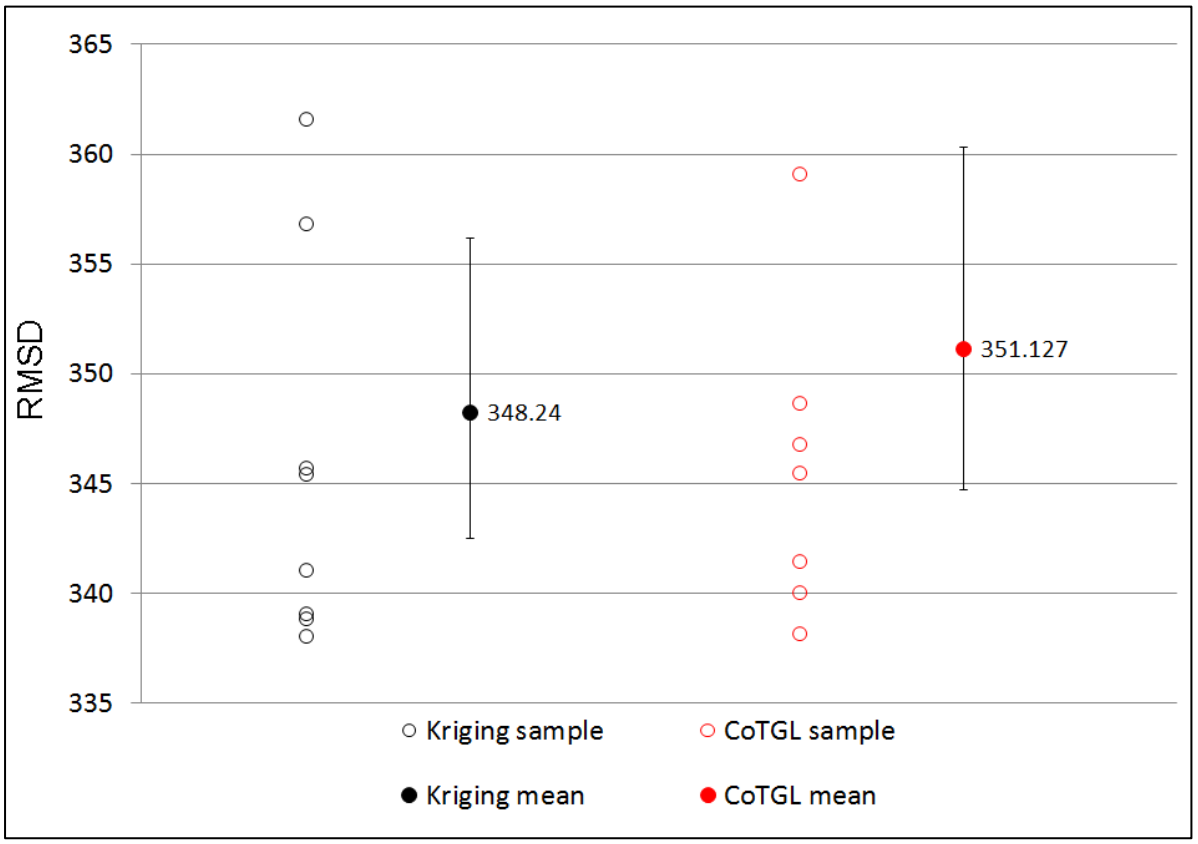

Fig. 7.32 Estimated means with 95% CI and original sample data of Kriging and CoTGL strategies for steady outlet temperature profile (RMSD)

Table 7.11 shows the upper and lower limit values of Kriging and CoTGL strategies 95% confidence intervals for steady outlet temperature profile RMSD. Figure 7.32 shows the comparison between the 95% confidence intervals on the Kriging and CoTGL means for steady outlet temperature profile RMSD. If the confidence intervals on the two sample estimates do not overlap, one can be confident that the true value (or population) of the estimate differs significantly, statistically (Cumming et al., 2005). Since, the confidence intervals for Kriging and CoTGL strategies in Figure 7.32 overlap considerably, no statistically significant difference would be observed on the population mean obtained by using Kriging and CoTGL strategies for outlet temperature RMSD.

(B) Outlet thermal NO (ppm):

Table 7.12 Lower and upper limits of 95% bootstrapped CI for Kriging and CoTGL strategies for steady outlet thermal NO (ppm)

Strategy	B	Lower limit (ppm)	Upper limit (ppm)
Kriging	1000	8.194	8.281
CoTGL	1000	8.218	8.431

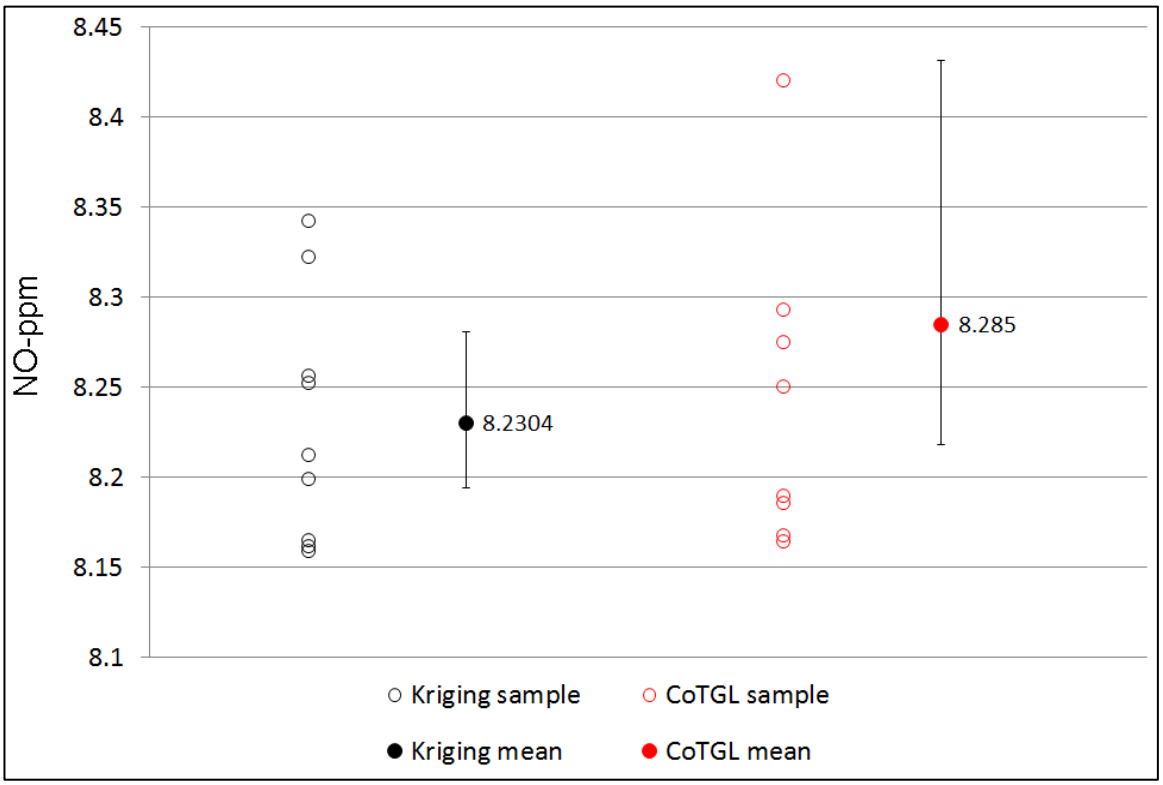

Fig. 7.33 Estimated means with 95% CI and original sample data of Kriging and CoTGL strategies for steady outlet thermal NO

Table 7.12 shows the upper and lower limit values of Kriging and CoTGL strategies 95% confidence intervals for steady outlet thermal NO. Figure 7.33 shows the comparison between the 95% confidence intervals on the Kriging and CoTGL means for steady outlet thermal NO. Similar to steady outlet temperature (RMSD), for outlet thermal NO the confidence intervals on Kriging and CoTGL mean do overlap but not considerably. Also the lower and upper bounds of the confidence interval for Kriging mean are narrower, compared to the CoTGL mean confidence interval. Hence, a statistically

significant difference would be observed on the population mean obtained by using Kriging and CoTGL strategies for outlet thermal NO.

7.4.2 Temporal domain

Table 7.13 Lower and upper limits of 95% bootstrapped CI for various strategies for time-averaged area-weighted outlet thermal NO (ppm)

Strategy	B	Lower limit (ppm)	Upper limit (ppm)
Kriging	5000	9.8025	9.8840
CoSUS	5000	9.8158	9.9732
CoTUS-a	1000	9.8472	10.0869
CoTUS-b	1000	9.8391	10.049
CoSTUS	10000	9.8254	10.0784

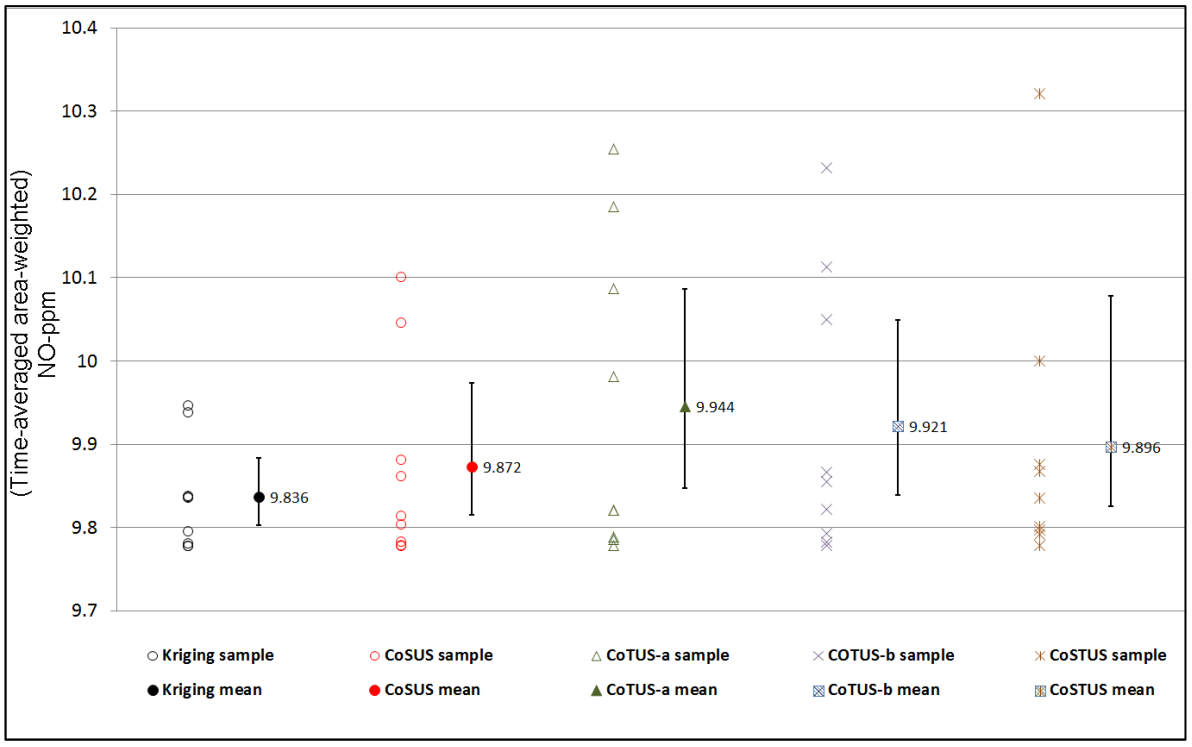

Fig. 7.34 Estimated means with 95% CI and original sample data of Kriging and various co-Kriging based design strategies for time-averaged outlet thermal NO (ppm)

Figure 7.34 shows the comparison between the 95% confidence intervals of Kriging and various co-Kriging based design strategies for time-averaged outlet thermal NO (ppm) with upper and lower bounds of the intervals listed in Table 7.13. It shows that the confidence intervals of Kriging and other co-Kriging based design strategies do overlap. However, the lower and upper bounds of the Kriging confidence interval are much narrower compared to confidence interval of any other co-Kriging based design strategy in temporal domain. Amongst co-Kriging based strategies, the confidence interval of CoSUS has the lowest sample mean, lowest variation in sample data and narrower upper and lower CI bounds.

7.5 Summary

Various co-Kriging based multi-fidelity design optimisation strategies – CoTGL, CoSUS, CoTUS and CoSTUS were developed and used to optimize the shape of a flame-stabilizer step in both spatial and temporal domains. All co-Kriging based design optimisation cycles were repeated on nine different initial samples, which revealed how the convergence search history varied, leading to different optimal designs. Later, the statistics of interest i.e. mean performance of each co-Kriging based design strategy over all the samples were compared against the mean performance of the Kriging based design strategy within the fixed computational budget. This showed that strategy CoTGL in the spatial domain (for steady outlet temperature profile and thermal NO) and strategies CoSUS and CoSTUS in the temporal domain (for time-averaged outlet thermal NO) found a good design earlier in the design process, after the DOE stage, compared to the standard Kriging strategy. However, the standard Kriging strategy outperforms all proposed co-Kriging based multi-fidelity strategies at the end of the optimisation cycle.

Since the sample size is small (N = 9), and the mean is only an estimate of the true mean, a confidence assessment was performed on all the co-Kriging based multi-fidelity strategies, in spatial and temporal domain, at the end of the optimisation cycle. This was compared against the confidence intervals of the Kriging strategy. It was observed that in the spatial domain, the confidence interval of CoTGL strategy overlaps considerably with the Kriging strategy for outlet temperature profile RMSD objective function whereas, for outlet thermal NO, the Kriging strategy confidence interval is much narrower and below the CoTGL strategy confidence interval. In the temporal domain, the confidence intervals of Kriging and co-Kriging based design strategies i.e. CoSUS, CoTUS and CoSTUS do overlap. However, the lower and upper bounds of the Kriging confidence interval are much narrower compared to the confidence interval of any other co-Kriging based multi-fidelity design strategy. Hence, the Kriging strategy outperforms the co-Kriging based design strategies at all times. However, evidence exists of finding a good design earlier in the process using co-Kriging based multi-fidelity design strategy.

Chapter 8

Time-parallel co-Kriging based multi-fidelity strategy for combustor design

In this chapter, a co-Kriging based multi-fidelity strategy involving a time-parallel CFD simulation concept is investigated for the design optimisation of the two-dimensional lean burn combustor. For this purpose, initially, two different time-parallel CFD simulation methods are developed for solving the temporally evolving combustor reactive flow-field using the commercial CFD code FLUENT™. The time-parallel combustor solution is compared against a traditional time-serial solution for identifying any benefits in terms of wall-clock time speed-up and its potential use for multi-fidelity design optimisation.

Subsequently, the proposed time-parallel CFD simulation method is used to seed multiple levels of fidelity within the framework of a multi-fidelity co-Kriging based design optimisation strategy. The developed design strategies are run within fixed computational budgets and on multiple initial samples, to collect statistical data with mean convergence behaviour used as a performance indicator. A confidence assessment of the newly developed strategies is also performed and compared against the traditional Kriging based design strategy to draw conclusions.

8.1 Introduction

To reduce the computational expense of a combustor simulation and to take advantage of increasing computational power, combustor simulations are often performed with spatial domain decomposition using a time-serial approach. In the time-serial method, the solution at each time-step is evaluated before starting the next time-step computation. This methodology employs spatial discretization which divides and solves

the spatial computational domain on multiple computing nodes (Trindade and Pereira, 2006). However, the time-serial methodology can be inefficient when the spatial dimension (or mesh count) of the problem is small and a large number of computing nodes are used. In such a case the communication costs between computing nodes due to data parallelism becomes significant. This demands a CFD simulation methodology which is 'purely' parallel, such that there is no data exchange cost overhead between two parallel computing nodes, thus giving a possibility of scaling the simulation to all available nodes efficiently. As the number of computing nodes available will naturally increase in the future (Trindade and Pereira, 2004), to fully exploit the available large number of computing nodes, time-parallel (or temporal domain decomposition) methods have some attraction.

The concept of time-parallel simulation was first conceptualized by Nievergelt in 1964 for the time-integration of ordinary differential equations. In time-parallel methods, the time-direction is discretized into many time-states where individual time-states of the flow-field are computed in parallel. The peculiarity here is that each time-state computation is independent of other time-states, such that no data transfer between two time-states occurs while the computation is being performed. Based on Nievergelt's work, much of the investigation of time-parallel methods was restricted to the solution of linear and non-linear ordinary differential equations (Miranker and Liniger, 1964, Keller, B., 1968, Chartier and Philippe, 1993), which highlighted some benefits of the methods in terms of computation speed-up obtained over time-serial methods.

In contrast, the development of time-parallel simulation methodologies for solving time-dependent partial differential equations has been attempted only recently. The method termed as the 'parareal' or 'parallel-in-time (PIT)' algorithm was first presented by Lions et al. in 2001 for numerical solution of time-dependent partial differential equations. The algorithm is based on a predictor-corrector scheme, where a coarse time-discretization predictor step (sequential) and a fine time-discretization corrector step (parallel) are evaluated alternatively until convergence. This algorithm has received much interest from many authors for the solution of a temporally evolving problems in fluids, structures and fluid-structure interactions (Farhat and Chandesris, 2003), Navier-Stokes equations (Fischer et al., 2003) and for reservoir simulation (Garrido et al., 2003). Also, many variants of the original 'parareal' algorithm have been developed to decompose the temporal domain of the specific problem under consideration (Baffico et al., 2002, Maday and Turinici, 2003). Further analysis of the 'parareal' algorithm's accuracy, stability and performance is discussed in more detail in (Gander and Vanderwalle, 2007, Bal, G., 2003, Saltz and Naik, 1988, Staff and Ronquist, 2003).

8.2 Time-serial combustor flow analysis

For time-serial combustor flow analysis, fine time-step size URANS simulations are typically started from an initial coarse time-step size URANS solution. In this way, faster convergence towards the final meta-stable state is achieved as compared to starting from quiescent initial conditions.

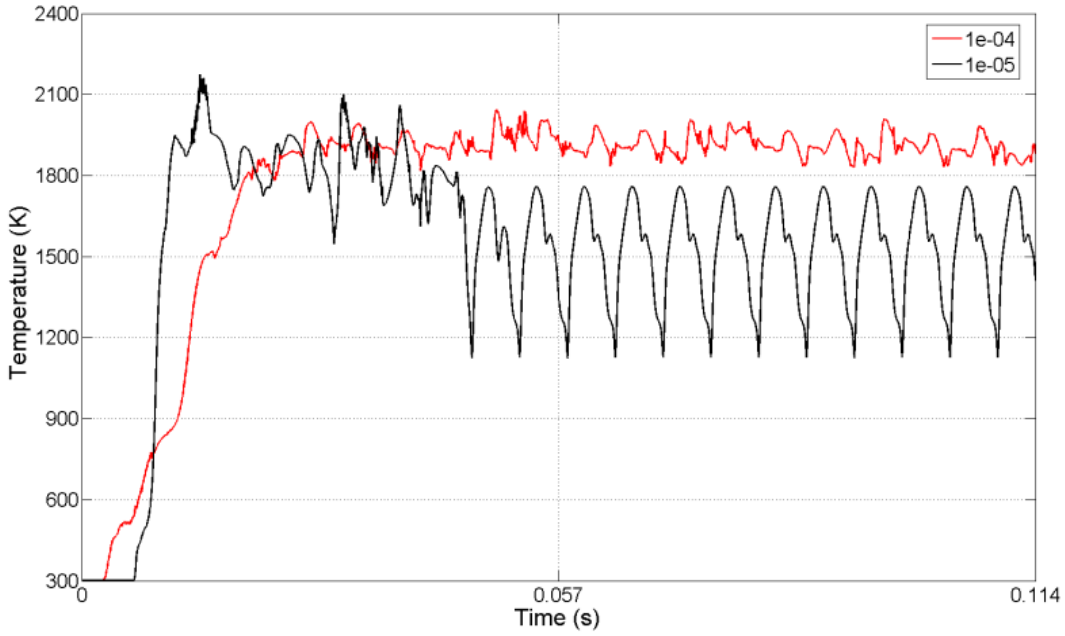

Fig. 8.1 Area-weighted outlet temperature (T_a) fluctuations as captured by URANS simulation using Δt = 1e-04s and Δt = 1e-05s over 20 inlet fluctuation cycles

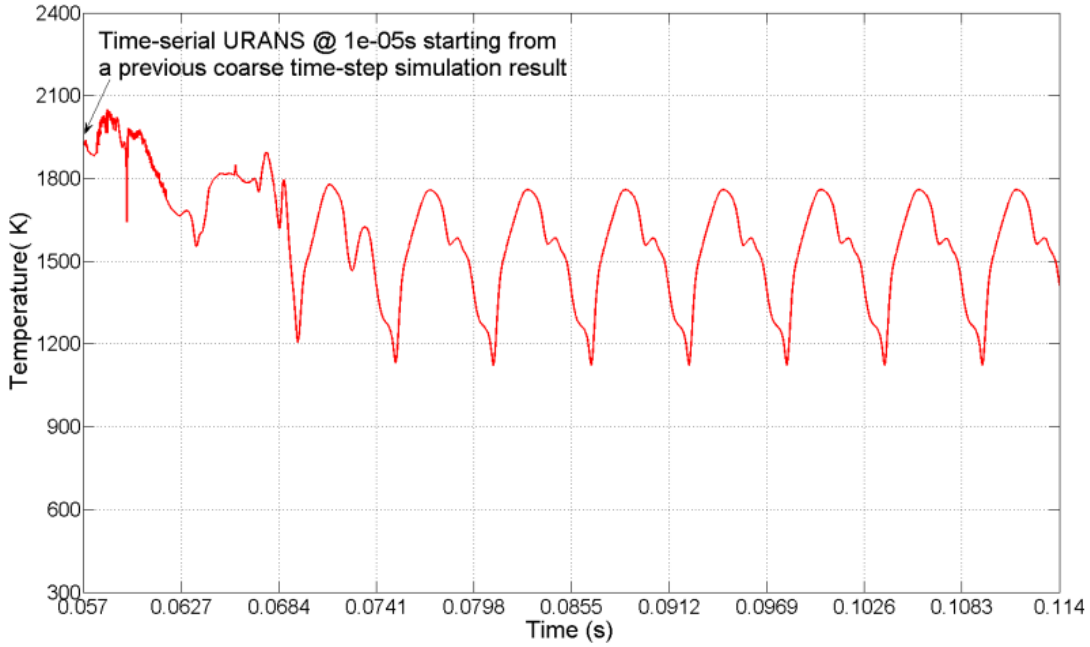

Fig. 8.2 Evolution of humming instability cycle in the flow-field as captured by URANS simulation with Δt = 1e-05s starting from a coarse time-step simulation result

Figure 8.1 shows the difference between the area-weighted outlet temperature (T_a) fluctuation captured by URANS simulations using time-step sizes of 1e-04s and 1e-05s over 20 inlet fluctuation cycles. Using Δt = 1e-04s, it is not possible to capture the reactive flow physics accurately and the outlet temperature above 1800K throughout the time domain. However, it provides a fast approximation of the reactive flow dynamics and can be used to start the fine time-step size simulation. Figure 8.2 shows the convergence of the time-serial URANS simulation using a combination of 1e-04s and 1e-05s time-step sizes. As seen in Figure 8.2, the fine time-step size (1e-05s) URANS simulation is started after running the coarse time-step size (1e-04s) URANS simulation for ten inlet velocity fluctuation cycles. Convergence to the humming instability cycle is achieved by the end of the fourth inlet fluctuation cycle. The total wall clock time required to achieve this is ~615 minutes which is significantly less than the ~1350 minutes required for the URANS simulation with Δt = 1e-05s starting from initial quiescent conditions.

8.3 Time-parallel combustor flow analysis

A time-parallel CFD simulation approach for solving transient combustor flow-field, as far as is known, has not been attempted previously. Two new time-parallel combustor CFD simulation methodologies based on the 'parareal' algorithm are developed in this section and compared against the traditional time-serial simulation result (c.f. Figure 8.2).

8.3.1 Time-parallel simulation method-A

Table 8.1. Time-parallel simulation method-A

Start

(1) Initialize a coarse time-step size computation on a specified time interval [0,**T**] (Sequential)

(2) Discretize the temporal domain [0,**T**] of the sequential solution in to N time-states of equal length

(3) For each subsequent iteration, compute a fine time-step size solution for each time-state (Parallel)

(4) Check for convergence (or M iterations)

End

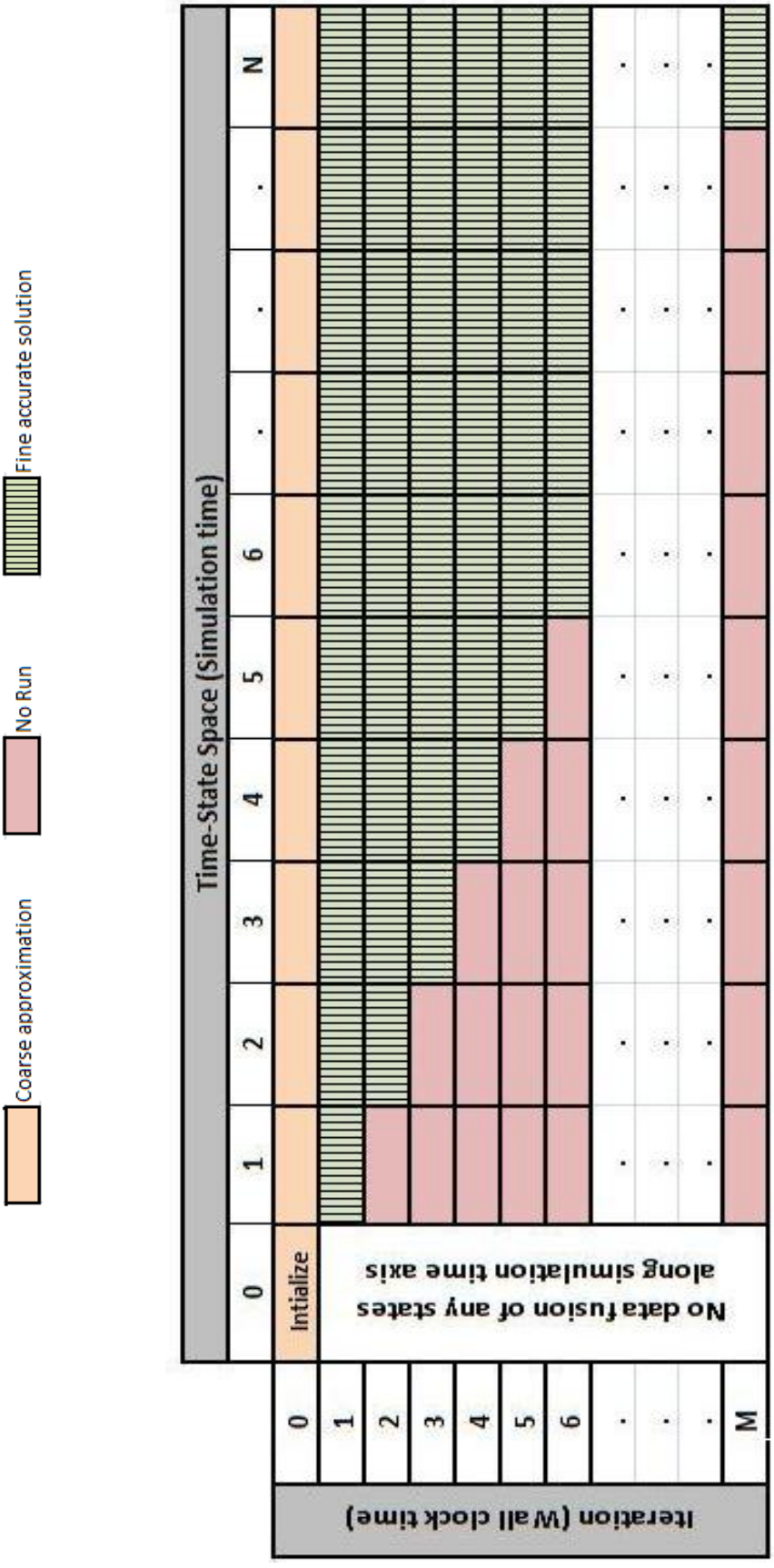

Fig. 8.3 A graphical representation of time-parallel simulation method-A

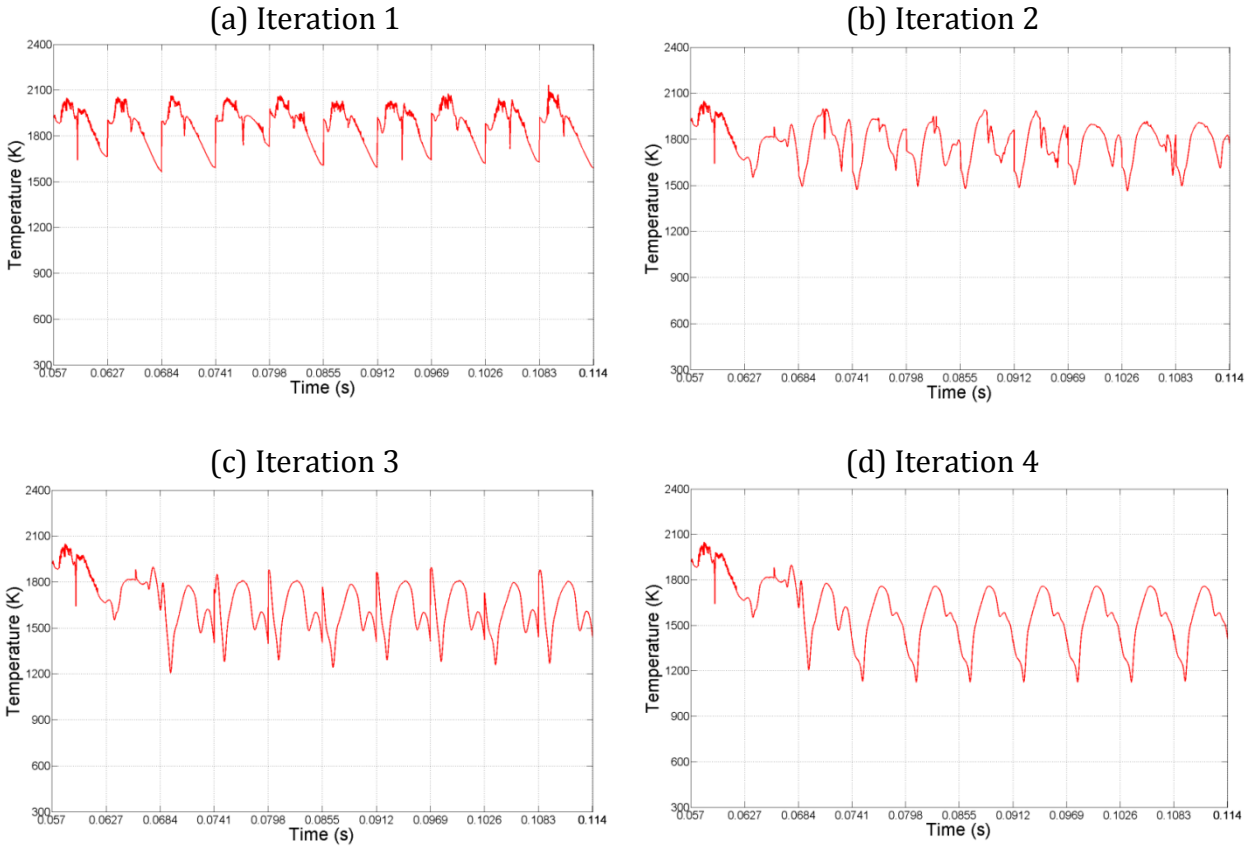

Fig. 8.4.Area-weighted average temperature (T_a) fluctuations at the outlet as captured by different iterations of time-parallel simulation method-A

Table 8.1 lists the key steps involved in the time-parallel simulation method-A. Figure 8.3 represents this method graphically. The first step (iteration 0) involves solving a coarse time-step size (1e-04s) URANS simulation between specified time interval [0, **T**], where **T** is the total flow time, sequentially. Next, at iteration 1, the temporal domain of the approximate solution is divided into N time-states of equal lengths (in terms of flow-time). At each time-state, a fine time-step size (1e-05s) URANS simulation is run, which is considered as the most accurate flow-field representation at that particular iteration and time-state space. Also, this iteration is evaluated entirely in parallel, such that each time-state solution is evaluated simultaneously on the parallel computing nodes (each being an 8-core process). Hence, at the cost of one time-state computation all time-states representing the entire flow-time domain [0, **T**] are evaluated.

If U represents an URANS solution for any time-state 'N' at any iteration level 'M', then the computational process in time-parallel method-A can be mathematically written as:

$$U_j^i = \Delta t_f[U_{j-1}^{i-1}] \qquad \text{Eq. (8.1)}$$

where

i = iteration number,$0 > i \leq M$

j = time-state number,$0 > j \leq N$

Δt_f = fine time-step size operator

Using Equation (8.1), the current time-states are evaluated and the iterations are continued until convergence to the humming instability cycle. However, as shown in Figure 8.3, the 'no-run' time-states represent the state of the flow-field which cannot be improved any further, as the solution corresponds to the final solution at that particular iteration level. Hence, these time-states are not evaluated. Also, the current time-state solution only depends on the solution evaluated in the past time-state of the previous iteration (in terms of simulation time). The continuous use of available accurate time-state solutions at a previous iteration level to seed the next iteration time-state evaluation is the key modification in this method-A as compared to original 'parareal' algorithm, which evaluates a new coarse time-step prediction at every iteration level (Lions et al., 2001).

Figure 8.4 shows the area-weighted outlet average temperature (T_a) fluctuation as captured by different iteration levels of time-parallel simulation method-A. Following the initialization using the coarse time-step size (1e-04s) URANS simulation (c.f. Figure 8.1) between flow-time domain [0.057s, 0.114s], the time-states at every iteration are evaluated in parallel. As seen in Figure 8.4, the convergence to the humming instability cycle is achieved by iteration 4, corresponding to four inlet fluctuation cycles. The state of the flow-field achieved by iteration 4 using time-parallel method-A matches the flow-field state as captured by the time-serial URANS simulation in Figure 8.2. However, no speed-up in terms of number of inlet fluctuation cycles (or wall-clock time) required to reach the humming instability cycle is observed, compared to the time-serial method.

8.3.2 Time-parallel simulation method-B

Table 8.2 lists the steps involved in applying time-parallel simulation method-B, which involves a data fusion† process between past and future time-state solutions, to evaluate the current time-state solution at the next iteration level. Figure 8.5 represents this methodology graphically. In contrast to method-A, all time-states at every iteration level are computed until solution convergence. Referring to Figure 8.5, the algorithm begins with a coarse time-step size (1e-04s) URANS evaluation as a sequential process. The coarse solution over entire flow-time [0, **T**] is then divided into N equal length time-states.

† See Appendix F

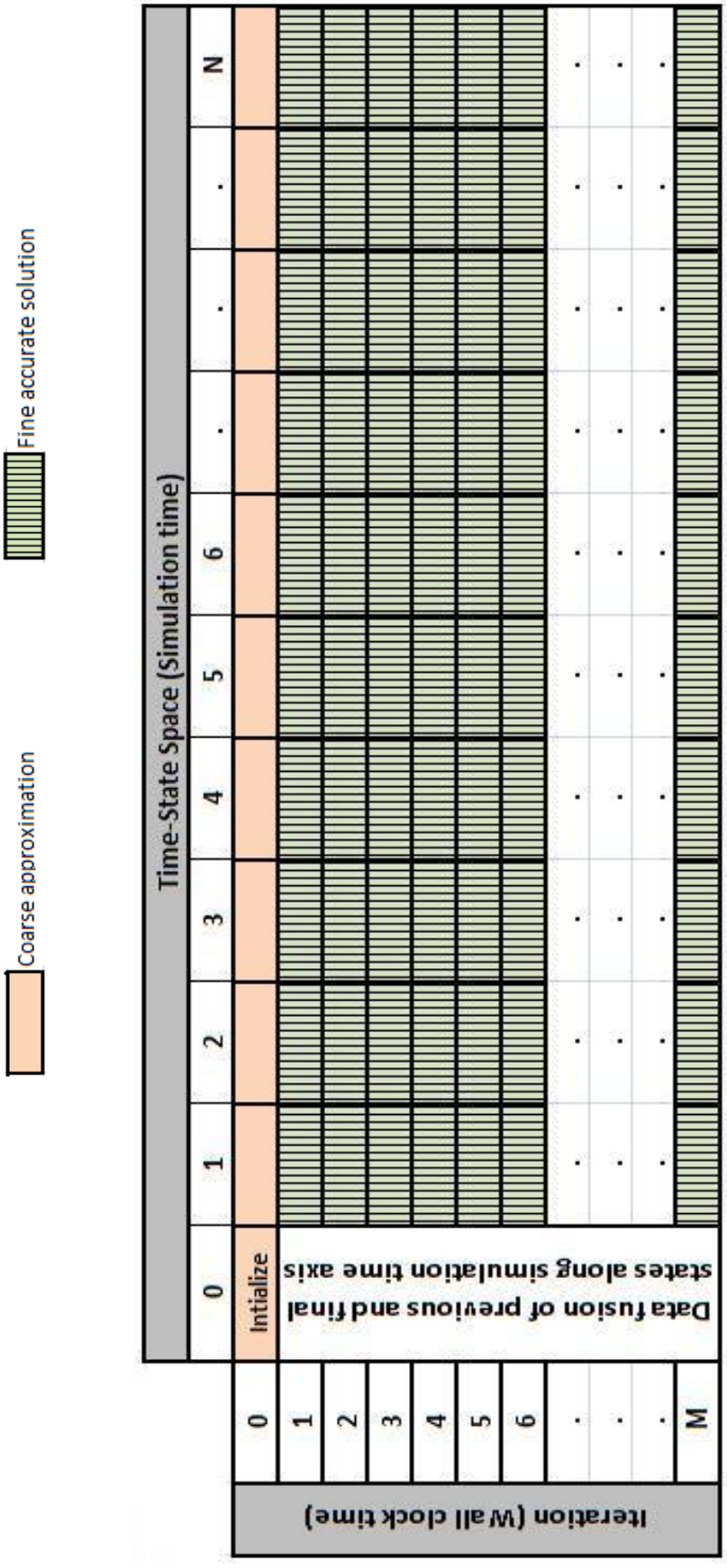

Fig. 8.5 A graphical representation of time-parallel simulation method-B

Table 8.2. Time-parallel simulation method-B

Start

(1) Initialize a coarse time-step size computation on a specified time interval [0,**T**] (Sequential)

(2) Discretize the temporal domain [0,**T**] of the sequential solution in to N time-states of equal lengths

(3) Perform data fusion between past and future (final)time-states (Parallel)

(4) At next iteration, compute a fine time-step size solution on the new data file for each time-state (Parallel)

(5) Repeat (3) and (4) until convergence

End

Table 8.3. Data fusion process for step (3) in Table 8.2

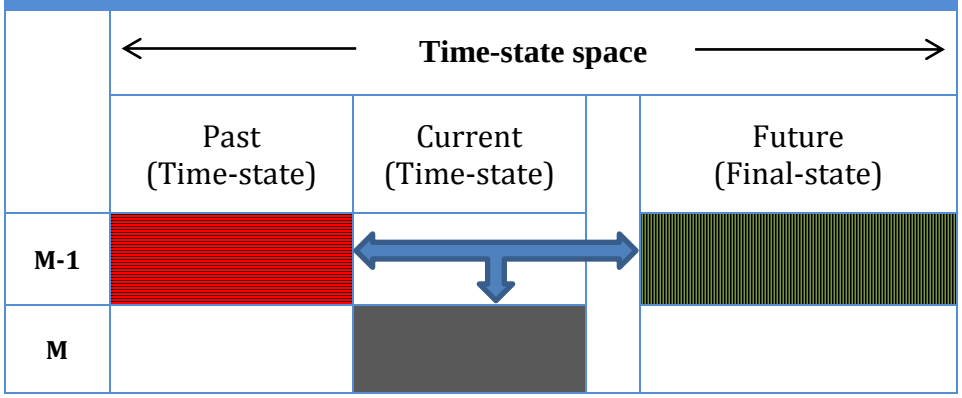

The next step involves a data fusion process, where the FLUENT™ data files at the end of each time-state (past) are blended† with the data file of the final (future) time-state to construct a new data file. These new data files are then used to evaluate all current time-states at the next iteration level. This process is represented graphically in Table 8.3. The current time- state solution, at iteration M, is obtained by running a fine time-step size simulation on a data file obtained by blending past and future time-states data at previous iteration level M-1.

† See Appendix F

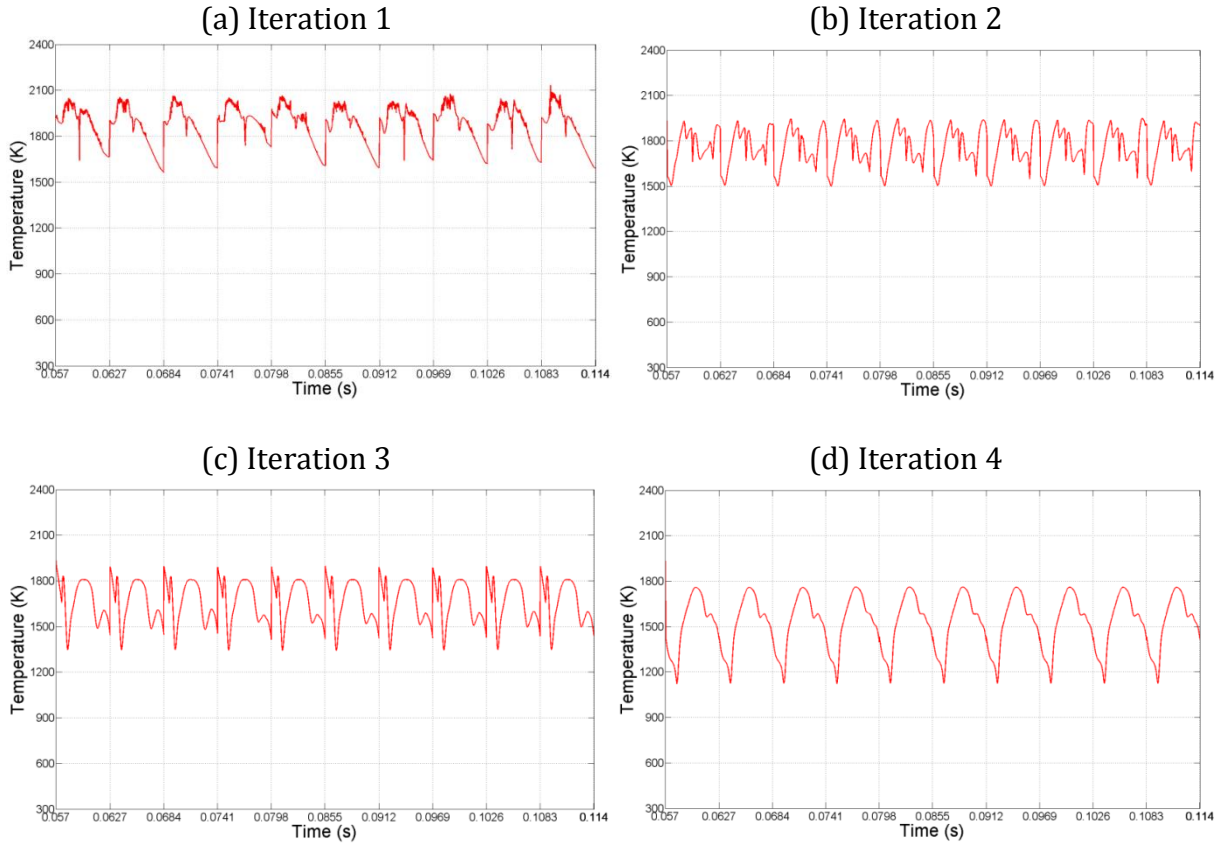

Fig. 8.6 Area-weighted average temperature (T_a) fluctuations at the outlet as captured by different iterations of time-parallel simulation method-B

The data fusion operation is performed in order to improve the quality of information available at each time-state level, which could potentially help in accelerating the convergence process (in terms of number of time-parallel iterations required) (Salinas, et al., 1996). The past time-state data is blended with the final time-state data because the solution obtained at the end of the flow-time is expected to be the most accurate from the previous time-state levels. Hence, this information is passed to all the previous time-states, using a blending factor α. In this study, a blending factor of 0.9 is used.

If U represents an URANS solution for any time-state 'N' at any iteration level 'M', then the computational process in time-parallel method-B with data fusion can be mathematically written as:

$$U_j^i = \Delta t_f \left[\alpha U_N^{i-1} + (1-\alpha) U_{j-1}^{i-1}\right] \qquad \text{Eq. (8.2)}$$

where

i = iteration number, $0 > i \leq M$

j = time-state number, $0 > j \leq N$

Δt_f = fine time-step size operator

α is the blending factor

Using Equation (8.2), all current time-states are evaluated and the iterations are continued until convergence to the humming instability cycle. Figure 8.6 shows the area-weighted outlet average temperature (T_a) fluctuation at different iteration levels of time-parallel algorithm method-B. Following the initialization using the coarse time-step size (1e-04s) URANS simulation (c.f. Figure 8.1) between flow-time domain [0.057s, 0.114s]; a data fusion is performed between each time-state and final time-state solution to construct a new data file for the next iteration level. As seen in Figure 8.6, the convergence to the humming instability cycle is achieved by iteration 4, again corresponding to four inlet fluctuation cycles.

In comparison to time-parallel method-A, the humming cycle appears over the entire simulation time-state space in method B, as a high blending factor of 0.9 is used. This helps to transfer the future (or final) time-state flow-field information across the entire time-state space. The state of the flow-field achieved by iteration 4 using time-parallel method-B matches with the flow-field state obtained using the time-serial URANS simulation depicted in Figure 8.2. However, no speed-up in terms of the number of inlet fluctuation cycles (or wall-clock time) required to reach the humming cycle is observed compared to the time-serial simulation method.

8.4 Co-Kriging based multi-fidelity design strategy using time-parallel unsteady RANS simulations (CoTPUS)

Two different time-parallel CFD simulation methods (A and B) were developed and investigated for unsteady combustor flow solution in the previous section. Although no speed-up advantage, in terms of convergence to humming instability, was obtained relative to the time-serial approach, it is observed that the time-parallel simulation method provides multiple stages of transient combustor flow-field solution data whilst converging towards a final converged state. In this section, results from the time-parallel simulation method-A is further used to formulate a co-Kriging based multi-fidelity strategy for combustor design optimisation. A steady-state RANS solution of the combustor is used to initialize the time-parallel solution iterations. Figure 8.7 shows the area-weighted temperature (T_a) fluctuations at the outlet of the baseline combustor geometry (c.f. Figure 5.3) as captured by Iteration 0 (time-serial) of the time-parallel simulation method-A with number of time-states N = 4.

Steady-state RANS combustor flow solution as an initialisation step for Iteration 0 using mesh 3 (c.f. Table 4.2)

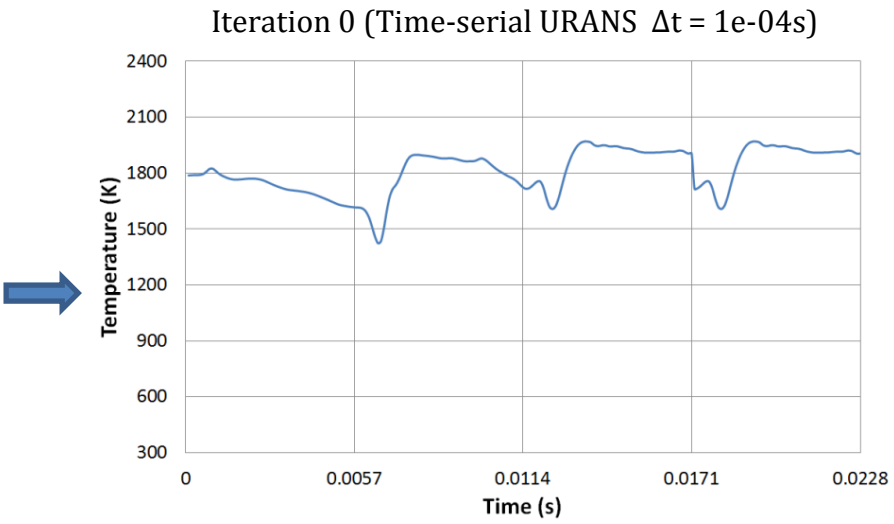

Fig. 8.7 Starting from a steady-state RANS solution, an area-weighted outlet temperature (T_a) fluctuations as captured by Iteration level 0 of the time-parallel simulation method-A (c.f. Figure 8.3) with N = 4

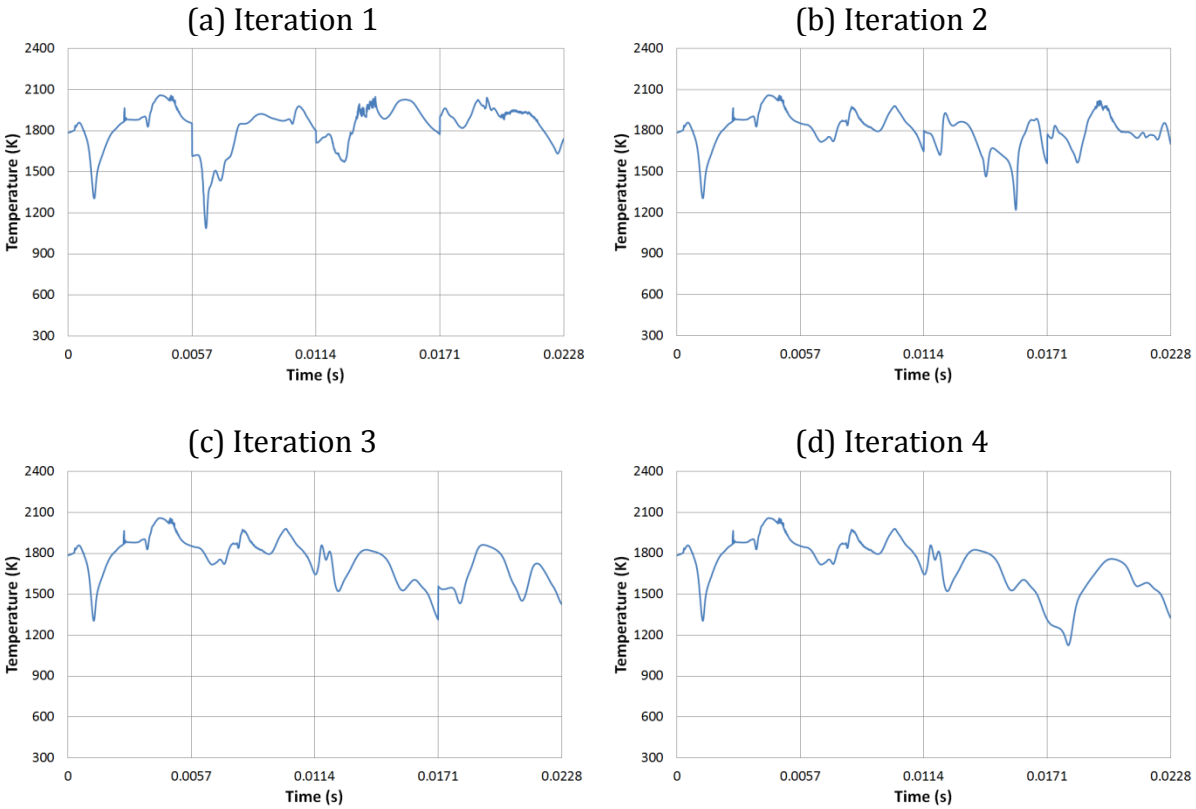

Fig. 8.8 Area-weighted temperature (T_a) fluctuations at the outlet as captured by different iterations of time-parallel simulation method-A

Figure 8.8 shows the state of the combustor outlet temperature fluctuations as captured by different iterations of time-parallel simulation method-A until convergence to humming instability cycle at iteration 4. Hence, iteration 4 is used as the high-fidelity time-parallel combustor analysis. For low-fidelity time-parallel analysis, two iteration levels, 1 and 2, are tested independently, leading to two variants of the CoTPUS strategy.

8.4.1 Choosing two levels of fidelities

8.4.1.1 CoTPUS-(a): For strategy CoTPUS-(a), the two fidelity levels are:

- lo-fi model: Time-parallel iteration level 1
- hi-fi model: Time-parallel iteration level 4

8.4.1.2 CoTPUS-(b): For strategy CoTPUS-(b), the two fidelity levels are:

- lo-fi model: Time-parallel iteration level 2
- hi-fi model: Time-parallel iteration level 4

To evaluate the objective function value for iterations 1 and 2, a time-average of the outlet temperature fluctuation across all four time-states (N=4) is computed. For iteration level 4, a time-average of only the final time-state (humming instability) is computed.

8.4.2 DOE and update points strategy

The computational cost ratio between the cheap low-fidelity (C) and expensive high-fidelity model (E) is used as the basis for determining total number of CFD evaluations.

Table 8.4 Relative overall budget of Kriging and CoTPUS strategies for time-averaged area-weighted outlet temperature optimisation

	Method	Given budget for high-fidelity CFD runs	Total no. of high-fidelity CFD runs performed	Cost ratio	Total no. of low-fidelity CFD runs performed
	Kriging	10	10	-	-
(2)	**CoTPUS** – (a)	10	7	$E \approx 3C$	9
(3)	**CoTPUS** – (b)	10	7	$E \approx 2C$	6

Table 8.4 shows the overall high and low fidelity CFD budgets for CoTPUS design strategies relative to the standard Kriging strategy (applied in Chapter 6) for time-averaged area-weighted outlet temperature.

Table 8.5 Details of DOE and update cycle budget of Kriging and CoTPUS strategies for time-averaged area-weighted outlet temperature optimisation

[Hi-Fi: No. of high-fidelity evaluations, Lo-Fi^F: No. of free low-fidelity evaluations Lo-Fi^X: No. of extra low-fidelity evaluations, EI: expected improvement update, BP: best predicted update]

	Kriging	CoTPUS-(a)			CoTPUS-(b)		
	Hi-Fi	Hi-Fi	Lo-Fi^F	Lo-Fi^X	Hi-Fi	Lo-Fi^F	Lo-Fi^X
DOE	4	4	10		4	7	
			4	6		4	3
Update 1	2 (1 EI, 1BP)	1 (1 EI)	2 (1 EI, 1BP)		1 (1 EI)	2 (1 EI, 1BP)	
			1 (EI)	1 (BP)		1 (EI)	1 (BP)
Update 2	2 (1 EI, 1BP)	1 (1 EI)	2 (1 EI, 1BP)		1 (1 EI)	2 (1 EI, 1BP)	
			1 (EI)	1 (BP)		1 (EI)	1 (BP)
Update 3	2 (1 EI, 1BP)	1 (1 EI)	2 (1 EI, 1BP)		1 (1 EI)	2 (1 EI, 1BP)	
			1 (EI)	1 (BP)		1 (EI)	1 (BP)

To initialize the design study, DOE sample points are generated using optimal Latin-Hypercube sampling (LHS) according to the computational budget shown in Table 8.5. This shows the complete details of the number of low and high fidelity evaluations in the DOE and update stages for the CoTPUS strategy relative to the Kriging strategy. As shown in Table 8.5, the total number of high-fidelity CFD runs over the optimisation cycle is limited to seven for both CoTPUS strategies. The remaining three high-fidelity runs are replaced by equivalent numbers of low-fidelity runs, as determined by the cost ratio between the low and high fidelity models (c.f. Table 8.4). However, the process of evaluating low-fidelity data is unique in the CoTPUS strategy. In a time-parallel unsteady flow analysis, only one simulation needs to be setup from which multi-level solutions are available. Thus, for a particular design point, the low-fidelity evaluations

(iterations 1 and 2) are available for free in the process of the high-fidelity (iteration 4) evaluation without any extra effort. This is the key difference and an advantage over the previous temporal domain co-Kriging based design strategies CoSUS, CoTUS and CoSTUS (applied in Chapter 7).

In addition to the free low-fidelity analysis (obtained during high-fidelity analysis), the 'extra' low-fidelity analysis effort can be applied elsewhere in the design space to get more information at the low-fidelity level which could enhance the overall quality of the co-Kriging model in the CoTPUS strategy. Table 8.5 shows that the total number of DOE points to be evaluated for CoTPUS-(a) is ten and for CoTPUS-(b) is seven. Low-fidelity data is evaluated at all DOE points, whereas the sampling points where high-fidelity data is evaluated are a subset of the full DOE. Figure 8.9 shows the representative DOE samples for strategies CoTPUS-(a) and (b). Nine such DOE samples for each strategy are generated†.

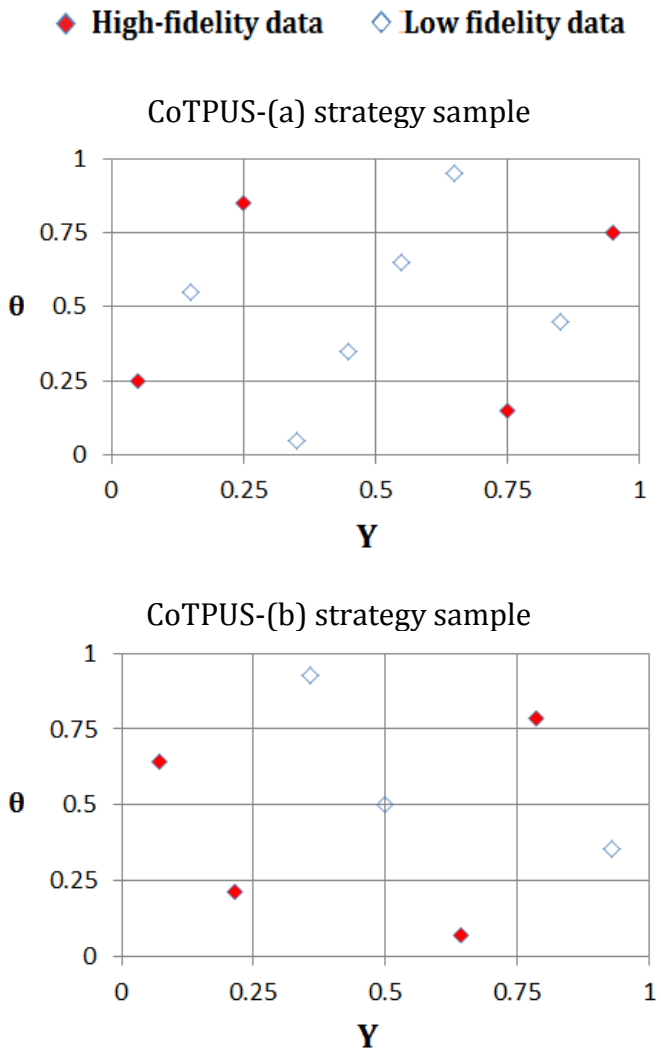

Fig. 8.9 Representative DOE samples for strategies CoTPUS-(a) and (b) using optimal Latin-hypercube method (c.f. Table 8.5 for sampling budget)

† See Appendix F

8.5 Results and discussions

8.5.1 Design optimisation using CoTPUS strategies

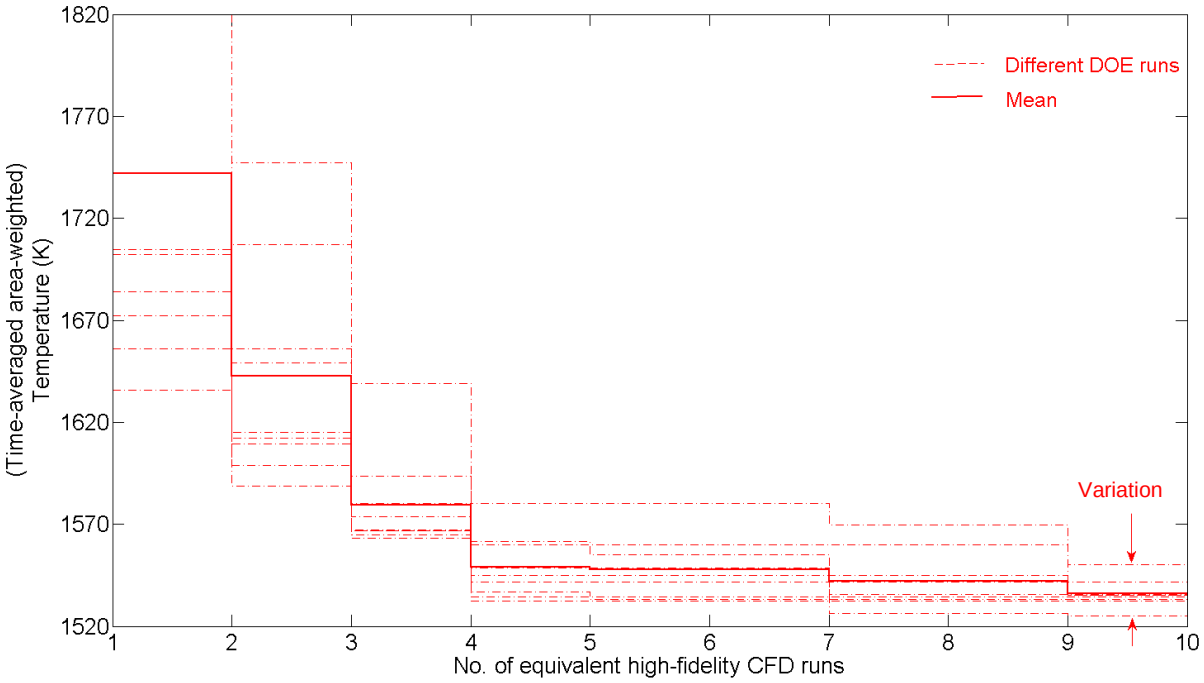

Fig. 8.10 Time-averaged area-weighted outlet temperature optimisation search histories using CoTPUS-(a) over a fixed computational budget (c.f. Table 8.5)

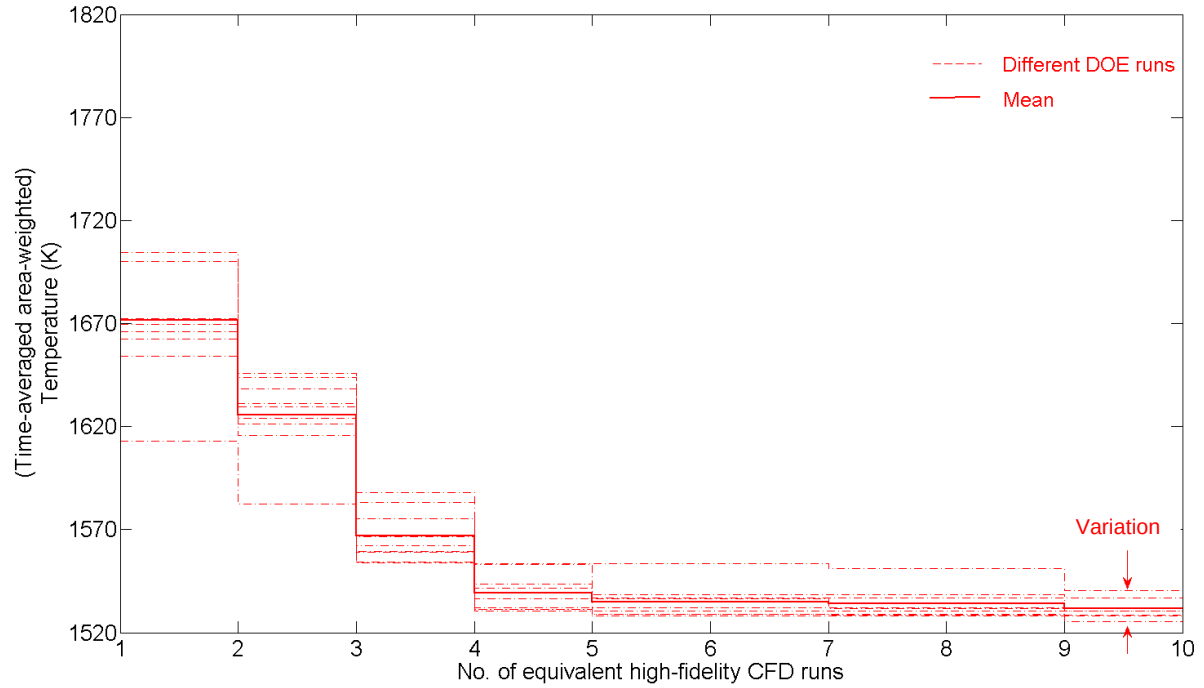

Fig. 8.11 Time-averaged area-weighted outlet temperature optimisation search histories using CoTPUS-(b) over a fixed computational budget (c.f. Table 8.5)

Figures 8.10 and 8.11 show the time-averaged area-weighted outlet temperature optimisation search histories for CoTPUS-(a) and CoTPUS-(b) strategies respectively. They also show the respective mean performances of each strategy for nine different DOE samples; over a fixed computational budget of high and low fidelity CFD runs (c.f. Table 8.5). Similar to the observation in Kriging and various co-Kriging strategies previously, the different initial samples have an effect on the way the CoTPUS design strategy progresses thus leading to a different optimal design at the end of the optimisation cycle.

A variation in the convergence behaviour of the optimisation search histories is also shown in Figures 8.10 and 8.11, which indicates that CoTPUS-(b) strategy has less variation about the mean compared to CoTPUS-(a) strategy.

8.5.2 Comparison between CoTPUS and Kriging strategy performance

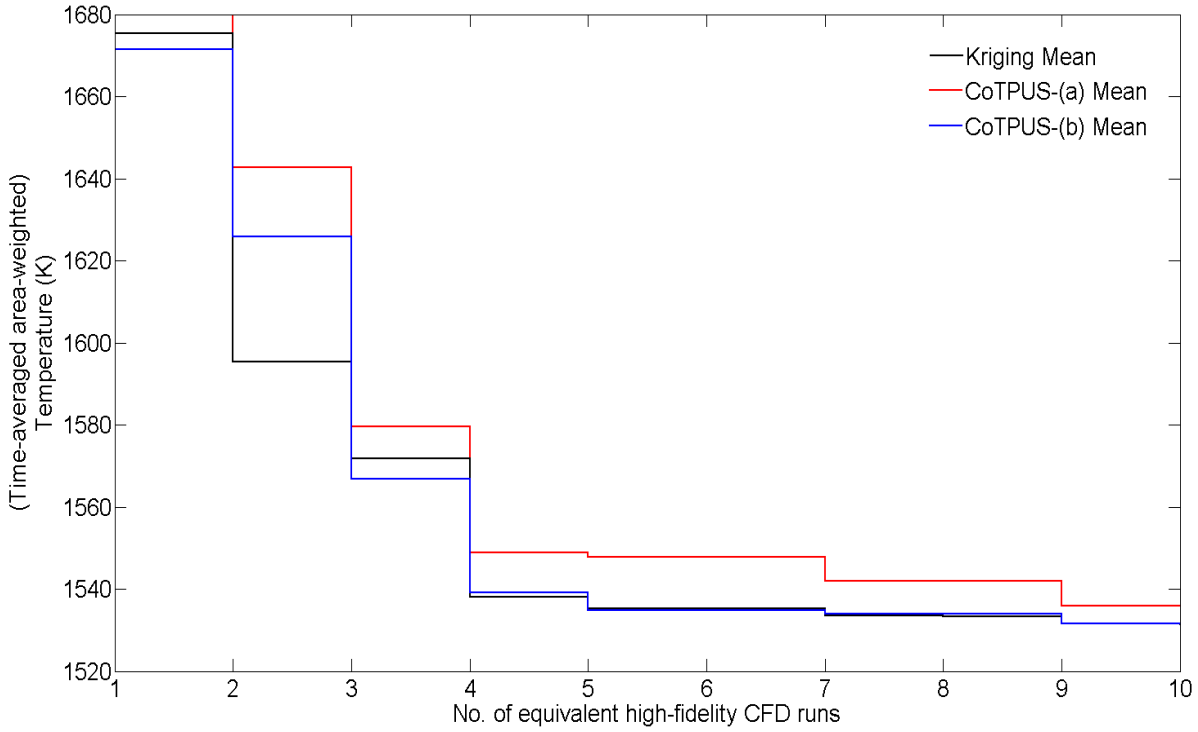

Fig. 8.12 Comparison between mean optimisation search histories of Kriging, CoTPUS-(a) and CoTPUS-(b) strategies for time-averaged area-weighted outlet temperature

Figure 8.12 shows the comparison between the mean optimisation search histories of Kriging, CoTPUS-(a) and CoTPUS-(b) strategies for time-averaged area-weighted outlet temperature. The CoTPUS-(a) strategy does not perform better than the Kriging strategy in terms of the mean convergence over the entire optimisation cycle. However, the CoTPUS-(b) strategy performs equally well compared to the Kriging strategy.

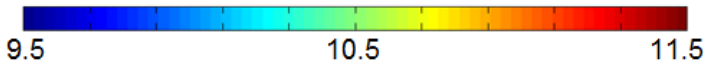

CoTPUS-(a) response surface consisting of best optimal design

(1) After DOE (2) After DOE + Updates

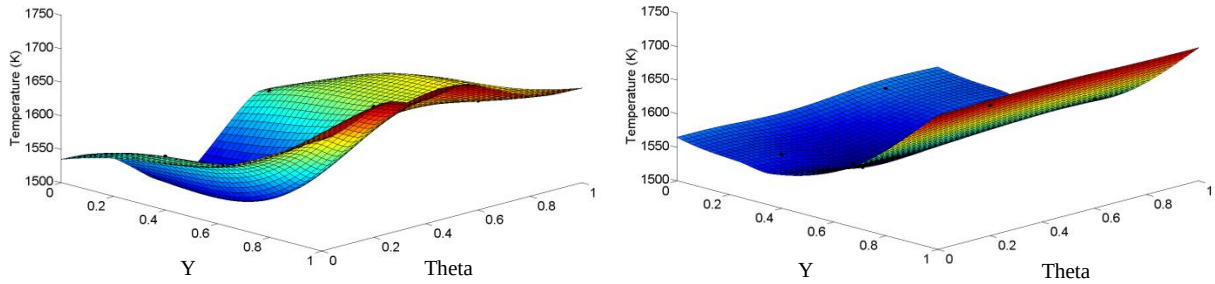

CoTPUS-(b) response surface consisting of best optimal design

(1) After DOE (2) After DOE + Updates

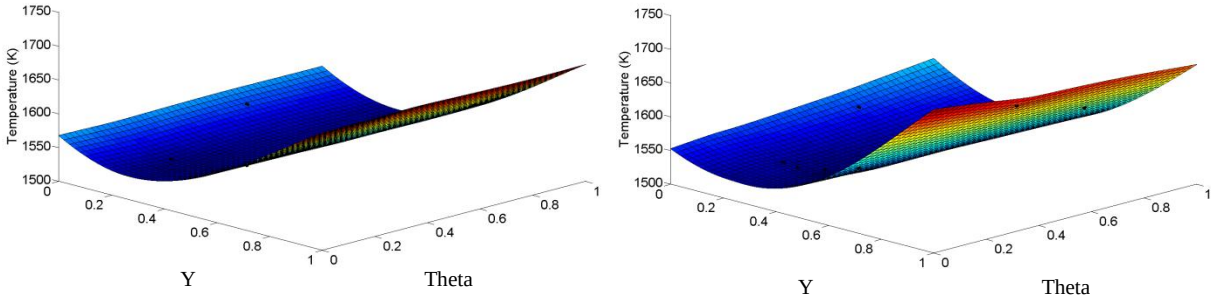

Kriging response surface consisting of best optimal design

(1) After DOE (2) After DOE + Updates

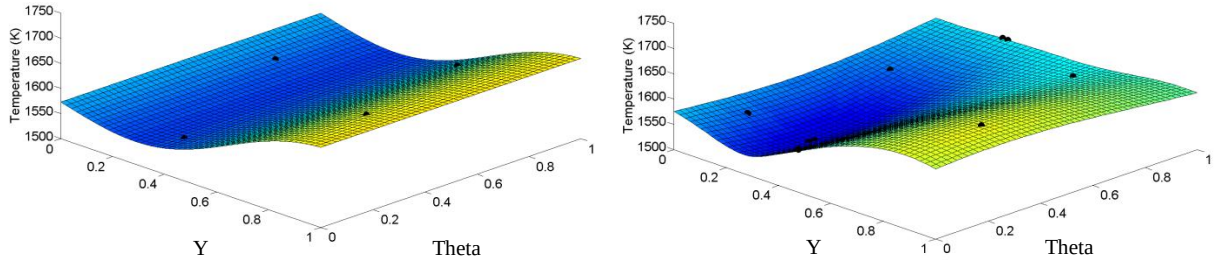

Fig. 8.13 Comparison between CoTPUS-(a), CoTPUS-(b) and Kriging response surfaces consisting of their respective best optimal designs for time-averaged area-weighted outlet temperature

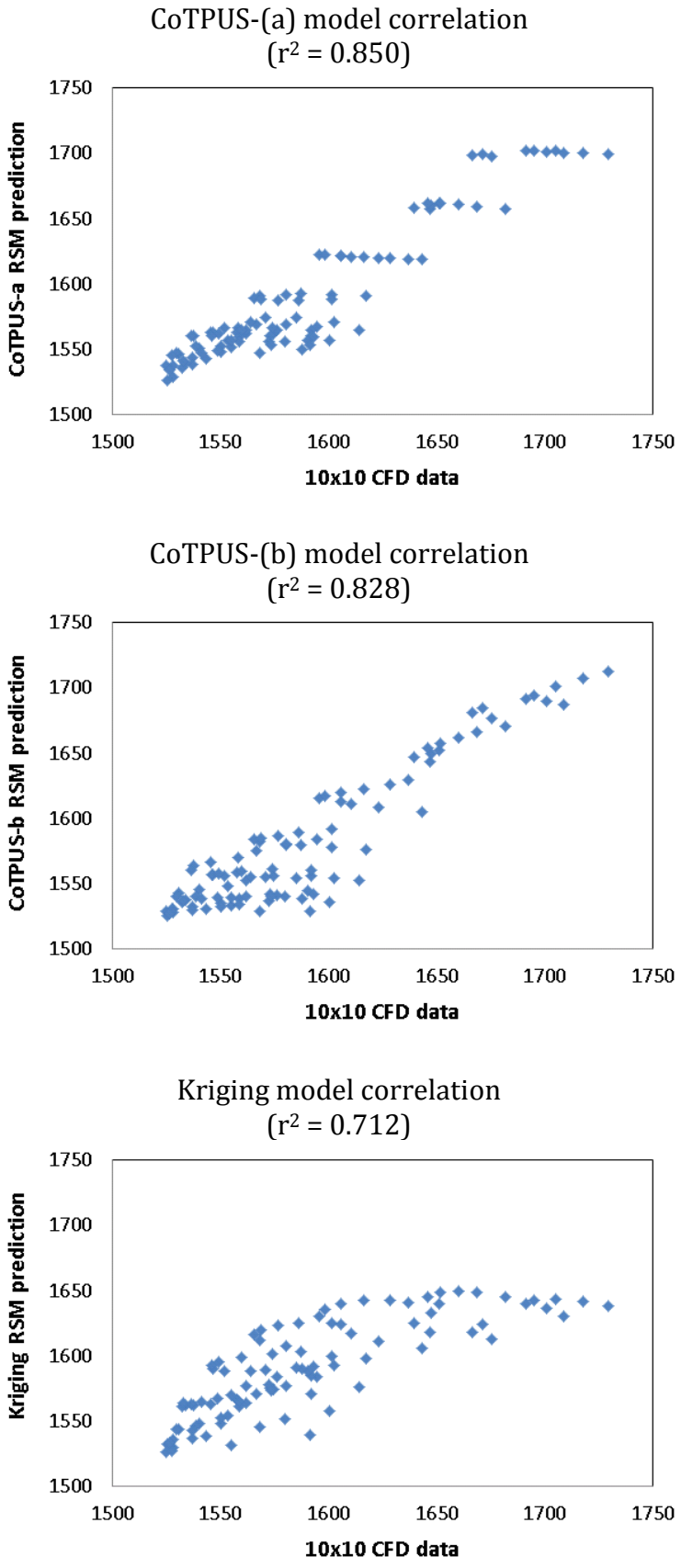

Fig. 8.14 Comparison between correlations of CoTPUS-(a), CoTPUS-(b) and Kriging RSM (after DOE + Updates) predictions with 10x10 CFD data for time-averaged area-weighted outlet temperature

Table 8.6 Comparison between the best optimal designs amongst all experiments found by Kriging and CoTPUS-(b) strategies for time-averaged outlet temperature

	Y	Θ	Time-averaged area-weighted outlet temperature (K)
Kriging	0.285	0.252	1524.82
CoTPUS-(a)	0.341	0.331	1525.32
CoTPUS-(b)	0.323	0.264	1525.23

Figure 8.13 shows the comparison between the response surfaces of CoTPUS-(a), CoTPUS-(b) and Kriging strategies containing their respective best optimal designs for time-averaged area-weighted outlet temperature. In comparison to the shape of the time-averaged outlet temperature RSM captured using 10x10 grid CFD evaluations (c.f. Figure 6.18), the CoTPUS-(b) strategy captures a more accurate shape of the response surface after both, the DOE and update stages relative to both the CoTPUS-(a) and Kriging strategies.

Figure 8.14 shows the comparison between the correlations of CoTPUS-(a), CoTPUS-(b) and Kriging RSM predictions with 10x10 CFD data. As per the scatterplots of Figure 8.14, the correlation between CoTPUS-(b) RSM prediction and 10x10 CFD data varies more linearly as compared to correlations between CoTPUS-(a) and Kriging RSM prediction with 10x10 CFD data. The best optimal designs (amongst all nine experiments) obtained by Kriging, CoTPUS-(a) and CoTPUS-(b) strategies are listed in Table 8.6.

8.6 Confidence assessment

In this section the confidence assessment on the estimated mean performances of the CoTPUS design strategies is performed to draw quantitative comparison against the Kriging strategy performance for time-averaged outlet temperature objective function. The two variants of the CoTPUS design optimisation strategy, CoTPUS-(a) and CoTPUS-(b) were applied on nine different DOE samples with mean performances shown in Figures 8.10 and 8.11 and comparison against the Kriging strategy mean performance shown in Figure 8.12.

Table 8.7 shows the relevant statistical estimates for time-averaged outlet temperature objective function data evaluated in this chapter, using strategies CoTPUS-(a) and CoTPUS-(b) in comparison against standard Kriging strategy.

Table 8.7 Relevant statistical estimates for time-average outlet temperature objective function data evaluated using strategies CoTPUS-(a) and CoTPUS-(b).

	Objective function		Sample mean (M)	Standard deviation	Standard error
Temporal domain	Time-averaged area-weighted outlet temperature	Kriging	1531.44	7.94	2.64
		CoTPUS-(a)	1535.89	6.84	2.28
		CoTPUS-(b)	1531.54	4.57	1.52

As shown in Table 8.7, the Kriging strategy has the lowest sample mean value at the end of the optimisation cycle, which is very closely matched by CoTPUS-(b) strategy. In terms of standard deviation and standard error both, CoTPUS-(a) and CoTPUS-(b) strategies perform better than the standard Kriging strategy. Overall it is observed that CoTPUS-(b) strategy has the best performance with low sample mean, standard deviation and standard error.

8.6.1 Bootstrapped CI for CoTPUS strategy

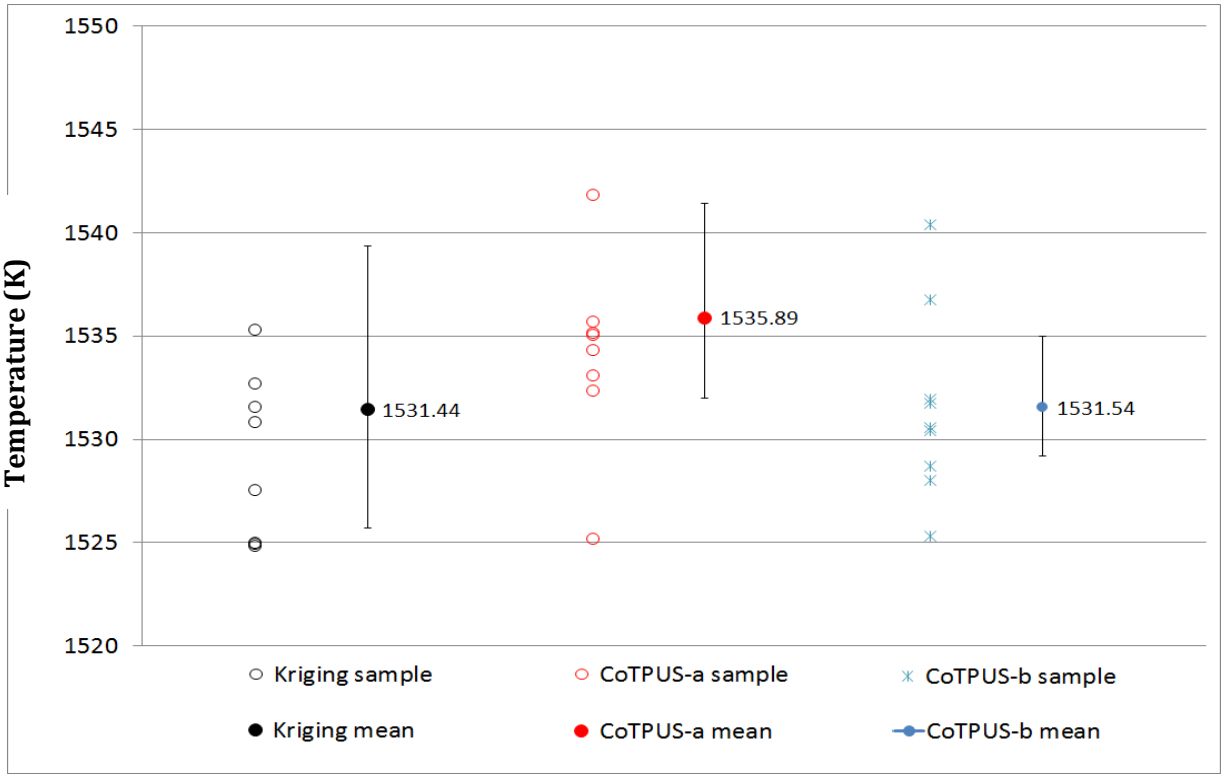

Fig. 8.15 Estimated means with 95% CI and original sample data of Kriging, CoTPUS-(a) and CoTPUS-(b) strategies for time-averaged area-weighted outlet temperature

Initially, a convergence test for bootstrap sample size B is performed to compute the confidence intervals of CoTPUS-(a) and CoTPUS-(b) strategies†. Based on this sample size B, a bootstrapped confidence interval is computed for both CoTPUS strategies.

Figure 8.15 shows the comparison between the 95% confidence intervals on the Kriging, CoTPUS-(a) and CoTPUS-(b) sample means for time-averaged area-weighted outlet temperature. The CoTPUS-(a) and CoTPUS-(b) confidence intervals are completely overlapped by Kriging strategy confidence intervals. However, the upper and lower limits of the CoTPUS-(b) strategy CI are much narrower relative to CoTPUS-(a) and Kriging strategies CI, which suggest that there is higher confidence in CoTPUS-(b) strategy's ability to have a population mean near the sample mean value.

8.7 Summary

In this chapter, two new time-parallel CFD simulation approaches are developed and tested on a two-dimensional unsteady combustor flow problem using a URANS formulation. Initially, the unsteady humming instability cycle in the combustor is simulated using a conventional time-serial methodology, which settles to the humming instability in four inlet fluctuation cycles. Later, the time-parallel simulation method-A and method-B (which involves a data fusion strategy) are developed independently and applied to simulate the humming instability cycle. Also, using time-parallel method-B, the humming cycle appears over the entire simulation time-state space. However, a clear advantage in terms of the number of inlet fluctuation cycles (or wall-clock time) required to reach the humming instability is not observed.

Further, using the time-parallel CFD simulation method-A, the intermediate un-converged solution states, which are observed in the process of convergence towards the final solution, are used to seed multiple levels of fidelity within the framework of a co-Kriging based design optimisation strategy, designated here as CoTPUS. The main advantage of the CoTPUS strategy over previously proposed temporal domain co-Kriging strategies CoSUS, CoTUS and CoSTUS (c.f. Chapter 7) is the possibility of setting up only a single combustor CFD simulation from which multiple fidelity levels are available. Also each high-fidelity time-parallel analysis provides a low-fidelity analysis for free, thus increasing the total number of low-fidelity data and further enhancing the co-Kriging models quality.

Two variants of CoTPUS strategy, CoTPUS-(a) and CoTPUS-(b), are investigated for combustor design optimisation over nine different samples. The mean performances of both strategies are compared against the Kriging strategy, which revealed that the CoTPUS-(a) strategy does not perform better than the standard Kriging strategy; whereas CoTPUS-(b) performs equally well. The bootstrapped 95% confidence interval (CI) evaluation on the sample mean performance of all three strategies, at the end of the

† See Appendix F

optimisation cycle, suggests that there is a significant overlap between the CI's. However, the upper and lower limits of the CoTPUS-(b) strategy CI are much narrower relative to the Kriging CI, indicating higher confidence in the CoTPUS-(b) strategy's ability to generate a population mean near the sample mean value.

Overall, the CoTPUS-(b) design strategy performs better than the standard Kriging based design strategy for the time-averaged area-weighted outlet temperature objective function.

Chapter 9

Conclusions and future work recommendations

9.1 Conclusions

Unsteady computational fluid dynamics (CFD) simulations are routinely used in the gas turbine industry to predict and visualize the complex reacting flow dynamics, combustion environment and emissions performance of a combustor. Given the complexity involved in obtaining accurate flow predictions and, due to the expensive nature of the simulations, conventional techniques for unsteady CFD based combustor design optimisation (e.g. direct global optimisation methods such as genetic algorithm or simulated annealing) are often ruled out, primarily due to the limits on available computing resources and time.

The design optimisation process normally requires a large number of analyses of the objective and constraint functions which necessitates a careful selection of fast, reliable and efficient computational methods for the unsteady CFD analysis and the optimization process. The current state-of-the-art in the context of combustor design and optimisation is the use of Kriging surrogate model based design strategies, which reduce the total number of high-fidelity unsteady CFD analyses required to reach an optimal design configuration. However, Kriging feasibility is limited by the total number of design variables, objective and constraint functions, as computationally expensive high-fidelity CFD analyses are typically used to construct the surrogate model.

To address these challenges an effort was made in this research to develop more efficient combustor design strategies in terms of minimizing the total number of high fidelity CFD runs required and to accelerate the process of finding a good design earlier

in the optimisation process. This resulted in novel contributions being made to the field of unsteady CFD based combustor design optimisation which are as follows:

(1) Development of a time-parallel CFD simulation method for solving transient combustor reactive flow

- Employing a temporal domain decomposition methodology
- Applied to simulate combustor reactive flow with and without data fusion

(2) Development and performance assessment of multi-fidelity design strategies using

(a) **co**-Kriging of **t**ime-**p**arallel **u**nsteady RANS **s**imulations (**CoTPUS**)

- Employing a time-parallel CFD simulation method providing multiple levels of simulation fidelities from a single simulation
    - Low-fidelity model: Initial iterations of time-parallel CFD simulation
    - High-fidelity model: Final iteration of time-parallel CFD simulation

(b) **co**-Kriging of **s**teady and **u**nsteady RANS **s**imulations (**CoSUS**)

- Employing steady and unsteady combustor RANS simulations on the same spatial resolution grid,
    - Low-fidelity model: Steady-state RANS simulation
    - High-fidelity model: Unsteady RANS simulation

(c) **co**-Kriging of varying **t**ime-step sizes **u**nsteady RANS **s**imulations (**CoTUS**)

- Employing two unsteady combustor RANS simulations with different time-step sizes on the same spatial resolution grid,
    - Low-fidelity model: Coarse time-step size unsteady RANS simulation
    - High-fidelity model: Fine time-step size unsteady RANS simulation

(d) **co**-Kriging of varying **s**patio-**t**emporal resolution **u**nsteady RANS **s**imulations (**CoSTUS**)

- Employing combustor RANS simulations with varying spatial and temporal resolution grids for combustor design optimisation

- Low-fidelity model: Coarse grid and time-step size unsteady RANS simulation
- High-fidelity model: Fine grid and time-step size unsteady RANS simulation

Additionally, each of the developed strategies has been assessed for confidence levels using the computational experiment data and a Bootstrap methodology. The results are then compared against a well-established Kriging based combustor design strategy.

In this thesis, initially, research was conducted in understanding modern lean burn combustion system configuration and design challenges (c. f. section 1.1.1) faced within Rolls-Royce PLC. Key reactive flow-field phenomena were identified which are of interest from a design optimisation perspective. Further, due to the very high computational cost of Rolls-Royce 3D combustor simulations, a 2D lean burn combustor test problem was identified from the literature as a practical problem for developing new design strategies.

The test combustor model selected to develop various multi-fidelity design optimisation strategies was the one used by Keller et al. (1984) in an experimental study of mechanisms of instabilities in turbulent combustion leading to flashback. A numerical study of steady and unsteady turbulent reactive processes behind a profiled backward-facing step in the 2D combustor was presented in Chapter 5. The steady RANS study identified a flame-front established behind the flame-stabilizer step whereas the unsteady RANS analysis revealed time-dependent, periodic humming cycle instability behind the step due to a forced sinusoidal velocity fluctuation at the combustor inlet. Thermal NO formation inside the combustor was also analyzed in both spatial and temporal domains.

Based on the combustor flow analysis, a Kriging based design optimisation strategy was applied in Chapter 6 to design a flame-stabilizer step by influencing the flame/vortex dynamics downstream. The objective functions used for design optimisation were the RMSD outlet temperature profile and thermal NO in the spatial domain. For design optimisation in the temporal domain, a humming cycle averaged area-weighted outlet temperature and thermal NO was used as the objective function. The Kriging design strategies for all objective functions were applied on nine different initial samples which showed the variation in the optimisation search histories convergence to the final optimal design. 95% bootstrapped confidence intervals were also evaluated on the mean performance of the Kriging strategy.

Chapter 7 presented various co-Kriging based multi-fidelity design optimisation strategies both in the spatial and temporal domains. In the spatial domain, a co-Kriging strategy using two different grid levels (CoTGL) was applied to design the flame

stabilizer step within a fixed computational budget. In the temporal domain, co-Kriging strategies using (a) steady and unsteady RANS simulations (CoSUS), (b) varying time-step sizes unsteady RANS simulations (CoTUS) and (c) varying spatio-temporal unsteady RANS simulations (CoSTUS) were developed and used to design the flame-stabilizer step. All co-Kriging based design strategies were repeated on nine different initial samples, which revealed how the convergence search history varied, leading to slightly different optimal designs at the end of the computational budget. Later, the statistics of interest i.e. mean performance of each co-Kriging based design strategy over all the samples were compared against the mean performance of the Kriging based design strategy within the fixed computational budget. This showed that strategy CoTGL in the spatial domain (for steady outlet temperature profile and thermal NO) and strategies CoSUS and CoSTUS in the temporal domain (for time-averaged outlet thermal NO) found a good design earlier in the design process, after the DOE stage, compared to the standard Kriging strategy. However, the standard Kriging strategy outperforms all proposed co-Kriging based multi-fidelity strategies at the end of the optimisation cycle. Also, the comparison between the 95% bootstrapped confidence intervals of Kriging and all co-Kriging based design strategies showed that the lower and upper bounds of the Kriging confidence interval are narrower compared to the confidence interval of any other co-Kriging based multi-fidelity design strategy. This indicates that there is a greater confidence in the Kriging strategy's ability to generate a population mean near the sample mean value.

In Chapter 8, a time-parallel CFD simulation approach for solving transient combustor flow was developed using a URANS formulation. Initially, the unsteady humming instability cycle in the combustor was simulated using a conventional time-serial methodology, which settled into the humming instability in four inlet fluctuation cycles. The two variants of the time-parallel CFD simulation approach, method-A and method-B (which involved a data fusion strategy) also successfully captured the humming instability cycle. However, a clear advantage in terms of the number of inlet fluctuation cycles (or wall-clock time) required to reach the humming instability was not observed. Further, using the time-parallel CFD simulation method-A, the intermediate un-converged solution states observed in the process of convergence towards the final solution, were used to seed multiple levels of fidelity within the framework of a co-Kriging based design optimisation strategy, designated as CoTPUS (co-Kriging using time-parallel unsteady RANS simulations). The two variants of CoTPUS strategy, CoTPUS-(a) and CoTPUS-(b), were investigated for combustor design optimisation over nine different samples. The mean performances of both strategies were compared against the Kriging strategy, which revealed that the CoTPUS-(a) strategy does not perform better than the standard Kriging strategy; whereas CoTPUS-(b) performs equally well. The bootstrapped 95% confidence intervals (CI) evaluation on the sample mean performance of all three strategies, at the end of the optimisation cycle, suggested that the Kriging strategy performs better than CoTPUS-(a), however, the upper and lower limits of the CoTPUS-(b) strategy CI are much narrower relative to the Kriging CI,

indicating higher confidence in the CoTPUS-(b) strategy's ability to generate a population mean near the sample mean value. Overall, the CoTPUS-(b) design strategy performed better than the standard Kriging based design strategy for the time-averaged area-weighted outlet temperature objective function. Additionally, the key advantage of the CoTPUS strategy over other temporal domain co-Kriging strategies CoSUS, CoTUS and CoSTUS is the possibility of setting up only a single combustor CFD simulation from which multiple fidelity levels are available. Also each high-fidelity time-parallel analysis provides a low-fidelity analysis for free, thus increasing the total number of low-fidelity data and further enhancing the co-Kriging models quality.

In conclusion, this research suggests that the developed co-Kriging based design optimisation strategies (CoTGL, CoSUS, CoSTUS and CoTPUS) performs as well as the standard Kriging based design strategy with evidence of the co-Kriging based strategies ability to find a good design earlier in the process of optimisation. Overall, for unsteady CFD based combustor design optimisation, a time-parallel CFD simulation based co-Kriging strategy (CoTPUS) performs better than the standard Kriging based design strategy in terms 95% confidence intervals.

9.2 Future work recommendations

Although many different co-Kriging based multi-fidelity design strategies were investigated in this thesis for combustor design optimisation in comparison to the Kriging based design strategy, using steady and unsteady CFD, there are still a number of areas for investigation in the future. The following are the future work recommendations:

First, the co-Kriging based multi-fidelity design strategy's ability to find an optimum design within the design space is dependent on the quality of the information available from low-fidelity model which could help in reducing the total amount of computational effort. In the co-Kriging approach applied in this thesis, the cost ratio between low and high fidelity models was used as the basis to determine the number of low and high fidelity CFD evaluations to be performed in each strategy. It was observed that with low cost ratios (e.g. expensive evaluation ~ twice cheap evaluation in strategy CoTUS), the amount of information available from low-fidelity model reduces due to less data points evaluation. With high cost ratios (e.g. expensive evaluation ~ eighteen times cheap evaluation in strategy CoSTUS), the amount of information available from the low-fidelity model increases due to more availability of data points. However, due to a very coarse low-fidelity model being evaluated, the quality of information available may not be very helpful to construct a co-Kriging model with good prediction capability. Thus it is necessary to establish a methodology, which could be referred to as a 'multi-fidelity

cost ratio test', where an optimal cost ratio between low and high-fidelity models could be setup.

Second, the proposed time-parallel CFD simulation approach for evaluating unsteady combustor flow did not provide an advantage over the time-serial CFD method and hence requires further attention, especially from the perspective of its iterative strategy. The progress of time-parallel CFD simulations towards convergence depends on the quality of information available at the initialization step i.e. from the coarse time-step size time-serial CFD simulation. Further investigation is needed in this direction with respect to different time-step size initialisation simulations. For the time-parallel CFD simulation employing data fusion, further investigation is needed to establish an optimal blending factor.

Third, amongst all proposed co-Kriging based design strategies using unsteady CFD, the time-parallel CFD simulation multi-fidelity design strategy appears to be the most promising for superior performance over the standard Kriging based strategy. This strategy needs further development, especially incorporating the data-fusion strategy, which could enhance the quality of the low-fidelity model further.

In addition to the above recommendations, all the proposed unsteady CFD based co-Kriging strategies needs to be further tested on higher dimensional studies including three and four variable design problems and three dimensional combustors. The Rolls-Royce three-dimensional lean burn combustor is the design problem to which the developed multi-fidelity design optimisation strategies would be applied. Further these strategies would also be formulated in to multi-objective co-Kriging based combustor design optimisation strategies for handling real-world combustor design challenges.

Appendices

Kriging model

A.1 Kriging methodology

Given two vectors of variables $\mathbf{X^i}$ and $\mathbf{X^j}$, each of length $\boldsymbol{l}$, the objective function values $\mathbf{Y}(\mathbf{X^i})$ and $\mathbf{Y}(\mathbf{X^j})$, depends on the distance between $\mathbf{X^i}$and $\mathbf{X^j}$. The function values will tend to be small if the distance $\|\mathbf{X^i} - \mathbf{X^j}\|$ is small. This can be statistically modeled by assuming the correlation between the two sets of random variables objective functions, $\mathbf{Y}(\mathbf{X^i})$ and $\mathbf{Y}(\mathbf{X^j})$, to be given by

$$\text{Corr}[\mathbf{Y}(\mathbf{X^i})\ \mathbf{Y}(\mathbf{X^j})] = \exp\left[-\sum_{k=1}^{l} \boldsymbol{\theta}_k \|\mathbf{X^{i_k}} - \mathbf{X^{j_k}}\|^{\boldsymbol{p}_k}\right] \qquad \text{Eq. (A.1)}$$

If $\mathbf{X^i} = \mathbf{X^j}$, the correlation is 1 and if $\|\mathbf{X^i} - \mathbf{X^j}\| \to \infty$, the correlation tends to zero. $\boldsymbol{\theta}_k$ and $\boldsymbol{p}_k$ are the hyper-parameters of the Kriging model, which are tuned to the response**,** in order to make new prediction $\widehat{\mathbf{Y}}(\mathbf{X})$. The hyperparameter $\boldsymbol{\theta}_k$ determines the rate of correlation decreases and is basically a width parameter which tells how far the influence of the sample point extends. It helps in high-dimensional problems to identify the most active variables by determining its relative size. The hyperparameter $\boldsymbol{p}_k$ is the smoothness parameter, which determines the smoothness of the function in the k^{th} coordinate direction. The value of $\boldsymbol{p}_k = 2$ help model smooth functions, whereas values of $\boldsymbol{p}_k$ close to 0 models non-smooth functions.

The functions value could be represented by a vector $\mathbf{Y}$ consisting of a series of n objective function values given by

$$\mathbf{Y} = \begin{bmatrix} \mathbf{Y}(\mathbf{X^1}) \\ . \\ . \\ . \\ \mathbf{Y}(\mathbf{X^n}) \end{bmatrix} \quad \text{Eq. (A.2)}$$

where the mean is $\mathbf{1}\mu$ and $\mathbf{1}$ is a n x 1 vector of ones. The covariance of $\mathbf{Y}$ is equal to

$$\text{Cov}(\mathbf{Y}) = \sigma^2\mathbf{R} \quad \text{Eq. (A.3)}$$

where σ^2 the variance and $\mathbf{R}$ is the n x n correlation matrix whose (i, j) elements are given by Equation (A.1).

The model parameters to estimate include μ, σ^2, $\boldsymbol{\theta}_k$ and $\boldsymbol{p}_k$. Values of hyperparameters $\boldsymbol{\theta}_k$ and $\boldsymbol{p}_k$, are chosen to maximize the likelihood on the observed data set $\mathbf{Y}$. This maximum likelihood function is written as

$$\frac{1}{(2\pi)^{\frac{n}{2}}(\sigma^2)^{\frac{n}{2}}|\mathbf{R}|^{\frac{1}{2}}}\exp\left[\frac{-(\mathbf{Y}-\mathbf{1}\mu)^{\mathrm{T}}\mathbf{R}^{-1}(\mathbf{Y}-\mathbf{1}\mu)}{2\sigma^2}\right] \quad \text{Eq. (A.4)}$$

and after taking natural log of Equation (A.4) and ignoring the constant terms,

$$-\frac{n}{2}\log(\sigma^2) - \frac{1}{2}\log(|\mathbf{R}|) - \frac{(\mathbf{Y}-\mathbf{1}\mu)^{\mathrm{T}}\mathbf{R}^{-1}(\mathbf{Y}-\mathbf{1}\mu)}{2\sigma^2} \quad \text{Eq. (A.5)}$$

Setting the derivatives of Equation (A.4) with respect to σ^2 and μ equal to zero, the optimal values of mean ($\hat{\mu}$) and variance ($\hat{\sigma}$) as functions of $\mathbf{R}$ could be obtained as:

$$\hat{\mu} = \frac{\mathbf{1}^{\mathrm{T}}\mathbf{R}^{-1}\mathbf{Y}}{\mathbf{1}^{\mathrm{T}}\mathbf{R}^{-1}\mathbf{1}} \quad \text{Eq. (A.6)}$$

$$\hat{\sigma} = \frac{(\mathbf{Y}-\mathbf{1}\hat{\mu})^{\mathrm{T}}\mathbf{R}^{-1}(\mathbf{Y}-\mathbf{1}\hat{\mu})}{n} \quad \text{Eq. (A.7)}$$

Substituting the Equations (A.6) and (A.7) into Equation (A.5) gives the concentrated log likelihood function

$$-\frac{n}{2}\log(\hat{\sigma}^2) - \frac{1}{2}\log(|\mathbf{R}|) \qquad \text{Eq. (A.8)}$$

which depends only on correlation $\mathbf{R}$ and hence on the hyperparameters $\boldsymbol{\theta}_k$ and $\boldsymbol{p}_k$. Equation (A.5) is maximized to get the estimates $\widehat{\boldsymbol{\theta}}_k$ and $\widehat{\boldsymbol{p}}_k$ and using these, $\hat{\mu}$ and $\hat{\sigma}$ are computed from Equations (A.6) and (A.7) respectively. The estimated parameters reflect the pattern of variation in the observed data. With fixed estimated parameters, to predict the value $\widehat{\mathbf{Y}}\mathbf{(X)}$ at a new location $\mathbf{X}$ which is consistent with the observed data, an augmented log-likelihood function is computed.

The augmented vector of objective function values is given by $\widetilde{\mathbf{Y}} = (\mathbf{Y^T}, \widehat{\mathbf{Y}})^{\mathrm{T}}$ when augmented by new prediction $\widehat{\mathbf{Y}}$, the value of which is to be determined.

The vector of correlations of $\widehat{\mathbf{Y}}\mathbf{(X)}$ with $\mathbf{Y}(\mathbf{X^i})$, for $i = 1, \ldots, n$:

$$\mathbf{r} = \begin{pmatrix} \mathrm{Corr}\left[\widehat{\mathbf{Y}}(\mathbf{X}), \mathbf{Y}(\mathbf{X^1})\right] \\ \vdots \\ \mathrm{Corr}\left[\widehat{\mathbf{Y}}(\mathbf{X}), \mathbf{Y}(\mathbf{X^n})\right] \end{pmatrix} \qquad \text{Eq. (A.9)}$$

The augmented correlation matrix is:

$$\widetilde{\mathbf{R}} = \begin{pmatrix} \mathbf{R} & \mathbf{r} \\ \mathbf{r^T} & 1 \end{pmatrix} \qquad \text{Eq. (A.10)}$$

The augmented log-likelihood function (with constant terms ignored) is:

$$-\frac{n}{2}\log(\hat{\sigma}^2) - \frac{1}{2}\log(|\widetilde{\mathbf{R}}|) - \frac{(\widetilde{\mathbf{Y}} - \mathbf{1}\hat{\mu})^{\mathrm{T}}\widetilde{\mathbf{R}}^{-1}(\widetilde{\mathbf{Y}} - \mathbf{1}\hat{\mu})}{2\hat{\sigma}^2} \qquad \text{Eq. (A.11)}$$

in which only the last term is dependent on $\widehat{\mathbf{Y}}$ and considered for maximization.

Substituting $\widetilde{\mathbf{Y}}$ and $\widetilde{\mathbf{R}}$ in Equation (A.5):

$$-\frac{\begin{pmatrix}\mathbf{Y}-\mathbf{1}\hat{\mu}\\ \hat{Y}-\hat{\mu}\end{pmatrix}^{\mathrm{T}}\begin{pmatrix}\mathbf{R} & \mathbf{r}\\ \mathbf{r}^{\mathbf{T}} & 1\end{pmatrix}^{-1}\begin{pmatrix}\mathbf{Y}-\mathbf{1}\hat{\mu}\\ \hat{Y}-\hat{\mu}\end{pmatrix}}{2\sigma^2} \qquad \text{Eq. (A.12)}$$

Using partitioned inverse formula (Theil, 1971) the expression for $\widetilde{\mathbf{R}}^{-\mathbf{1}}$ is then substituted in Equation (A.6). The augmented log-likelihood function is then expressed as a quadratic function of $\widehat{\mathbf{Y}}$ (Jones, 2001). Setting its derivative with respect $\widehat{\mathbf{Y}}$ equal to zero and solving for $\widehat{\mathbf{Y}}$ gives the Kriging predictor:

$$\widehat{\mathbf{Y}}(\mathbf{X}) = \hat{\mu} + \mathbf{r}^{T}\mathbf{R}^{-1}(\mathbf{Y} - \mathbf{1}\hat{\mu}) \qquad \text{Eq. (A.13)}$$

Consideration for numerical noise:

The CFD simulations, although deterministic, involves discretization and iterative solution procedure, thus making itself susceptible to numerical noise. Due to presence of noise, the resulting landscape is no longer smooth and continuous but appears as a random scatter about the smooth trend. Hence, given the potentially noisy nature of CFD simulations due to discretization and iterative solution, during the construction of a surrogate model, it is very important to consider regression to counter numerical noise (Forrester et al., 2006). With regression applied to often interpolation Kriging technique, the observed data does not necessarily correlate with the resulting model. In correlation matrix **R**, a constant term λ is added to the diagonal, resulting in **R**+λ**I** , where **I** is an *n* x *n* identity matrix.

The estimated mean and variance as per Equations (A.6) and (A.7) respectively are then given as:

$$\hat{\mu} = \frac{\mathbf{1}^{\mathrm{T}}(\mathbf{R} + \lambda\mathbf{I})^{-1}\mathbf{Y}}{\mathbf{1}^{\mathrm{T}}(\mathbf{R} + \lambda\mathbf{I})^{-1}\mathbf{1}} \qquad \text{Eq. (A.14)}$$

$$\hat{\sigma} = \frac{(\mathbf{Y} - \mathbf{1}\hat{\mu})^{\mathrm{T}}(\mathbf{R} + \lambda\mathbf{I})^{-1}(\mathbf{Y} - \mathbf{1}\hat{\mu})}{n} \qquad \text{Eq. (A.15)}$$

Thus with regression Kriging, $\boldsymbol{\theta}_k$, $\boldsymbol{p}_k$ and λ are the hyperparameters to be estimated for construction the surrogate model.

A.2 List of RSM techniques and update methodologies

Table A.1 Different types of response surfaces and search methods as classified by Jones (2001)

(1) Response surfaces			(2) Update point search method					
			Two-stage approach				One-stage approach	
			Minimize response surface (or best predicted point)	Minimize a lower bounding function	Maximize the probability of improvement	Maximize the expected improvement	Goal seeking - to find point that achieves a given goal	Optimisation - to find point that minimizes the objective function
Non-interpol-ating	Quadratic polynomial		✓	X	X	X	X	X
Interpol-ating	Fixed basis function	Cubic spline, Thin plate spline, Multi-quadric	✓	X	X	X	✓	✓
	Tuned basis function	Kriging	✓	✓	✓	✓	✓	✓

Reactive flow modelling

B.1 Reynolds and Favre averaging

Turbulent reacting flow comprises of fluctuating velocity field, which helps to mix all transported quantities including momentum, energy and species concentration, also causing the fluctuation of the transported quantities themselves (Peters, 2000). The fluctuations exist from smallest to largest scales, at high and low frequency, and are very expensive to resolve directly (e.g. using DNS). However, the instantaneous (or exact) governing equations (see Equations 3.2, 3.8, 3.9 and 3.10) can be time-averaged, ensemble-averaged, mass-weighted averaged (or density weighted) or filtered to remove small scale turbulent motions and to be replaced by a model to simulate their behaviour. This reduces the computational cost, making it practical to simulate turbulent reacting flow.

In Reynolds-averaging, any solution variable f_i can be split into its mean (ensemble averaged or time-averaged) component and fluctuating contribution

$$f_i = \overline{f}_i + f_i' \qquad \text{Eq. (B.1)}$$

where $\overline{f}_i$ and f_i' are the mean (averaged) and fluctuating components (i = 1, 2, 3), respectively. The averaged component is usually defined as an ensemble-average (i.e. average of a large number of instances at the same instant of the same flow-field). For steady mean flow, this average is replaced by a time-average over a sufficiently long period of time, t

$$\overline{f}_i = \frac{1}{t}\int_0^t f_i(t')dt' \qquad \text{Eq. (B. 2)}$$

The strength of turbulence is given by turbulence intensity *I*:

$$I = \frac{\sqrt{f'^2}}{\overline{f}} \qquad \text{Eq. (B.3)}$$

In turbulent combustion with turbulence intensity, turbulent kinetic energy and its distribution over different length scales interact with the flame (Poinsot and Veynante, 2005).

Substituting Reynolds averaged quantities (using Equations B.1 and B.2) in the instantaneous continuity equation gives (B.f. Eq. 3.2) gives:

$$\frac{\partial\overline{\rho}}{\partial t} + \frac{\partial}{\partial x_i}(\overline{\rho u}_i) = -\frac{\partial}{\partial x_i}\left(\overline{\rho' u'}_i\right) \qquad \text{Eq. (B.4)}$$

which contains the unclosed quantity $\overline{\rho' u'}_i$ corresponding to the correlation between density and velocity fluctuations, and requires modelling as the mass source term. This complexity, introduced by Reynolds averaging with regards to unclosed quantities, is particularly critical for the reaction source terms in the species equation and energy equation (Echekki, 2011). From a combustion CFD perspective, this process is difficult to handle and to avoid this, mass-weighted (or density weighted) averaging called Favre averaging is preferred (Favre, 1969; Williams, 1985; Kuo, 1986). The Favre-average $\tilde{f}_i$ is expressed as

$$\tilde{f}_i = \frac{\overline{\rho f}}{\overline{\rho}} \qquad \text{Eq. (B.5)}$$

Any solution variable f_i can be split into a Favre mean and fluctuating component

$$f_i = \tilde{f}_i + f_i'' \qquad \text{Eq. (B.6)}$$

$$\text{with } \widetilde{f''}_i = 0$$

The symbol '∼' denotes the density-weighted ensemble average. With density-weighted averaging the need to explicitly represent the density-momentum and density-scalar correlations is eliminated (Kuo, 1986; Poinsot and Veynante, 2005). The Favre-averaged continuity, momentum, species and energy equations are now given as:

Continuity equation:

$$\frac{\partial \overline{\rho}}{\partial t} + \frac{\partial}{\partial x_i}(\overline{\rho}\tilde{u}_i) = 0 \qquad \text{Eq. (B.7)}$$

Momentum equation:

$$\frac{\partial}{\partial t}(\overline{\rho}\tilde{u}_j) + \frac{\partial}{\partial x_i}(\overline{\rho}\tilde{u}_i\tilde{u}_j) = -\frac{\partial \overline{p}}{\partial x_j} + \frac{\partial}{\partial x_i}(\overline{\tau}_{ij} - \overline{\rho}\widetilde{u''_\iota u''_j}) \qquad \text{Eq. (B.8)}$$

Species equation:

$$\frac{\partial}{\partial t}((\overline{\rho}\tilde{Y}_k) + \frac{\partial}{\partial x_i}(\overline{\rho}\tilde{u}_i\tilde{Y}_k) = -\frac{\partial}{\partial x_i}(\overline{V_{k,i}Y_k} + \overline{\rho}\widetilde{u''_\iota Y''_k}) + \overline{\dot{\omega}}_k \qquad \text{Eq. (B.9)}$$

For k = 1 to N

Energy equation:

$$\frac{\partial}{\partial t}(\overline{\rho}\tilde{h}_s) + \frac{\partial}{\partial x_i}(\overline{\rho}\tilde{u}_i\tilde{h}_s) = \overline{\dot{\omega}}_T + \frac{\overline{Dp}}{Dt} + \frac{\partial}{\partial x_i}\left(\overline{\lambda\frac{\partial T}{\partial x_i}} - \overline{\rho}\widetilde{u''_\iota h''_s}\right) + \frac{\partial}{\partial x_i}\overline{(\rho\sum_{k=1}^{N} h_{s,k}Y_kV_{k,i})} + \overline{\tau_{ij}\frac{\partial u_i}{\partial x_j}} + \overline{\dot{Q}} + \overline{\rho\sum_{k=1}^{N} Y_k f_{k,i}V_{k,i}} \qquad \text{Eq. (B.10)}$$

where

$$\frac{\overline{Dp}}{Dt} = \frac{\partial \overline{p}}{\partial t} + \overline{u_i\frac{\partial p}{\partial x_i}} = \frac{\partial \overline{p}}{\partial t} + \tilde{u}_i\frac{\partial \overline{p}}{\partial x_i} + \overline{u''_i\frac{\partial p}{\partial x_i}}$$

Using Favre-averaged Equations (B.7) to (B.10), the turbulent reacting flow can be effectively modelled; however it requires proper closures for the unknown quantities (Kuo, 1986; Poinsot and Veynante, 2005). These are Reynolds stresses ($\widetilde{u''_i u''_j}$), species ($\widetilde{u''_i Y''_k}$) and enthalpy ($\widetilde{u''_i h''_s}$) turbulent fluxes, laminar diffusive fluxes for species or enthalpy ($\overline{V_{k,i} Y_k}$), species chemical reaction rates ($\overline{\dot{\omega}_k}$) and pressure–velocity correlation ($\overline{u''_i \frac{\partial p}{\partial x_i}}$). Of these various unknown quantities, only Reynolds stresses closure using a turbulence model is discussed here. For more detail on other closure strategies refer to Kuo (1986), Poinsot and Veynante (2005), Echekki (2011).

B.2 Turbulence model

From an engineering perspective, it is the mean reacting flow and certain mean quantities that are of prime focus. The Reynolds-averaged or Favre-averaged momentum equations contain the unknown quantities such as $\overline{u'_i u'_j}$ or $\widetilde{u''_i u''_j}$ respectively, known as Reynolds stresses. These terms requires a closure and a turbulence model is often employed to model the behaviour of Reynolds stresses and its effect on the mean flow behaviour.

The turbulence models for reacting flows are similar to models used for non-reacting flows modified in terms of Favre averaging. The classical methods for turbulence modelling could be considered in two categories. One based on the Boussinesq hypothesis as proposed by Joseph Boussinesq (1887) viz. zero-equation mixing length model, one-equation Prandtl-Kolmogorov model and two-equation *k*-*ε* and *k*-*ω* models. And others based on evaluating the Reynolds stress terms directly using transport equations e.g. Reynolds stress model and algebraic stress models.

Though the Reynolds stress model is more accurate in predicting the behaviour of Reynolds stresses (used in analysis of Rolls-Royce 3D combustor, Chapter 4), its computation cost is significantly higher than models based on the Boussinesq hypothesis. Hence, from an engineering design and optimisation point of view, the *k*-*ε* turbulence model based on the Boussinesq hypothesis is used in 2D combustor modelling and further design simulations. For more information on other models, see Malalasekera (1995), Pope (2000), Kuo (1986), Poinsot and Veynante (2005).

B.2.1 Boussinesq approach

Based on the turbulence viscosity assumption of Boussinesq (Hinze, 1975; Tennekes and Lumley, 1972) the Favre-averaged turbulent Reynolds stresses are described as (Kuo, 1986; Peters, 2000; Poinsot and Veynante, 2005)

$$\overline{\rho}\widetilde{u''_i u''_j} = -\mu_T\left(\frac{\partial \tilde{u}_i}{\partial x_j}+\frac{\partial \tilde{u}_j}{\partial x_i}-\frac{2}{3}\delta_{ij}\frac{\partial \tilde{u}_k}{\partial x_k}\right)+\frac{2}{3}\overline{\rho}k \qquad \text{Eq. (B.11)}$$

where

$\mu_T = \overline{\rho}\nu_T$ is the turbulent dynamic viscosity

ν_T is the kinematic viscosity

δ_{ij} is the Kronecker symbol

k is the turbulent kinetic energy

The turbulent kinetic energy

$$k = \frac{1}{2}\sum_{k=1}^{3}\widetilde{u''_k u''_k} \qquad \text{Eq. (B.12)}$$

In Equation (B.11), the main unknown is the turbulent or eddy viscosity term μ_T , which needs to be evaluated.

B.2.2 Two – equation standard *k-ε* model

The zero-equation and one-equation turbulence models lack the ability to capture recirculating flow dynamics accurately, as they neglect convective and diffusive turbulence properties (Malalasekera, 1995). The two-equation *k-ε* model considers the dynamics of turbulence, focusing on the mechanisms affecting the turbulent kinetic energy in particular (Tennekes and Lumley, 1972; Malalasekera, 1995).

In the two-equation *k*-ε model, the turbulent viscosityμ_T is estimated by (Jones and Launder, 1972)

$$\mu_T = \overline{\rho}C_\mu\frac{k^2}{\varepsilon} \qquad \text{Eq. (B.13)}$$

where, the turbulent kinetic energy k and the dissipation rate ε are described by two balance equations given as

$$\frac{\partial}{\partial t}(\overline{\rho}k) + \frac{\partial}{\partial x_i}(\overline{\rho}\tilde{u}_i k) = \frac{\partial}{\partial x_i}\left[\left(\mu + \frac{\mu_T}{\sigma_k}\right)\frac{\partial k}{\partial x_i}\right] + P_k - \overline{\rho}\varepsilon \qquad \text{Eq. (B.14)}$$

$$\frac{\partial}{\partial t}(\overline{\rho}\varepsilon) + \frac{\partial}{\partial x_i}(\overline{\rho}\tilde{u}_i \varepsilon) = \frac{\partial}{\partial x_i}\left[\left(\mu + \frac{\mu_T}{\sigma_\varepsilon}\right)\frac{\partial \varepsilon}{\partial x_i}\right] + C_{\varepsilon 1}\frac{\varepsilon}{k}P_k - C_{\varepsilon 2}\overline{\rho}\frac{\varepsilon^2}{k} \qquad \text{Eq. (B.15)}$$

where

P_k is the source term given by $-\overline{\rho}\widetilde{u''_\iota u''_\jmath}\frac{\partial \tilde{u}_i}{\partial x_j}$

$\overline{\rho}\widetilde{u''_\iota u''_\jmath}$ are the Reynolds stress terms evaluated using Eq. (B.11)

The model constants usually used are (Wilcox, 2006):

$C_\mu = 0.09$, $\sigma_k = 1.0$, $\sigma_\varepsilon = 1.3$, $C_{\varepsilon 1} = 1.44$ and $C_{\varepsilon 2} = 1.92$

The advantages and disadvantages of using the standard two-equation k-ε model for reacting flows can be summarized as follows (Malalasekera, 1995; Poinsot and Veynante, 2005):

Advantages:

- Simplicity and low computational cost compared to Reynolds stress model
- Higher accuracy compared to zero and one-equation model
- Availability of turbulent time scales estimates k/ε and $\sqrt{\varepsilon/\nu}$ used in turbulent combustion model for evaluating integral and Kolmogorov length scales respectively
- Well-established and most widely validated

Disadvantages:

- Assumption of homogeneous and isotropic turbulence
- Unable to capture swirling flows and stress-driven secondary flows accurately
- In combustion, flame flapping and intermittency related low frequency turbulent motions are underestimated

B.3 Partially premixed combustion model

The partially premixed combustion model in FLUENT™ version 12.1 is used for modelling the combustor flow in this thesis. This model can be utilized to model fully premixed combustion as well (Theory guide, ANSYS FLUENT™ 12.1 2009). Hence, although the 2D lean burn combustor operates in the fully premixed regime, the partially premixed model is used to keep the modelling approach in consistence with the Rolls-Royce 3D lean burn combustor which operates under partially premixed conditions. The partially premixed model is essentially a combination of premixed and non-premixed combustion models. It solves transport equations for the reaction progress variable $\tilde{c}$, mean mixture fraction $\tilde{z}$ and mixture fraction variance $\widetilde{z''}$. A description of the equations used in premixed and non-premixed combustion model is presented in this section.

B.3.1 Premixed combustion model:

Premixed combustion modelling involves predicting the interaction of turbulent eddies or vortices with a propagating flame front in a mixture of premixed reactants. The turbulent premixed combustion model solves the transport equation for the reaction progress variable (Zimont et al. 1995, 1998, 2001) given as

$$\frac{\partial}{\partial t}(\overline{\rho}\tilde{c}) + \frac{\partial}{\partial x_i}(\overline{\rho}\tilde{c}\tilde{u}_i) = \frac{\partial}{\partial x_i}\left(\overline{\rho}\overline{D}\frac{\partial \tilde{c}}{\partial x_i} - \overline{\rho}\widetilde{u_i''c''}\right) + \overline{\rho}S_c \qquad \text{Eq. (B.16)}$$

where;

$\overline{\rho}$ is the mean density

$\tilde{c}$ is the Favre-averaged reaction progress variable

$\overline{\rho}\overline{D}\frac{\partial \tilde{c}}{\partial x_i}$ is the average thermal diffusion term

S_c is the reaction progress source term

The reaction progress variable ($\tilde{c}$)

$$\tilde{c} = \frac{\sum_{k=1}^{N}\tilde{Y}_k}{\sum_{k=1}^{N}\tilde{Y}_{k,ad}} \qquad \text{Eq. (B.17)}$$

where

N is the number of species

$\tilde{Y}_k$ is the Favre-averaged mass fraction of species k

$\tilde{Y}_{k,ad}$ is the Favre-averaged mass fraction of species k after complete adiabatic combustion

According to Eq. (B.17), if $\tilde{c} = 0$ the mixture is unburnt and if $\tilde{c} = 1$, the mixture is considered to be burnt. The source term is given by

$$\overline{\rho} S_c = \overline{\rho}_u \overline{U}_T \left| \frac{\partial \tilde{c}}{\partial x_i} \right| \qquad \text{Eq. (B.18)}$$

where

$\overline{\rho}_u$ is the density of unburnt mixture

$\overline{U}_T$ is the turbulent flame speed

The turbulent flame speed prediction is the key to the premixed combustion model and is influenced by laminar flame speed, flame front wrinkling by large-scale eddies and flame thickening by small scale eddies (Zimont et al., 1998). It is given by

$$\overline{U}_T = A u' \left(\frac{\tau_t}{\tau_c} \right)^{1/4} \qquad \text{Eq. (B.19)}$$

where

A is the model constant

u' is the RMS velocity

τ_t is the turbulence time scale

τ_c is the chemical time scale

For more discussion on premixed combustion model, see Kuo (1986), Poinsot and Veynante (2005), Zimont (2000) and Zimont et al. (1995, 1998 and 2001).

B.3.2 Non-premixed combustion model:

In a non-premixed combustion process, the fuel and oxidizer enter the combustion system separately. The flame-front does not propagate through the system but rather is located where fuel and oxidizer meet (Kuo, 1986; Poinsot and Veynante, 2005). Compared to a premixed turbulent combustion system, the main difference lies in the definition of boundary conditions and in the use of mixture fraction z, which is the mass fraction that originates from the fuel stream. In systems with separate fuel and oxidizer streams (with reference states (T_F^0, Y_F^0) for fuel and (T_O^0, Y_O^0) for oxidizer) under certain set of simplifying assumptions†, the instantaneous thermochemical state of the fluid is related to the mixture fraction

$$z = \frac{sY_F - Y_O + Y_O^0}{sY_F^0 + Y_O^0} \qquad \text{Eq. (B.20)}$$

where

s is the stoichiometric ratio

Y_F is the fuel mass fraction

Y_O is the oxidizer mass fraction

The turbulent non-premixed combustion model solves the transport equation for the Favre-averaged mean mixture fraction $\tilde{z}$ and in addition a conservation equation for the mixture fraction variance $\widetilde{z''}$ (Sivathanu and Faeth, 1990; Poinsot and Veynante, 2005) given as

$$\frac{\partial}{\partial t}(\overline{\rho}\tilde{z}) + \frac{\partial}{\partial x_i}(\overline{\rho}\tilde{z}\tilde{u}_i) = \frac{\partial}{\partial x_i}\left(\overline{\rho D \frac{\partial z}{\partial x_i}} - \overline{\rho}\widetilde{u_i'' z''}\right) + S_m \qquad \text{Eq. (B.21)}$$

where

$\overline{\rho}\overline{D}\frac{\partial\tilde{c}}{\partial x_i}$ is the average thermal diffusion term

S_m is the source term solely due to transfer of mass from liquid fuel droplets or reacting particles to the gas phase

The closed equation for mixture fraction variance $\widetilde{z''}$, used widely in combustion CFD codes is given by (see Poinsot and Veynante, 2005 for derivation):

$$\frac{\partial}{\partial t}\left(\overline{\rho}\widetilde{z''^2}\right)+\frac{\partial}{\partial x_i}\left(\overline{\rho}\widetilde{z''^2}\tilde{u}_i\right) = \frac{\partial}{\partial x_i}\left(\overline{\rho}\frac{\nu_T}{S_{ct_1}}\frac{\partial\widetilde{z''^2}}{\partial x_i}\right)+2\overline{\rho}\frac{\nu_T}{S_{ct_2}}\frac{\partial\tilde{z}}{\partial x_i}\frac{\partial\tilde{z}}{\partial x_i}-c\tilde{\rho}\frac{\varepsilon}{k}\widetilde{z''^2} \quad \text{Eq. (B.22)}$$

where

ν_T is the turbulent viscosity provided by the turbulence model

S_{ct_1} and S_{ct_2} are the turbulent Schmidt numbers

c is a model constant of order unity

The transport equations for reaction progress variable $\tilde{c}$ (c.f. Eq. B.16), mean mixture fraction $\tilde{z}$ (c.f. Eq. B.21) and mixture fraction variance $\widetilde{z''}$ (c.f. Eq. B.22) together represent the partially premixed combustion model.

Thus, the Favre-averaged Navier-Stokes Equations B.7, B.8, B.9, B.10 along with the standard k-ε turbulence model Equations B.14 and B.15 and partially combustion model Equations B.16, B.21 and B.22 are solved for predicting turbulent reacting combustor flow in Chapters 4 and 5.

In addition to these equations, the turbulence-chemistry interaction models are solved to account for fluctuations in the average values of mixture fraction, species fraction, density and temperature in relation to instantaneous turbulent reacting flow field (Fluent 12.1 theory guide, 2009). The coupling between the turbulent flow field and heat release chemistry is performed by a conserved scalar approach in limits of infinitely fast chemistry using a beta-probability density function (PDF) approach for mixture fraction variable. The local density, temperature, and species concentration are stored as functions of Favre-averaged mixture fraction, its variance and enthalpy via a look-up table consisting of PDF weighted equilibrium values (See Kuo, 1986; Poinsot

and Veynante, 2005; Fluent 12.1 theory guide, 2009 for more details on turbulence-chemistry interaction modelling).

B.4 Pollutant model for NOx

The process of formation and destruction of nitrogen oxides in combustion systems requires simulation of both the turbulent reacting fluid dynamics and chemical kinetics in the system and coupling of these with nitrogen pollutant kinetics (Hill and Smoot, 2000; Barths et al., 1998). Hence, it is currently unfeasible to simulate lengthy, detailed chemical and nitrogen kinetic mechanisms simultaneously with a turbulent mixing process. A practical approach widely employed is to use a nitrogen kinetic mechanism with minimum number of reactions, global in nature, and approximate the essential features of NOx formation and destruction (Hill and Smoot, 2000).

B.4.1 Governing equation for NOx transport

During combustion, the nitrogen from combustion air or fuel is converted into nitrogen containing pollutants such as NO, NO_2, N_2O, NH_3 and HCN (Hewson and Bollig, 1996). The pollutant species formed depends primarily on temperature and fuel/air ratio in the combustion system. For gas-phase reacting systems, NOx formation and destruction can be classified in at least four separate processes: thermal NO, prompt NO, fuel NO and NO reburning. Of these four processes, thermal NO is discussed in more detail below, as it is used for combustor NOx analysis in this thesis. For more details on other processes, refer to Hill et al. (2000).

The governing transport equation for NO species is given as:

$$\frac{\partial}{\partial t}\left(\overline{\rho}\tilde{Y}_{NO}\right) + \frac{\partial}{\partial x_i}\left(\overline{\rho}\tilde{Y}_{NO}\tilde{u}_i\right) = \frac{\partial}{\partial x_i}\left(\overline{\rho D \frac{\partial Y_{NO}}{\partial x_i}}\right) + S_{NO} \qquad \text{Eq. (B.23)}$$

where;

$\tilde{Y}_{NO}$ is the Favre-averaged mean NO mass fraction

$\overline{D}$ is the average effective diffusion coefficient

S_{NO} is the source term to be determined for different NOx mechanisms

Equation B.23 is valid for thermal and prompt NOx mechanisms only as fuel NOx mechanisms are more involved and requires tracking of nitrogen-containing intermediate species (Miller, 19889; Fluent 12.1 theory guide, 2009).

B.4.2 Thermal NO mechanisms

The NO formation process is described by the widely accepted Zeldovich two-step mechanism (Malte and Pratt, 1974; Visona, 1996):

$$N_2 + O \rightleftharpoons NO + N \qquad \text{Eq. (B.24a)}$$

$$N + O_2 \rightleftharpoons NO + O \qquad \text{Eq. (B.24b)}$$

In addition to Equations (B.24a) and (B.24b), a further NO reaction is added to the thermal NO mechanism and is referred to as to extended Zeldovich mechanism, particularly important at fuel-rich and near-stoichiometric conditions, given as

$$N + OH \rightleftharpoons NO + H \qquad \text{Eq. (B.24c)}$$

Thermal NO is formed by oxidation of nitrogen in air at high temperatures. The rate of formation of thermal NO is highly dependent on temperature, residence time, and atomic concentration (Hayhurst and Vince, 1980). The rate of consumption of free nitrogen atoms becomes equal to the rate of its formation in the presence of sufficient oxygen and therefore a quasi-steady state is established. Based on a quasi-steady assumption of [N] and using Equations (B.24a), (B.24b) and (B.24c) the rate of formation of NO is given by (Bowman, 1975)

$$\frac{d[NO]}{dt} = 2[O]\left[\frac{k_1[N_2] - \frac{k_{-1}k_{-2}[NO]^2}{k_2[O_2]}}{1 + \frac{k_{-1}[NO]}{k_2[O_2] + k_3[OH]}}\right] \qquad \text{Eq. (B.25)}$$

where

k_1, k_2 and k_3 are rate constants for forward reactions whereas k_{-1}, k_{-2} are reverse rate constants (m^3/gmol.s)

Further as suggested by Zeldovich, assuming equilibrium values of stable species [N_2] and [O_2], to predict NO formation, [O] and [OH] free radicals concentrations must be calculated. The different methods to calculate these concentrations are discussed in Coelho and Carvalho (1995), Chen et al. (1996) and Fluent 12.1 theory guide (2009).Thus to solve the transport equation for NO_x species (Eq. B.23), the source term is

$$S_{NO} = M_{w,NO} \frac{\mathrm{d[NO]}}{\mathrm{dt}} \qquad \text{Eq. (B.26)}$$

where

$M_{w,NO}$ molecular weight of NO

$\frac{\mathrm{d[NO]}}{\mathrm{dt}}$ is rate of thermal NO formation computed from Eq. (B.25)

2D Combustor flow solution

C.1 Species model for combustor flow

Partially premixed combustion systems are premixed flames with non-uniform fuel-oxidizer mixtures (equivalence ratios) which include premixed jets discharging into a quiescent atmosphere, lean premixed combustors with diffusion pilot flames and/or cooling air jets, and imperfectly mixed inlets. The 2D test combustor is modeled to operate at lean conditions, capturing the humming cycle instability which occurs at an equivalence ratio of Φ = 0.86. The equivalence ratio is a central parameter for premixed gases. Lean combustion is defined as combustion in which the mixture equivalence ratio is less than 1. Perfectly premixed systems can also be modeled using the partially premixed combustion model in FLUENT™. This is used for modelling lean combustion in the 2D combustor.

Since air is the source of oxygen for burning in a premixed propane/air mixture, the burning of propane under stoichiometry (Ø = 1) is given as follows:

$$C_3H_8 + 5O_2 + 18.8N_2 \longrightarrow 3CO_2 + 4H_3O + 18.8N_2 \qquad \text{Eq. (C.1)}$$

For a stoichiometric mixture of propane with air, the mass stoichiometric ratio, ***s,*** is 3.63 and the fuel mass fraction (Y_F^{st}) is 0.060.

In hydrocarbon/air flames, the fresh gases contain fuel, O_2 and N_2 with typically 3.76 models of nitrogen for 1 mole of oxygen. Since the sum of mass fractions must be unity, according to Poinsot et el., 2005, the fuel mass fraction is given as:

$$Y_F = \frac{1}{1 + \frac{S}{\emptyset}\left(1 + 3.76\frac{W_{N_2}}{W_{O_2}}\right)} \qquad \text{Eq. (C.2)}$$

For ∅ = 0.86 and *S = 3.63*, the fuel mass fraction is 0.052 according to Equation D2.

Species settings for premixed inlet boundary conditions:

The mass fraction of the fuel composition is set to $Y_{C_3H_8}$ = 1.0 in the boundary tab while generating PDF mixture table, the mean mixture fraction is set to $\bar{\bar{f}}$ = 0.052 and progress variable $\bar{C}$ = 0 at the inlet boundary conditions panel. The mixture fraction variance, $\overline{f'^2}$ = 0.

Laminar flame-speed for propane/air mixture:

The propane/air mixture will burn only in the locations where the turbulent flame speed S_T is able to sustain the mixture velocity $\tilde{u}$ (i.e. $S_T = \tilde{u}$). The turbulent flame speed is influenced by the following:

- laminar flame speed, S_L, which, in turn, is determined by the fuel concentration, temperature, and molecular diffusion properties, as well as the detailed chemical kinetics
- flame front wrinkling and stretching by large eddies, and flame thickening by small eddies

For premixed systems, laminar flame speed is approximately constant throughout the domain. Fluent automatically selects the pre-PDF-polynomial function for laminar flame speed, indicating that the piecewise-linear polynomial function from the PDF look-up table is used to compute the laminar flame speed.

C.2 Convergence history for steady RANS isothermal solution

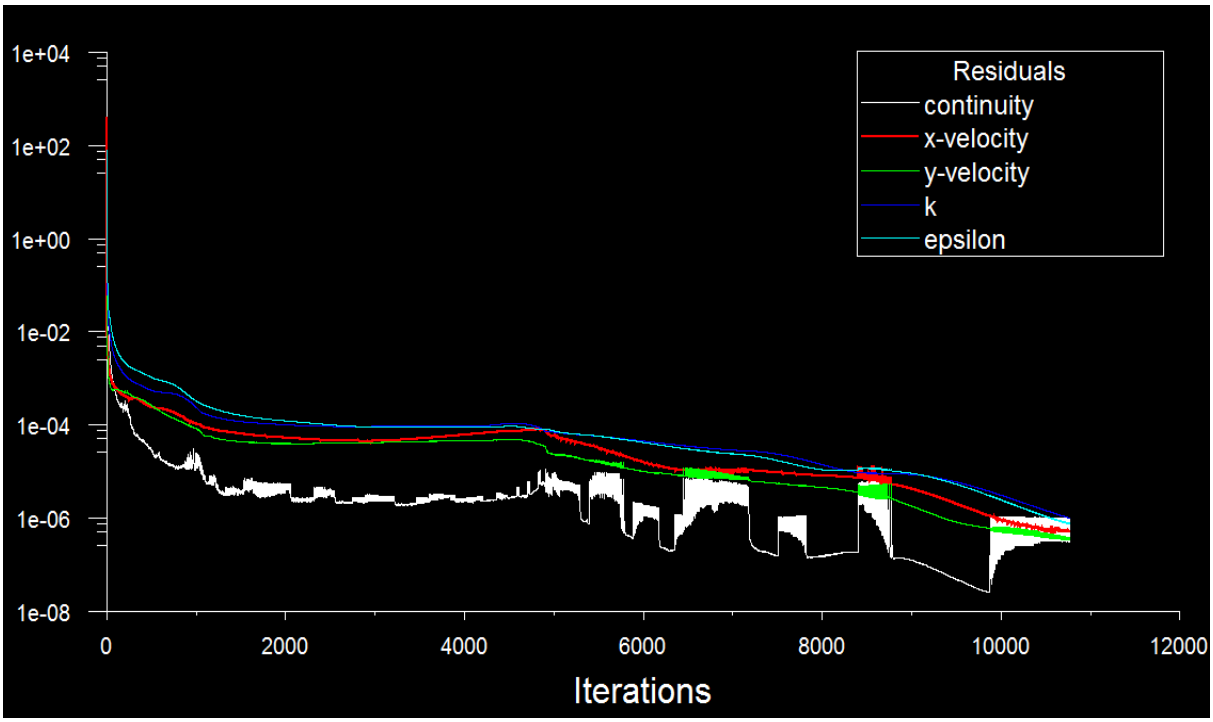

Fig. C.1 Residuals for steady RANS isothermal solution

C.3 Convergence history for steady RANS reactive solution

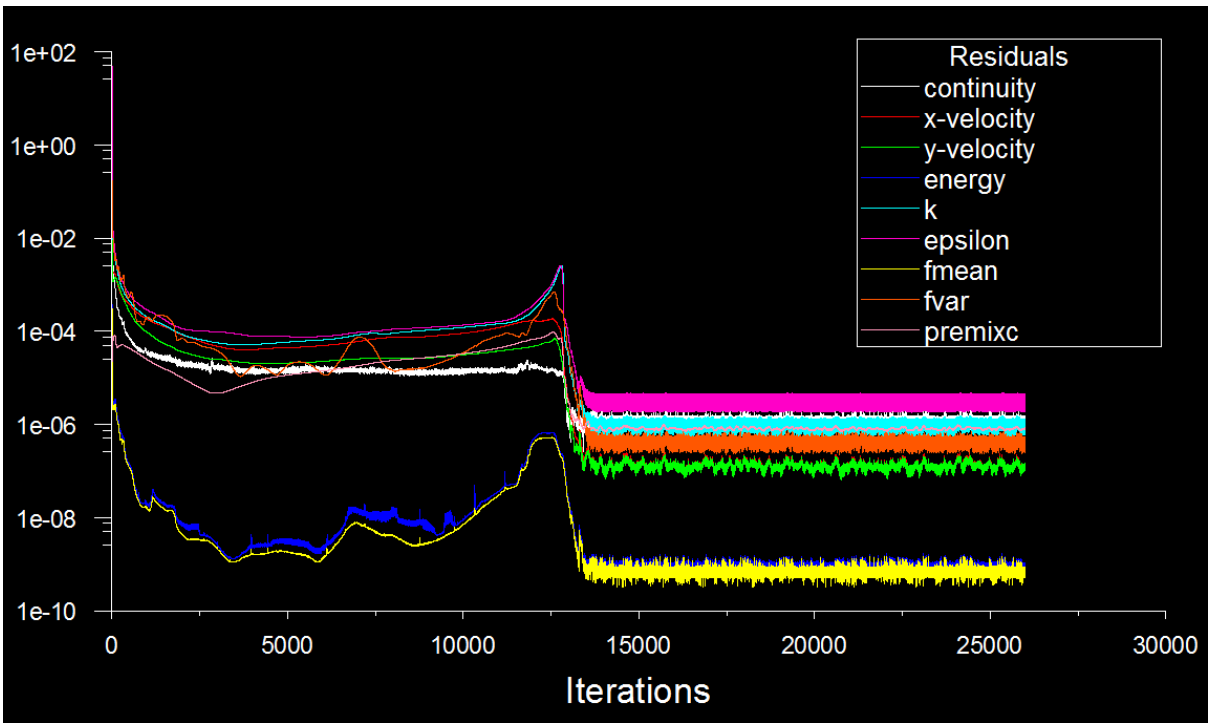

Fig. C.2 Residuals for steady RANS isothermal solution

C.4 Convergence history for pollutant NO using steady RANS

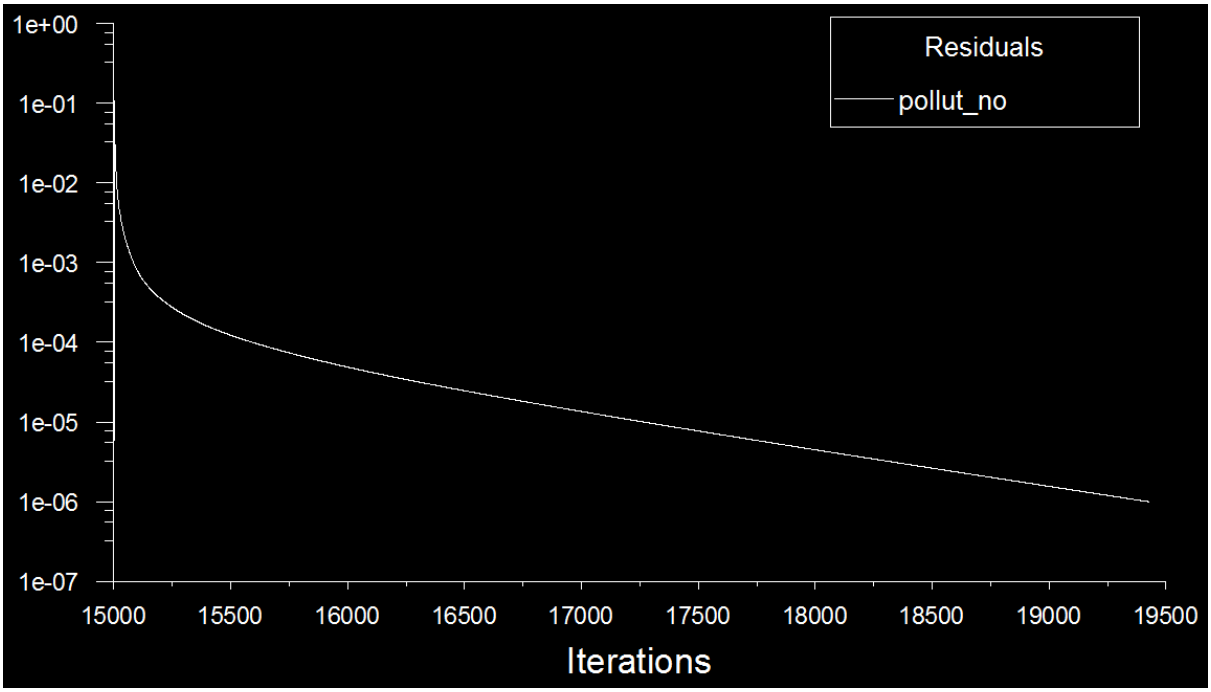

Fig. C.3 Residuals for NO using solution steady RANS

Kriging based combustor design strategy

D.1 Ranking of DOE samples as per objective function values

Table D.1 Ranking of Kriging design strategy search histories for steady outlet temperature profile RMSD using different starting samples (c.f. Figure 6.25)

Optimal RMSD	DOE sample
338.09 (Best)	4
338.89	8
339.13	9
341.11	1
345.43	5
345.76	2
356.83	3
361.61	6
367.33 (Worst)	7

Table D.2 Ranking of Kriging design strategy search histories for steady outlet thermal NO using different starting samples (c.f. Figure 6.25)	
Optimal outlet thermal NO ppm	DOE sample
8.159 (Best)	4
8.162	9
8.165	2
8.199	5
8.212	6
8.253	1
8.256	8
8.322	7
8.342 (Worst)	3

Table D.3 Ranking of Kriging design strategy search histories for time-averaged area-weighted outlet temperature using different starting samples (c.f. Figure 6.25)	
Optimal time-averaged area-weighted outlet temperature (K)	DOE sample
1524.87 (Best)	5
1524.96	1
1525.03	7
1527.56	3
1530.86	8
1531.59	6
1532.74	4
1535.31	2
1550.04 (Worst)	9

Table D.4 Ranking of Kriging design strategy search histories for time-averaged area-weighted outlet thermal NO using different starting samples (c.f. Figure 6.25)	
Optimal time-averaged area-weighted outlet thermal NO (ppm)	DOE sample
9.778	1
9.775	9
9.781	5
9.795	2
9.836	6
9.837	8
9.838	3
9.940	7
9.946	4

D.2 Bootstrap sample convergence study

(1) Spatial domain

(a) Outlet temperature profile RMSD:

Table D.5 Convergence study for number of bootstrap samples B for steady outlet temperature profile RMSD								
B	50	100	1000	5000	10000	20000	40000	80000
SE'	3.120	3.706	3.519	3.372	3.464	3.432	3.430	3.432

Table D.5 shows that beyond B = 5000, the bootstrap standard error (SE') value of ~3.4 doesn't change significantly further. Figure D.1 shows sampling data distribution about the mean. The original dataset X with sample size N = 9, does not follow a normal distribution, whereas the bootstrap sampling distribution based on B=100, 5000 and 20000 samples approximately follow normal distribution. However, at B = 5000 the distribution curve looks converged without any significant change further.

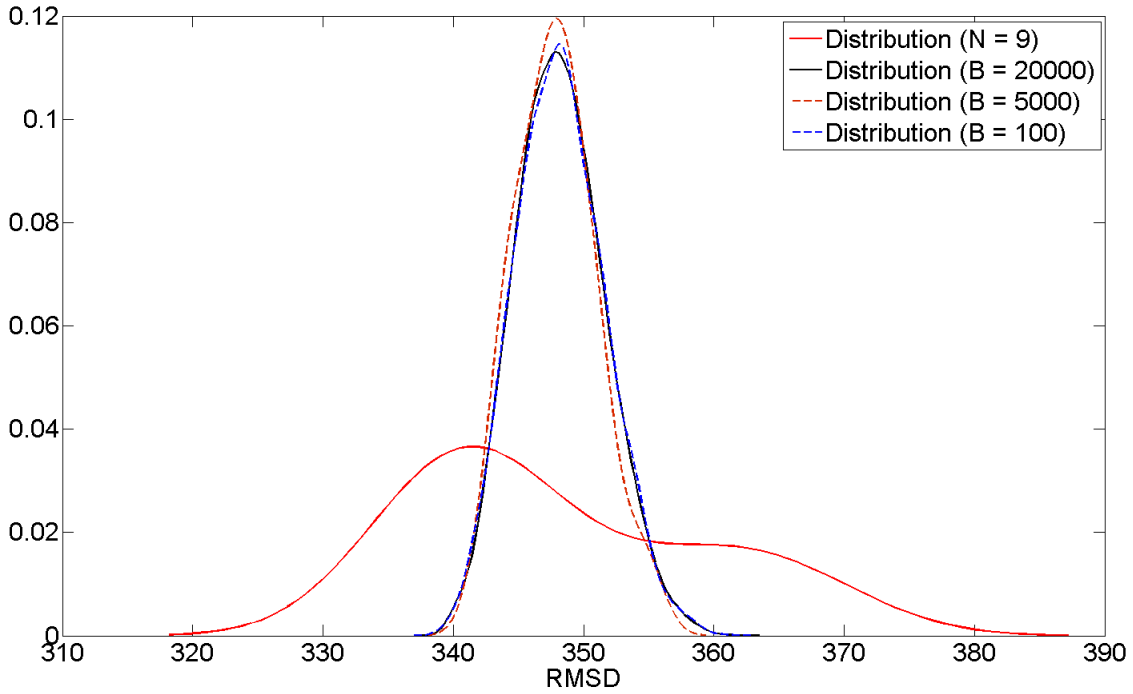

Fig. D.1 Sampling distribution of original dataset X around the estimated mean M = 348.24 compared with bootstrap distribution around bootstrap mean M' = 348.25 for outlet temperature profile RMSD

(b) Outlet thermal NO (ppm):

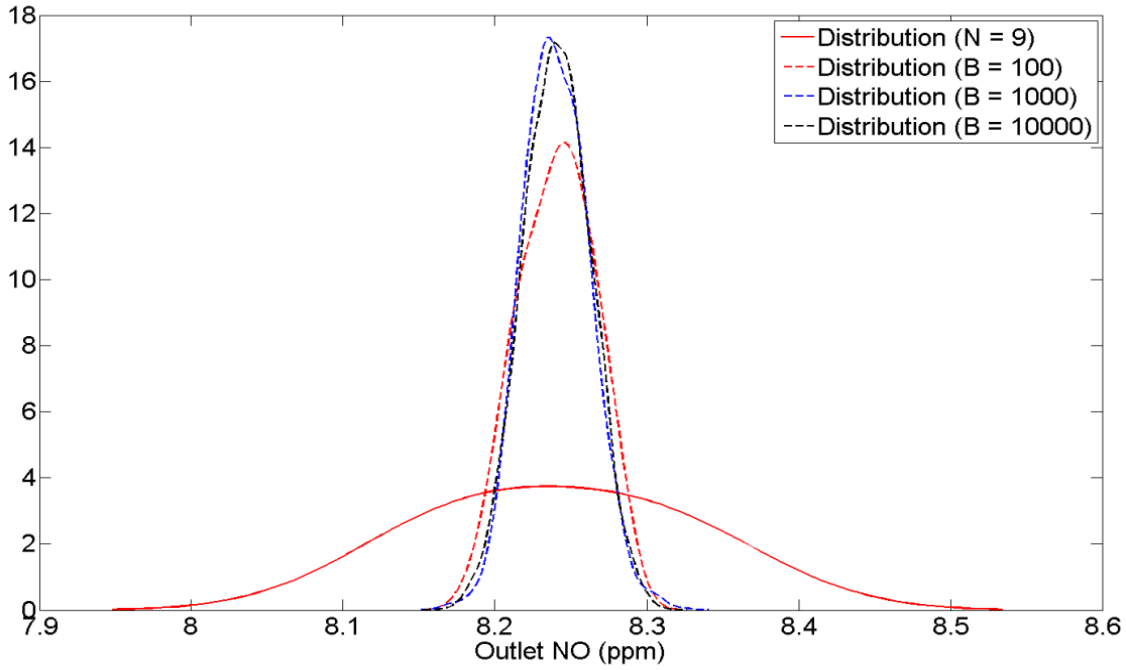

Fig. D.2 Sampling distribution of original dataset X around estimated mean M = 8.230 compared with bootstrap distribution around bootstrap mean M' = 8.231 for outlet thermal NO

Table D.6 Convergence study for number of bootstrap samples B for steady outlet thermal NO (ppm)								
B	50	100	1000	5000	10000	20000	40000	80000
SE'	0.022	0.021	0.021	0.021	0.021	0.021	0.021	0.021

Similar to the outlet temperature profile objective function bootstrap analysis, Table D.6 shows that the bootstrap standard error value at B=100 appears to be converged with no further change in its value as B increases. Figure D.2 shows original data and bootstrapped data distribution about the mean. With sample size N = 9, the sampling distribution is not normal, whereas the bootstrap sampling distribution with B=100, 1000 and 10000 are approximately normal. However, at B = 1000 the sampling distribution curve appears to be converged without any significant change.

(2) Temporal domain

Similar to the bootstrap sample size B analysis in spatial domain, the convergence analysis is performed on temporal domain objective functions to determine size of B.

(a) Time-averaged (area-weighted) outlet temperature (K):

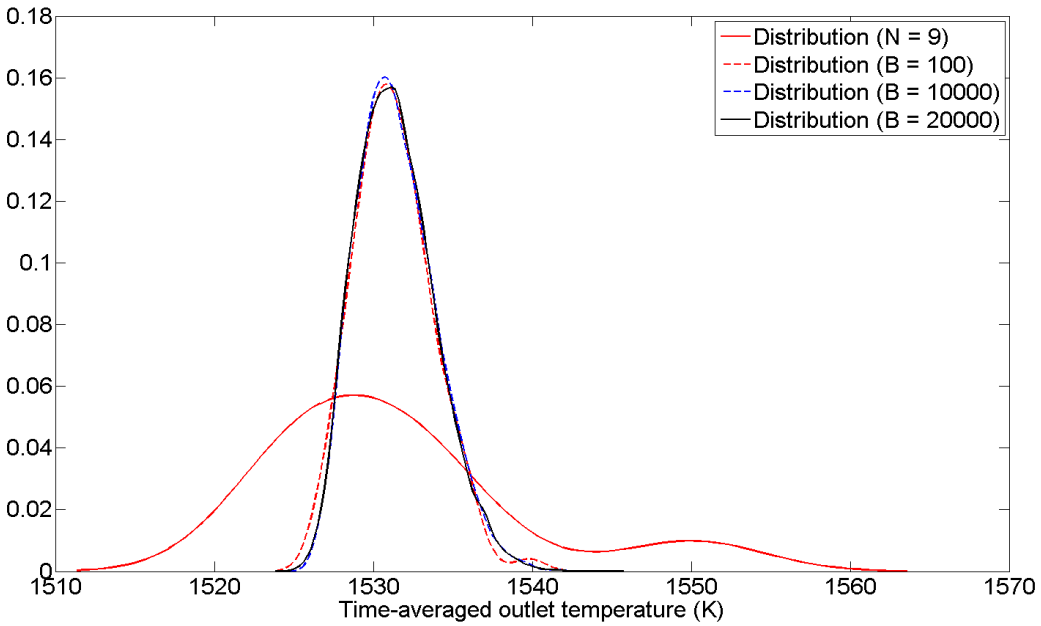

Fig. D.3 Sampling distribution of original dataset X around the estimated mean M = 1531.44 compared with bootstrap distribution around bootstrap mean M' = 1531.40 for time-averaged outlet temperature

Table D.7 Convergence study for number of bootstrap samples B for time-averaged area-weighted outlet temperature (K)								
B	50	100	1000	5000	10000	20000	40000	80000
SE'	2.634	2.451	2.535	2.456	2.511	2.505	2.500	2.500

(b) Time-averaged (area-weighted) outlet thermal NO (ppm):

Table D.8 Convergence study for number of bootstrap samples B for time-averaged area-weighted outlet thermal NO (ppm)								
B	50	100	1000	5000	10000	20000	40000	80000
SE'	0.0202	0.0214	0.0201	0.0204	0.0205	0.0205	0.0205	0.0205

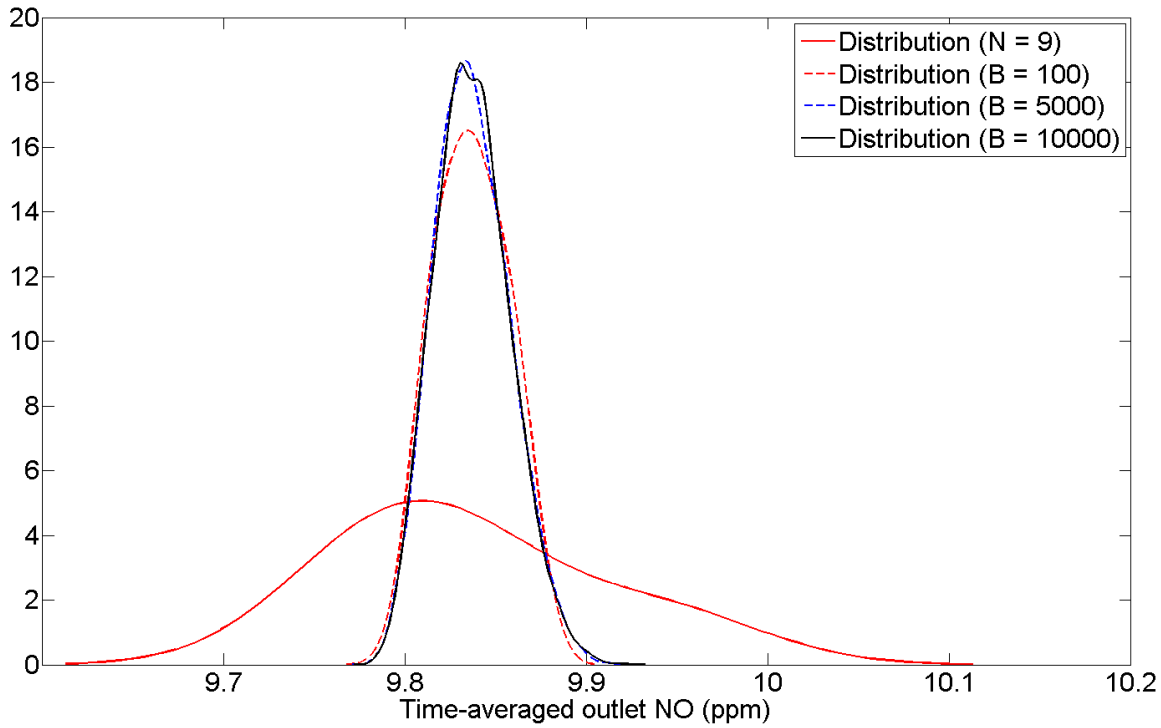

Fig. D.4 Sampling distribution of original dataset X around the estimated mean M = 9.836 compared with bootstrap distribution around the bootstrap mean M' = 9.837 for time-averaged outlet thermal NO

Co-Kriging based combustor design strategy

E.1 Co-Kriging methodology

Co-Kriging is an extension to the original form of Kriging methodology, which correlates multiple sets of data. Given two vectors of variables $\mathbf{X_c^i}$ and $\mathbf{X_e^j}$, where $\mathbf{X_c^i}$ is the vector of cheap (or low-fidelity) evaluation points ($\mathbf{i} = 1,..\ n_c$), and $\mathbf{X_e^j}$ is the vector of expensive (or high-fidelity) evaluation points with ($\mathbf{j} = 1,..\ n_e$), the combined set of sample points

$$\mathbf{X} = \begin{bmatrix} \mathbf{X_c^i} \\ \mathbf{X_e^j} \end{bmatrix} = \begin{bmatrix} \mathbf{x_c^1} \\ . \\ . \\ \mathbf{x_c^{n_c}} \\ \mathbf{x_e^1} \\ . \\ . \\ \mathbf{x_e^{n_e}} \end{bmatrix} \qquad \text{Eq. (E.1)}$$

The objective function values could be represented by a vector $\mathbf{Y}$ consisting of all cheap $[\mathbf{Y_c}(\mathbf{X_c^i})]$ and expensive $[\mathbf{Y_e}(\mathbf{X_e^j})]$ objective function values given by

$$\mathbf{Y} = \begin{bmatrix} \mathbf{Y_c}(\mathbf{X_c^i}) \\ \mathbf{Y_e}(\mathbf{X_e^j}) \end{bmatrix} = \begin{bmatrix} \mathbf{Y_c}(\mathbf{x_c^1}) \\ . \\ . \\ \mathbf{Y_c}(\mathbf{x_c^{n_c}}) \\ \mathbf{Y_e}(\mathbf{x_e^1}) \\ . \\ . \\ \mathbf{Y_e}(\mathbf{x_e^{n_e}}) \end{bmatrix} \qquad \text{Eq. (E.2)}$$

For two levels of fidelities in the co-Kriging methodology, according to auto-regressive model of Kennedy and O'Hagan (2000),

$$\mathrm{Cov}\left[\mathbf{Y_e}(\mathbf{x^i})\, \mathbf{Y_c}(\mathbf{x}) \middle| \mathbf{Y_c}(\mathbf{x^i})\right] = 0, \qquad \forall \mathbf{x} \neq \mathbf{x^i} \qquad \text{Eq. (E.3)}$$

Equation E.3 is a Markov property, which indicates that at a particular location, nothing more can be learnt about the expensive function from the cheap function if the value of the expensive function is known at that location. Hence all inaccuracies lie only in the cheap model. For making use of cheap function data, a correction process is required to formulate the difference between the cheap and expensive function.

If $\mathbf{G_e}$ and $\mathbf{G_c}$ are the Gaussian realization of the expensive and cheap functions respectively, then using the auto-regressive model the approximation of the expensive function is given as the sum of the scaled cheap function realization (with scaling factor ρ), and a Gaussian process representing the difference between the expensive function and the scaled cheap function (Kennedy and O'Hagan, 2000), given as

$$\mathbf{G_e}(\mathbf{x}) = \rho \mathbf{G_c}(\mathbf{x}) + \mathbf{G_d}(\mathbf{x}) \qquad \text{Eq. (E.4)}$$

The covariance of **Y,** for two-levels of fidelities, similar to that of Kriging (Equation B.3) is:

$$\mathrm{Cov}[\mathbf{Y_c}(\mathbf{X_c^i}), \mathbf{Y_c}(\mathbf{X_c^i})] = \sigma_c{}^2 \mathbf{R_c}(\mathbf{X_c^i}, \mathbf{X_c^i}) \qquad \text{Eq. (E.5)}$$

$$\mathrm{Cov}[\mathbf{Y_e}(\mathbf{X_e^j}), \mathbf{Y_c}(\mathbf{X_c^i})] = \rho\sigma_c{}^2 \mathbf{R_c}(\mathbf{X_c^i}, \mathbf{X_e^j}) \qquad \text{Eq. (E.6)}$$

$$\mathrm{Cov}\left[\mathbf{Y_e}(\mathbf{X_e^j}), \mathbf{Y_e}(\mathbf{X_e^j})\right] = \rho^2 {\sigma_c}^2 \mathbf{R_c}(\mathbf{X_e^j}, \mathbf{X_e^j}) + {\sigma_d}^2 \mathbf{R_d}(\mathbf{X_e^j}, \mathbf{X_e^j}) \quad \text{Eq. (E.7)}$$

where ${\sigma_c}^2$ is the variance in the cheap model and $\mathbf{R_c}$ and $\mathbf{R_d}$ are the correlation matrices. The covariance matrix using Equations (E.5), (E.6) and (E.7) is given as:

$$\mathbf{C} = \begin{pmatrix} {\sigma_c}^2 \mathbf{R_c}(\mathbf{X_c^i}, \mathbf{X_c^i}) & \rho {\sigma_c}^2 \mathbf{R_c}(\mathbf{X_c^i}, \mathbf{X_e^j}) \\ \rho {\sigma_c}^2 \mathbf{R_c}(\mathbf{X_e^j}, \mathbf{X_c^i}) & \rho^2 {\sigma_c}^2 \mathbf{R_c}(\mathbf{X_e^j}, \mathbf{X_e^j}) + {\sigma_d}^2 \mathbf{R_d}(\mathbf{X_e^j}, \mathbf{X_e^j}) \end{pmatrix} \quad \text{Eq. (E.8)}$$

The elements of two correlations matrices $\mathbf{R_c}$ and $\mathbf{R_d}$ are of the same form as Equation B.1 and the hyperparameters to be determined are $\boldsymbol{\theta_c}, \boldsymbol{p_c}, \boldsymbol{\theta_d}, \boldsymbol{p_d}$ along with the scaling factor ρ.

The estimates of cheap model hyperparameters μ_c ,${\sigma_c}^2$, $\boldsymbol{\theta_c}$ and $\boldsymbol{p_c}$ are found by maximizing the log-likelihood function

$$\frac{1}{(2\pi)^{\frac{n}{2}}({\sigma_c}^2)^{\frac{n}{2}} |\mathbf{R_c}(\mathbf{X_c^i}, \mathbf{X_c^i})|^{\frac{1}{2}}} \exp\left[\frac{-(\mathbf{Y_c} - \mathbf{1}\mu_c)^{\mathrm{T}} \mathbf{R_c}(\mathbf{X_c^i}, \mathbf{X_c^i})^{-1} (\mathbf{Y_c} - \mathbf{1}\mu_c)}{2{\sigma_c}^2}\right] \quad \text{Eq. (E.9)}$$

and after taking natural log of Equation (E.9) and ignoring the constant terms,

$$-\frac{n_c}{2}\log({\sigma_c}^2) - \frac{1}{2}\log\left(\left|\mathbf{R_c}(\mathbf{X_c^i}, \mathbf{X_c^i})\right|\right) - \frac{(\mathbf{Y_c} - \mathbf{1}\mu_c)^{\mathrm{T}} \mathbf{R_c}(\mathbf{X_c^i}, \mathbf{X_c^i})^{-1} (\mathbf{Y_c} - \mathbf{1}\mu_c)}{2{\sigma_c}^2} \quad \text{Eq. (E.10)}$$

Setting the derivatives of Equation (E.10) with respect to ${\sigma_c}^2$ and μ_c equal to zero, the optimal values of mean ($\hat{\mu_c}$) and variance ($\hat{\sigma_c}^2$) as functions of $\mathbf{R_c}(\mathbf{X_c^i}, \mathbf{X_c^i})$ could be obtained as:

$$\hat{\mu_c} = \frac{\mathbf{1}^{\mathrm{T}} \mathbf{R_c}(\mathbf{X_c^i}, \mathbf{X_c^i})^{-1} \mathbf{Y_c}}{\mathbf{1}^{\mathrm{T}} \mathbf{R_c}(\mathbf{X_c^i}, \mathbf{X_c^i})^{-1} \mathbf{1}} \quad \text{Eq. (E.11)}$$

$$\hat{\sigma_c}^2 = \frac{(\mathbf{Y_c} - \mathbf{1}\hat{\mu_c})^{\mathrm{T}} \mathbf{R_c}(\mathbf{X_c^i}, \mathbf{X_c^i})^{-1} (\mathbf{Y_c} - \mathbf{1}\hat{\mu_c})}{n_c} \quad \text{Eq. (E.12)}$$

Substituting Equations (E.11) and (E.12) into Equation (E.10) gives the concentrated log likelihood function

$$-\frac{n_c}{2}\log(\hat{\sigma}_c{}^2) - \frac{1}{2}\log(|\mathbf{R_c}(\mathbf{X_c^i}, \mathbf{X_c^i})|) \quad \text{Eq. (E.13)}$$

which depends only on the correlation $\mathbf{R_c}(\mathbf{X_c^i}, \mathbf{X_c^i})$. Equation (E.13) is maximized to get the estimates $\widehat{\boldsymbol{\theta}}_\mathbf{c}$ and $\widehat{\boldsymbol{p}}_\mathbf{c}$ and using these, $\hat{\mu}_c$ and $\hat{\sigma}_c{}^2$ are computed from Equations (E.11) and (E.12) respectively.

To estimate model hyperparameters μ_d , $\sigma_d{}^2$,$\boldsymbol{\theta}_\mathbf{d}$ and $\boldsymbol{p}_\mathbf{d}$, the difference model is defined as:

$$\mathbf{Y_d} = \mathbf{Y_e} - \rho\mathbf{Y_c}(\mathbf{X_e}) \quad \text{Eq. (E.14)}$$

The log-likelihood function for the expensive function is:

$$-\frac{n_e}{2}\log(\sigma_d{}^2) - \frac{1}{2}\log(|\mathbf{R_c}(\mathbf{X_c^i}, \mathbf{X_c^i})|) - \frac{(\mathbf{Y_d} - \mathbf{1}\mu_d)^T\mathbf{R_d}(\mathbf{X_e^j}, \mathbf{X_e^j})^{-1}(\mathbf{Y_d} - \mathbf{1}\mu_d)}{2\sigma_d{}^2} \quad \text{Eq. (E.15)}$$

Again setting the derivatives of Equation (E.15) with respect to $\sigma_d{}^2$ and μ_d equal to zero,

$$\hat{\mu}_d = \frac{\mathbf{1}^T\mathbf{R_d}(\mathbf{X_e^j}, \mathbf{X_e^j})^{-1}\mathbf{Y_d}}{\mathbf{1}^T\mathbf{R_d}(\mathbf{X_e^j}, \mathbf{X_e^j})^{-1}\mathbf{1}} \quad \text{Eq. (E.16)}$$

$$\hat{\sigma}_d{}^2 = \frac{(\mathbf{Y_d} - \mathbf{1}\hat{\mu}_d)^T\mathbf{R_d}(\mathbf{X_e^j}, \mathbf{X_e^j})^{-1}(\mathbf{Y_d} - \mathbf{1}\hat{\mu}_d)}{n_e} \quad \text{Eq. (E.17)}$$

Substituting Equations (E.16) and (E.17) into Equation (E.15) gives the concentrated log likelihood function

$$-\frac{n_e}{2}\log(\hat{\sigma}_d{}^2) - \frac{1}{2}\log(|\mathbf{R_c}(\mathbf{X_c^i}, \mathbf{X_c^i})|) \quad \text{Eq. (E.18)}$$

Equation (E.18) is maximized to get the estimates $\widehat{\boldsymbol{\theta}}_{\mathbf{d}}$, $\widehat{\boldsymbol{p}}_{\mathbf{d}}$ and $\hat{\rho}$. Using these estimates, $\hat{\mu}_{\mathrm{d}}$ and ${\hat{\sigma}_{\mathrm{d}}}^2$is computed from Equations (E.16) and (E.17) respectively.

To make a co-Kriging prediction at a new expensive point, a method similar to Kriging is applied (c.E. Section B.1). With fixed estimated parameters, to predict the value $\widehat{\mathbf{Y}}_{\mathbf{e}}(\mathbf{x})$ at a new location $\mathbf{X}$ which is consistent with the observed data, an augmented log-likelihood function is computed.

The augmented vector of objective function values is given by $\widetilde{\mathbf{Y}} = [{\mathbf{Y}_{\mathbf{c}}}^{\mathbf{T}}, {\mathbf{Y}_{\mathbf{e}}}^{\mathbf{T}}\, \widehat{\mathbf{Y}}_{\mathbf{e}}(\mathbf{x})]^{\mathrm{T}}$ when augmented by a new expensive prediction point $\widehat{\mathbf{Y}}_{\mathbf{e}}(\mathbf{x})$, the value of which is to be determined. The column vector of covariance of $\widehat{\mathbf{Y}}_{\mathbf{e}}(\mathbf{x})$ with $\mathbf{Y}(\mathbf{X})$ is given by:

$$\mathbf{c} = \begin{pmatrix} \rho {\hat{\sigma}_{\mathrm{c}}}^2 \mathbf{R}_{\mathbf{c}}(\mathbf{X}_{\mathbf{c}}^{\mathbf{i}}, \mathbf{x}) \\ (\rho^2 {\hat{\sigma}_{\mathrm{c}}}^2 + {\hat{\sigma}_{\mathrm{d}}}^2)\mathbf{R}_{\mathbf{d}}(\mathbf{X}_{\mathbf{e}}^{\mathbf{j}}, \mathbf{x}) \end{pmatrix} \qquad \text{Eq. (E.19)}$$

and the augmented covariance matrix

$$\tilde{\mathbf{C}} = \begin{pmatrix} \mathbf{C} & \mathbf{c} \\ \mathbf{c}^{\mathbf{T}} & (\rho^2 {\hat{\sigma}_{\mathrm{c}}}^2 + {\hat{\sigma}_{\mathrm{d}}}^2) \end{pmatrix} \qquad \text{Eq. (E.20)}$$

Using Equation (E.20), an augmented likelihood function is computed similar to Equations (E.10) and (E.15). Maximizing this function and using method similar to Kriging (c.E. Section 2.4), the MLE of $\widehat{\mathbf{Y}}_{\mathbf{e}}(\mathbf{x})$ is obtained as:

$$\widehat{\mathbf{Y}}_{\mathbf{e}}(\mathbf{x}) = \hat{\mu} + \mathbf{c}^{\mathbf{T}}\mathbf{C}^{-\mathbf{1}}(\mathbf{Y} - \mathbf{1}\hat{\mu}) \qquad \text{Eq. (E.21)}$$

Equation E.21 is the expression for the co-Kriging predictor.

Similar to the Kriging prediction error, the co-Kriging prediction error is computed as:

$$\hat{s}^2(\mathbf{x}) \approx \left[\rho^2 {\hat{\sigma}_{\mathrm{c}}}^2 + {\hat{\sigma}_{\mathrm{d}}}^2 - \mathbf{c}^{\mathbf{T}}\mathbf{C}^{-\mathbf{1}}\mathbf{c} + \frac{1 - \mathbf{1}^{\mathbf{T}}\mathbf{C}^{-\mathbf{1}}\mathbf{c}}{\mathbf{1}^{\mathbf{T}}\mathbf{C}^{-\mathbf{1}}\mathbf{c}}\right] \qquad \text{Eq. (E.22)}$$

E.2 DOE samples of various co-Kriging based design strategies

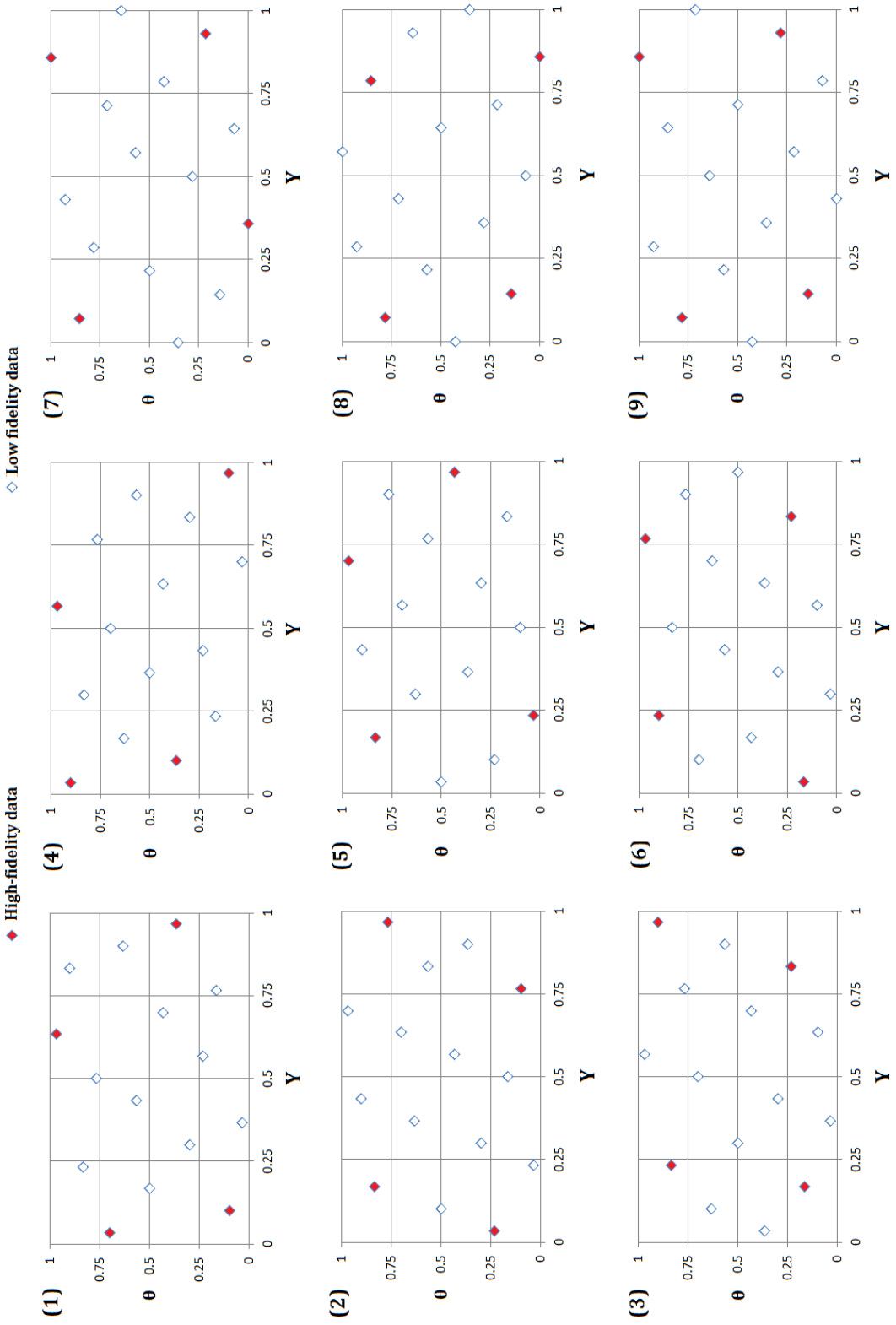

Fig. E.1 Different optimal Latin-Hypercube samples (LHS) for strategy CoTGL

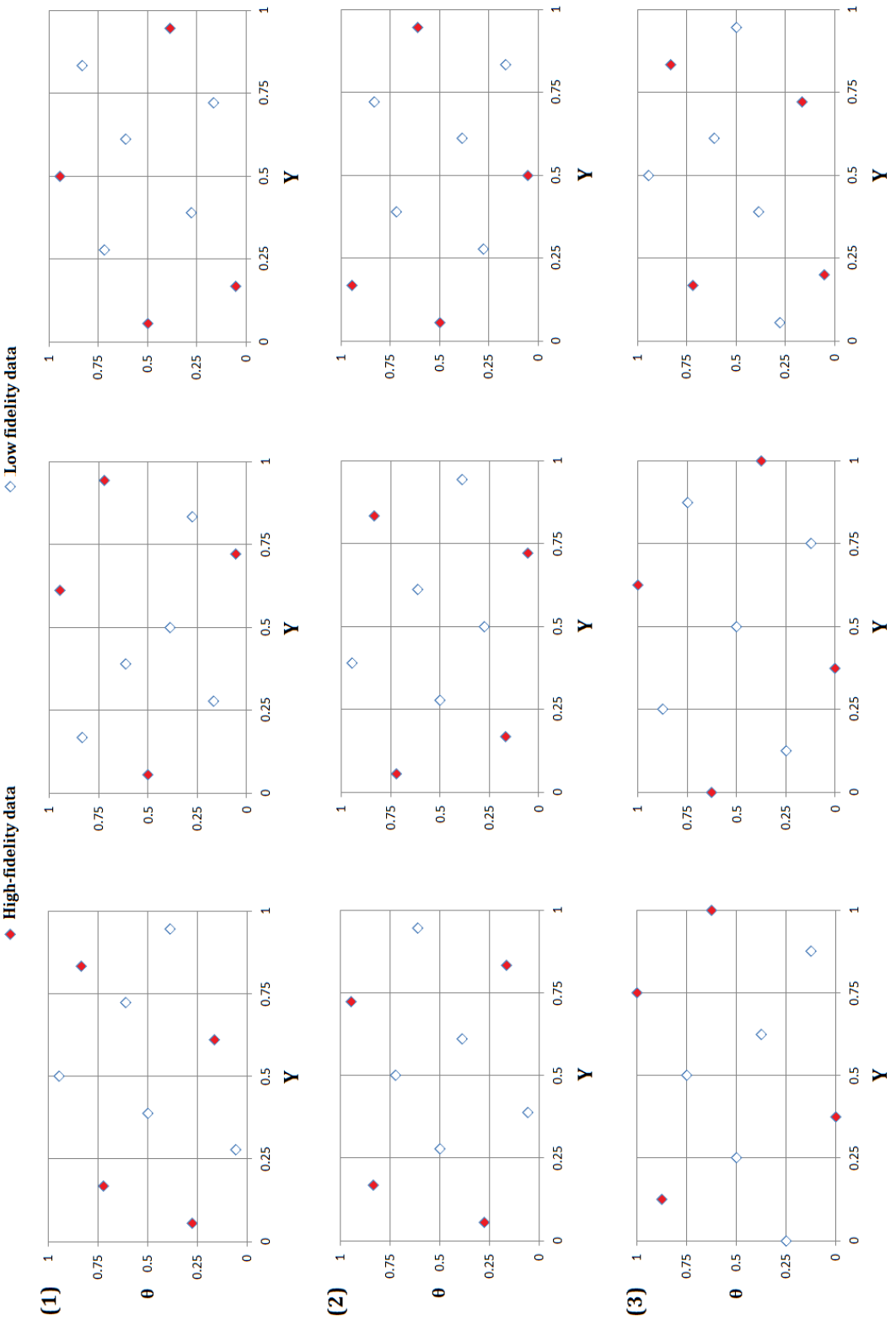

Fig. E.2 Different optimal Latin-Hypercube samples (LHS) for strategy CoSUS

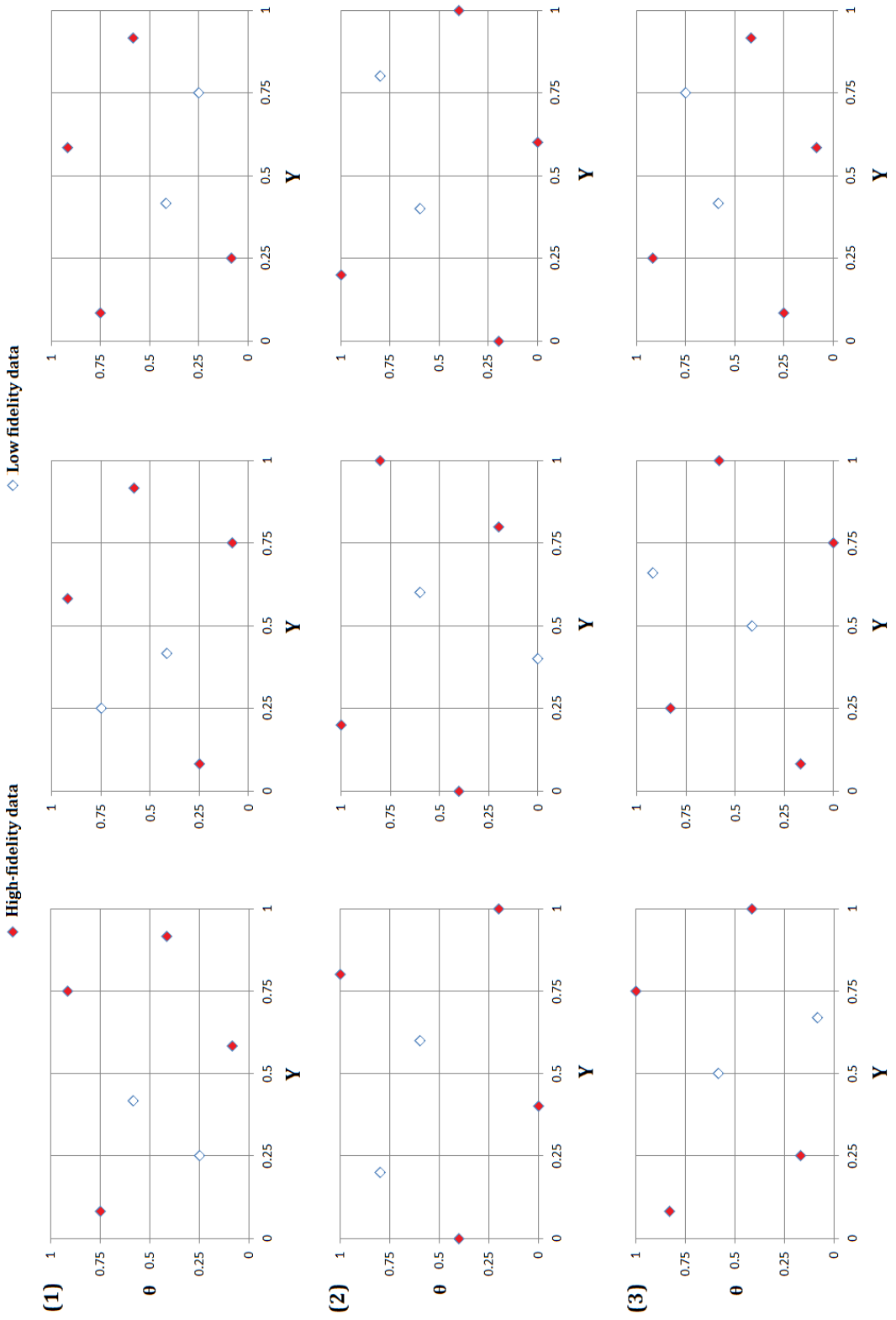

Fig. E.3 Different optimal Latin-Hypercube samples (LHS) for strategy CoTUS-(a)

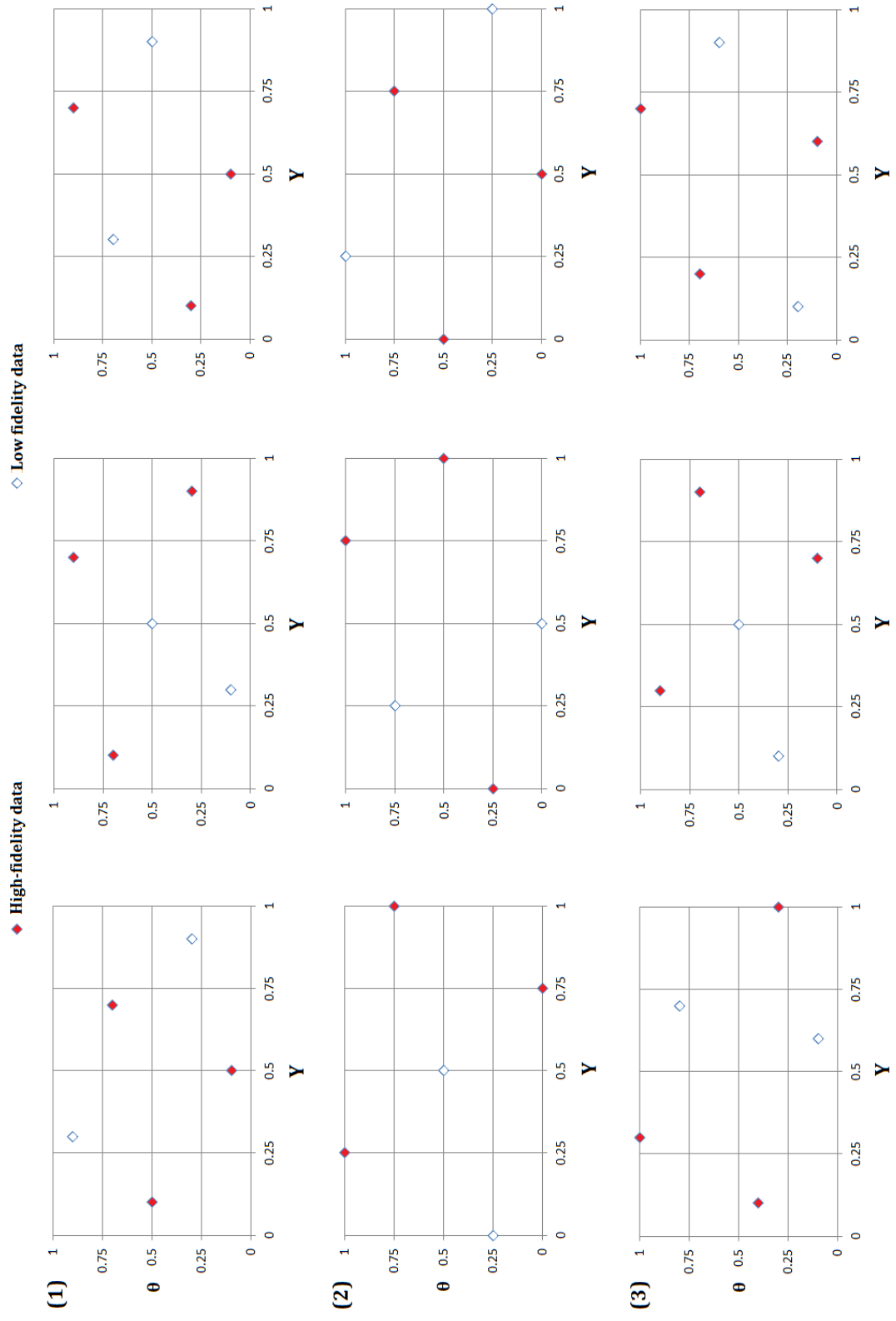

Fig. E.4 Different optimal Latin-Hypercube samples (LHS) for strategy CoTUS-(b)

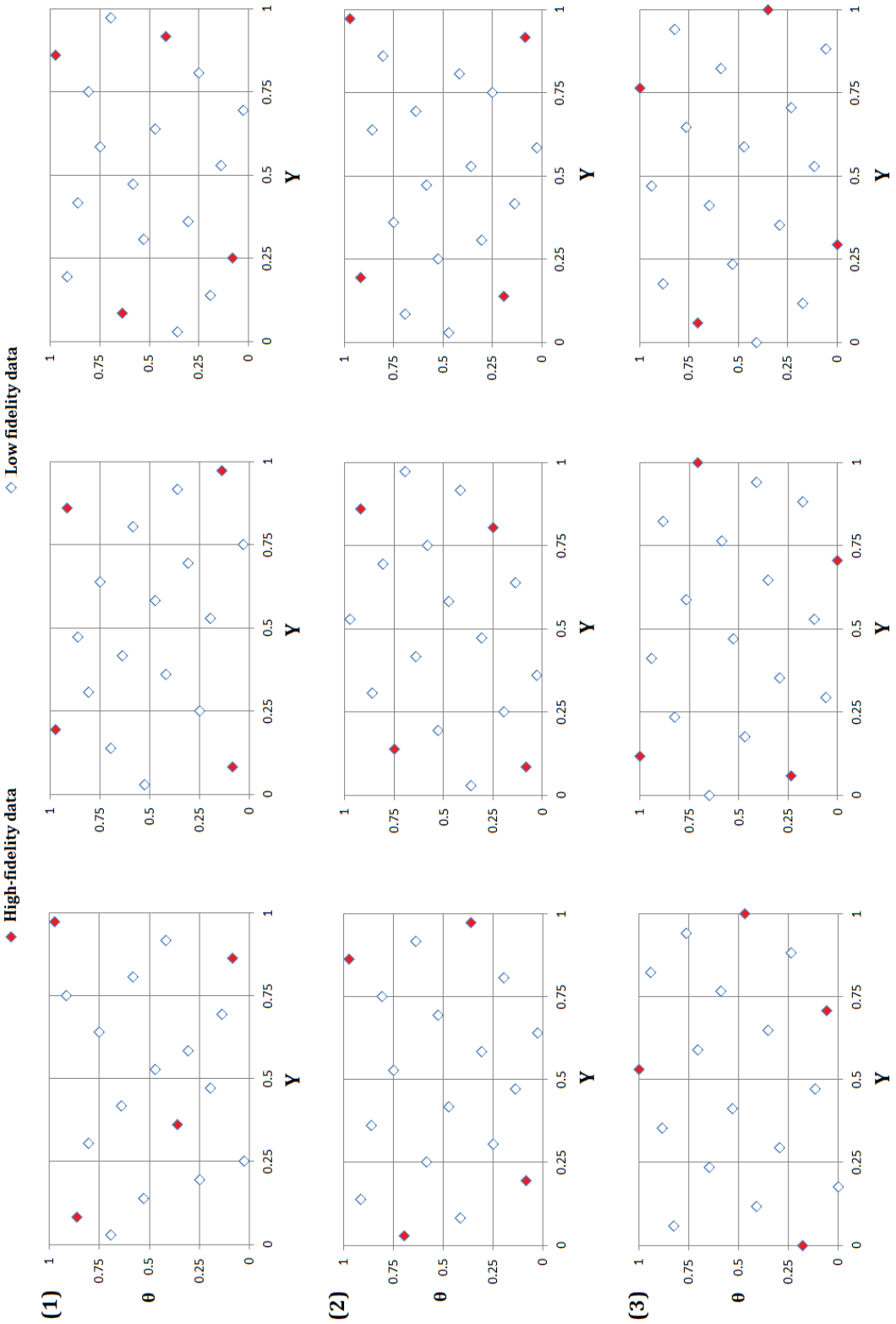

Fig. E.5 Different optimal Latin-Hypercube samples (LHS) for strategy CoSTUS

E.3 Ranking of DOE samples as per objective function values

Table E.1 Ranking of CoTGL design strategy search histories for steady outlet temperature profile RMSD using different starting samples (c.f. Figure E.1)	
Optimal RMSD	DOE sample
338.22 (best)	7
340.08	1
341.42	2
345.52	9
346.84	3
348.71	5
359.13	8
367.44	4
372.75 (Worst)	6

Table E.2 Ranking of CoTGL design strategy search histories for steady outlet thermal NO using different starting samples (c.f. Figure E.1)	
Optimal outlet thermal NO ppm	DOE sample
8.165 (best)	9
8.168	5
8.185	1
8.193	8
8.250	2
8.275	3
8.293	7
8.420	6
8.616 (worst)	4

Table E.3 Ranking of CoSUS design strategy search histories for time-averaged area-weighted outlet thermal NO using different starting samples (c.f. Figure E.2)	
Optimal time-averaged area-weighted outlet thermal NO (ppm)	DOE sample
9.778 (best)	8
9.782	6
9.789	2
9.800	5
9.815	4
9.866	9
9.889	1
10.050	7
10.107 (worst)	3

Table E.4 Ranking of CoTUS-(a) design strategy search histories for time-averaged area-weighted outlet thermal NO using different starting samples (c.f. Figure E.3)	
Optimal time-averaged area-weighted outlet thermal NO (ppm)	DOE sample
9.778 (best)	7
9.785	1
9.789	3
9.821	5
9.825	8
9.981	9
10.087	4
10.185	2
10.254 (worst)	6

Table E.5 Ranking of CoTUS-(b) design strategy search histories for time-averaged area-weighted outlet thermal NO using different starting samples (c.f. Figure E.4)	
Optimal time-averaged area-weighted outlet thermal NO (ppm)	DOE sample
9.778 (best)	5
9.782	9
9.793	1
9.826	7
9.855	8
9.864	2
10.049	6
10.113	3
10.232 (worst)	4

Table E.6 Ranking of CoSTUS design strategy search histories for time-averaged area-weighted outlet thermal NO using different starting samples (c.f. Figure E.5)	
Optimal time-averaged area-weighted outlet thermal NO (ppm)	DOE sample
9.778 (best)	7
9.791	9
9.797	5
9.800	4
9.835	3
9.867	8
9.876	1
9.999	6
10.321 (worst)	2

E.4 Bootstrap sample convergence study

(1) Spatial domain

(a) Outlet temperature profile RMSD:

Table E.7 Convergence study for number of bootstrap samples B to be used in strategy CoTGL for outlet temperature profile RMSD								
B	50	100	1000	5000	10000	20000	40000	80000
SE'	3.555	3.947	3.831	3.834	3.877	3.88	3.88	3.88

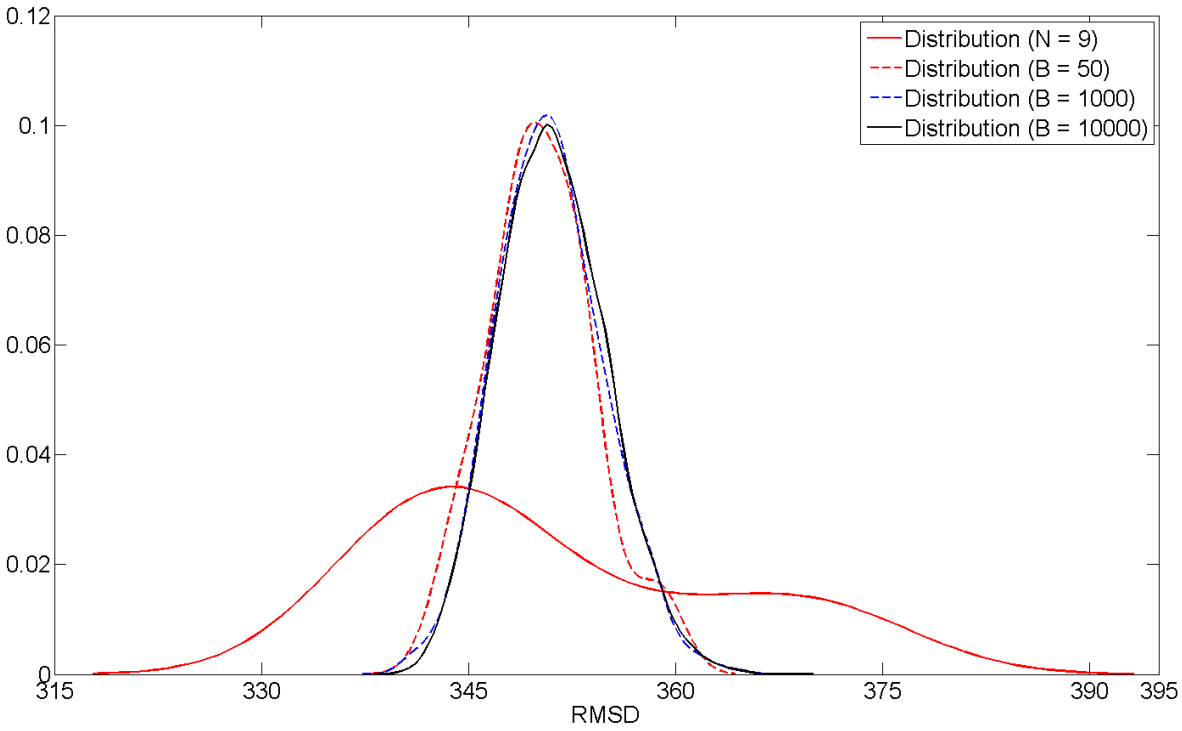

Fig. E.6 Sampling distribution of original dataset (N = 9) compared with bootstrap distribution for strategy CoTGL for outlet temperature profile RMSD

Table E.7 shows the variation of the bootstrap standard error with number of bootstrap samples B, which appears to be converged at B = 10000.

Figure E.6 shows original data and bootstrapped data distribution (for increasing B) about their respective mean values. With sample size N = 9, the sampling distribution is not normal, whereas the bootstrap sampling distribution with B=1000 and 10000 are approximately normal. At B = 1000 the sampling distribution curve appears to be converged without any significant change.

(b) Outlet thermal NO (ppm):

Table E.8 Convergence study for number of bootstrap samples B to be used in strategy CoTGL for outlet thermal NO (ppm)								
B	50	100	1000	5000	10000	20000	40000	80000
SE'	0.041	0.047	0.046	0.047	0.046	0.046	0.046	0.046

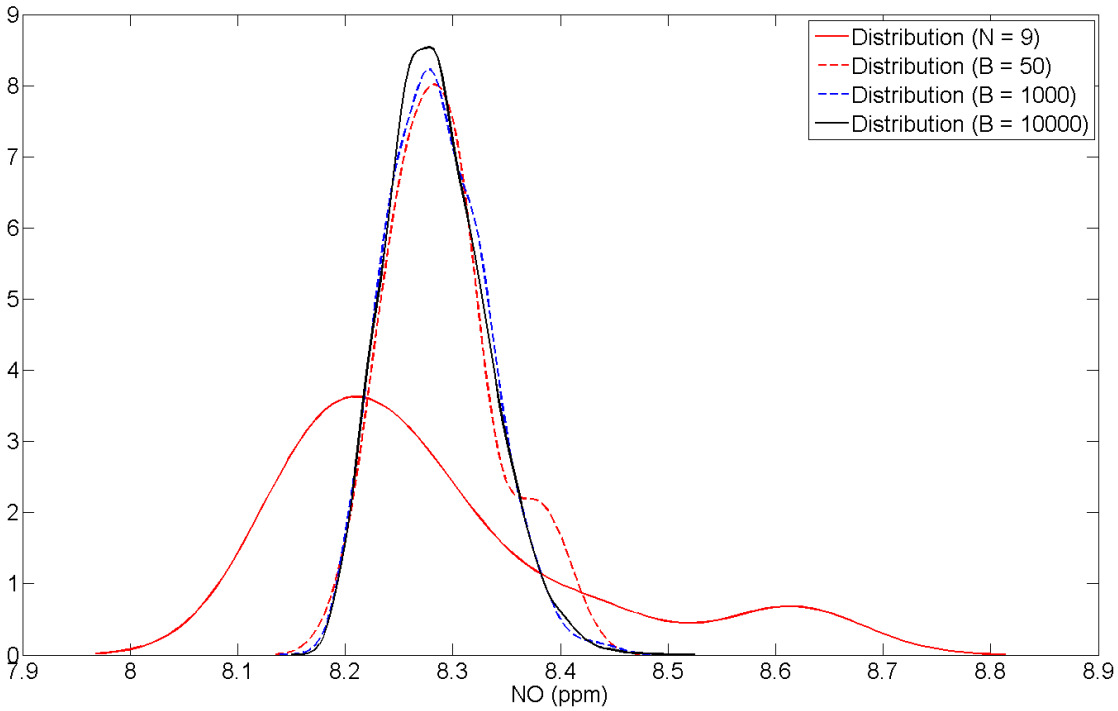

Fig. E.7 Sampling distribution of original dataset (N = 9) compared with bootstrap distribution for strategy CoTGL for outlet thermal NO

Table E.8 shows that the bootstrap standard error value at B=100 converges with no further change in its value as B increases. Figure E.7 shows original data and bootstrapped data distribution about their respective mean values. With sample size N = 9, the sampling distribution is not normal, whereas the bootstrap sampling distribution with B=50, 1000 and 10000 are approximately normal. However, at B = 1000 the sampling distribution curve appears to be converged without any significant change.

(2) Temporal domain

Similar to the bootstrap sample size analysis in spatial domain, the convergence test is performed on temporal domain objective function to determine size of B.

Table E.9 Convergence study for number of bootstrap samples B to be used for all co-Kriging strategies in temporal domain

Strategy		No. of bootstrap samples							
		50	100	1000	5000	10000	20000	40000	80000
CoSUS	Bootstrapped standard error (SE')	0.043	0.039	0.038	0.038	0.038	0.038	0.038	0.038
CoTUS-(a)		0.050	0.063	0.059	0.06	0.059	0.059	0.059	0.059
CoTUS-(b)		0.054	0.059	0.050	0.052	0.052	0.052	0.052	0.052
COSTUS		0.061	0.057	0.052	0.055	0.054	0.054	0.054	0.054

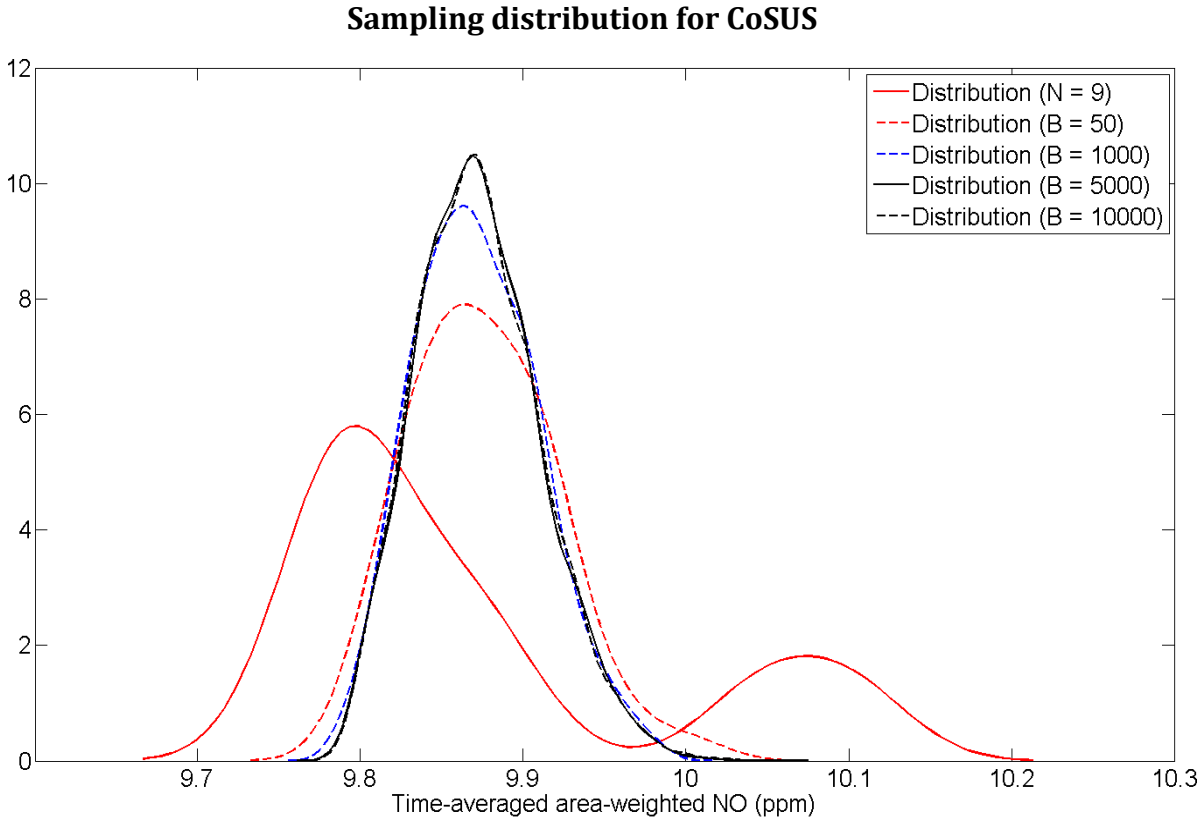

Fig. E.8 Sampling distribution of original dataset (N = 9) compared with bootstrap distribution for strategy CoSUS

Sampling distribution for CoTUS-(a)

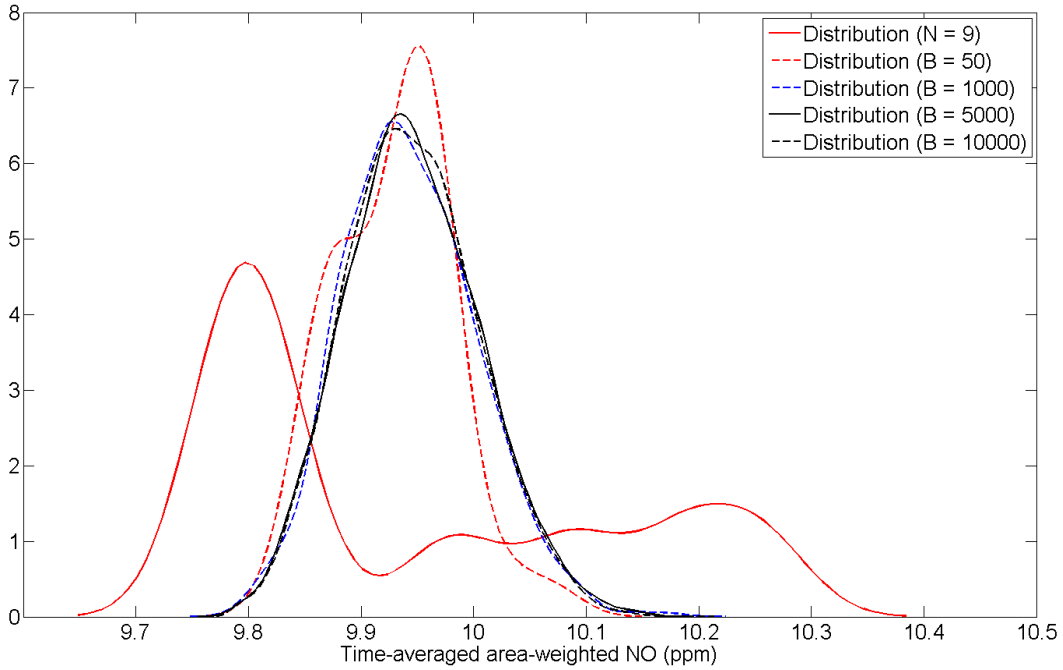

Fig. E.9 Sampling distribution of original dataset (N = 9) compared with bootstrap distribution for strategy CoTUS-(a)

Sampling distribution for CoTUS-(b)

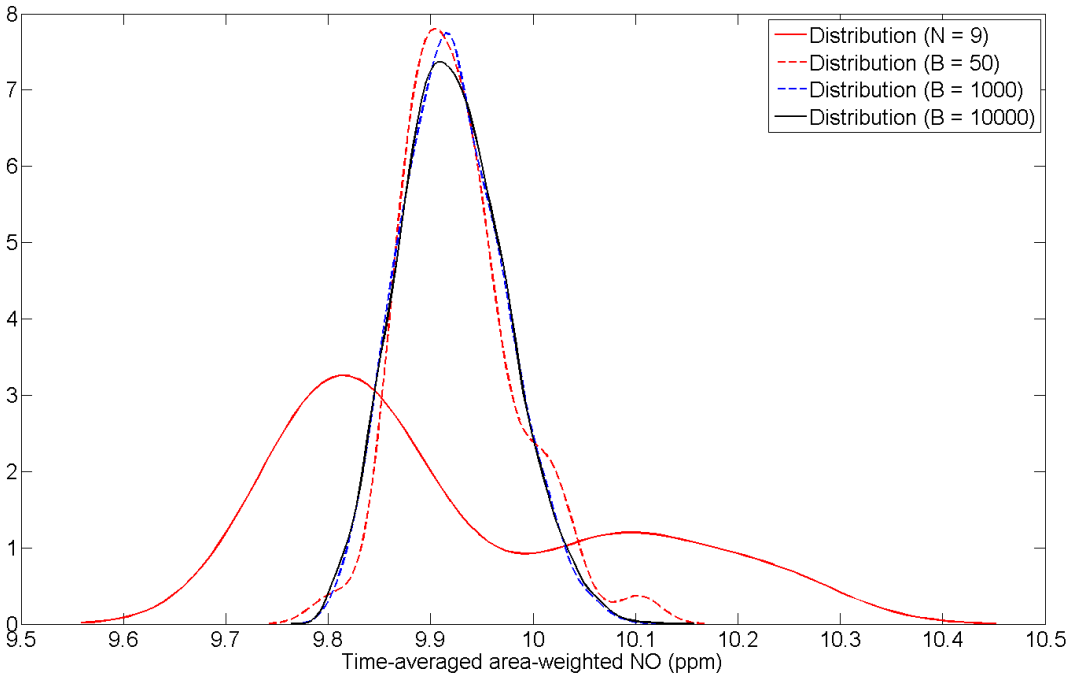

Fig. E.10 Sampling distribution of original dataset (N = 9) compared with bootstrap distribution for strategy CoTUS-(b)

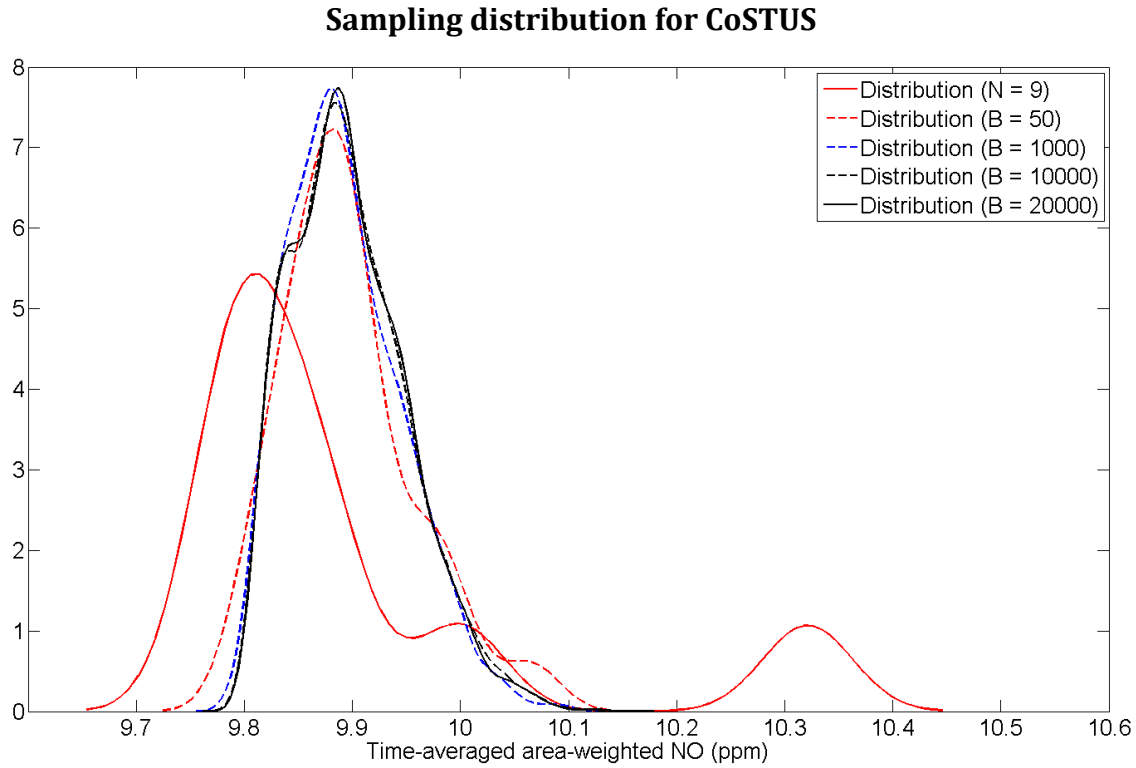

Fig. E.11 Sampling distribution of original dataset (N = 9) compared with bootstrap distribution for strategy CoSTUS

Time-parallel co-Kriging based combustor design strategy

F.1 Data fusion strategy for FLUENT data files

The data fusion process is used to combine data from multiple sources and gather that information in order to achieve inferences, which will be more efficient and potentially more accurate than if they were achieved by means of a single source. The expectation is that fused data is more informative than the original inputs.

For time-parallel simulation method-B, which requires a data fusion strategy, the following steps are performed in order to obtain a modified FLUENT data file using information from the past and future time-states:

(1) Set blending factor for data fusion, α

(2) Perform data mapping operation – this step maps all the required data within the FLUENT data files of past and future time-states.

(3) Perform data modification operation – this step modifies the header section of the FLUENT data files which consists of the information regarding the total number of flow variables and their data sets.

(4) Perform data fusion operation – this step blends (using blending factor from step 1) the individual sections of data from two source FLUENT data files and stores it into an independent new data file.

(5) Perform data integration operation – this step integrates the newly fused data file with a FLUENT header file resulting into a new blended FLUENT data file.

Figure F.1 represents the above steps graphically.

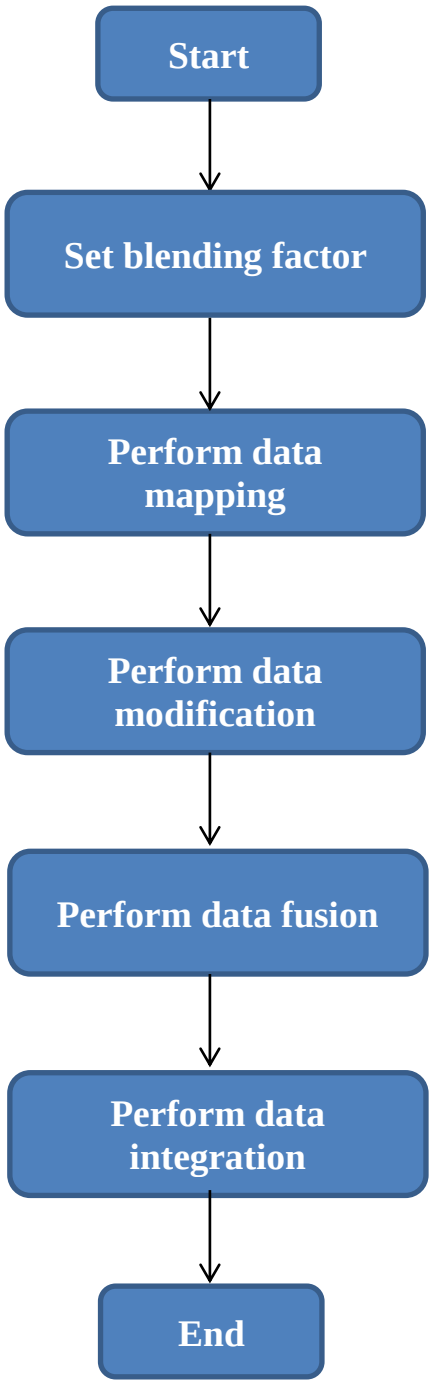

Fig. F.1 Overview of processes involved in the data fusion strategy

F.2 DOE samples of CoTPUS design strategies

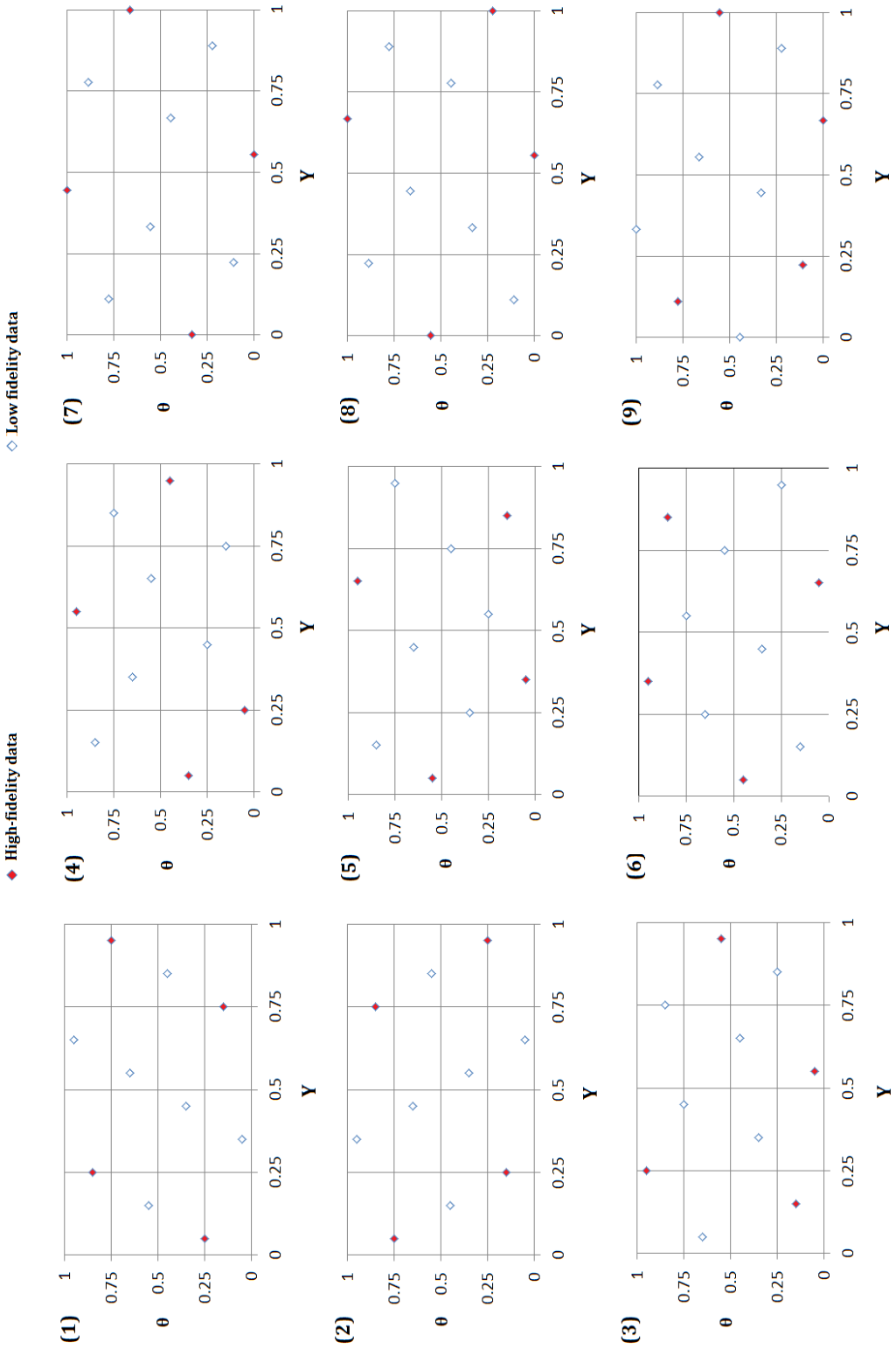

Fig. F.2 Different optimal Latin-Hypercube samples (LHS) for strategy CoTPUS-(a)

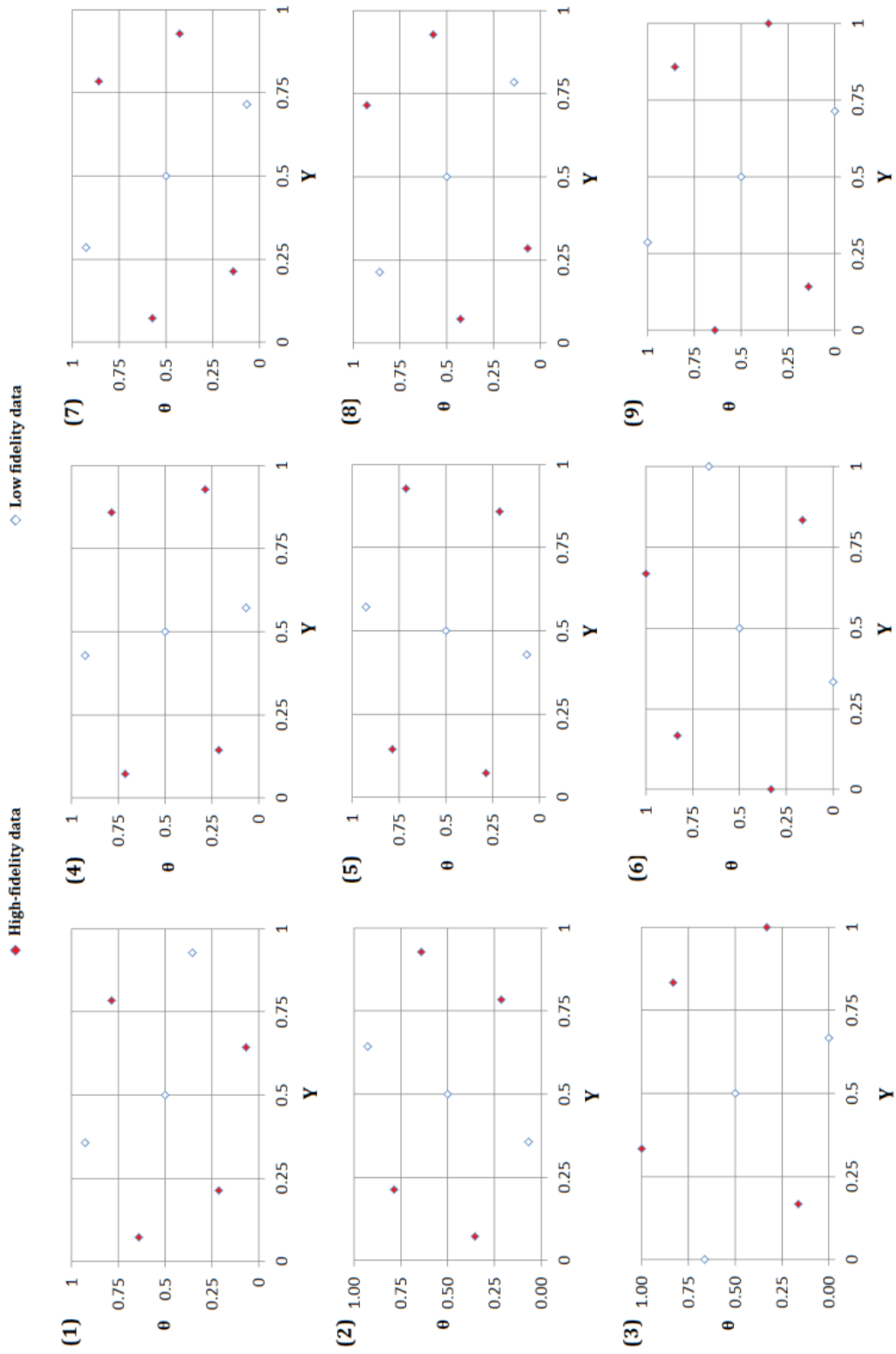

Fig. F.3 Different optimal Latin-Hypercube samples (LHS) for strategy CoTPUS-(b)

F.3 Ranking of DOE samples as per objective function values

Table F.1 Ranking of CoTPUS-(a) design strategy search histories for time-averaged area-weighted outlet temperature using different starting samples (c.f. Figure F.2)

Optimal time-averaged area-weighted outlet temperature (K)	DOE sample
1525.32 (best)	2
1532.39	4
1533.14	7
1534.37	6
1535.08	1
1535.18	3
1535.73	9
1541.85	5
1550.09 (worst)	8

Table F.2 Ranking of CoTPUS-(b) design strategy search histories for time-averaged area-weighted outlet temperature using different starting samples (c.f. Figure F.3)

Optimal time-averaged area-weighted outlet temperature (K)	DOE sample
1525.23(best)	1
1528.03	8
1528.72	4
1530.42	5
1530.56	7
1531.74	6
1531.94	2
1536.78	3
1540.41(worst)	9

F.4 Bootstrap sample convergence study

(1) CoTPUS-(a)

Table F.3 Convergence study for number of bootstrap samples B to be used for CoTPUS-(a) strategy CI								
B	50	100	1000	5000	10000	20000	40000	80000
SE'	1.894	2.292	2.137	2.149	2.151	2.151	2.151	2.151

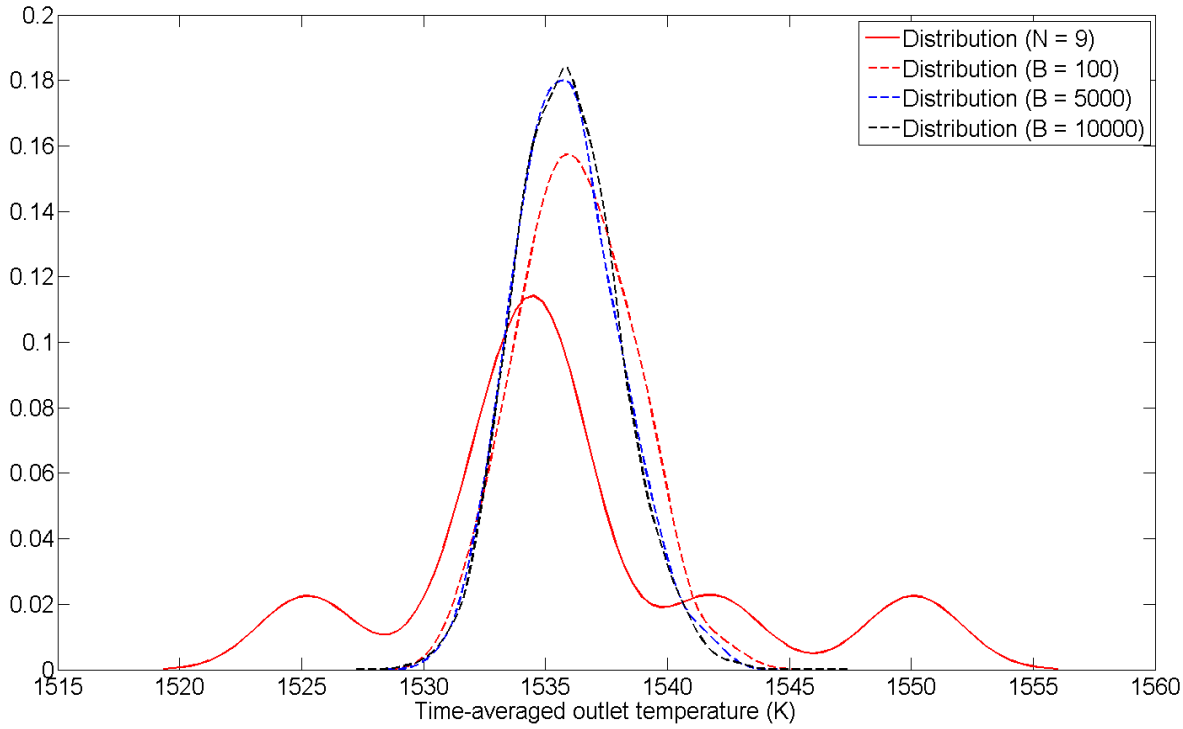

Fig. F.4 Sampling distribution of original dataset (N = 9) compared with bootstrap distribution for strategy CoTPUS-(a) for time-averaged outlet temperature (K)

(2) CoTPUS-(b)

Table F.4 Convergence study for number of bootstrap samples B to be used for CoTPUS-(b) strategy CI								
B	50	100	1000	5000	10000	20000	40000	80000
SE'	1.544	1.572	1.461	1.448	1.445	1.448	1.448	1.448

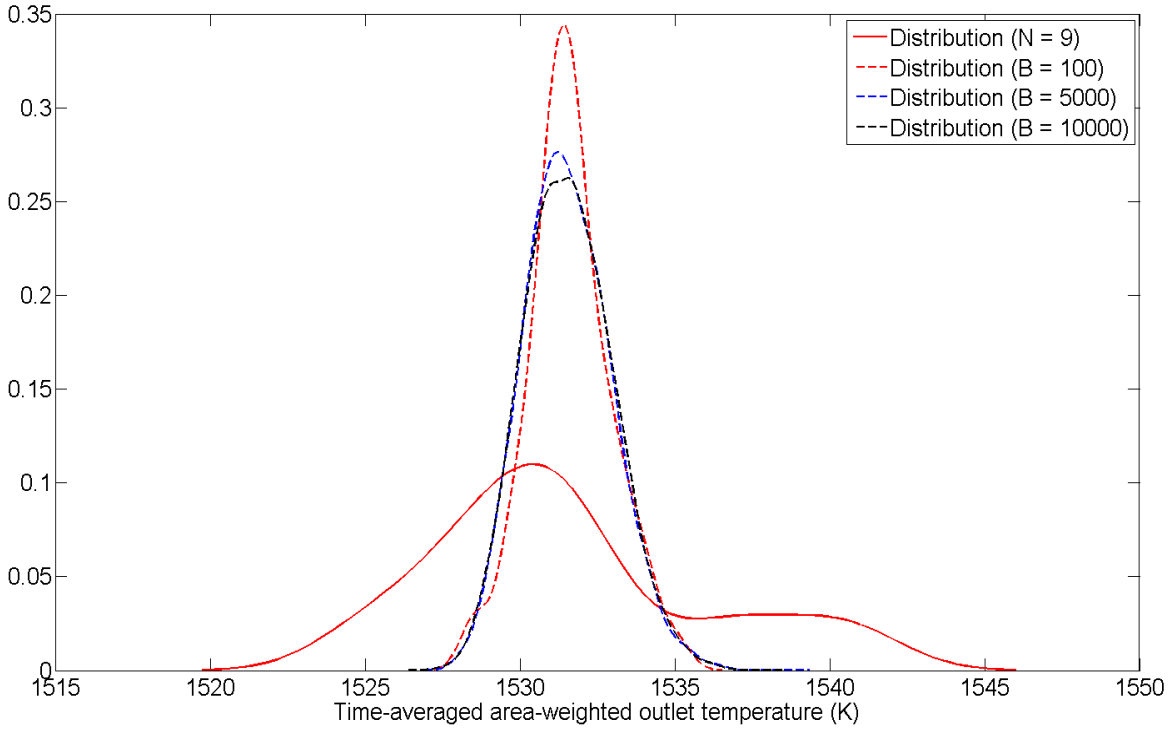

Fig. F.5 Sampling distribution of original dataset (N = 9) compared with bootstrap distribution for strategy CoTPUS-(b) for time-averaged outlet temperature (K)

Tables F.3 and F.4 show the bootstrap sample size convergence study on the CoTPUS-(a) and (b) strategies bootstrapped standard error. The number of bootstrap samples B appears to be converged at B = 5000 for both CoTPUS strategies. Figures F.4 and F.5 show the original data and bootstrapped data distribution (for increasing values of B) about their respective mean values.

References

Advisory Council for Aeronautics Research in Europe, 2001, European Aeronautics: A Vision for 2020, European Commission, Belgium

Advisory Council for Aeronautics Research in Europe, 2002, The Challenge of the Environment, Strategic Research Agenda, Vol. 2(3), European Commission, Belgium

Alecci, M., Cammarata, G., Petrone, G., 2005, Analysis and Modelling of a Low NOx Swirl Burner, Proc. COMSOL Multiphysics User's Conference

Altay, H. M., Speth, R. L., Hudgins, D. E., Ghoniem, A. F. Flame-vortex interaction driven combustion dynamics in a backward-facing step combustor, Combustion and Flame, 156(5):1111-1125

Anacleto, P. M., Fernandes, E. C., Heitor, M. V., Shtork, S. I., 2003, Swirl flow structure and flame characteristics in a model lean premixed combustor, Combustion Science and Technology, 175:1369-1388

Anand, M. S., Priddin, C. H., 2001, Combustion CFD – A Key Driver to Reducing Development Cost and Time, 15th International Symposium on Air Breathing Engines, Bangalore, India. ISABE-2001-1087

Baffico, L., Bernard, S., Maday, Y., Turinici, G., Zerah, G., 2002, Parallel-in-time molecular-dynamics simulations, Physical Review, E66:057701

Bal, G., 2003, On the convergence and the stability of the parareal algorithm to solve partial differential equations, Proceedings of the 15th International Domain Decomposition Conference (Berlin), Kornhuber, R., Hoppe, R.H.W., Peeriaux, J.,

Pironneau, O., Widlund, O. B. and Xu, J. Edition, 40:426-432

Broomhead, D. S., Loewe, D., 1988, Multivariate functional interpolation and adaptive networks, Complex systems, 2: 321-355

Beer, J. M., Chigier, N. A., 1983, Combustion Aerodynamics, Wiley, New York

Bernier, D., Lacas, F., Candel, S., 2004, Instability mechanisms in a premixed prevaporized combustor, Journal of Propulsion and Power, 20 (4): 648–656

Charest, M. R. J., 2005, Design methodology for a lean premixed prevaporized can combustor, MSc Thesis, Carleton University, Ontario

Chartier, P., Philippe, B., 1993, A parallel shooting technique for solving dissipative ODE's, Computing, 51:209-236

Cohen, J. M., Anderson, T., J., 1996, Experimental investigation of near blow out instabilities in a lean premixed step combustor AIAA 96-0819, 34th Aerospace Sciences Meeting, Reno, NV

Cohen, J. M., Proscia, W., 2005, Characterization and control of Aero engine Combustion Instability: Pratt and Whitney and NASA Experience Chapter 6. In: T. Lieuwen and V. Yang, Editors, Combustion instabilities in gas turbine engines: operational experience, fundamental mechanisms, and modeling, Progress in Astronautics and Aeronautics, 113–144

Correa, S.M., 1998, Power Generation and Aero Propulsion Gas Turbines: From Combustion Science to Combustion Technology, Proceedings of Combustion Institute, **27:**1793–1807

Crocco, L., Cheng, S. I., 1956, Theory of combustion instability in liquid propellant rocket motors, Butterworths Scientific Publications, London

Dellenback, P. A., Metzger, D. E., Neitzel, G. P., 1988, Measurements in turbulent swirling flow through an abrupt axisymmetric expansion, AIAA Journal, 26 (6):669–681

Derek Dunn-Rankin, 2008, Lean Combustion – Technology and Control, Elsevier, USA

Despierre, A., Stuttaford, P. J., Rubini P. A., 1997, Preliminary gas turbine combustor design using a genetic algorithm, 97-GT-72, International Gas Turbine and Aero-engine Congress and Exhibition, Orlando USA

Dowling, A. P., 2000, Instability in lean premixed combustors, Proc. Inst. Mech. Eng. 214 (A):317–331

Duchaine, F., Morel, T., Gicquel, L. Y. M., 2009, Computational-Fluid-Dynamics based Kriging optimization tool for aeronautical combustion chambers, AIAA Journal, 47-3

Ducruix, S., Schuller, T., Durox, D., Candel, S., 2003, Combustion dynamics and instabilities: Elementary coupling and driving mechanisms, Journal of Propulsion and Power, 19 (5):722–733

Dulikravich, G., S., Dennis, B. H., Martin, T. J., Egorov, I. N., 2001, Multi-disciplinary analysis and design optimisation, Mini-Symposium on Inverse Problems –State of the Art and Future Trends, XXIV Brazilian Congress on Applied and Computational Mathematics, Brazil

Dunham, D., Spencer, A., McGuirk, J., Dianat, M., 2009, Comparison of Unsteady Reynolds averaged Navier Stokes and Large Eddy Simulation Computational Fluid Dynamics Methodologies for Air Swirl Fuel Injectors, Journal of Engineering for Gas Turbines and Power, 131(1): 011502

Echekki T., Mastorakos, E., 2011, Turbulent Combustion Modelling: Advances, New Trends and Perspectives, Springer

Efron, B., 1979, Computers and the theory of statistics: Thinking the unthinkable, SIAM Review, 21(4):460-480

Efron, B., Tibshirani R., 1993, An Introduction to the Bootstrap, Chapman and Hall, London

Farhat, C., Chandesris, M., 2003, Time-decomposed parallel time-integrators: Theory and feasibility studies for fluid, structure and fluid structure applications, Journal of Numerical Methods in Engineering, 58:1397-1434

Fick, W., Griffiths, A.J., O'Doherty, T., 1997, Visualization of the Precessing Vortex Core in an Unconfined Swirling Flow, Optical Diagnostics in Engineering, 2(1):19-31

Fick, W., Syred, N., Griffiths, A. J., O'Doherty, T., 1996, Phase-averaged temperature characterization in swirl burners, Journal of Power and Energy, 210(A):383–395

Fischer, P. F., Hecht, F., Maday, Y., 2003, "A parareal in time semi-implicit approximation of the Navier-Stokes equations," Proceedings of the 15th International Domain Decomposition Conference (Berlin), Kornhuber, R., Hoppe, R.H.W., Peeriaux, J., Pironneau, O., Widlund, O. B. and Xu, J. Edition, Vol. 40:433-440

Fokaides, P., Weib, M., Kern, M., Zarzalis, N., 2009, Experimental and Numerical Investigation of Swirl Induced Self Excited Instabilities at the Vicinity of an Airblast Nozzle, Flow, Turbulence and Combustion, 10:1386-6184

Foller, S., 2006, Lean Burn, Aero-Engine, Fuel Injector Aero-Thermal Optimization Studies, Diploma thesis, Technical University Munich, Munich, Germany

Forrester A. I. J., 2004, Efficient global optimisation using expensive CFD simulations. PhD thesis, University of Southampton, Southampton, UK

Forrester, A. I. J., Sóbester, A., Keane, A. J., 2008, Engineering design via surrogate modelling : a practical guide, Wiley, Chichester

Forrester, A. I. J., Keane, A. J., 2009, Recent advances in surrogate-based optimization, Progress in Aerospace Sciences, 45(1-3):50-79

Fritz, J., Kroner, M., Sattelmayer, T., 2004, Flashback in a Swirl Burner with Cylindrical Premixing Zone, Journal of Engineering for Gas Turbines and Power, 126: 267-283

Froud, D., O'Doherty, T., Syred, N., 1995, Phase Averaging of the Precessing Vortex Core in a Swirl Burner Under Piloted and Premixed Combustion Conditions, Combustion and Flame, 100:407-412

Garrido, I., Espedal, M. S., Fladmark, G. E., 2003, A convergence algorithm for time parallelization applied to reservoir simulation, Proceedings of the 15th International Domain Decomposition Conference (Berlin), Kornhuber, R., Hoppe, R.H.W., Peeriaux, J., Pironneau, O., Widlund, O. B. and Xu, J. Edition,40:469-476

Gander, M., Vandewalle, S., 2007, Analysis of the parareal time-parallel time-integration method, SIAM Journal on Scientific Computing, 29(2), 556-578

Goldberg, D. E., 1989, Genetic Algorithms in Search, Optimization and Machine Learning, Kluwer Academic Publishers, Boston, MA

Ghoniem, A. F., Park, S., Wachsman, A., Annaswamy, A., Wee, D., Altay, H. M., Mechanism of combustion dynamics in a backward facing step stabilised premixed flame, Proceedings of the Combustion Institute, 30(2): 1783-1790

Gouws, J. J., 2007, Combining a one-dimensional empirical and network solver with computational fluid dynamics to investigate possible modifications to a commercial gas turbine combustor, MEng Thesis, University of Pretoria, Pretoria, South Africa

Gulati, T., Tolpadi, A., Vanduesen, G., 1994. Effect of dilution air on scalar flow field at the combustor exit. AIAA Conference, 94–0221.

Gupta, A. K., Beer, J. M., Swithenbank, J., 1977, Concentric multi-annular swirl burner, stability limits and emission characteristics, Proceedings of the Combustion Institute, 14:79–91

Gupta, A. K., Lilley, D. J., Syred, N., 1984, Swirl Flows. Tunbridge Wells, Abacus Press, UK

Gutmann, H. M., 2001, A radial basis function method for global optimization, Journal of Global Optimization, 19(3):201-227

Hall, M. G., 1972, Vortex breakdown, Annual Review of Fluid Mechanics, 4:195–218

Hammond, D. C., Mellor, A. M., 1970, A preliminary investigation of gas turbine combustor modelling, Combustion Science and Technology, 2:67-80

Hastie, T., Tibshirani, R., Friedman, J., 2001, The Elements of Statistical Learning; Data Mining, Inference, and Prediction, Springer series in statistics, Springer, New York

Hill, S. C., Smoot,, L. D., Modelling of nitrogen oxides formation and destruction in combustion systems, Progress in Energy and Combustion Science, 26:417-458

Hirschfelder, J.; Curtiss, C. F.; Bird, R. B., 1954. Molecular Theory of Gases and Liquids, Wiley, New York

Holdeman, J. D., Mongia, H. C., Mularz, E. J., 1989, Assessment, development and application of combustor aerothermal methods, NASA TM-4087, USA

Holdeman, J.D., Liscinsky, D.S., Oechsle, V.L., Samuelsen, G.S., Smith, C.E., 1997. Mixing of multiple jets with a confined subsonic cross flow. Part 1: Cylindrical duct. Journal of engineering for gas turbine and power, 119:852–862

Holland, J. H., 1975, Adaptation in natural and artificial systems, University of Michigan Press, USA

Huang, Y., Yang, V., 2009, Dynamics and Stability of Lean-Premixed Swirl-Stabilized Combustion, Progress in Energy and Combustion Science, 35(4):293-364

Huck, K. L., and Marek, C. J., 1978, Lean Combustion Limits of a Confined Premixed Prevaporized Propane Jet, NASA, TM-78868

Jeong, S., Minemura, Y., Obayashi, S., 2006, Optimisation of combustion chamber for diesel engine using Kriging model, Journal of Fluid Science and Technology, 1(2), 138-146

Jochmann, P., Sinigersky, A., Hehle, M., Schafer, O., Koch, R., Bauer, H.J., 2006, Numerical Simulation of a Precessing Vortex Breakdown, International Journal of Heat and Fluid Flow, 27:192-203

Jones, A.T., 1945, Singing Flames, Journal of the Acoustical Society of America, 16(4),

254-266

Jones, D. R., 2001, A taxonomy of global optimization methods based on response surfaces, Journal of Global Optimization, 21(4):345-383

Keller, H. B., 1968, Numerical Methods for Two-Point Boundary Value Problems, Blaisdell, Waltham, MA

Keller, J. O., Vaneveld, L., Korschelt, D., Hubbard, G. L., Ghoniem, A. F., Daily, J. W., and Oppenheim, A. K., 1982, Mechanism of Instabilities in Turbulent Combustion Leading to Flashback, AIAA Journal, 20:254–262

Kim, J., Kline, S. J., and Johnston, J. P., 1978, Investigation of Separation and Reattachment of a Turbulent Shear Layer : Flow Over a Backward-Facing Step, Thermo sciences Division, Dept. of Mechanical Engineering, Stanford University Rept. MD-37

Krige, D.G., 1951, "A Statistical Approach to Some Basic Mine Valuation Problems on the Witwatersrand," Journal of the Chemical, Metallurgical and Mining Engineering Society of South Africa, 52/6, pp.119-139

Kuo, K. K., 1986, Principles of Combustion, Wiley-Interscience, New York

Lai, M. K., Reynolds, R. S., Armstrong, J., CFD-based parametric design tool for gas turbine combustors from compressor deswirl exit to turbine inlet, GT2002-30090, ASME Turbo Expo 2002: Power for Land, Sea and Air, Amsterdam, Netherlands

Le Conte, J., 1858, Philosophical Magazine HP, 235

Lefebvre, A., H., 1977, Lean Premixed/Prevaporized Combustion, NASA CP-2016

Lefebvre, A.H., 1983, Gas Turbine Combustion, Taylor and Francis, Philadelphia

Leibovich, S., 1978, The structures of vortex breakdown, Annual Review of Fluid Mechanics, 10:221–246

Leibovich, S., 1984, Vortex stability and breakdown: survey and extension, AIAA Journal, 22:1192–1206

Lewis, B., Elbe, G. V., 1987, Combustion, Flames and Explosions of Gases, Academic Press, Pennsylvania

Lieuwen, T., 2003, Modeling premixed combustion-acoustic wave interactions: A review, Journal of Propulsion and Power, 19 (5):765–781

Lieuwen, T., Yang, V., 2005, Combustion Instabilities in Gas Turbine Engines – operational experience, fundamental mechanisms, and modelling, Progress in Astronautics and Aeronautics, 210

Lions J., Maday, Y., Turinici, G., 2001, Resolution d'EDP par un schema en temps 'parareel', Comptes Rendus des Séances de l Academie des Sciences, Paris, Séries I, Mathematique, 332 :661-668

Locatelli, M., 1997, Bayesian algorithms for one-dimensional global optimisation, Journal of Global Optimisation, 10:57-76

Lucca-Negro, O., O'Doherty, T., 2001, Vortex Breakdown: A Review, Progress in Energy and Combustion Science, 27, 431-481

Mackay, M. D., Beckman, R. J., Conover, W., J., 1979, A comparison of three methods for selecting values of input variables in the analysis of output from computer code, Technometrics, 21:239-245

Maday, Y., Turinici, G., 2003, Parallel-in-time algorithms for quantum control: The parareal time-discretization scheme, International Journal of Quantum Chemistry, 93(3), 223-228

Malalasekara, W., Veersteeg, H. K., 1995, An Introduction to Computational Fluid Dynamics, Longman Scientific and Technical, England

Malte, P. C., Pratt, D. T., 1974, Measurement of atomic oxygen and nitrogen oxides in jet stirred combustion engines, Proceedings of the combustion institute, 15:1061

Matthews, P. C., Blessing, L. T. M., Wallace, K. M., 2002, The introduction of a design heuristics extraction method, Advanced engineering informatics, 16(1):3-19

McGuirk, J. J., Spencer, A., 2000, Coupled and uncoupled CFD prediction of the characteristics of jets from combustor air admission ports, ASME 2000-GT-0125

Mellor, A. M., 1976, Gas Turbine Engine Pollution, Progress in Energy and Combustion Science, Pergamon Press, Oxford, England, I:111-133

Mellor, A.M., 1990, Design of Modern Gas Turbine Combustor, Academic Press, England

Miranker, W. L., Liniger, W., 1964, Parallel methods for the numerical integrating of ordinary differential equations, Mathematics of Computation, 91:303-320

Mongia, H. C., 1998, Aero-Thermal Design and Analysis of Gas Turbine Combustion

Systems: Current Status and Future Direction, AIAA Paper No. 98-3982

Mongia, H. C., 2001, A Synopsis of Gas Turbine Combustor Design Methodology Evolution of Last 25 Years, ISABE-2001-1086

Mongia, H. C., Held, T. J., Hsiao, G. C., Pandalai, R. P., 2005, Incorporation of combustion instability issues into design process: GE aero-derivative and aero engines experience Chapter 3. In: T. Lieuwen and V. Yang, Editors, Combustion instabilities in gas turbine engines: operational experience, fundamental mechanisms, and modeling, Progress in Astronautics and Aeronautics, 43–64

Morris, M. D., Mitchell, T. J., 1995, Exploratory designs for computational experiments, Journal of Statistical Planning and Inference, 43:381–402

Motsamai O. S., Visser J. A., and Morris R. M., 2008, Multi-disciplinary design optimization of a combustor. Engineering Optimization, 40(2):137-156

Myers, R. H., Montgomery, D. C., 1995, Response surface methodology: process and product optimization using designed experiments, Wiley, New York

Najm, H. N., Ghoniem, A. F., 1994, Coupling Between Vorticity and Pressure Oscillations in Combustion Instability, Journal of Propulsion and Power,10(6)

Nievergelt, 1964, Parallel methods for integrating ordinary differential equations, Communications of the ACM, 7 (12):731-733

Nightingale, P., 2000, The Product-Process-Organization Relationship in Complex Development Projects, Research Policy, Elsevier, 29: 913-930

Paschereit, C. O., Gutmark, E., Weisenstein, W., 1998, Structure and Control of thermoacoustic instabilities in a gas-turbine combustor, Combustion Science and Technology, 138:213–232

Patel, N., Menon, S., 2008, Simulation of spray-turbulence-flame interactions in a lean direct injection combustor, Combustion and Flame, 153:228-257

Peters, N., 2000, Turbulent Combustion, Cambridge University Press, UK

Poinsot, T. J., Trouve A. C., Veynante, D. P., Candel, S. M., Esposito, E., J., 1987, Vortex-driven Acoustically Coupled Combustion Instabilities, Journal of Fluid Mechanics, 177:265-292

Pope, S. B., Turbulent Flows, Cambridge University Press, UK

Powell, M. J. D., 1987, Radial basis functions for multivariate interpolation: a review,

In Algorithms for Approximation, Clarendon press, Oxford, UK

Poinsot, T., Veynante, D., 2005, Theoretical and Numerical Combustion, Edwards Inc., USA

Rayleigh, J., W., S., 1945, The Theory of Sound: Volume 2, Dover Publications, New York, 224-7

Rogero J.M, 2003, A Genetic algorithms based optimisation tool for the preliminary design of gas turbine combustors,PhD Thesis, Cranfield University

Rogero, J.M., Rubini, P. A., 2001, Optimisation of combustor wall heat transfer and pollutant emissions for preliminary design using evolutionary techniques, Proceddings of ISOABE, Bangalore, India (ISBN 1-56347-515-4)

Renard, P. H., Thevenin, D., Rolon, J., C., Candel, S., 2000, Dynamics of flame/vortex interactions, Progress in Energy and Combustion Sciences, 225-282

Rizk, N.K., Mongia, H.C., Gas turbine combustor design methodology, CONF-8606184, AIAA Joint Propulsion Conference, Huntsville, USA

Robinson, T., D., Willcox, K., E., Eldred, M. S., Haimes, R., 2006, Multifidelity Optimization for Variable-Complexity Design, 11th AIAA/ISSMO Multidisciplinary Analysis and Optimization Conference, Virginia, AIAA 2006-7114

Rolls-Royce, 2007, The Jet Engine, Key Publishing, UK

Roshko, A., 1976, Structure of Turbulent Shear Flows: A New Look, AIAA Journal, 14: 1349-1357

Roux, S., Lartigue, G., Poinsot, T., Meier, U., Berat, C.,2005, Studies of Mean and Unsteady Flow in a Swirled Combustor using Experiments, Acoustic Analysis and Large Eddy Simulations, Combustion and Flame, 141:40-54

Sacks, J., Welch, W. J., Mitchell, T. J., Wynn, H., P., 1989, Design and analysis of computer experiments, Statistical Science, 4(4): 409-435

Salinas, A. R., Richardson, C., Abidi, M. A., Gonzalez, R. C., 1996, Data fusion: Colour edge detection and surface reconstruction through regularization, IEEE Transactions on Industrial Electronics, 43 (3)

Saltz, J. H., Naik, V. K., 1988, Towards developing robust algorithms for solving partial differential equations on MIMD machines, Parallel Computing, 6:19-14

Saravanamuttoo, H. I. H., Rogers, G. F. C., Cohen, H., Straznicky, P. V., Gas Turbine

Theory, Prentice Hall, England

Sarpkaya, T., 1971, On stationary and travelling vortex breakdown, Journal of Fluid Mechanics, 45:545–559

Schildmacher, K.-U., Koch, R., Krebs, W., Prade, B., 2003, Experimental Investigation of the Interaction of Flame Front Fluctuations with Combustion of a Premixing as Turbine Burner, Duetscher Flammentag,, 21:297-302

Selle, L., Lartigue, G., Poinsot, T., Koch, R., Schildmacher, K.-U., Krebs, W., Kaufmann, P., Veynante, D., 2004, Compressible Large Eddy Simulation of Turbulent Combustion in Complex Geometry on Unstructured Meshes, Combustion and Flame, 137, 489-505

Seo S., 1999, Parametric study of lean-premixed combustion instability in a pressurized model gas turbine combustor. Ph.D. Thesis, Department of Mechanical and Nuclear Engineering, The Pennsylvania State University, University Park, PA

Sivaramakrishna, G., 2010, Design analysis and CFD studies on gas turbine combustors, DRDO Science Spectrum, 1-8

Sobol, I. M., 1979, On the systematic search in a hypercube, SIAM Journal of Numerical Analysis, 16:790–793

Song, W., Keane, A. J., 2005, A new hybrid updating scheme for an evolutionary search strategy using genetic algorithms and kriging, 47th AIAA/ASME/ASCE/AHS/ASC Structures, Structural Dynamics and Materials Conference. 46th AIAA/ASME/ASCE/AHS/ASC Structures, Structural Dynamics & Materials Conference, American Institute of Aeronautics and Astronautics, 1-8.

Spadaccini, L. J., 1974, Low Emission Combustors for Gas Turbine Power plants, Combustion Science and Technology, 9:133-136

Staff, G., Ronquist, E., Stability of the parareal algorithm, Proceedings of the 15th International Domain Decomposition Conference (Berlin), Kornhuber, R., Hoppe, R.H.W., Peeriaux, J., Pironneau, O., Widlund, O. B. and Xu, J. Edition, 40:449-456

Statnikov, R. B., Matusov, J. B., 1995, Multicriteria optimization and engineering: theory and practice, Chapman & Hall, New York

Stuttaford, P. J., Rubini, P. A., 1996, Preliminary gas turbine combustor design using a network approach, ASME Turbo Expo, 96-GT-135

Stuttaford, P. J., Rubini, P. A., 1997, Assessment of a radiative heat transfer model for a new gas turbine combustor preliminary design tool, AIAA 97-0294, 35th Aerospace

Sciences Meeting and Exhibition, Reno, NV

Sutton, G. P., Biblarz, O., 2000, Rocket propulsion elements (7th ed.), John Wiley and Sons

Syred, N., Beer, J., 1972, The damping of precessing vortex cores by combustion in swirl generators, Astronautica Acta, 17:783–801

Syred, N., Beer, J.M., 1974, Combustion in Swirling Flows - A Review, Combustion and Flame, 23:143-201

Syred, N., Fick, W., O'Doherty, T., Griffiths, A. J.,1997, The effect of the precessing vortex core on combustion in a swirl burner, Combustion Science and Technology, 125:139–157

Tangermann, E., Pfitzner, M., 2009, Evaluation of Combustion Models for Combustion-Induced Vortex Breakdown, Journal of Turbulence, 10:N7

Theory Guide, 2009, ANSYS FLUENT™ Version 12.1

Thibaut, D., Candel, S., 1998, Numerical Study of Unsteady Turbulent Premixed Combustion: Application to Flashback Simulation, Combustion and Flame, 113:53-65

Toal, D. J. J., Bressloff, N. W., Keane, A. J., 2008, Kriging hyperparameter tuning strategies, AIAA Journal, 46(5):1240-1252

Trindade, J. M. F., Pereira, J. C. F., 2004, Parallel-in-time simulation of the unsteady Navier-Stokes equations for incompressible flow, International Journal for Numerical Methods in Fluids, 45(10):1123-1136

Trindade, J. M. F., Pereira, J. C., F., 2006, Parallel in time simulation of two-dimensional, unsteady, incompressible laminar flows, Numerical Heat Transfer, Part B, 50:25

User's Guide, 2006, FLUENT™ Version 6.3

Venkataraman, K. K., Lee, B. J., Preston, L. H., Simons, D. W., Lee, J. G., and Santavicca, D., A., 1999, Mechanism of Combustion Instability in a Lean Premixed Dump Combustor, Journal of Propulsion and Power, 15 (6):909–918

Wagner, T., Emmerich, M., Deutz, A., Ponweiser, W., 2011, On expected improvement criteria for model based multi-objective optimisation, Parallel Problem Solving From Nature, Lecture Notes in Computer Science, 6238:718-727

Wang, S., Yang, V., Hsiao, G., Hsieh, S., Mongia, H., C., 2007, Large-eddy simulations of gas-turbine swirl injector flow dynamics, Journal of Fluid Mechanics, 583:99-122

Wankhede, M. J., Bressloff, N. W., Keane, A. J., Caracciolo, L., Zedda, M., 2010, An analysis of unstable flow dynamics and flashback mechanism inside a swirl-stabilised lean burn combustor, Proc. ASME Turbo Expo 2010: Power for Land, Sea and Air, GT2010-22253, Glasgow, UK

Wankhede, M. J., Bressloff, N. W., Keane, A. J., 2011, Combustor design optimisation using co-Kriging of steady and unsteady turbulent combustion, Proc. ASME Turbo Expo 2011, GT2011-46420, Vancouver, Canada

Wankhede, M. J., Bressloff, N. W., Keane, A. J., 2011, Combustor design optimisation using co-Kriging of steady and unsteady turbulent combustion, Journal of Engineering for Gas Turbines and Power, GTP-11-1113, 133(12), (DOI: 10.1115/1.4004155)

Weiss R. R., 1966, An introduction to combustion instability in liquid propellant rocket engines. AFRPL-TR-66-150, Edwards, CA

Williams, F. A., 1985, Combustion Theory, Benjamin Cummings, CA

Yu, K., H., Trouvé, A., Daily, J., W., 1991, Low-frequency pressure oscillations in a model ramjet combustor, Journal of Fluid Mechanics, 232:47-72

Yuret, D., Maza, M., 1993, Dynamic hill climbing: Overcoming the limitations of optimization techniques, Second Turkish Symposium on Artificial Intelligence and Neural Networks, 254

Zinn, B. T., Lieuwen, T., 2005, Combustion Instabilities: Basic concepts Chapter 1. In: T. Lieuwen and V. Yang, Editors, Combustion instabilities in gas turbine engines: operational experience, fundamental mechanisms, and modeling, Progress in Astronautics and Aeronautics, 3–24

Zukowski, E. E., Marble, F. E., 1956, Proc. Gas Dynamics Symposium on Aerothermodynamics, North-western University, Evanstopn, 205